Self-organization of sediment transport in alluvial rivers

Anaïs Abramian

UNIVERSITÉ SORBONNE PARIS CITÉ

Thèse préparée à l'Institut de Physique du Globe de Paris
École doctorale STEP'UP - ED 560
Équipe de Dynamique des Fluides Géologiques

Auto-organisation du transport sédimentaire dans les rivières alluviales

par

Anaïs Abramian

Soutenue le 15 novembre 2018

Thèse de doctorat des Sciences de la Terre et de l'Environnement
Spécialité : Géophysique
dirigée par Olivier Devauchelle & Eric Lajeunesse

devant un jury composé de :

Pascale Aussillous	Rapporteure
Valérie Vidal	Rapporteure
Philippe Claudin	Examinateur
Philippe Gondret	Examinateur
Claude Jaupart	Examinateur
Olivier Devauchelle	Co-encadrant de thèse
Eric Lajeunesse	Directeur de thèse

Remerciements

Merci Eric, merci Olivier. Vous m'avez proposé un sujet de thèse passionnant et vous m'avez accordé votre confiance tout au long de ces trois années de thèse. Grâce à votre enthousiasme, votre exigence et votre patience, j'ai appris ce qu'était le métier de chercheur dans les meilleurs conditions. Vous m'avez transmis le plaisir que vous avez à travailler, et vous m'avez donné envie de continuer dans la recherche, en tout cas pour les quelques années à venir.

Merci également à Pascale Aussillous, qui a rapporté ce manuscrit avec beaucoup de bienveillance : c'était toujours un vrai plaisir de te croiser en conférence ou au laboratoire lors de ma thèse. Valérie Vidal a également rapporté mon travail : merci pour tes questions et tes remarques qui ont amélioré ce manuscrit, ainsi que le soin que tu as eu à relire ma thèse en détails. Je t'ai rencontrée dès mon M1 pour faire un projet expérimental sur « le bruit des volcans ». C'est sans aucun doute lors de ce projet que mon attrait pour la géophysique a débuté. Merci à Philippe Gondret, qui m'a suivie depuis mon M2 en tant que membre de mon comité de thèse, puis de mon jury de thèse ; merci à Philippe Claudin, dont les remarques sont toujours très intéressantes ; et enfin merci Claude Jaupart, qui veille sur tous les doctorants du laboratoire avec attention et bienveillance, et qui est l'une des raisons pour laquelle nous nous sentons si bien en DFG.

Les permanents du laboratoire n'y sont pas pour rien non plus ! Merci à François (Métivier), le chef de la géomorpho, pour ta bonne humeur et ta disponibilité. Tu assures aussi bien lors de l'organisation de notre mission de terrain en Chine, qu'à la tête de l'UFR. Merci à Edouard (Kaminski) avec qui j'ai eu un immense plaisir à enseigner les TPs et les TDs et qui m'a appris beaucoup sur l'enseignement à l'université. C'était extrêmement agréable de pouvoir proposer des nouveautés, d'en discuter et, parfois, de les tenter. Merci à tous les autres membres permanents de DFG : ce labo est très chaleureux grâce à votre bonne humeur permanente. J'ai également enseigné avec des enseignants chercheurs d'autres laboratoires de l'IPG et j'y ai toujours pris un très grand grand plaisir. Je remercie tout particulièrement la team TP dont font partie Alex (Fournier) et Pascal (Godefroy), sans qui ces TPs ne fonctionneraient pas si bien. Enfin, Zarie (Rouas) fait marcher cette UFR

comme sur des roulettes, ce qui a rendu l'enseignement à STEP d'autant plus agréable.

Évidemment, la bonne ambiance qui règne au sein de DFG est aussi due aux doctorants. Merci aux vieux qui m'ont accueillie chaleureusement : Adrien, Alberto, Samuel, Loïc, etc. Merci aux jeunes qui rendent la pause café très ~~longue~~ conviviale : Cyril(s), Valentin, Viviane, Audrey, Alexandra. Enfin, je remercie tout particulièrement Pauline, avec qui j'ai beaucoup interagi sur le travail, et pas seulement ! C'est toujours un plaisir de discuter avec toi.

Merci aux chercheurs hors du laboratoire qui m'ont suivie tout au long de ce travail de thèse : Sylvain Courrech du Pont, membre de mon comité de thèse, Pierre-Yves Lagrée, souvent en visite à l'IPG, qui a toujours de bons conseils. Merci à l'école doctorale, qui m'a permis de faire un séjour à l'étranger durant l'été 2017. J'ai fait partie, pendant 3 mois, de l'équipe de Shmuel Rubinstein (Harvard University, Cambridge, USA). Thanks Shmuel : you hosted me in the best conditions, and gave me some of your passion on mechanical instabilities. Thanks to Emmanuel (Virot) : I learnt a lot with you, and your references to all these old, fancy papers are always awesome. Thanks also to the PhD students at the SMR lab : Lisa, Ryan, Sam, etc., whom I spent also a very nice conference trip in Israel.

Merci à ceux que j'ai rencontré avant ma thèse, et qui m'ont donné envie de faire de la physique. Je pense notamment à Jeremie Palacci, ainsi qu'à deux de mes profs de prépa qui ont beaucoup compté lors de mon cursus : Emmanuel Angot et Marie-Pierre Rey-Nony. Vos cours resteront des exemples pour moi.

Mes amis de toute part ont été formidables lors de ces trois ans, ainsi que le jour de ma soutenance. Merci à tous pour cette journée que vous m'avez faite passer. Merci aux anciens de l'ENS : Clara, Laura, car sans vous ma licence et mon master (et mes vacances) auraient été bien différents ! Vous avez été aussi très présentes lors de ces 3 années. Merci Helmy pour nos discussions passionnantes, entre autre sur la physique. Merci à Valentin pour tout ce que tu as fait pour préparer le jour de ma soutenance. Pendant ma thèse, j'ai eu l'occasion à plusieurs reprises de recroiser des personnes du M2 ; je pense en particulier à Pierre (Barrat-Charlaix) et à nos conversations interminables. Enfin, merci à mes plus vieilles amies, aussi, Morgane, Lauranne, Aline, pour votre soutien sans faille !

Merci évidemment à mes deux parents, qui, depuis toujours me soutiennent et m'encouragent dans tous mes choix : vous m'avez fait confiance dès mon plus jeune âge tout en m'accordant une grande liberté. J'ai beaucoup de chance d'avoir des parents comme vous. Merci à ma petite soeur Sophie : je t'aime et je t'admire énormément.

Table des matières

Introduction générale

Une rivière alluviale, contrairement à une rivière à fond rocheux, s'écoule sur une épaisse couche de sédiments (Fig. 1). Lorsqu'elle creuse son lit, elle entraîne, transporte, dépose des sédiments, et façonne ainsi sa propre forme (Leopold & Wolman 1957). Cette forme s'ajuste rapidement aux forçages extérieurs, qu'ils soient anthropiques, climatiques ou tectoniques, ce qui la rend constamment mobile. Par exemple, la rivière Kosi, qui prend sa source dans l'Himalaya et qui coule dans la région densément peuplée du Bihar en Inde, a changé régulièrement de lit au cours des siècles passés (Fig. 2, Gole & Chitale (1966)). Ces modifications brutales du cours d'une rivière, appelées avulsions, sont régulièrement observées dans les deltas ou sur les cônes alluviaux, où les sédiments sont déposés en masse par la rivière.

Malgré l'évolution constante de son cours, une rivière favorise le développement d'une société. Les populations s'implantent près de ses berges pour s'approvisionner en eau courante ou faciliter les transports de marchandises et de voyageurs. De ce fait, l'Homme cherche à domestiquer les cours d'eau pour les mettre en valeur et protéger les territoires environnants.

Pour contrôler la forme et la dynamique d'une rivière, on peut avoir recours à différents ouvrages. Par exemple, un système de digues restreint la rivière Kosi au bord ouest du cône alluvial et empêche ses avulsions catastrophiques (Sinha 2008, Mishra *et al.* 2008). Un immense barrage a également été construit dans les années 1960 à la frontière indo-népalaise. Il alimente un réseau de canaux d'irrigations sur une zone de 250 km^2 et fournit 20 MW d'électricité par an aux deux pays. Ces installations ont permis d'accroître l'activité agricole de cette région et ont contribué à son développement.

Cependant, l'aménagement de la Kosi a fortement impacté sa dynamique. Les sédiments qu'elle a déposés ont surélevé son lit et fragilisé ses digues. Suite à une forte mousson, le 18 août 2008, une brèche s'est formée et la rivière a brutalement abandonné son lit au profit d'un ancien tracé, inondant des villes, des villages et des terrains agricoles (Sinha 2008; 2009). Elle a détruit ainsi des centaines de milliers d'habitations et a entraîné le déplacement de plus d'un million de personnes.

En résumé, l'attractivité d'un fleuve s'accompagne d'une urbanisation ainsi que d'une concentration des populations et des activités dans des zones à risque d'inondation. C'est

FIGURE 1 – Photographie de l'Ain à Saint-Maurice-de-Gourdans, Port Galland (France). Le lit de cette rivière alluviale est composée de galets, dont la taille est comprise entre 1 et 100 mm. L'échelle approximative est donnée par les baigneurs.

le cas de la plupart des métropoles européennes et mondiales, comme Paris, Londres, ou New York. Il est donc nécessaire de comprendre comment une rivière alluviale façonne son lit et sélectionne son cours pour concevoir des aménagements durables.

Du point de vue géologique, les rivières jouent un rôle fondamental dans le cycle de formation et d'érosion de la croûte terrestre (cycle géologique). Elles incisent les reliefs, concentrent la majorité des flux de matière sur les continents et façonnent la surface continentale (Allen 1997).

De l'amont vers l'aval, la rivière est successivement un lieu d'érosion, de transit, puis de dépôt. Sa charge sédimentaire est le résultat de l'interaction, soit chimique soit mécanique, entre l'eau et les roches. Selon sa charge sédimentaire, elle acquiert différentes morphologies le long de son parcours. Une morphologie en tresses est associée à un transport de sédiments intense, tandis qu'une rivière à chenal unique se trouve généralement en plaine et transporte moins de sédiments (Métivier & Barrier 2012).

La rivière achemine ensuite la plupart de cette charge sédimentaire vers les océans (Anderson & Anderson 2010). Cependant, une partie des sédiments transportés par la rivière peut aussi s'accumuler à la sortie des chaînes de montagnes et former des dépôts stratifiés sur des épaisseurs qui peuvent atteindre plusieurs kilomètres. L'analyse statigraphique de

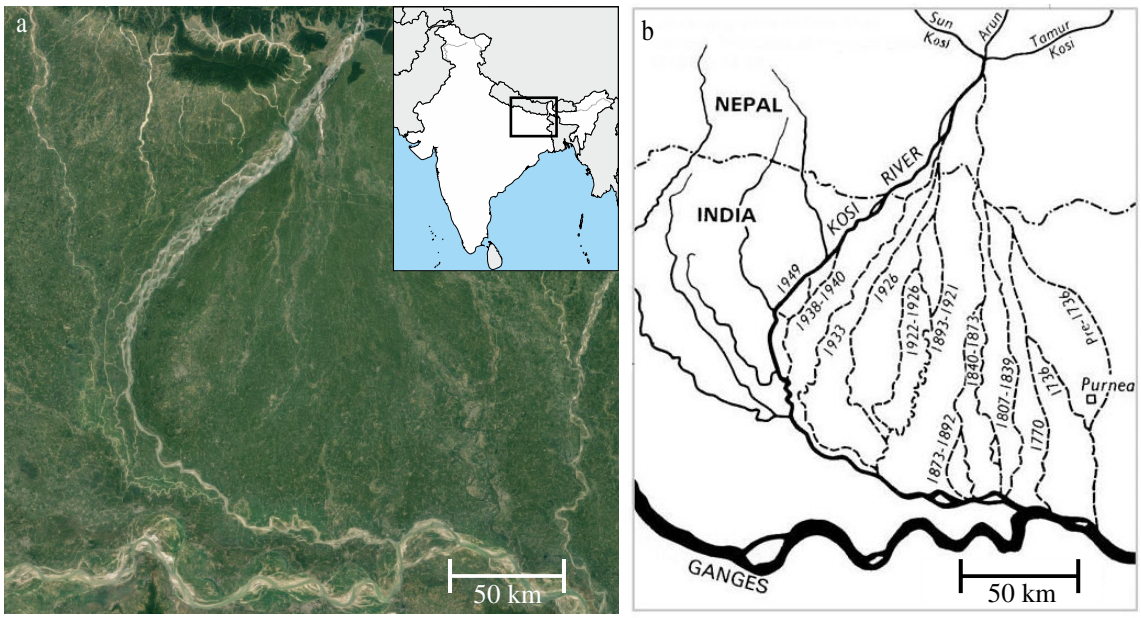

FIGURE 2 – Evolution du lit de la rivière Kosi (Inde). a. Vue satellite du cône alluvial de la rivière Kosi, qui se jette dans le Gange. Encadré en haut à droite : situation géographique du cône, au nord-est de l'Inde (carte générée via le site d-maps.com). Crédits : Google Earth. b. Evolution du cours de la Kosi depuis le 18ème siècle, d'après Gole & Chitale (1966).

ces couches nous renseigne sur le climat passé des continents (Romans *et al.* 2016).

Pour reconstituer les paléo-flux d'une rivière à partir des sédiments qu'elle a déposés, il est nécessaire de comprendre la physique du transport sédimentaire, et comment celui-ci s'adapte aux forçages extérieurs. Il s'agit également de comprendre comment le transport de sédiments s'organise dans une rivière, et comment il contrôle sa forme.

Comme pour tout système naturel, la dynamique d'une rivière dépend de nombreux paramètres : contexte géologique et climatique, apport en sédiments, distribution de taille des sédiments, temps de retour des crues, végétation, etc. La plupart de ces paramètres varient simultanément d'un site à l'autre. Il est donc souvent difficile d'isoler l'influence d'un paramètre uniquement à partir d'observations de terrain.

Pour s'affranchir de ces difficultés, on peut étudier la formation des rivières à l'aide d'expériences de laboratoire en conditions contrôlées (Paola *et al.* 2009, Paola & Leeder 2011). L'objectif est de simplifier le système naturel pour n'en étudier que les mécanismes clés. L'intérêt de cette démarche est de tester des modèles en réduisant les échelles de temps et en contrôlant les paramètres de forçage. C'est cette approche que nous adopterons dans ce manuscrit.

L'objectif de cette thèse est donc d'étudier l'influence de l'apport en sédiments sur la

morphologie, la dynamique et la stabilité d'une rivière. Pour ce faire, nous nous appuyons sur des expériences de laboratoire en conditions simplifiées : lit sédimentaire composé d'une taille unique de grains et écoulement laminaire.

Dans le premier chapitre, nous présentons une synthèse des connaissances actuelles sur la morphologie des rivières et la modélisation du transport sédimentaire. En nous appuyant sur des observations de terrain, nous relions la morphologie des rivières à leur débit d'eau. Ensuite, nous décrivons des études qualitatives concernant l'influence du transport de sédiments sur la forme d'une rivière. Enfin, nous présentons les modèles utilisés en transport sédimentaire.

Chapitre 1

État de l'art

Sommaire

1.1 Taille des rivières alluviales : la loi de Lacey

1.1.1 Définition et problématique

Une rivière alluviale s'écoule sur une plaine composée de sédiments mobiles (aussi appelés alluvions), dont la taille et la composition varient d'un site à l'autre. Suivant la taille des sédiments, on distingue les rivières graveleuses, dont les grains sont d'une taille supérieure au millimètre, des rivières sableuses, dont la taille des grains est comprise entre 0.05 et 1 mm (Allen 1985).

Une rivière alluviale construit son lit de la manière suivante : l'écoulement entraîne les grains, ce qui modifie sa morphologie, et, par conséquent, l'écoulement lui-même. Ce dernier modifie à son tour le transport de sédiments, et ainsi de suite. Ce couplage entre l'écoulement et le transport sédimentaire contrôle la forme des rivières dans la nature.

La rivière Kaidu est un exemple de rivière alluviale qui s'écoule dans la région du Tianshan en Chine (Fig. 1.1). Cette rivière forme des méandres et maintient une largeur à peu près constante, d'environ 25 mètres, sur plusieurs kilomètres. Ainsi, le couplage entre écoulement et transport est capable de sélectionner une largeur et une taille d'équilibre.

Dans cette partie, nous dressons l'état des connaissances sur les mécanismes qui contrôlent la largeur et plus généralement la forme d'un chenal alluvial.

1.1.2 Observations de terrain

De nombreuses campagnes de terrain ont mis en évidence des corrélations entre les caractéristiques morphologiques d'une rivière (largeur, profondeur, pente) et certains pa-

FIGURE 1.1 – Exemple d'une rivière alluviale : rivière Kaidu (Tian-Shan, Chine) vue de haut. Crédits : Google Earth.

ramètres de contrôle comme le débit d'eau, le débit de sédiments ou la taille des sédiments (Leopold & Maddock 1953, Parker *et al.* 2007). L'une des corrélations les plus remarquables est connue sous le nom de la loi de Lacey. Elle relie la largeur de la rivière W à son débit Q_w (Lacey 1930),

$$W \propto Q_w^{1/2} . \tag{1.1}$$

Cette loi d'échelle couvre une large gamme de largeurs et de débits : allant des ruisseaux de quelques centimètres de large ($W \sim 10\,\mathrm{cm}$ et $Q_w \sim 1\,\mathrm{L/s}$), jusqu'à l'Amazone de largeur $W \sim 1\,\mathrm{km}$ et débit $Q_w \sim 10^5\,\mathrm{m}^3/\mathrm{s}$ (Fig. 1.2a). De plus, cette corrélation fonctionne indépendamment des conditions environnementales (végétation, climat, lithologie, etc.), suggérant un mécanisme physique commun.

Un autre paramètre morphologique de la rivière est sa pente longitudinale S, le long de son écoulement. Sur le terrain, elle est souvent extrapolée à partir d'une mesure de la pente moyenne de la surface de l'eau. Ces mesures suggèrent l'existence d'une corrélation entre la pente d'une rivière S et son débit (Fig. 1.2b),

$$S \propto Q_w^{-1/2} . \tag{1.2}$$

La pente d'une rivière est cependant une quantité difficile à mesurer sur le terrain, ce qui explique que cette relation soit plus bruitée que la loi de Lacey.

Glover & Florey (1951) furent les premiers à proposer une explication de ces deux lois empiriques. Leur modèle repose sur l'hypothèse qu'une rivière ajuste sa forme de façon à ce que les grains qui composent son lit soient immobiles. Pour traduire mathématiquement cette hypothèse, il nous faut à présent définir le seuil d'entraînement d'une particule soumise à un écoulement.

1.1.3 Seuil de mise en mouvement : nombre de Shields

Lorsqu'un fluide s'écoule sur une couche de sédiments, il applique une force tangentielle à la surface du lit (Fig. 1.3a). Cette force s'exprime en fonction du cisaillement fluide τ,

$$f_t = \alpha \tau d_s^2 , \tag{1.3}$$

où d_s est la taille d'un grain, et α est un coefficient sans dimension qui dépend de la forme du grain et de la nature de l'écoulement.

Cette force tend à déloger un grain tandis que son poids le retient. Ce dernier, normal à la surface du lit, s'écrit,

$$f_n = \beta(\rho_s - \rho_f) g d_s^3 , \tag{1.4}$$

où ρ_f, ρ_s et g correspondent à la densité du fluide, à celle du grain et à la gravité respectivement. Le coefficient β dépend de la forme des grains : $\beta = \pi/6$ pour une sphère, ou $\beta = 1$

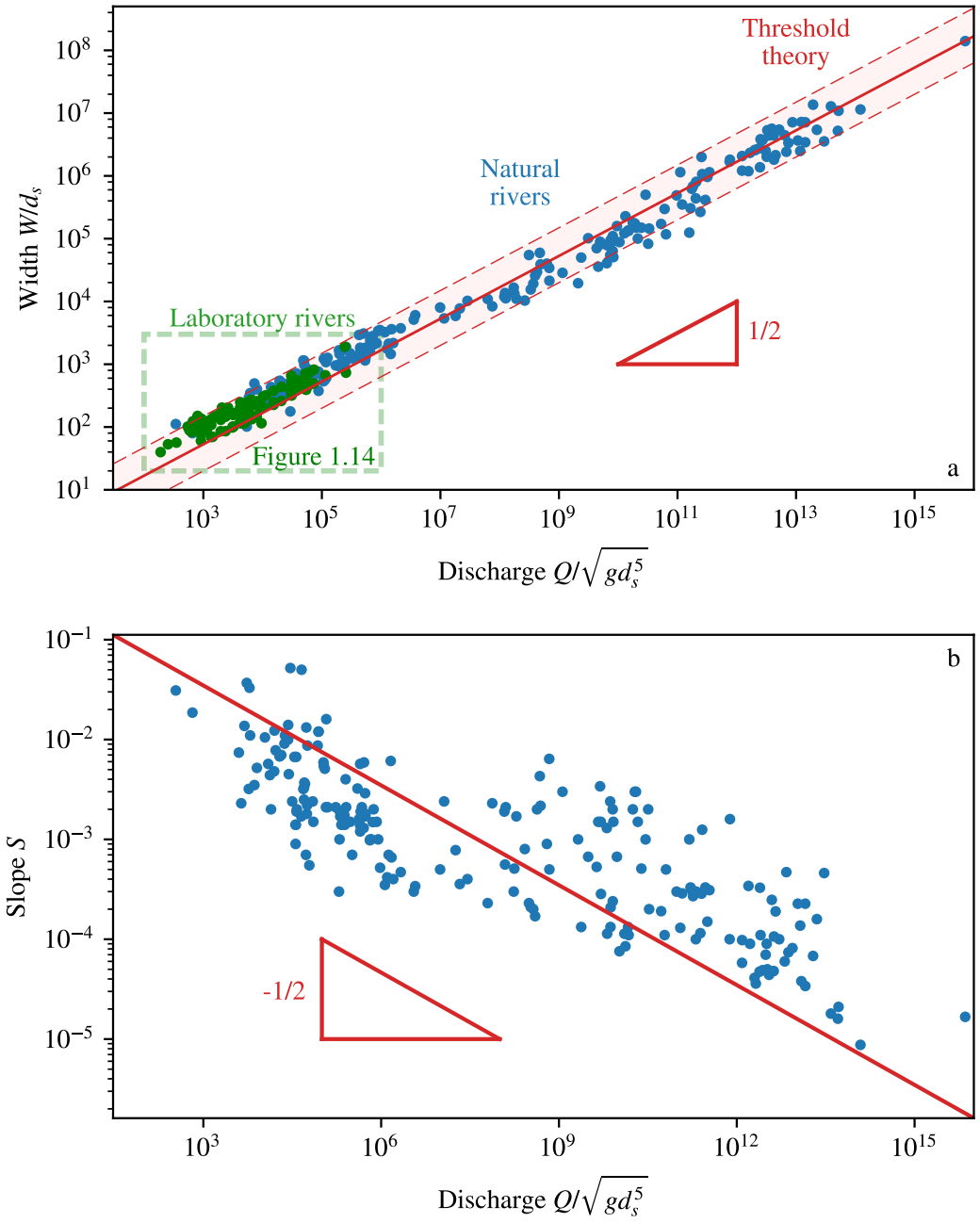

FIGURE 1.2 – Corrélation empirique entre la morphologie des rivières et leur débit d'eau. D'après Li *et al.* (2015) et Métivier *et al.* (2017). a. Largeur d'une rivière en fonction de son débit d'eau adimensionné (d_s correspond à la taille du sédiment). En bleu : données de terrain. En vert : données expérimentales. Ligne rouge : prédiction de la théorie du seuil (équation (1.21)). b. Pente d'une rivière en fonction de son débit d'eau adimensionné. Points : données de terrain. Ligne rouge : loi empirique (équation (1.2)).

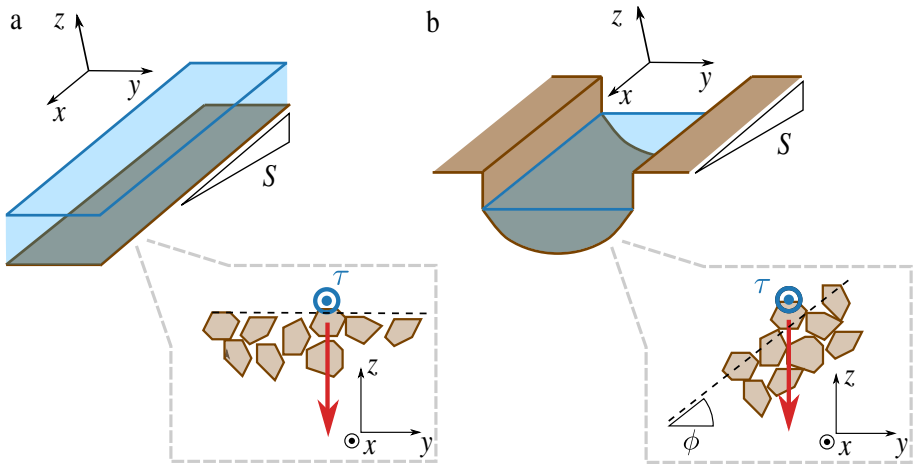

FIGURE 1.3 – Bilan des forces s'exerçant sur un grain au niveau de la surface du lit. Marron : lit de sédiment. Bleu : écoulement fluide. a. Lit Plat. b. Chenal.

pour un cube, par exemple (Seizilles 2013).

D'après la loi de Coulomb, le paramètre qui contrôle le transport des grains est le rapport entre ces deux forces : le cisaillement fluide et le poids apparent du grain,

$$\mu = \frac{f_t}{f_n} = \frac{\alpha\tau}{\beta(\rho_s - \rho_f)gd_s}\,. \tag{1.5}$$

Au seuil d'entraînement des grains, ce rapport est le coefficient de frottement μ_t. Si $\mu > \mu_t$, l'écoulement est capable d'entraîner un grain.

En géomorphologie fluviale, on utilise traditionnellement le nombre de Shields θ (Shields 1936) :

$$\theta = \frac{\tau}{(\rho_s - \rho_f)gd_s} = \frac{\beta}{\alpha}\mu\,, \tag{1.6}$$

Au seuil d'entraînement, le nombre de Shields prend la valeur

$$\theta_t = \frac{\beta}{\alpha}\mu_t\,, \tag{1.7}$$

où θ_t est appelé nombre de Shields critique.

Les expériences montrent que le nombre de Shields critique dépend au premier ordre de l'écoulement au voisinage du lit et de la taille des grains (Shields 1936, Julien 1995, Buffington 1999, Paphitis 2001). Cette dépendance peut s'exprimer en fonction du nombre de Reynolds de grain, défini par,

$$Re_s = \frac{u_s d_s}{\nu}\,. \tag{1.8}$$

où u_s est la vitesse du fluide proche des grains, et ν est la viscosité cinématique du fluide. Des modèles semi-empiriques permettent d'avoir une expression du nombre de Shields critique en fonction du nombre de Reynolds de grain selon le régime turbulent ou laminaire (Fig. 1.4).

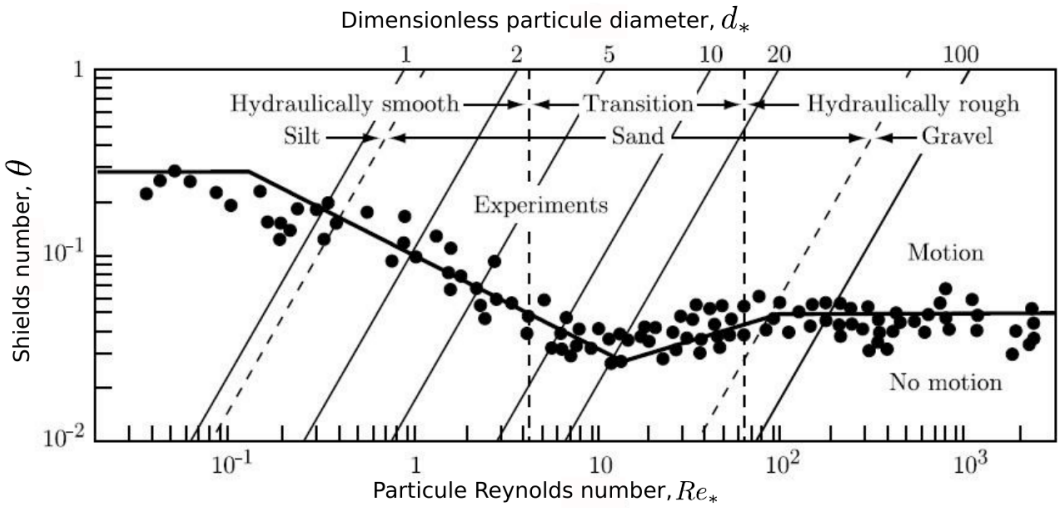

FIGURE 1.4 – Valeur seuil du nombre de Shields θ_t en fonction du nombre de Reynolds de grain, Re_s. Points : données expérimentales. Lignes : modèle empirique. D'après Julien (1995), Buffington (1999).

Toutefois, les mesures expérimentales du nombre de Shields critique sont délicates. La définition expérimentale du seuil est un critère subjectif, car celui-ci est franchi lorsqu'une fraction minimale de grains entrent en mouvement. Cette fraction peut varier d'une expérience à l'autre (Yalin 1977, Buffington & Montgomery 1997, Shvidchenko *et al.* 2001).

De plus, les fluctuations d'un écoulement dues à la turbulence amplifient la nature aléatoire de l'entraînement d'un grain (Dancey *et al.* 2002, Ancey & Heyman 2014). Pour s'affranchir de cet effet, de nombreuses études ont été effectuées en régime laminaire (Loiseleux *et al.* 2005, Ouriemi *et al.* 2007, Lobkovsky *et al.* 2008, Agudo & Wierschem 2012, Seizilles *et al.* 2014).

Le nombre de Shields critique dépend également de l'arrangement initial du lit de grains (Papanicolaou *et al.* 2002). Un lit compact sera plus difficile à mettre en mouvement et aura un nombre de Shields critique plus élevé qu'un lit peu dense.

Enfin, Houssais *et al.* (2015) ont mis en évidence l'existence du mouvement lent du lit en dessous de la couche de grains mobiles. Ce phénomène de « creep » est observé avant même le seuil d'entraînement des grains, ce qui remet en question la notion de seuil de transition au delà d'un nombre de Shields critique, au moins dans les écoulements visqueux.

1.1.4 Forme d'équilibre d'une rivière : la théorie du seuil

Selon le raisonnement de Glover & Florey (1951), la rivière organise spontanément son lit de façon à ce que les sédiments soient au seuil d'entraînement. Autrement dit, l'écoulement entraîne et dépose du sédiment jusqu'à ce que les contraintes tangentielles et normales s'ajustent pour que le grain atteigne le seuil de mise en mouvement. Dans ces

conditions, plus aucun grain n'est transporté par l'écoulement dans une rivière à l'équilibre.

Contrairement au cas d'un lit plat discuté dans le paragraphe 1.1.3 (Fig. 1.3a), une rivière forme un chenal dont la profondeur D varie en fonction de la coordonnée transverse y (Fig. 1.3b). Dans cette géométrie, le poids apparent du grain présente une composante tangentielle en plus de sa composante normale. Dans ces conditions, l'expression des forces normale et tangentielle appliquées sur un grain à la surface du lit devient

$$f_n^2 = [\beta(\rho_s - \rho_f)gd_s^3 \cos\phi]^2 \,, \tag{1.9}$$

$$f_t^2 = [\alpha\tau d_s^2 + \beta(\rho_s - \rho_f)gd_s^3 S]^2 + [\beta(\rho_s - \rho_f)gd_s^3 \sin\phi]^2 \,, \tag{1.10}$$

où ϕ est l'angle du lit par rapport à l'horizontale, dans la direction transverse à l'écoulement (Fig. 1.3b). La pente du chenal dans le sens de l'écoulement S est généralement comprise entre 10^{-6} et 10^{-1}, et a donc une contribution négligeable sur le poids d'un grain.

La condition de seuil s'écrit donc

$$\left(\frac{\alpha\tau}{\beta(\rho_s - \rho_f)gd_s}\right)^2 + \sin^2\phi = \mu_t^2 \cos^2\phi \,. \tag{1.11}$$

La contrainte τ est induite par l'écoulement, qui lui-même dépend de la forme du chenal. Il nous faut son expression pour fermer le système.

Dans un premier temps, nous considérons que l'angle ϕ est suffisamment faible pour utiliser l'approximation de Saint-Venant : nous négligeons le transfert de quantité de mouvement dans la direction transverse à l'écoulement, car nous considérons la largeur de la rivière bien supérieure à sa profondeur. C'est le cas de la plupart des rivières naturelles, pour lesquelles les rapports d'aspects varient entre 10 et 100 (Fig. 1.6). A l'aide d'un bilan de forces sur une section de la rivière, on déduit que la contrainte correspond au poids de l'eau projeté dans la direction de l'écoulement,

$$\tau = \rho_f g D S \,, \tag{1.12}$$

où D est la profondeur du chenal, qui dépend de la coordonnée transverse y. Cette expression est valable aussi bien en régime turbulent qu'en régime laminaire (Glover & Florey 1951, Henderson 1961, Seizilles *et al.* 2013).

En accord avec l'approximation de Saint-Venant, on peut considérer que $\cos\phi \approx 1$, et la condition de seuil (équation (1.11)) devient ainsi (Glover & Florey 1951)

$$\left(\frac{DS}{L}\right)^2 + \left(\frac{\partial D}{\partial y}\right)^2 = \mu_t^2 \tag{1.13}$$

où l'on définit la longueur caractéristique

$$L = \frac{\theta_t(\rho_s - \rho_f)d_s}{\mu_t \rho_f}\,. \tag{1.14}$$

Cette longueur, qui ne dépend que de la nature des sédiments et du fluide, est de l'ordre de la taille du grain.

Sur les berges, la profondeur s'annule ($D = 0$). D'après l'équation (1.13), la pente vaut donc le coefficient de frottement solide μ_t. Au centre du chenal, la pente s'annule, et la profondeur maximale est donc $D_{\max} = \mu_t L/S$ (Seizilles *et al.* 2013).

Une solution de l'équation différentielle (1.13) est donc

$$D(y) = \frac{\mu_t L}{S} \cos\left(\frac{Sy}{L}\right), \tag{1.15}$$

ce qui prédit une largeur de rivière égale à

$$W = \frac{\pi L}{S}\,. \tag{1.16}$$

Pour une largeur de rivière donnée, une unique pente d'équilibre est possible, et inversement. Il est donc impossible d'imposer à la fois la pente et la largeur de la rivière : c'est elle qui acquiert sa pente d'équilibre.

Enfin, le rapport d'aspect d'une rivière au seuil est constant,

$$\frac{W}{D_{\max}} = \frac{\pi}{\mu_t} \approx 4 \quad \text{et} \quad \frac{W}{\langle D \rangle} = \frac{\pi^2}{2\mu_t} \approx 7 \tag{1.17}$$

À notre connaissance, la forme en cosinus prédite par la théorie du seuil (équation (1.15)) n'a pas été testée expérimentalement en régime turbulent. Cependant, comme cette forme ne dépend pas de la nature de l'écoulement, Seizilles *et al.* (2013) ont mis en place un dispositif expérimental pour reproduire au laboratoire des rivières miniatures en régime laminaire. Il s'agit d'un lit incliné, couvert de sédiments, à l'entrée duquel on injecte un liquide visqueux. Au bout de quelques heures, un chenal se forme spontanément et chaque grain qui compose son lit est au seuil de mise en mouvement. En mesurant la section de leurs rivières expérimentales, Seizilles *et al.* (2013) ont démontré la validité de la théorie du seuil dans le cas laminaire (Fig. 1.5).

1.1.5 Largeur d'équilibre d'une rivière au seuil

Connaissant la forme de la rivière au seuil, il nous reste à déterminer la vitesse de l'écoulement pour calculer son débit. Cette expression varie selon le régime (laminaire ou turbulent) de l'écoulement.

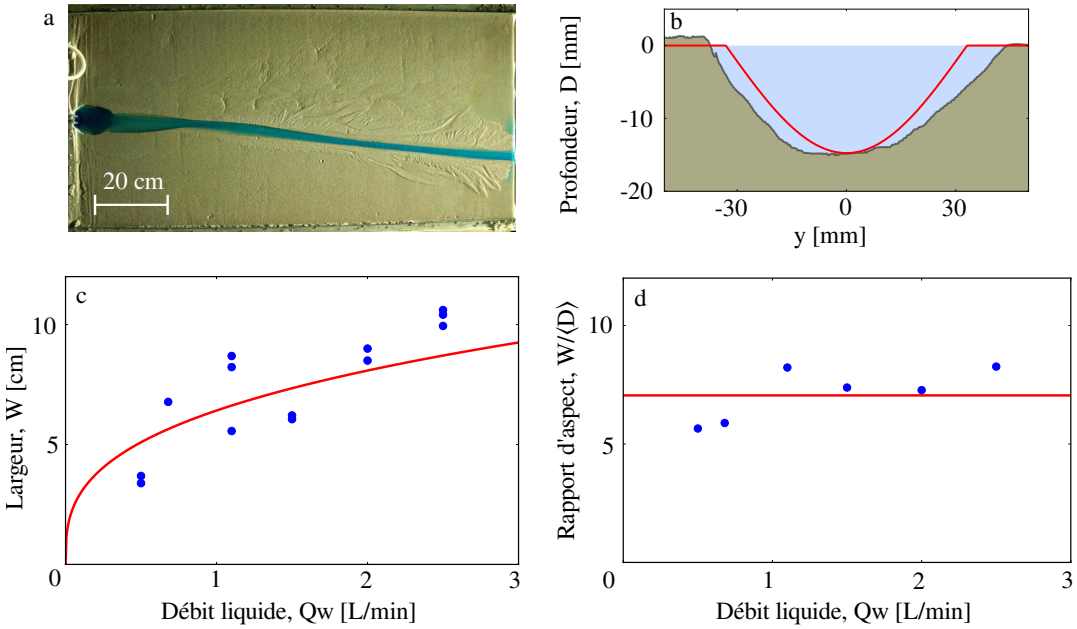

FIGURE 1.5 – Etude expérimentale de la morphologie d'une rivière de laboratoire en régime laminaire. D'après Seizilles *et al.* (2013). a. Rivière expérimentale vue de haut. La rivière (colorée en bleu) s'écoule de la gauche vers la droite. b. Section d'une rivière expérimentale en condition laminaire. Marron : lit de sédiments. Bleu : écoulement. Ligne rouge : théorie du seuil. c. Largeur des rivières en fonction de leur débit Q_w. Bleu : points expérimentaux. Ligne rouge : théorie du seuil (équation (1.26)). d. Rapport d'aspect des rivières en fonction de leur débit Q_w. Bleu : points expérimentaux. Ligne rouge : théorie du seuil (équation (1.17)).

Régime turbulent

Dans le cas turbulent, on peut utiliser une relation empirique pour avoir une expression de la contrainte exercée par l'écoulement sur le lit :

$$\tau = c_f \rho_f U^2 \,, \tag{1.18}$$

où c_f est un coefficient de friction turbulent, aussi appelé coefficient de Chézy. Il est de l'ordre de 0.04 pour les rivières naturelles (Andreotti *et al.* (2011), p. 443). La vitesse prend la forme suivante :

$$U = \sqrt{\frac{gDS}{c_f}} \,. \tag{1.19}$$

Dans ces conditions, les lois d'échelles de la largeur et de la pente deviennent

$$S = I \left(\frac{g\mu^3}{c_f} \right)^{1/4} L^{5/4} Q_w^{-1/2} \,, \tag{1.20}$$

$$W = \frac{\pi L}{S} = \frac{\pi}{I} \left(\frac{\mu_t^2 c_f}{gL} \right)^{1/4} Q_w^{1/2} \,, \tag{1.21}$$

où I est un coefficient défini par

$$I = \int_{-\pi/2}^{\pi/2} \cos^{3/2} x \, \mathrm{d}x \approx 1.75 \,. \tag{1.22}$$

Cette relation est en accord avec la loi empirique de Lacey (équation (1.1)) pour les données de terrain (Fig. 1.2a). Cependant, le pré-facteur dépend de nombreux paramètres. Certains sont constants dans la nature, comme la densité de l'eau ($\rho_f \approx 1000$ kg/m^3) et des sédiments, souvent du sable, ($\rho_s \approx 2650$ kg/m^3) ou l'angle de repos ($\mu_t \approx 0.7$). D'autres paramètres varient d'un site à l'autre, comme la taille des grains d_s ou le coefficient de Chézy c_f. Sur la figure 1.2, la courbe théorique, tracée avec des valeurs typiques ($c_f = 0.1$ et $\theta_t = 0.05$), est adimensionnée par la taille du grain. La zone colorée correspond à la variabilité des paramètres (Métivier *et al.* 2017).

Régime laminaire

Pour s'affranchir des relations empiriques liées à la turbulence, Seizilles *et al.* (2013) ont testé la théorie du seuil avec des expériences en écoulement laminaire. Dans ce cadre et sous l'approximation de Saint-Venant, le profil de vitesse U a la forme d'un écoulement de Poiseuille unidimensionnel et dépend de la profondeur D comme suit :

$$U = \frac{gSD^2}{3\nu} \,, \tag{1.23}$$

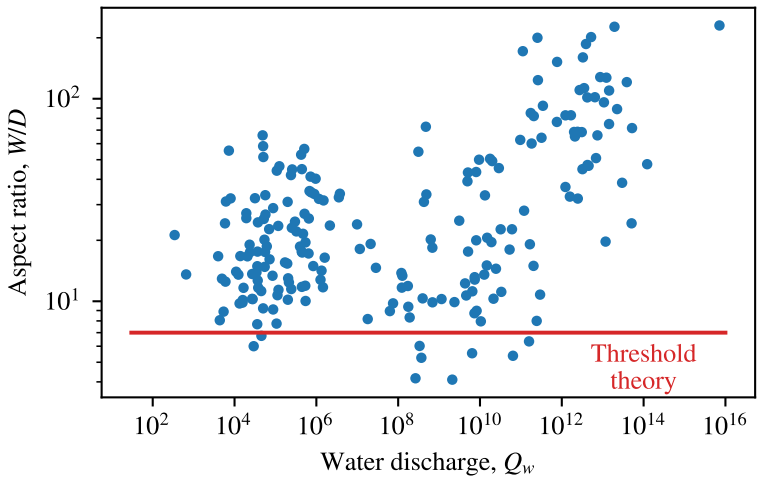

FIGURE 1.6 – Rapport d'aspect W/D en fonction du débit d'eau. D'après Li *et al.* (2015). En bleu : données de terrain. En rouge : la théorie du seuil prédit un rapport d'aspect constant égal à $\pi^2/2\mu_t$ (eq. (1.17)).

où ν est la viscosité cinématique du fluide. Le débit du chenal est alors

$$Q_w = \int_{\text{chenal}} U D \, \mathrm{d}y = \frac{4}{9}\mu^3 \frac{g}{\nu}\frac{L^4}{S^3} \tag{1.24}$$

Par conséquent, la théorie du seuil conduit aux deux lois d'échelle (Seizilles *et al.* 2013) :

$$S = \mu_t \left(\frac{4g}{9\nu}\right)^{1/3} L^{4/3} Q_w^{-1/3}\,, \tag{1.25}$$

$$W = \frac{\pi L}{S} = \frac{\pi}{\mu_t}\left(\frac{9\nu}{4gL}\right)^{1/3} Q_w^{1/3}\,. \tag{1.26}$$

Ainsi, la largeur et la pente d'équilibre d'une rivière s'adaptent à son débit. L'équation (1.26) est l'analogue de la loi de Lacey en régime laminaire, avec un exposant 1/3 (au lieu de 1/2 en turbulent). Cette expression est en bon accord avec les mesures expérimentales de Seizilles *et al.* (2013) (Fig. 1.5).

Conclusion

La théorie du seuil prédit correctement la forme en cosinus des rivières expérimentales dont les berges sont au seuil de mise en mouvement. Elle rend compte également, au premier ordre, de l'évolution de la largeur des rivières naturelles en fonction de leur débit (Fig. 1.2a).

Cependant, les mesures de terrain montrent que le rapport d'aspect d'une rivière, défini comme le rapport entre sa largeur et sa profondeur, varie de manière significative d'un site à l'autre. Les valeurs sont dispersées et la théorie du seuil semble seulement prédire une

Rivière	**Débit d'eau** (m^3/s)	**Débit de sédiments** ($10^6 t/an$)
Brahmaputra	15 000	1670
Amazone	480 000	1000
Danube	6 500	67
Kosi	2 036	43

TABLE 1.1 – Estimations du débit d'eau moyen et du débit de sédiments à l'embouchure de différentes rivières. D'après Milliman & Meade (1983) et Sinha (2009).

borne inférieure (Fig. 1.6).

Une cause probable de ce désaccord entre la théorie du seuil et les données de terrain est que la plupart des rivières naturelles transportent des sédiments. Les sédiments qui composent le lit des rivières alluviales ne sont donc pas au seuil de mise en mouvement, mais sont transportés par l'écoulement.

Dans la section suivante, nous proposons un aperçu des connaissances concernant l'influence du transport sédimentaire sur la morphologie des rivières, en nous fondant sur des observations de terrain et de laboratoire.

1.2 Influence du transport de sédiments sur la morphologie d'une rivière

Bien que la théorie du seuil prédise au premier ordre la largeur des rivières naturelles, elle sous-estime en général leur rapport d'aspect. Cet écart entre théorie et observations de terrain peut provenir de l'influence du transport sédimentaire dans les rivières, qui n'est pas prise en compte dans la théorie du seuil.

En effet, en incisant les reliefs, les rivières entraînent avec elles de la matière sous forme de sédiments. A l'échelle du globe, on estime qu'elles déchargent chaque année 13.5 milliards de tonnes de sédiments vers les océans (Milliman & Meade 1983). La quantité de sédiments dépend principalement de l'aire du bassin versant, de sa topographie et de la lithologie du sol et varie selon les rivières (Tableau 1.1). Cette quantité évolue également en fonction du climat (Mueller & Pitlick 2013).

La taille et la composition des sédiments résultent des processus d'altération physico-chimiques du sol. Les grains de petite taille comme les limons et les argiles sont assez légers pour être retenus en suspension dans l'écoulement. Les sables et les graviers, eux, sont transportés près du lit et avancent par bonds successifs. Ce mode de transport, appelé charriage, contrôle au premier ordre la forme du lit. C'est donc celui que l'on étudiera dans ce manuscrit.

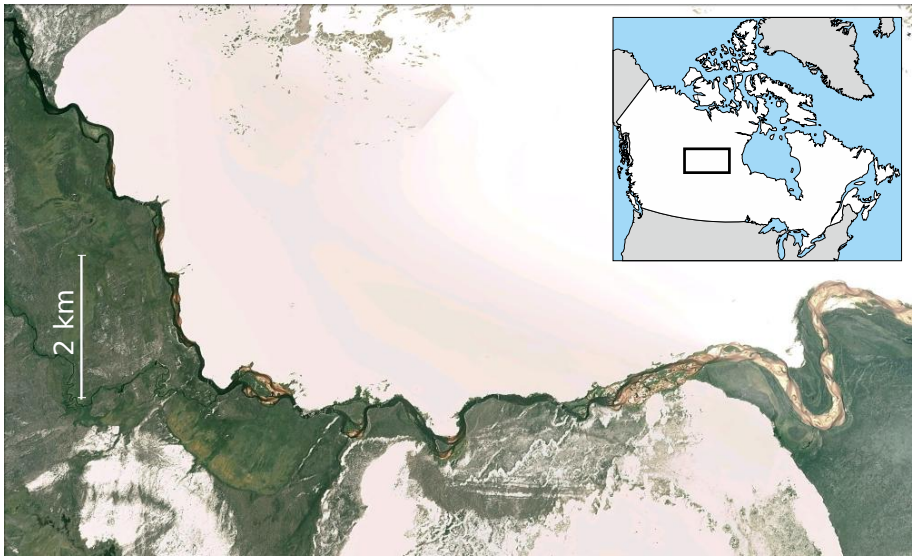

FIGURE 1.7 – Rivière Wiliam vue de haut (Canada). La rivière s'écoule de la gauche vers la droite. Crédits : Google Earth. Encadré en haut à droite : localisation géographique de la rivière au Canada (carte générée via le site d-maps.com).

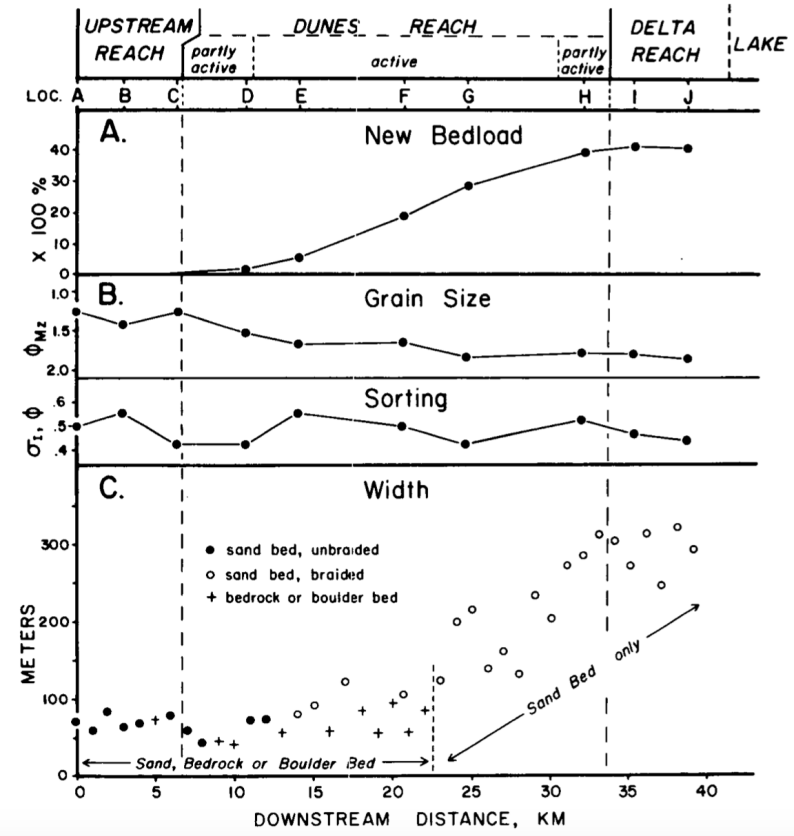

FIGURE 1.8 – Evolution de la morphologie de la rivière William (Canada) le long de son cours. D'après Smith & Smith (1984). A. Évolution du transport de sédiments en fonction de la distance longitudinale. B et C. Caractéristiques des grains (taille et granulométrie) en fonction de la distance longitudinale. D. Largeur de la rivière le long de son cours.

1.2.1 Largeur de la rivière

De nombreuses observations de terrains suggèrent que le flux de sédiments exerce un contrôle fort sur la morphologie d'une rivière. L'exemple le plus frappant est sans doute celui de la rivière William, qui se situe dans l'état du Saskatchewan, au Canada (Smith & Smith 1984). Cette rivière forme initialement un chenal étroit et profond, puis atteint un champs de dunes au niveau du lac Athabasca, où elle se charge en sédiments (Fig. 1.7). En l'espace de 25 km, son débit solide est multiplié par 40, sa largeur passe de 50 à 300 mètres, et sa forme évolue d'un chenal unique vers une tresse (Fig. 1.8).

Les observations de terrain compilées par Métivier & Barrier (2012) viennent compléter celles de Smith & Smith (1984). Elles suggèrent également que le rapport d'aspect d'une rivière augmente avec le débit de sédiments (Fig. 1.9).

Parker (1978a) est le premier à proposer un modèle pour expliquer l'élargissement d'une rivière lorsqu'elle transporte des sédiments. Les grains qui composent le lit de la rivière sont entraînés par l'écoulement et voyagent dans la direction de la force qui s'exerce sur eux. Lorsqu'ils se trouvent au centre du chenal, cette force est parallèle à l'écoulement. En revanche, sur les berges, cette force possède une composante transverse à l'écoulement, à cause de la pente du lit. Par l'action de leur poids, la trajectoire des grains est donc légèrement déviée vers le centre du chenal (Seizilles (2013), Ch. 5). Ce mécanisme érode les berges du chenal qui s'élargit progressivement.

Si rien ne compense ce mécanisme, la rivière devrait donc s'élargir indéfiniment. Or, sur le terrain, on observe que les rivières aqcuièrent une largeur d'équilibre. Pour résoudre ce paradoxe, souvent nommé "paradoxe de Parker", Parker propose différents mécanismes capables de compenser l'érosion des berges (Parker 1978a;b).

Dans une rivière sableuse, où la suspension des sédiments est prédominante, Parker (1978a) suggère que la diffusion de particules du centre du chenal vers les berges induit un flux de grains, transverse à l'écoulement, capable de contrebalancer l'érosion des berges. Dans les rivière graveleuses, cependant, les sédiments ne sont pas transportés en suspension, mais sont charriés par l'écoulement et restent près du lit de la rivière. Parker (1978b) propose donc un autre mécanisme pour équilibrer l'effet de la gravité : la diffusion de quantité de mouvement de l'écoulement, liée à la turbulence. Cette diffusion aurait pour effet de diminuer la contrainte exercée par l'écoulement au niveau des berges. Cette contrainte pourrait atteindre une valeur inférieure à la contrainte seuil d'entraînement des grains. Dans ce cas, les berges ne transporteraient aucun grain, et le flux gravitaire s'annulerait. Cependant, ces mécanismes sont difficiles à caractériser sur le terrain ou au laboratoire et n'ont jamais été testés expérimentalement. Dans ce manuscrit, nous nous inspirerons de ces modèles pour prédire la forme d'équilibre d'une rivière de laboratoire (Ch. 2 et 3).

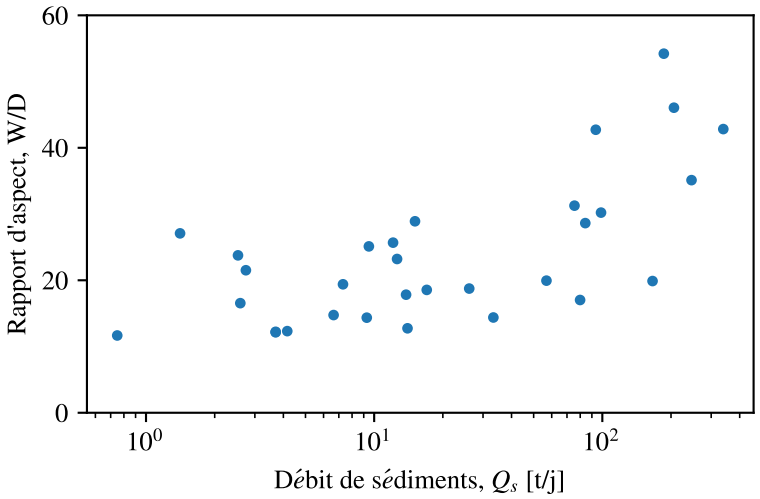

FIGURE 1.9 – Rapport d'aspect de rivières naturelles en fonction de leur débit de sédiments. Rivières graveleuse en Idaho. Données de King *et al.* (2004) compilées par Métivier & Barrier (2012).

1.2.2 Transition morphologique

En plus de son élargissement, les travaux de Smith & Smith (1984) suggèrent que la rivière William subit une transition morphologique au-delà d'un certain débit sédimentaire (Fig. 1.8). Alors qu'elle forme initialement un chenal unique, elle se déstabilise en tresses lorsqu'elle se charge en sédiments.

Cette transition de morphologie est observée sur d'autres sites. Par exemple, lorsque la rivière Illgraben rejoint le Rhône, elle le charge en sédiments et en débris (Berger *et al.* 2011). Le Rhône transite donc d'un chenal initialement unique à une morphologie en tresses qui s'entre-chevauchent (Fig. 1.10).

Ces morphologies de rivières ont fait l'objet d'une classification empirique basée sur des paramètres mesurés sur le terrain, comme le rapport d'aspect, la taille des sédiments, ou la pente d'une rivière. Leopold & Wolman (1957) sont les premiers à introduire une pente critique pour distinguer les rivières en tresses des chenaux uniques (Fig. 1.12),

$$S = 0.0125\ Q_w^{-0.44}, \tag{1.27}$$

où Q_w est le débit d'eau de la rivière en m^3/s et S sa pente longitudinale. En dessous de cette pente critique, Leopold & Wolman (1957) observent principalement des rivières à chenal unique. Au delà de cette pente critique, la plupart des rivières forment des tresses.

Pourtant, Paola (2001) suggère que la pente élevée d'une rivière en tresses est due à son transport sédimentaire. Le critère sur la pente d'une rivière serait donc une conséquence et non une cause de cette transition. Dans ce cas, l'intensité du transport par charriage semble bien être un paramètre essentiel à la transition d'une rivière vers les tresses (Carson

FIGURE 1.10 – Transition méandre-tresse du Rhône (Suisse) du à un apport élevé en sédiments. Coordonnées : 46°18'19.38"N, 7°38'25.96"E. Crédits : Google Earth.

FIGURE 1.11 – Transition méandre-tresse de la rivière Kaidu (Tian Shan, Chine) du à un apport élevé en sédiments. Coordonnées : 43°3'55.67"N, 84°21'37.72"E. Crédits : Google Earth.

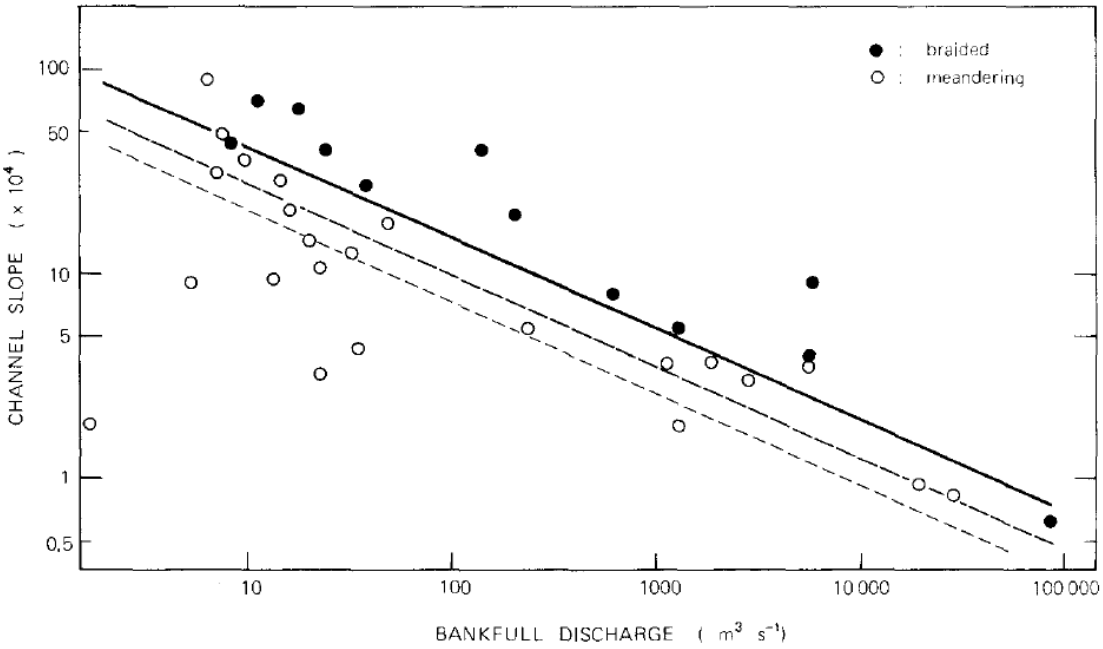

FIGURE 1.12 – Transition tresses-méandres. D'après Leopold & Wolman (1957) et Carson (1984). Points remplis : rivières en tresses. Points vides : rivières en méandres. Ligne pleine : critère de Leopold & Wolman (1957) (équation (1.27)). Lignes en pointillées : corrections effectuées par Carson (1984).

1984, Church 1992; 2006). Les travaux actuels tentent donc de relier la morphologie d'une rivière à leur concentration en sédiments charriés (Mueller & Pitlick 2014).

Pour prédire théoriquement cette transition tresse-méandre, le mécanisme proposé est relié à l'instabilité de barres alternées (Parker 1976). Les barres alternées sont des accumulations de sédiments sur les berges des rivières, successivement sur le bord droit puis gauche d'une rivière, lui donnant l'aspect d'un méandre.

Le mécanisme d'instabilité des barres alternées est le même que celui des chevrons (Andreotti *et al.* 2012). Cependant, la longueur d'onde qui sépare deux barres alternées est sélectionnée par la largeur du chenal. Lorsque la rivière a une largeur suffisamment élevée, des barres pourraient se développer en son centre et conduire à des tresses (Colombini *et al.* 1987, Seminara 2010).

Même si ce mécanisme d'instabilité a été caractérisé sur le terrain et au laboratoire (Devauchelle *et al.* 2010b, Charru *et al.* 2013), la transition méandre-tresse n'a jamais été clairement observée.

1.2.3 Rivières de laboratoire

D'après les observations de terrain, une augmentation de la charge sédimentaire dans une rivière a deux principales conséquences. Cela provoque un élargissement de la rivière

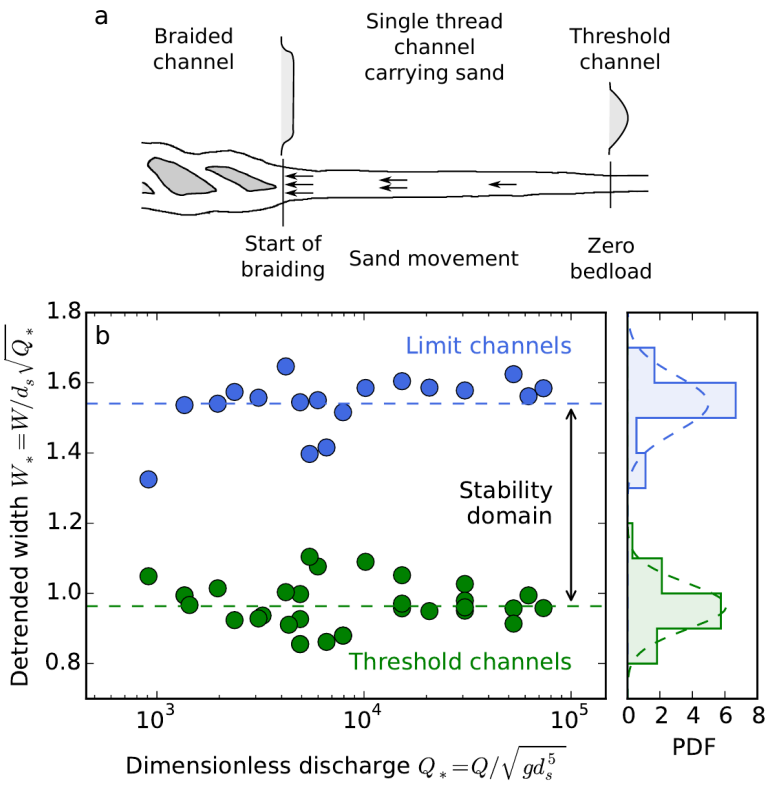

FIGURE 1.13 – Influence of sediment transport in laboratory channels (Stebbing's experiments). a. Régime transitoire des rivières de laboratoire de Stebbings (1963). Écoulement de la droite vers la gauche. b. Largeur de la rivière divisée par $\sqrt{Q_w}$ et normalisée par la taille des grains d_s. En vert : mesure au niveau du seuil. En bleu : mesure à la limite de déstabilisation lors de l'expérience de Stebbings (1963). D'après Métivier *et al.* (2017).

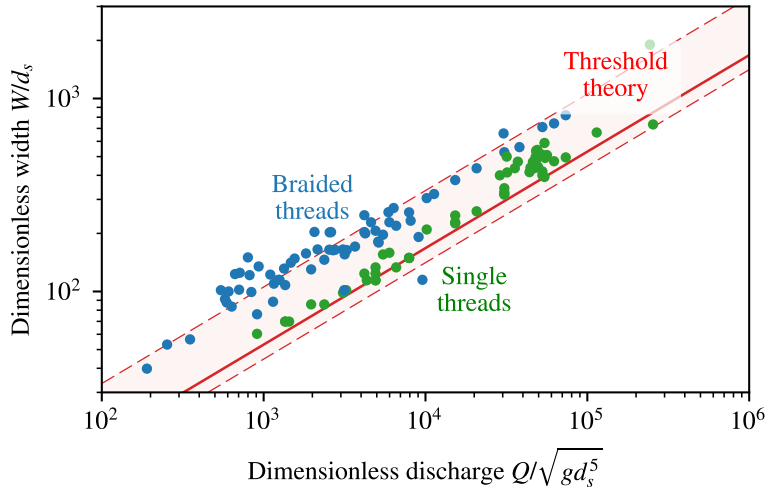

FIGURE 1.14 – Théorie du seuil pour les rivières de laboratoire. En vert : chenal unique. En bleu : tresses. Ligne rouge : théorie du seuil. La zone rouge indique l'incertitude des paramètres lors des expériences. D'après Métivier *et al.* (2017).

et parfois une transition de forme : un chenal initialement unique peut se déstabiliser en tresses.

Stebbings (1963) est le premier à avoir tenté de reproduire ces observations au laboratoire. Son expérience consiste à imposer un débit d'eau constant à l'entrée d'un chenal initialement creusé dans un lit de sédiments uniformes. L'écoulement déloge et entraîne des grains de ce chenal. Le transport par charriage s'intensifie alors progressivement le long du chenal, et celui-ci adapte sa forme selon le débit sédimentaire. Petit à petit, le chenal s'élargit, jusqu'à former des tresses (Fig. 1.13b). Ces observations semblent être en accord avec les données de terrain discutées dans les paragraphes 1.2.1 et 1.2.2.

Malheureusement, Stebbings (1963) n'a pas mesuré le débit de sédiments local des rivières. En revanche, il a mesuré la largeur des rivières expérimentales à l'entrée du chenal (correspondant à la largeur du chenal au seuil de mise en mouvement), et juste avant qu'elles se déstabilisent en tresses (lignes verticales, Fig. 1.13a). Ces résultats suggèrent que les chenaux sont stables si leur largeur est comprise entre la largeur seuil et la largeur limite de déstabilisation, comme indiqué sur la figure 1.13b (Métivier *et al.* 2017).

Ces observations ont été généralisées à d'autres rivières de laboratoire par Métivier *et al.* (2017). En effet, en se focalisant sur les rivières de laboratoire de la figure 1.2a, on s'aperçoit qu'elles suivent deux tendances distinctes selon leur morphologie. Les chenaux uniques suivent la loi de Lacey, mais les chenaux qui composent des tresses sont légèrement décalées vers le haut (Fig. 1.14).

Conclusion

Sur le terrain comme au laboratoire, l'accroissement du transport sédimentaire a deux principales conséquences : l'élargissement d'un chenal et sa déstabilisation en tresses. Pour étudier les mécanismes responsables de ces observations, commençons par décrire la physique du transport sédimentaire.

1.3 Physique du transport par charriage

Nous avons vu que la morphologie d'une rivière résulte du couplage entre l'écoulement et le transport de sédiments. Nous décrivons donc dans cette section les mécanismes qui contrôlent le transport de sédiments par charriage, qui est le mode le plus susceptible de contrôler la morphologie d'une rivière. Nous commençons par présenter le modèle d'érosion-dépôt développé par Charru *et al.* (2004a).

1.3.1 Entraînement, transport et dépôt

Lorsque la contrainte exercée par l'écoulement est juste au-dessus de sa valeur seuil, la gravité maintient les grains proches du lit. Ils se déplacent alors en roulant, glissant et

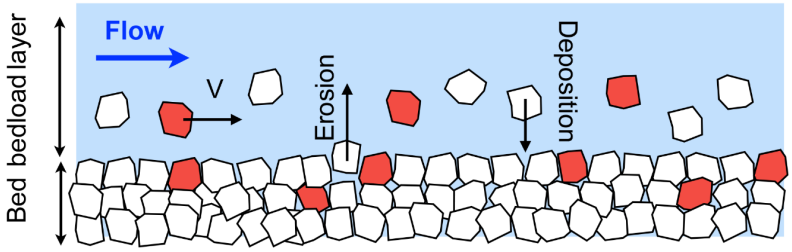

FIGURE 1.15 – Transport par charriage sur un lit granulaire cisaillé par un écoulement uniforme et stationnaire. Définition du taux d'érosion et du taux de dépôt. D'après Lajeunesse *et al.* (2017).

rebondissant sur le lit, puis finissent par sédimenter et se reloger parmi les grains immobiles du lit. Ce mode de transport est appelé transport par charriage (Fig. 1.15).

Le débit de sédiments résulte d'un échange continu entre les grains entraînés et déposés. L'ensemble des grains mobiles forment une couche dont l'épaisseur est de l'ordre de la taille d'un grain d_s. On peut définir ainsi une densité surfacique de grains en mouvement n, et le flux de sédiments par unité de largeur s'écrit alors

$$q_s = nv\,, \tag{1.28}$$

où v est la vitesse moyenne d'un grain. Si la densité est suffisamment faible, c'est-à-dire $nd_s^2 \ll 1$, les grains mobiles n'interagissent pas entre eux, à l'image des molécules dans un un gaz parfait.

Comme la couche de grains en mouvement est localisée près du lit, l'intensité du transport est principalement contrôlée par la contrainte fluide au niveau du lit. Lorsque celle-ci augmente, le flux de grains s'intensifie. Pour déterminer l'expression qui relie le transport de sédiments à la contrainte exercée par l'écoulement, il est nécessaire de connaître la concentration surfacique de grains en mouvement n et leur vitesse moyenne v. Dans les sections suivantes, nous déterminons leurs expressions dans le cas d'un écoulement visqueux.

Vitesse d'un grain

Lorsqu'un grain est entraîné par le fluide, sa vitesse augmente jusqu'à atteindre une vitesse proche de celle de l'écoulement u_s. Dans un écoulement laminaire, la vitesse du fluide à proximité du lit est reliée à la contrainte τ :

$$\frac{du_s}{dz} = \frac{\tau}{\eta}\,, \tag{1.29}$$

où η est la viscosité du fluide. Ainsi, à une hauteur d_s, la vitesse du fluide est de l'ordre de

$$u_s \sim \frac{\tau}{\eta}\, d_s\,. \tag{1.30}$$

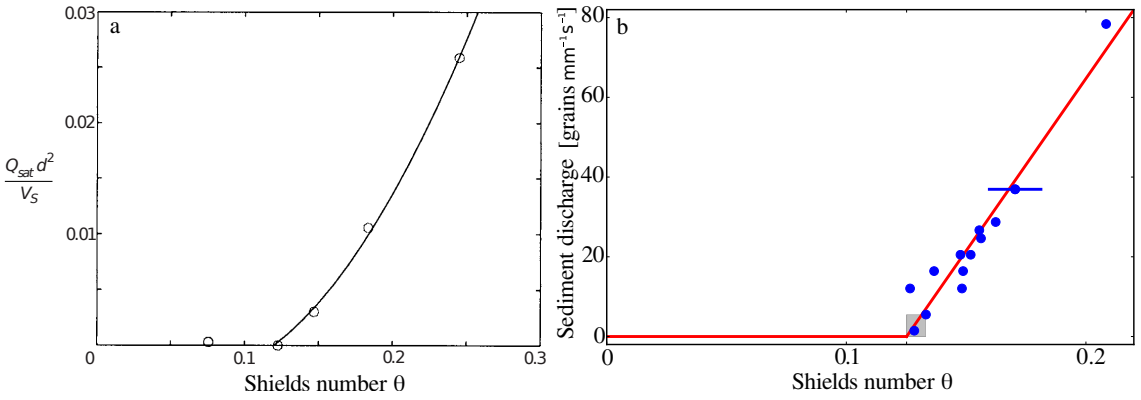

FIGURE 1.16 – Lois de transport expérimentales. a. Expérience et modèle de Charru *et al.* (2004a). b. Expérience de Seizilles *et al.* (2014). En bleu : points expérimentaux. En rouge : équation (1.41).

Cette vitesse peut s'exprimer en fonction du nombre de Shields,

$$u_s \sim 18\ \theta\ V_s\,, \tag{1.31}$$

où V_s est la vitesse de Stokes. Elle correspond à la vitesse de sédimentation d'une particule sphérique dans un liquide visqueux et s'écrit,

$$V_s = \frac{\Delta\rho g d_s^2}{18\eta}\,. \tag{1.32}$$

En considérant que la vitesse moyenne d'un grain charrié est proportionnelle à celle du fluide au voisinage du lit, on obtient :

$$v = c_v\ V_s\ \theta\,, \tag{1.33}$$

où c_v est un coefficient empirique, de l'ordre de 0.4 (Seizilles *et al.* 2014).

Concentration des grains en mouvement

La conservation de la masse de sédiments dans la couche charriée nous donne

$$\frac{\partial n}{\partial t} + \vec{v}\cdot\vec{\nabla} n = \dot{n}_e - \dot{n}_s\,, \tag{1.34}$$

où $\dot{n}_e$ et $\dot{n}_s$ correspondent aux taux d'érosion et de sédimentation, respectivement (Fig. 1.15).

Une particule entraînée par l'écoulement rebondit sur le lit avec une fréquence caractéristique, de l'ordre de l'inverse du temps que met une particule à sédimenter d'une taille

	Régime laminaire Charru *et al.* (2004b)	Régime turbulent Lajeunesse *et al.* (2010)
V_s	$\frac{(\rho_s - \rho)\, g\, d_s^2}{18\, \rho\, \nu}$	$\sqrt{\frac{\rho_s - \rho}{\rho}\, g\, d_s}$
$\frac{V}{V_s}$	$1.8\, \theta$	$4.4\left(\theta^{1/2} - \theta_t^{1/2}\right) + 0.11$
$\dot{n_e}$	$0.03\, \frac{1}{d_s^2}\, \frac{V_s}{d_s}\, (\theta - \theta_\mathrm{t})$	$1.14\, \frac{\rho}{\rho_s}\, \frac{1}{d_s^2}\, \frac{V_s}{d_s}\, (\theta - \theta_\mathrm{t})$
$\dot{n_d}$	$0.07\, n\, \frac{V_s}{d_s}$	$0.09\, n\, \frac{V_s}{d_s}$

TABLE 1.2 – Expressions du taux d'érosion, de déposition et de la vitesse moyenne des grains selon le régime d'écoulement.

de grain,

$$\frac{1}{t_d} \propto \frac{V_s}{d_s}\,. \tag{1.35}$$

Chaque fois que la particule atteint le lit, elle a une probabilité finie de se faire piéger. Si l'on suppose cette probabilité uniforme, le taux de déposition est proportionnel au nombre de grains mobiles et à la fréquence de rebond,

$$\dot{n_d} = c_d\; n\; \frac{V_s}{d_s}\,, \tag{1.36}$$

où c_d est un coefficient que l'on peut déterminer empiriquement (Charru *et al.* 2004a).

Le taux d'érosion est proportionnel au nombre de grains au repos par unité de surface, de l'ordre de $1/d_s^2$, divisé par un temps caractéristique d'érosion. Ainsi,

$$\dot{n_e} \propto \frac{1}{d_s^2}\frac{1}{t_e}\,. \tag{1.37}$$

Des expériences montrent que ce temps typique d'érosion est inversement proportionnel à l'écart au seuil, de sorte que

$$\dot{n_e} = c_e \frac{1}{d_s^2}\frac{V_s}{d_s}(\theta - \theta_t)\,, \tag{1.38}$$

où c_e est un coefficient déterminé empiriquement (Charru *et al.* 2004a).

Transport stationnaire

Dans le cas stationnaire et homogène, la concentration de grains en mouvement n [m^{-2}] est proportionnelle à l'écart au seuil :

$$n = \frac{\alpha_n}{d_s^2} \left(\theta - \theta_t\right). \tag{1.39}$$

où α_n est un coefficient sans dimension, typiquement $\alpha_n \sim 0.1$ (Seizilles *et al.* 2013).

Les grains ont également une vitesse v donnée par l'équation (1.33). Proche du seuil, lorsque $\theta \approx \theta_t$, on considère

$$v \sim \alpha_v V_s \,, \tag{1.40}$$

où α_v est égal à $c_v\,\theta_t$.

Le flux de grains dans le sens de l'écoulement s'écrit donc,

$$q_s = \alpha_v V_s n \,, \tag{1.41}$$

où $\alpha_v \sim 0.4$ (Seizilles *et al.* 2013). Enfin, en combinant les équations (1.39) et (1.41), on obtient une loi de transport, couramment utilisée dans la littérature,

$$q_s = \frac{\alpha_n \alpha_v}{d_s^2} \left(\theta - \theta_t\right). \tag{1.42}$$

Cette loi est retrouvée à partir d'autres modèles statistiques (Aussillous *et al.* 2016, Yan *et al.* 2016). Le tableau 1.2 résume l'expression de la vitesse d'un grain, du taux d'érosion et de sédimentation, et de la loi de transport en régime laminaire.

Le même raisonnement peut être suivi pour le régime turbulent, en utilisant une relation de fermeture empirique pour relier la vitesse du fluide à la contrainte qu'il exerce sur le lit (Lajeunesse *et al.* 2010). La deuxième colonne du tableau 1.2 résume les expressions de la vitesse d'un grain, du taux d'érosion et de sédimentation, et de la loi de transport en régime turbulent.

A l'aide du modèle d'érosion-dépôt, nous avons relié le flux de sédiments à la contrainte cisaillante du fluide, dans le cas d'un lit plat et d'un transport uniforme, quel que soit le régime d'écoulement. Cependant, des fluctuations spatiales du flux de sédiments peuvent entraîner la diffusion des grains (Furbish *et al.* 2012b;c). Dans la suite, nous étudions en particulier les variations transverses à l'écoulement, qui peuvent avoir une influence sur la morphologie d'une rivière.

1.3.2 Diffusion transverse à l'écoulement

Dans ce paragraphe, nous étudions la diffusion transverse de grains, entraînée par des inhomogénéités de concentrations (Nikora *et al.* 2002, Seizilles *et al.* 2014).

La figure 1.17a montre quelques trajectoires de grains charriés par un écoulement laminaire. A cause de la rugosité du lit, leur trajectoire est légèrement déviée dans la direction transverse à l'écoulement. Pour quantifier ces déviations, on définit la variance σ_y^2 pour N particules :

$$\sigma_y^2(x) = \frac{1}{N}\sum_{i=1}^{N} y_i(x)^2\,, \tag{1.43}$$

où $y_i(x)$ est la position d'une particule dans la direction perpendiculaire à l'écoulement (Seizilles *et al.* 2014).

Les expériences de Seizilles *et al.* (2014) montrent que la variance σ_y^2 croît proportionnellement à la distance parcourue x (Fig. 1.17b),

$$\sigma_y^2 = 2\ell_d x\,. \tag{1.44}$$

De manière équivalente, on a :

$$\sigma_y^2 = 2\ell_d v t\,, \tag{1.45}$$

où ℓ_d est une longueur caractéristique appelée longueur de diffusion, et égale à $\ell_d = 0.03\,d_s$ dans les expériences de Seizilles *et al.* (2014).

Le fait que la variance σ_y^2 dépende linéairement du temps montre que les grains suivent une marche aléatoire dans la direction transverse à l'écoulement. Lorsqu'un grain avance, il fait un pas aléatoirement à gauche ou à droite, avec une probabilité égale.

Les grains mobiles sur le fond du lit constituent ainsi une collection de marcheurs aléatoires, qui diffusent lorsqu'il existe un gradient transverse de concentration. Ce flux de particules est orienté vers les zones les moins peuplées en grains mobiles et son intensité est proportionnelle au gradient de concentration :

$$q_d = -\ell_d V \frac{\partial n}{\partial y}\,. \tag{1.46}$$

Ce mécanisme de diffusion est susceptible de jouer un rôle dans la dynamique des rivières, où des gradients transverses de transport sédimentaires sont omniprésents. Une rivière en chenal unique transporte par exemple plus de sédiments en son centre, où la contrainte exercée par l'écoulement est plus élevée. De même, lorsque des barres alternées se forment sur son lit, des gradients transverses de concentrations apparaissent. On s'attend donc à ce que ce mécanisme joue un rôle majeur dans la sélection de la forme d'une rivière.

1.4 Conclusion et objectifs du manuscrit

Dans ce chapitre, nous avons dressé un bref état des connaissances sur la morphologie des rivières alluviales. Deux principaux paramètres semblent contrôler la forme d'une rivière : son débit d'eau et son débit de sédiments.

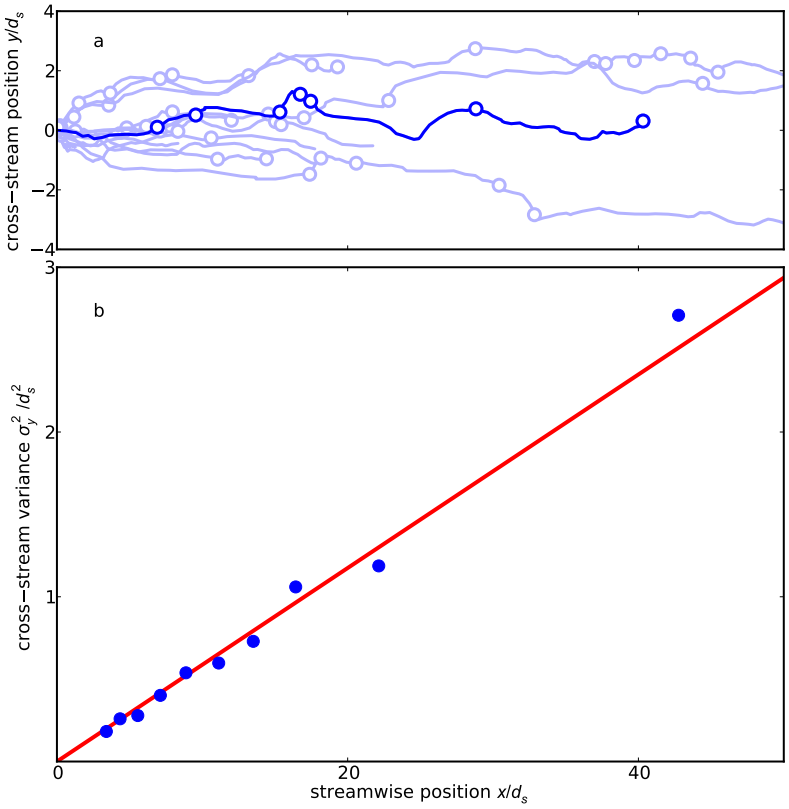

FIGURE 1.17 – Diffusion transverse des grains. D'après Seizilles *et al.* (2014). a. Grains transportés par charriage sur un lit de sédiments. Trajectoires renormalisées par la position initiale. b. Dispersion des grains en fonction de leur position longitudinale. Bleu : points expérimentaux. Rouge : relation linéaire ajustée sur les données.

Au premier ordre, le débit d'eau contrôle la forme et la pente d'une rivière (section 1.1). Supposant qu'une rivière s'ajuste de sorte que les grains qui composent son lit soient au seuil d'entraînement, sa section forme un cosinus (paragraphe 1.1.4). Cette théorie, connue sous le nom de la théorie du seuil, a été testée expérimentalement en conditions laminaires (paragraphe 1.1.5). Elle explique, au premier ordre, la loi de Lacey, selon laquelle la largeur d'une rivière naturelle est proportionnelle à la racine de son débit d'eau (Fig. 1.3).

Pourtant, le rapport d'aspect d'une rivière naturelle, défini comme le rapport entre sa largeur et sa profondeur, est généralement sous estimé par cette théorie. Les données de terrain suggèrent que le transport de sédiments, dont le rôle est négligé par la théorie du seuil, contrôle également la forme des rivières (1.2). Lorsqu'une rivière transporte des sédiments, elle a tendance à s'élargir, et donc à accroître son rapport d'aspect. Cependant, jusqu'à présent, l'influence du débit de sédiments sur la forme d'une rivière n'est comprise qu'empiriquement.

Un des objectifs de ce manuscrit est de comprendre comment une rivière ajuste sa largeur au transport sédimentaire. Cette étude permettrait par exemple de mesurer la charge sédimentaire d'une rivière uniquement à partir d'images satellites, s'affranchissant ainsi des difficultés de mesures de débits de sédiments sur le terrain (Mouyen *et al.* 2018). Cette méthode s'appliquerait également à des rivières difficiles d'accès (Smith *et al.* 1996). Enfin, elle pourrait être extrapolée pour étudier les processus d'érosion à la surface d'autres planètes ou satellites, comme Titan, où des chenaux et des motifs d'érosion fluviatile ont été observés (Jaumann *et al.* 2008).

Un autre paramètre qui dépend du débit sédimentaire d'une rivière est sa pente longitudinale, c'est-à-dire dans la direction de l'écoulement (section 1.2). La pente d'une rivière contrôle celle des cônes alluviaux, qui se trouvent généralement à la sortie des chaînes de montagnes (Delorme 2017). Ces zones de dépôts sédimentaires sont utilisées pour reconstituer le climat passé des continents, selon les paléo-flux d'eau et de sédiments. Pour mesurer les paléo-flux d'une rivière à partir des sédiments qu'elle a déposés, il faut estimer le volume des dépôts et donc la pente du cône. Ainsi, mieux comprendre l'influence du débit de sédiments sur la pente d'une rivière est primordial pour évaluer l'ampleur des changements climatiques passés et estimer les transferts de masses sur les continents.

Lorsqu'il est suffisamment élevé, le débit de sédiments d'une rivière peut déstabiliser son cours pour former des tresses (paragraphe 1.2.2). Un autre objectif de ce manuscrit sera d'étudier la stabilité d'une rivière à chenal unique vis à vis du forçage sédimentaire.

Toutes ces problématiques sont liées au couplage entre le transport sédimentaire et l'écoulement (section 1.3). Malgré le nombre de publications dans ce domaine, ce couplage écoulement-transport et ses conséquences sur la morphologie d'une rivière sont encore mal compris aujourd'hui. Cette problématique constitue la base de ce manuscrit. Il s'agit de comprendre les mécanismes physiques à l'échelle du grain, de les modéliser, et d'étudier

leur influence, à grande échelle, sur la morphologie d'une rivière.

Pour ce faire, nous avons choisi une approche expérimentale. Seizilles (2013) a montré que l'on peut étudier le couplage écoulement-transport en utilisant des rivières expérimentales en conditions laminaires. Ces conditions d'écoulement permettent de s'affranchir des difficultés liées à la turbulence, et des lois empiriques qui y sont associées. L'objectif est donc (i) de former des rivières au laboratoire, (ii) d'étudier la sensibilité de ces rivières à ses paramètres d'entrée : son débit d'eau et, surtout, de sédiments.

1.5 Organisation du manuscrit

Dans le chapitre 2, nous commençons par étudier expérimentalement l'influence du transport de sédiment sur une rivière dont nous fixons la largeur. Nous nous concentrons ainsi sur le couplage écoulement-transport à l'échelle du grain. Nous utilisons un canal dans lequel un écoulement visqueux entraîne un lit sédimentaire. Nous mesurons le transport sédimentaire et la forme du lit, ce qui nous amène à modéliser leur interaction.

Le chapitre 3 confronte ce modèle à des rivières de laboratoire dont la largeur n'est plus fixée. Nous utilisons un plan incliné, recouvert d'une couche épaisse de sédiments sur lequel un fluide visqueux s'écoule. Une rivière de quelques centimètres de large se forme spontanément. Cette forme dépend des flux d'eau et de sédiments que l'on injecte à l'entrée.

Dans le chapitre 4, nous identifions le mécanisme par lequel la rivière sélectionne sa taille en fonction des paramètres de forçage, comme les débits d'eau et de sédiments. Nous développons un modèle théorique que nous comparons ensuite à nos données expérimentales.

Enfin, nous nous intéressons à la stabilité d'une rivière à chenal unique lorsqu'elle transporte des sédiments. Le chapitre 5 présente ainsi une instabilité associée à la diffusion transverse du flux sédimentaire.

Chapter 2

Self organisation of sediment transport in a flume

Contents

2.1 Introduction

At first order, the water discharge of a river controls its shape and its size, as discussed in the first chapter of this manuscript (section 1.1). Assuming its bed is at the threshold of motion, a river is bound to acquire a cosine cross section at equilibrium (Henderson 1961). This theory, known as the threshold theory, gives a physical interpretation of the empirical Lacey's law, according to which the width of an alluvial river is proportional to the square root of its discharge (Lacey 1930, Métivier *et al.* 2017).

By definition, this theory cannot take sediment transport into account. Field observations, however, indicate that this process influences a river's shape (section 1.2). Specifically, rivers generally accommodate additional bedload by widening their channel. More remarkably, intense sediment transport may split the river course into a braid. Although these features have been observed previously in the laboratory, the relation between the shape of a river and its sediment discharge remains unclear and there is no theoretical framework to explain quantitatively these observations.

To address this problem, we choose to use laboratory experiments. We start by investigating the coupling between the shape of an erodible bed and its sediment transport in an idealised geometry: a sediment bed confined between two walls (flume). In this setup, a viscous fluid shears the sediment bed, composed of a single size of grains. We use a viscous fluid to keep the flow laminar and escape the complications of turbulence. The bed adopts a different cross section and downstream slope, depending on the fluid and sediment discharges that we inject into the flume (section 2.3).

Our aim, then, is to model the bed's equilibrium. To do so, we track travelling grains to understand how they distribute themselves onto the bed (section 2.4). We then propose a model that couples the bed elevation and the local flux of grains (section 2.7).

2.2 Experimental setup

The experimental setup, sketched on figure 2.1, is a flume (length 1 m, width 3 cm) filled with plastic sediment grains (density $\rho_s = 1520\,\mathrm{g/L}$). Grains have a non-spherical irregular shape; their size varies slightly from grain to grain, although the distribution of particle size is centered around a mean diameter $d_s = 830\,\mu\mathrm{m}$ (Fig. 2.4b, section A.1).

At the inlet of the channel, we inject a mixture of glycerol (40%) and water (60 %) (density $\rho_f \approx 1160\,\mathrm{g/L}$, viscosity $\nu \approx 10\,\mathrm{cP}$) at a constant discharge (Fig. 2.3).

Meanwhile, a conveyor belt brings grains from a tank to the channel and delivers a sediment discharge proportional to its pulley velocity. The pulley is controlled by a stepper motor, the velocity of which depends on the delay between two steps. This feeder stands on a scale which continously measures the sediment mass injected into the flume (Fig. 2.2a). The sediment input is stable and reproducible (Fig. 2.4a). It is inversely

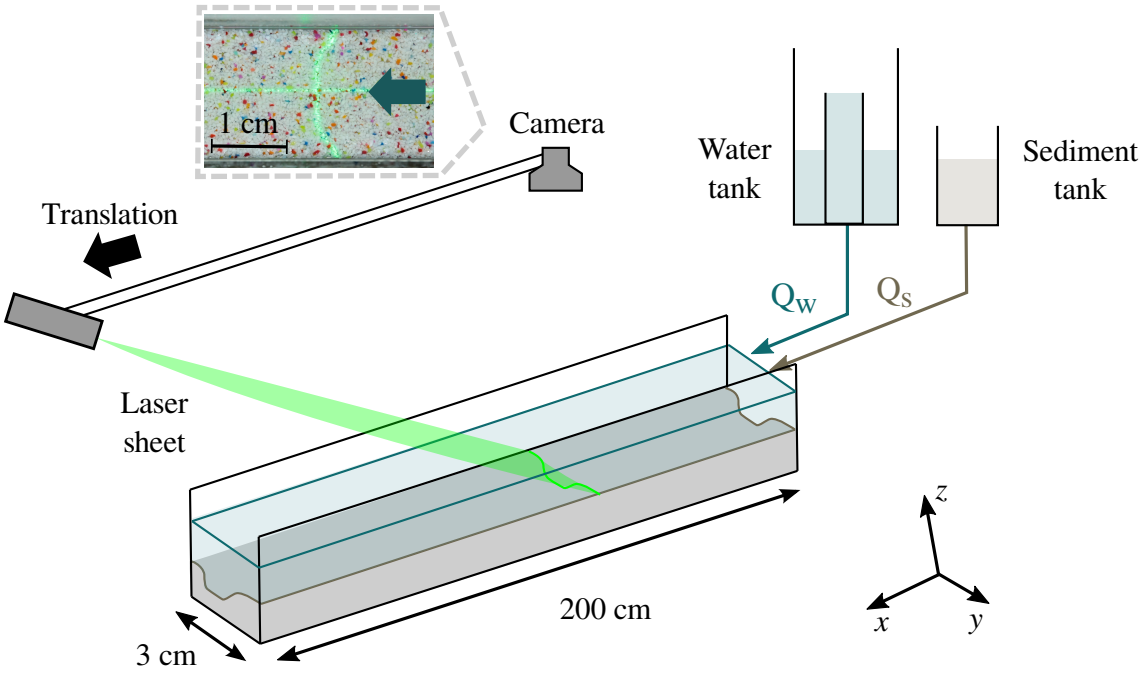

Figure 2.1 – Setup of the flume experiment fed by plastic sediment grains and a mixture of water and glycerol. A camera and a laser sheet are fixed on a rail placed above the channel, allowing them to translate over 20 cm in the downstream direction (x-direction).

proportional to the delay between two motor steps (Fig. 2.4b). Delorme (2017) describes this conveyor system in details.

As the fluid flows above the sediment layer, it entrains some of the superficial grains. The flux of grains is heterogeneous across the channel and seems higher in the center. Conjointly, the bed adjusts progressively its shape and its downstream slope, and curves near its center. This is likely due to the confinement of the fluid between two walls, that makes the flow-induced shear stress vary across the channel.

After approximately one day, there is no visible change of the bed elevation and of the downstream slope; the bed seems to have reached steady state. This equilibrium is dynamical, meaning that sediment grains are constantly travelling along the flow. The sediment flux is more intense in the center of the channel, where the flow is deeper. On both sides, the bed forms banks made up of virtually immobile grains.

We perform 5 experimental runs, where we maintain the fluid discharge Q_w around

Run	Q_w [L/min]	Q_s [g/min]	Re_s	Tracking duration [frames]	Tracking colors
1	1.12	0.65	0.90	300803	Blue, red
2	1.11	0.34	0.91	204978	Blue, red
3	1.13	0.33	0.84	372266	Blue
4	0.87	0.37	0.83	543528	Blue, red, orange
5	0.83	0.74	0.75	208289	Blue

Table 2.1 – Experimental parameters for the 5 runs.

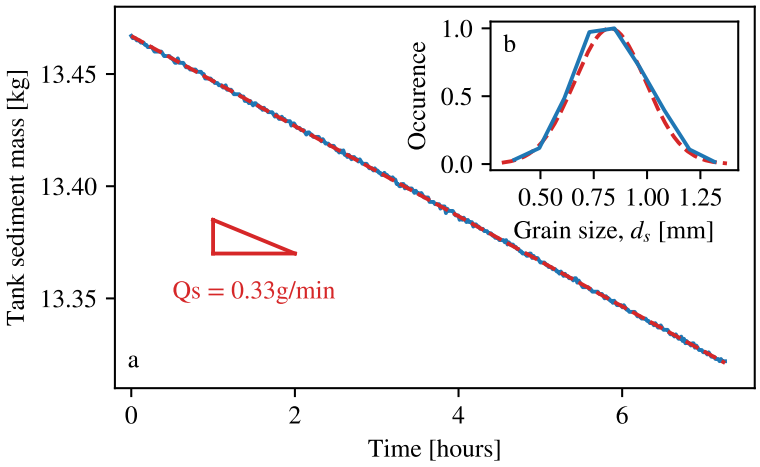

Figure 2.2 – Measurement of the sediment input. a. Mass of sediment remaining in the tank, as a function of time. The slope of this curve corresponds to the sediment discharge delivered by the conveyor belt. b. Grain-size distribution of our plastic sediment.

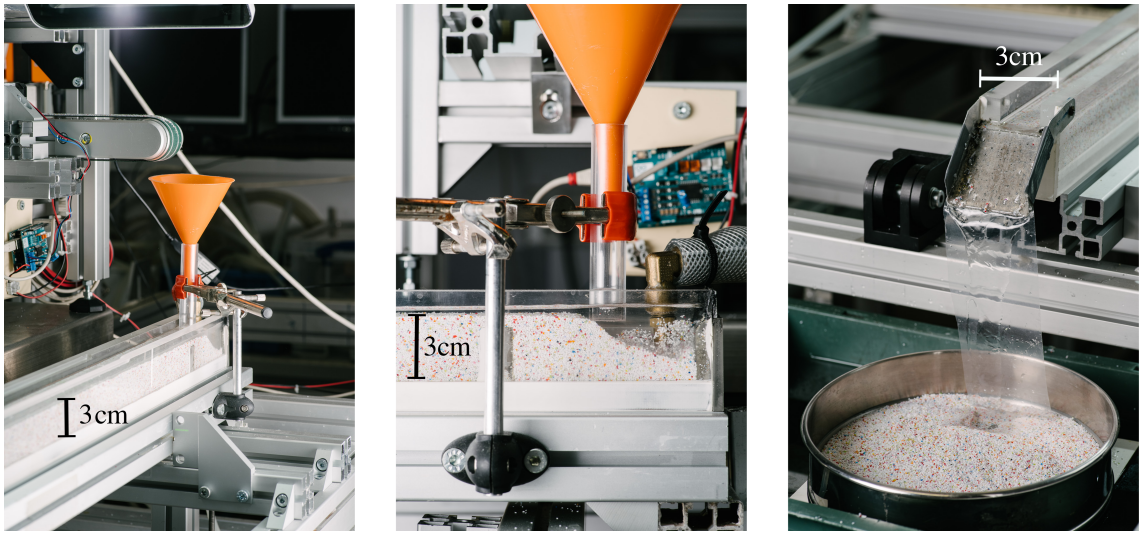

Figure 2.3 – Details of the flume experiment. *Left.* Flume inlet. Grains delivered by the sediment feeder fall into a funnel which directs them into the channel. *Center.* Detail of the flume inlet. Sediment grains fall from the funnel. They initially stay at the surface of the flow, and gradually settle on the bed. They are then entrained by the flow as bedload. *Right.* Flume outlet. Grains are separated from the fluid by a sieve. The funnel diameter is 10 cm and the flume width is 3 cm.

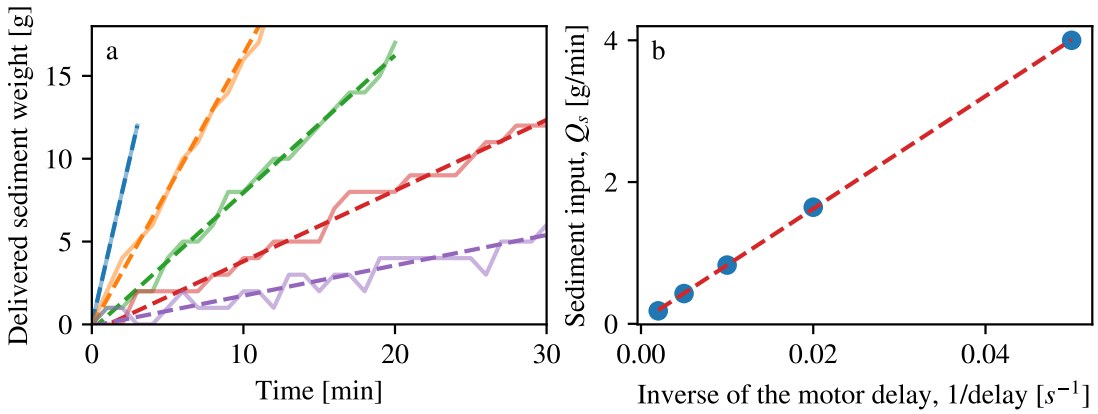

Figure 2.4 – Calibration of the sediment feeder. The gap between the tank and the conveyor belt is about 5 mm. a. Sediment mass delivered by the sediment feeder per unit of time for different motor velocities. The slope of this curve is the sediment discharge delivered by the sediment feeder. Dashed lines: linear fits. b. Sediment discharge as a function of the motor velocity, which is proportional to the inverse of the delay between two motor step.

1 L/min, while varying the sediment discharge Q_s (Table 2.1). For all these runs, we observe the same phenomena, although the bed seems to reach a slightly different shape. In particular, when the sediment discharge is higher, the bed seems flatter in the center and the travelling grains are more numerous there.

In the following, we investigate how the bed evolves when the sediment discharge varies and how the sediment flux is distributed across the stream. To do so, we measure the bed cross section and the local sediment flux (sections 2.3 and 2.4). Based on these measurements, we then deduce the transport law (section 2.5) and the diffusion length of our grains ℓ_d (section 2.6). Finally, we model the relation between the bed elevation and the sediment flux.

2.3 Cross section

2.3.1 Bed elevation

At equilibrium, the active sediment bed reaches a shape which seems invariant in the flow direction x. Upon the interruption of the flow and sediment input, bedload transport stops almost immediately and the bed morphology freezes, while the fluid slowly drains out of the channel. Once the sediment bed is dry, we can measure its shape based on the deviation of the laser sheet (Fig. 2.1). In this section, we present the calibration and the measurement of the dry bed elevation.

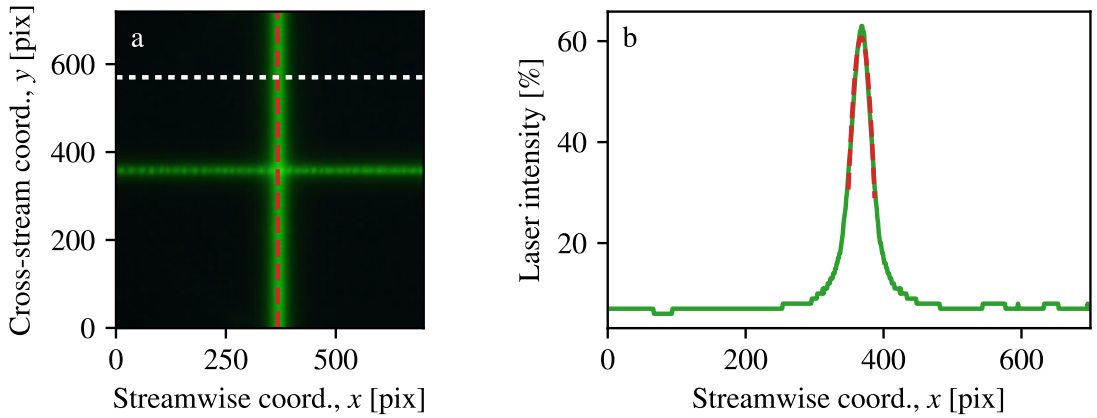

Figure 2.5 – Laser line projected onto the milk surface. a. Laser sheet on the milk surface, seen from the top. The laser line along the streamwise direction allows us to align the laser sheet with the bed. Dashed red line: location of the laser maximum intensity. Dashed white line: $y = 570$. b. Image intensity along the white dashed line of a. ($y = 570$). Fit of the value by a 2-order polynomial function near the rough maximum. Laser width : 20 pixels.

Laser sheet

A laser sheet is placed on a rail above the flume. With a stepper motor, we can translate it automatically over a distance of 20 centimetres in the downstream direction x (Fig. 2.1). Its translation velocity depends on the pulley velocity and is about 2 mm/s. We control its velocity by an Arduino card connected to a computer.

A camera placed above the flume translates with the laser and records its projection onto the bed surface, at a frame rate of 50 fps (Fig. 2.5a). The coordinate of this deviation depends on the bed elevation h through

$$h = x_{\text{laser}} \tan \theta_{\text{laser}} , \tag{2.1}$$

where θ_{laser} is the angle of the laser with respect to the horizontal, and x_{laser} is the deviation of the laser line (Fig. 2.6). The coefficient of proportionality in this relation, $\tan \theta_{\text{laser}}$, is measured by a calibration, that we describe in the next paragraph.

Calibration

To calibrate our laser scanner, we swap the sediment flume for a tube filled with milk. The latter combines a horizontal and white diffusive surface, the height of which we can vary easily by adding or removing milk.

The laser sheet is projected onto the milk surface (Fig. 2.5a). We first detect its position with image analysis. Figure 2.5b shows the intensity of the laser along a downstream line (white, dashed line of 2.5a); 0 corresponds to a black pixel, and 100 to a bright color (green,

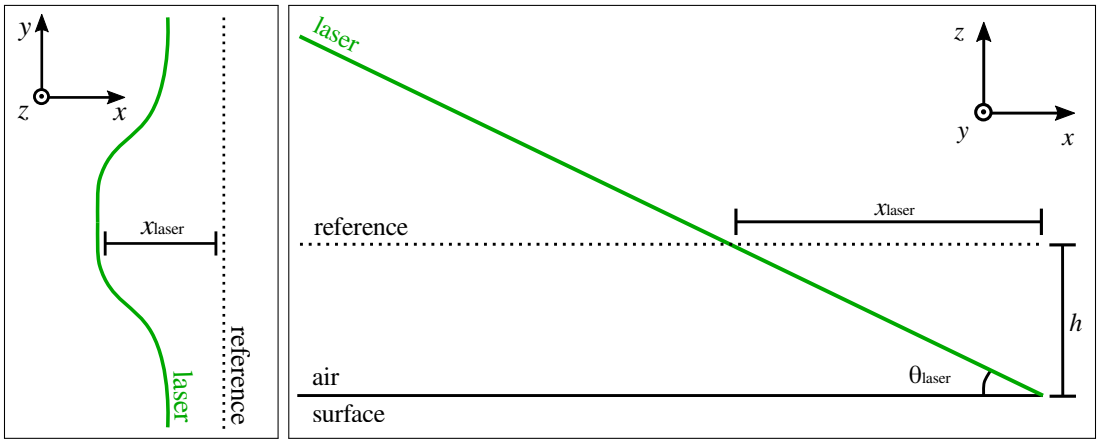

Figure 2.6 – Laser deviation x_{laser} as a function of the bath or the bed elevation h: Top and side view.

here). The intensity shows a peak, which corresponds to the location of the laser line. A fit of the peak with a second-order polynomial allows us to locate the maximum of intensity. Repeating this process, we extract the position of the entire laser line : $x_{laser}(y)$.

We then translate the laser over 20 centimetres in the downstream direction, and compute the average of the laser location $\langle x_{laser} \rangle$ (red, dashed lines of Fig. 2.7a).

Then, we sequentially raise the surface elevation by adding exactly 25.0 cL of milk per step. This addition of milk results in a level change of $\Delta h = 0.57 \pm 0.08$ cm (the total surface of the basin is $4.39 \cdot 10^2$ cm^2). This change of level moves the intersection of the laser sheet with the milk surface. We iterate our image analysis and locate the new laser deviation for different elevations of the milk surface. This procedure yields the relation between the surface elevation h and the averaged laser location (Fig. 2.7c):

$$h \text{ [cm]} = (0.0031 \pm 0.0002)\langle x_{laser} \rangle \text{ [pixels]} \tag{2.2}$$

which corresponds to a laser angle θ_{laser} of 28.3°.

We check the cross-stream flatness of the surface by looking at the fluctuation of x_{laser} around its average for each step (Fig. 2.7b). We observe a curvature of the milk surface of less than 1 pixel of laser deviation, corresponding to an uncertainty on the height of 80 μm. This curvature might be due to surface tension, or to lens-induced distortion.

Finally, we can also measure the downstream slope of our laser scanner. To do so, we plot the averaged laser location $\langle x_{laser} \rangle$ as a function of the laser scanner position (Fig. 2.7d). The downstream slope is less than 2 pixels in 20 cm, which corresponds to a slope of 0.3 ‰. It is the slope of the scanner path with respect to the horizontal. In the following, we will assume that our scanner is perfectly horizontal, and treat this value as our uncertainty on slope measurements (§ 2.3.2).

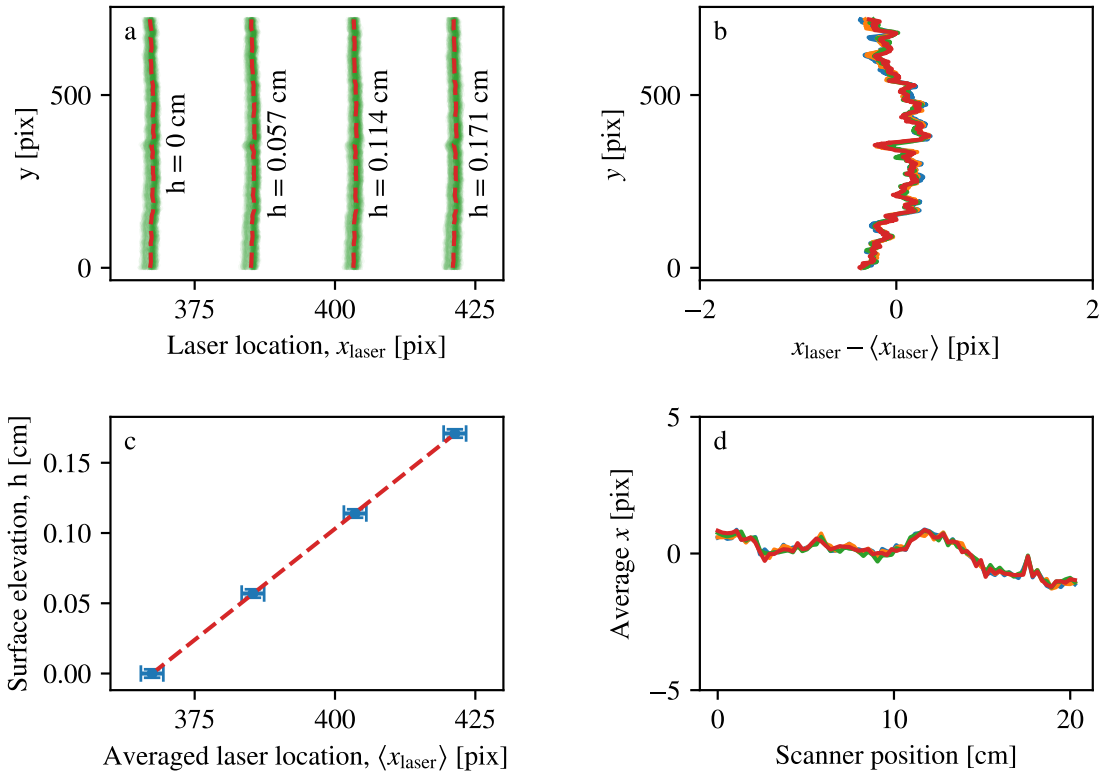

Figure 2.7 – Calibration of the laser scanner with a milk bath. a. Laser location for different bath elevations. Dashed red lines : Location of the laser intensity peak. b. Laser location across the channel: deviation from its mean value. Each color corresponds to a bath elevation. c. Calibration curve: elevation of the milk surface as a function of the laser location. Blue points: measurements. Red dashed line: linear fit. d. Cross-stream average of the laser line as a function of its downstream position.

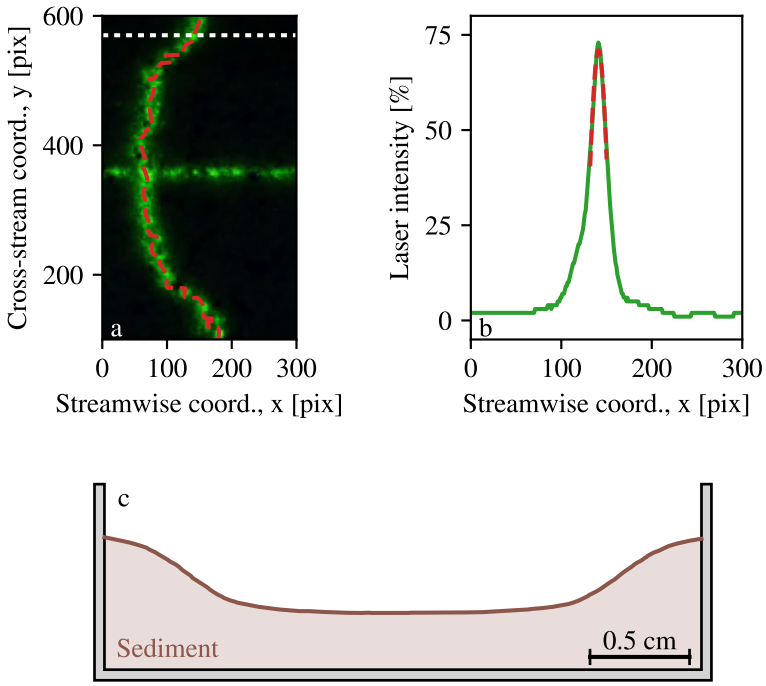

Figure 2.8 – Bed-elevation measurement. Example of run 2 (Tab. 2.1). a. Laser sheet projected on the channel bed (top view), after smoothing with a 4-pixels wide Gaussian filter. b. Image intensity along the white, dashed line of figure a (y = 570). Fit of the intensity by a second-order polynomial. Laser width : 20 pixels. c. Sediment bed elevation measured by the deviation of the laser sheet. The distance between the flume bottom and the minimum of the bed elevation is arbitrary.

Bed cross section

Based on the calibration relation between the laser location and the surface elevation (equation (2.2)), we measure the elevation of the sediment bed, once the channel is dry, at the end of an experimental run.

To do so, we translate the laser sheet over a streamwise distance of 20 centimetres to scan the bed and obtain a movie with the laser deviation due to the bed elevation. First, we reduce the noise due to the bed roughness by averaging the movie over 10 consecutive frames.

Then, we locate the laser line x_{laser} on each averaged frame with the procedure described above (Fig. 2.8a and b). The bed elevation $h(y)$ is then proportional to the laser deviation. Finally, we average the bed elevation on all the frames and obtain the profile showed on figure 2.8c.

This method allows us to measure the bed elevation with an accuracy of $\Delta h = 80\,\mu$m $= 0.1\,d_s$. The associated image analysis procedure is quick (less than one hour of computer time for each run).

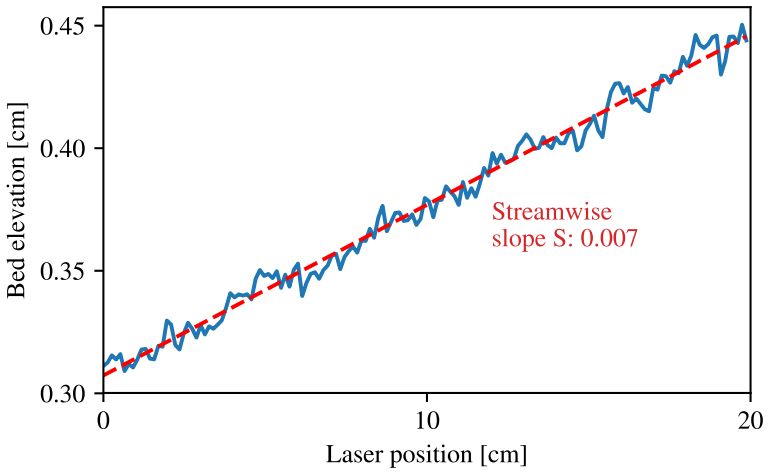

Figure 2.9 – Downstream-slope measurement. Example of run 2 (Tab. 2.1). In blue: sediment bed elevation along the streamwise direction. Dashed red line: linear fit.

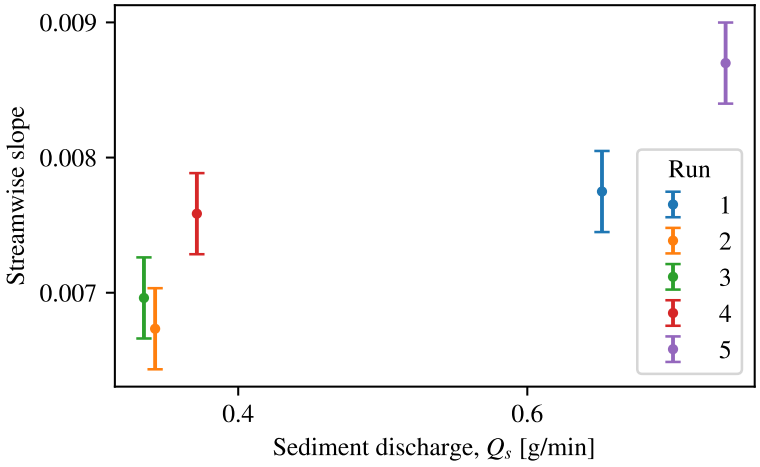

Figure 2.10 – Downstream slope of sediment beds as a function of the sediment discharge. Each color corresponds to a run of table 2.1.

2.3.2 Downstream slope

At equilibrium, the bed cross section is invariant in the x-direction. However, the bed lowers continuously downstream, meaning that it has reached a downstream slope S. The corresponding shift of the laser line allows us to measure this slope.

When we plot the mean elevation of the bed as a function of the laser streamwise position, we find a continuous increase (Fig. 2.9). The proportionality coefficient of this curve is the downstream slope of the bed. In the case of the experimental run 2 (Tab. 2.1),

$$S = (7.0 \pm 0.3) \cdot 10^{-3} \,. \tag{2.3}$$

The uncertainty corresponds to the slope of the scanner path, measured during the calibration (section 2.3.1).

We measure the equilibrium slope of the sediment bed for each experimental run. We observe that the latter increases with the sediment input (Fig. 2.10). This indicates that the bed self adjusts to the sediment input.

2.3.3 Flow depth

The laser scanner allows us to measure both the bed elevation h and its downstream slope S. However, we also need the flow depth to get a complete picture of the flume's cross section.

As we know both the bed elevation and the flume width, the position of the flow surface depends on the water discharge Q_w, which reads:

$$Q_w = \iint u \, \mathrm{d}y \, \mathrm{d}z \,. \tag{2.4}$$

where u is the flow velocity. Consequently, we first calculate the flow velocity as a function of the surface elevation.

As the Reynolds number in our experiments remains around 10, the flow is laminar. The downstream invariance of the flow then simplifies the Navier-Stokes equations. Also, the flow is at steady state, which removes the dependence of the equation with time. Finally, the flow velocity satisfies the Stokes equation, which takes the form of a Poisson equation in this geometry,

$$\eta \nabla^2 u = -\rho_f g S \,. \tag{2.5}$$

Equation (2.5) involves only parameters that we have measured, such as the slope S. We now supplement equation (2.5) with two boundary conditions. First, the velocity vanishes on the sediment bed and on the side walls (no-slip condition, $u = 0$). Secondly, the shear stress vanishes on the flow surface (free-surface condition, $\partial_y u = 0$).

To calculate the flow velocity u, we now solve equation (2.5) numerically with the

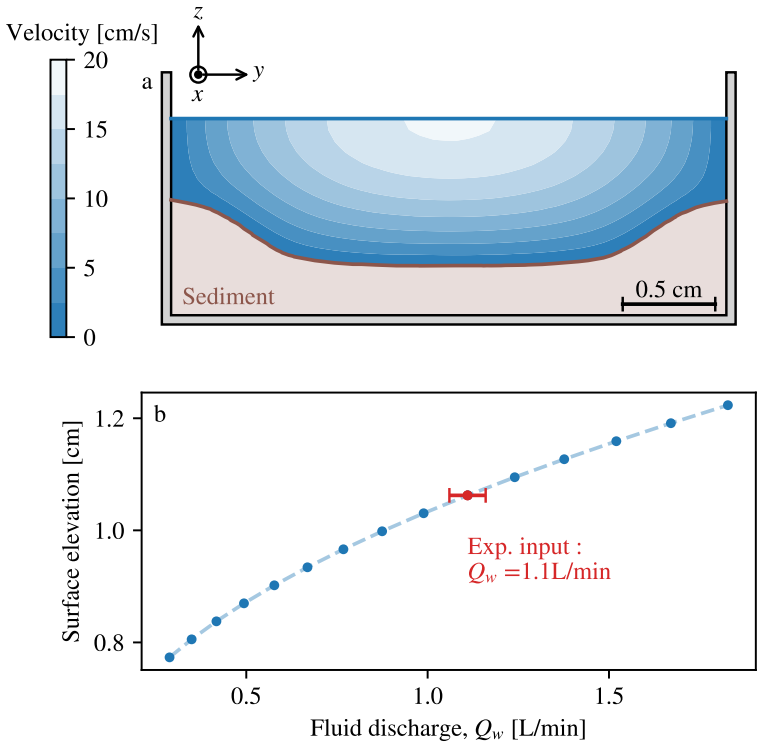

Figure 2.11 – Flow numerical computation. Example of run 2 (Tab. 2.1). a. Velocity field in the channel cross section for a given flow depth. b. Flow depth as a function of the fluid discharge. Blue points: numerical computation. Red point: experimental value.

finite-elements software FreeFem++ (Hecht 2012). We use our experimental bed elevation as a boundary. We supplement it with two vertical side walls and fix the surface elevation. We can then compute the corresponding velocity field inside this domain (Fig. 2.11a).

Then, the integration of the flow velocity across the stream yields the fluid discharge for a given surface elevation. We iterate this process for different surface elevations. To deduce the flow surface in our flume experiment, we interpolate the elevation which corresponds to our fluid discharge input (Fig. 2.11b).

In the case of run 2 displayed in figure 2.11, we find the surface elevation at 1.06 ± 0.03 cm, which corresponds to a maximum depth of 0.79 ± 0.03 cm.

We measure the flow depth for each experimental run. Here again, we observe that the sediment bed adjusts its depth to the sediment input. In particular, it decreases as a function of the sediment discharge, although this trend remains of the order of the measurement uncertainty (Fig. 2.12).

2.4 Sediment flux

As the bed reaches its equilibrium shape, sediment transport distributes itself into a steady profile across the stream. In this section, we explain how we measure the sediment-

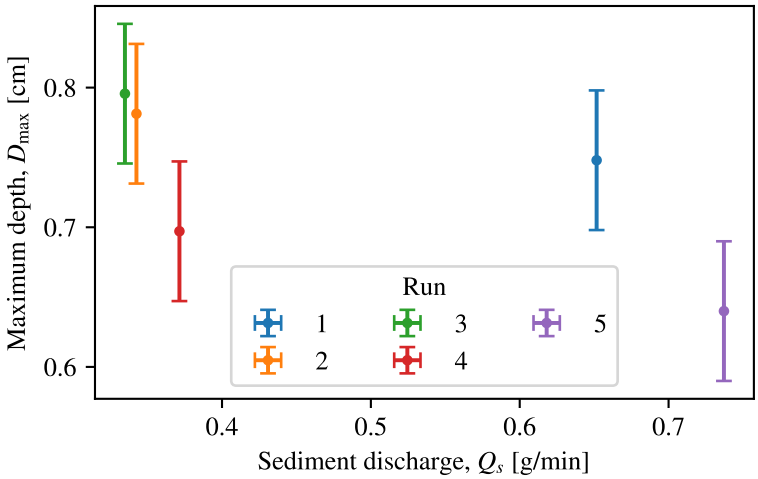

Figure 2.12 – Maximum flow depth as a function of the sediment discharge. Each color corresponds to a run of table 2.1.

flux profile across the flume.

2.4.1 Bedload movies

A camera (Canon 700D) placed above the flume records the motion of the particles over the bed with a frequency of 50 frames per second.

The camera field of view covers an area of 6 centimetres in the sreamwise direction, and 3.5 centimetres in the cross-stream direction (slightly more than the entire channel width), with a resolution of 1280×1024 pixels. A LED light panel illuminates this area enough to fix the time exposure at 0.01 second for a f/8 lens aperture.

The camera's memory allows us to record only 10-minutes movies. To improve the statistical relevance of our measurements, we record 10 sequences of 10 minutes for each run.

2.4.2 Particles tracking

Different methods of image processing have been previously developed to track bedload particles. Some experimenters tracked particles manually (Charru *et al.* 2004a). Since then, computerized methods have much improved as they benefitted from the development of particle image velocimetry. To track black tracers in a crowd of white grains, one can use a threshold on the light intensity (Seizilles *et al.* 2014). When the moving grains are not contrasted enough with the underlying bed, some experimenters used a method based on background subtraction (Heyman & Ancey (2014)).

Here, since our grains are colored, we track them with a colorimetric method. The image processing consists in three steps: (i) color conversion of the images, (ii) centre

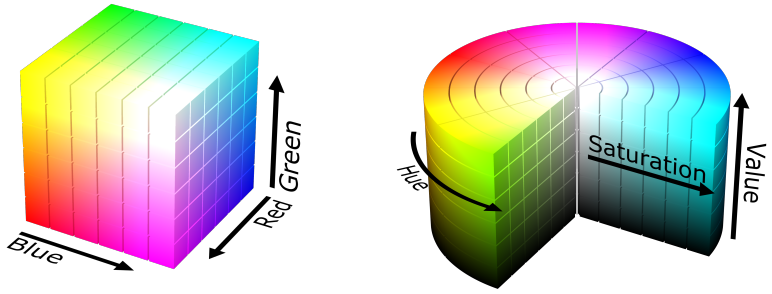

Figure 2.13 – Illustration of the RGB (left) and HSV (right) color systems. Credits: Wikipedia Creative Commons.

detection and (iii) trajectories reconstruction. In the next section, we provide details for each step.

HSV color system

Each frame is recorded in the RGB (Red, Green, Blue) color system, in which red, green and blue light are mixed to reproduce colors (Fig. 2.13a). However, the relationship between the amounts of red, green, and blue light and the resulting color is not intuitive. The human eye may, for example, find two colors close whereas they do not have similar coordinates in the RGB system (Table 2.2). A transformation enables us to convert colors from the RGB to the HSV color system.

Unlike RGB, HSV (Hue, Saturation, Value) color system separates the color information from the image intensity and lightness (Fig. 2.13b). The hue (H) of a color refers to which pure color it resembles (Fig. 2.13b). For example, the two colors that we considered previously, close in tints, have a similar hue (Tab. 2.2). More generally, all tints, tones and shades of a pure color have the same hue. The saturation (S) of a pixel encodes how white it is. A pure blue is fully saturated (S = 1), whereas tints of blue have saturations less than 1. White has a saturation of 0. The value (V) of a pixel, also called its lightness, describes how dark its color is. A value of 0 is black, and an increasing lightness moves the color away from black.

We now apply this conversion to our bedload movies. For a single frame, we compute the histogram of the hue (Fig. 2.14). We distinguish 6 major peaks which correspond to classes of grains (blue, red, orange, green, etc.). To track a class of grains, we define a hue range. For example, the blue grains are in the range 0–81 (Fig. 2.14).

	Red	Green	Blue	Hue
	0.211	0.149	0.597	68°
	0.495	0.483	0.721	60.5°

Table 2.2 – Different colors and their coordinates in the rgb system. Corresponding hue.

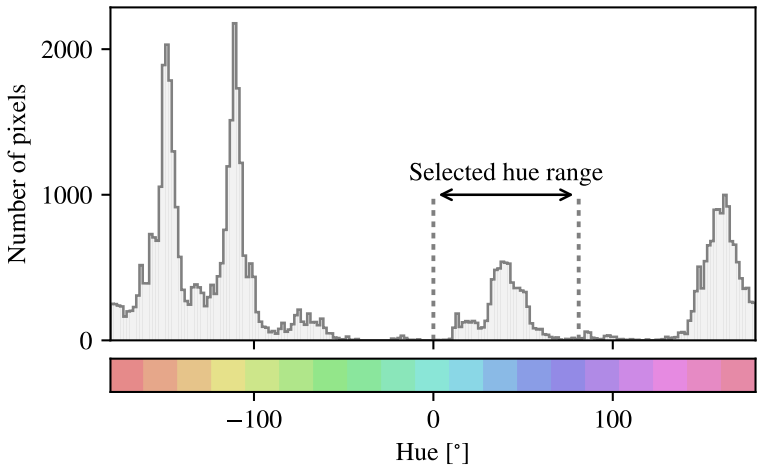

Figure 2.14 – Histogram of hues from the picture of figure 2.15a. Selected hue range: [0, 81], corresponding to blue hues. The colorbar indicates the hue values for a saturation of 0.5 and a value of 0.8.

Grain positions

Once we have chosen the range of hues, we discriminate pixels based on their saturation, which we require to be higher than 0.3. This criterion gives a map, characterised by clusters of pixels, and corresponding to individual grains of this class (Fig. 2.15). We detect the local maxima of this criterion, which gives us the positions of the corresponding grains.

To avoid detecting twice the same grain, we define a minimum distance between two maxima. The number of detected grains depends on this parameter (Fig. 2.16a). We fix it at 10 pixels, which corresponds to a grain size. We also convolve the criterion picture with a Gaussian filter to reduce the noise. Here again, the number of detected grains depends on the size of this filter, which we fix at 10 pixels (Fig. 2.16b).

Dependence of the detection on the flow depth

Our tracking method is based on top-view movies. However, the flow depth varies across the channel. We have to ensure that the number of particles our algorithm detects is not biased by the fluid depth.

To do so, we use an independent experiment. It is a flat sediment bed, covered by a fluid layer. No particle is moving. We simply detect, at rest, a certain number of grains as a function of the fluid depth. We start from a fluid depth of 30 mm and we sequentially reduce the fluid depth by removing some fluid with a syringe. Then, we plot the number of detected grains as a function of the fluid depth (Fig. 2.17).

For a transparent liquid, there is no bias. The number of detected particles varies by less than ±5% (Fig. 2.17, in blue). This means that even if the fluid depth is not constant across the channel, we are able to track particles without significant bias, provided the

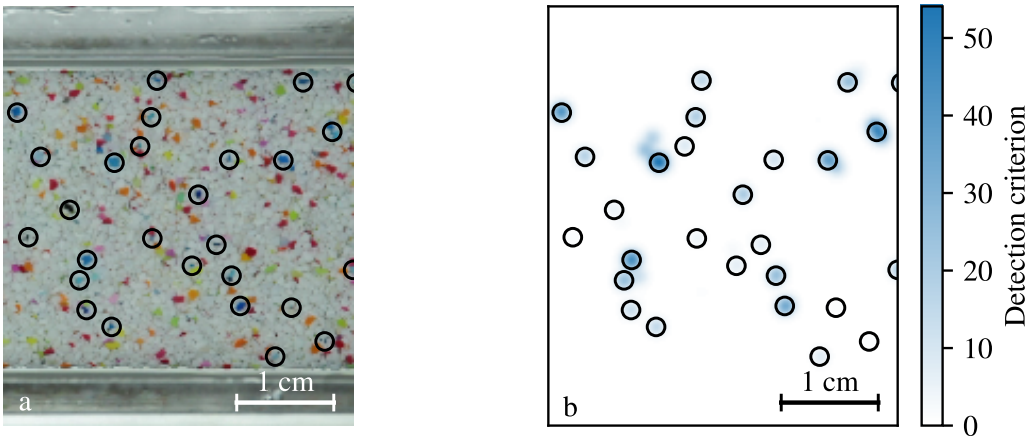

Figure 2.15 – Grain detection in our experimental flume. a. Image of the channel seen from the top. Black circles: detected blue grains. b. Detection criterion on the image. Black circles: location of the maxima.

liquid is transparent.

Grains trajectories

The method described above yields, for each frame, the positions of grains belonging to a same class. We now need to identify these grains on two successive frames to build their trajectories.

The simplest way to reconstruct a trajectory is to link each particle to its nearest neighbour in the next frame. This method, however, does not yield the most likely set of particle couples: the optimal set depends on the distribution of all the particles. Consequently, we use an equivalent of the Hungarian algorithm, which optimises a global cost function based on all particles positions (Munkres 1957, Heyman & Ancey 2014). We provide the corresponding codes in appendix A (section A.4).

With this procedure, we sometimes loose track of some particles, either because they collide with another particle and they appear as a single large particle, or because they are covered by travelling particles. We thus allow a certain number of frames over which a grain can disappear (typically 10 frames). Table 2.3 summarizes the parameters we choose for the whole procedure.

Then, we record the trajectories' coordinates and the time of their appearance. Figure 2.18 shows 15 trajectories from run 2. This enables us to check if the algorithm works, but it is difficult to do so for all trajectories (typically 30000 per experimental run).

In the next section, we compute the sediment flux based on these trajectories. We will also show how we evaluate the reliability of our measurements.

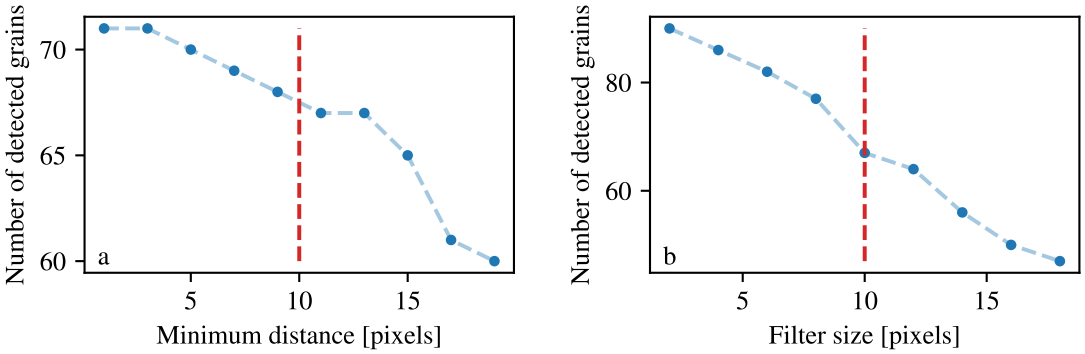

Figure 2.16 – Dependence of the number of detected grains on the tracking parameters. a. Number of detected grains as a function of the minimum distance between two maxima. b. Number of detected grains as a function of the Gaussian-filter size. The dashed red lines correspond to the values we chose.

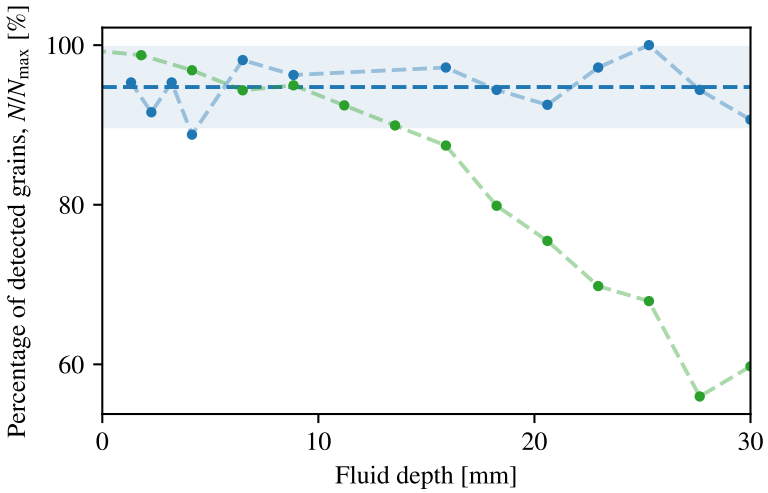

Figure 2.17 – Number of detected grains as a function of the fluid depth. Blue: transparent fluid. Green: fluid with blue dye.

Name	Value
Frame number	39312
Frame per seconds	50.0
Resolution [pixels/cm]	170
Blue hues range	0 – 81
Minimum saturation	0.3
Filter size [pixels]	10
Minimum distance [pixels]	10
Absolute threshold	0
Appearance probability length [number of frames]	10
Disappearance probability length [number of frames]	10

Table 2.3 – Tracking parameters.

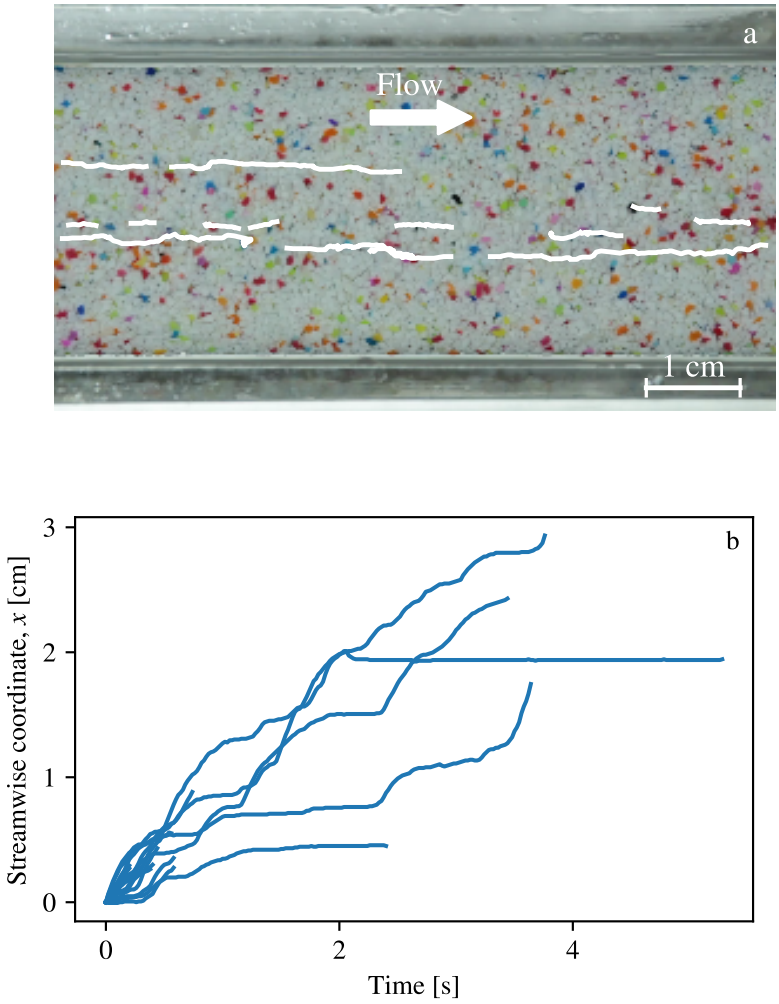

Figure 2.18 – Selection of 15 trajectories of sediment grains. a. Channel seen from the top. White: selection of grains trajectories. b. Streamwise position of particles as a function of time. Horizontal segments correspond to deposited grains.

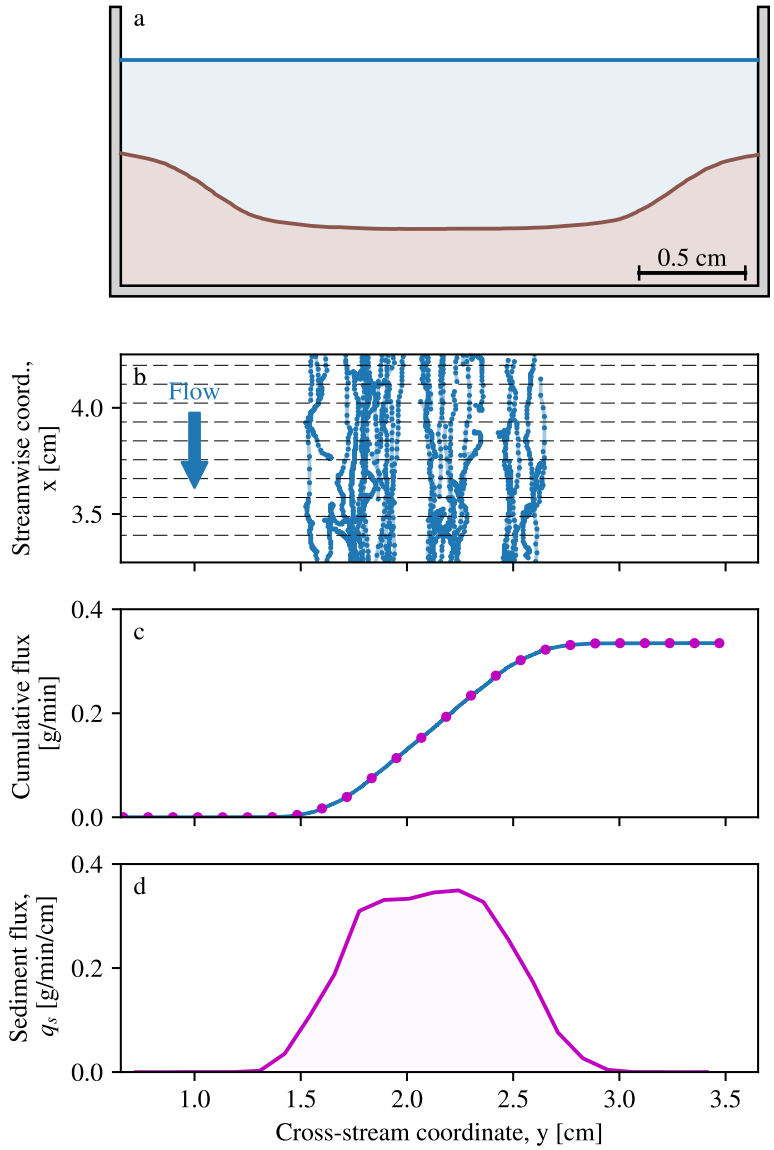

Figure 2.19 – Cross section and sediment-flux profile. Run 2 : Q_w = 1.1 L/min, Q_s = 0.34 g/min. a. Cross section. Brown: sediment. Blue: flow. b. Selection of grain trajectories. Grey dashed lines: crossing lines where the cumulative sediment flux is computed. c. Cumulative sediment flux. In blue: raw data. Magenta points: data distributed into 30 bins. d. Sediment-flux profile, calculated from the binned cumulative sediment flux.

2.4.3 Sediment-flux profile

Based on the trajectories of individual grains, we now compute the local sediment flux. To do so, we define an imaginary line perpendicular to the flume cross section (one of the dashed grey lines in Fig. 2.19b). Each time a trajectory crosses this line, we record the position y_{cross} of the crossing. We then attribute to this position the value s, which is equal to +1 if the trajectory crosses the line in the downstream direction. Conversely, if a trajectory crosses this line in the upstream direction, $s = -1$. We then iterate this procedure for 100 imaginary lines (Fig.2.19b).

Based on these quantities, we define the cumulative distribution of crossings over the flume cross section,

$$C(y) = \sum_{y_{\text{cross},i}<y} s_i \,. \tag{2.6}$$

According to this definition, this function starts from 0 on the left wall, increases with the cross-stream coordinate, and reaches its maximum on the other side of the channel. As we tracked a class of grains, and not all the travelling grains, we normalise this distribution with the input sediment discharge that we measure independently with the scale (Fig.2.19c).

The derivative of the cumulative distribution provides us with the sediment-flux profile across the channel (Fig.2.19d):

$$q_s(y) = \frac{\mathrm{d}C(y)}{\mathrm{d}y} \,. \tag{2.7}$$

However, we first need to smooth out the cumulative distribution to reduce the noise which the numerical derivation exaggerates. Thus, we fix the number of bins N_{bins} on which we interpolate the distribution (Fig. 2.19c, points). The aspect of the sediment profile then depends on the number of bins. For $N_{\text{bins}} = 200$, the standard deviation on q_s varies from 0.03 to 0.1, depending on the location in the channel (Fig. 2.20a). Conversely, a small number of bins ensures a good precision, but a low resolution (Fig. 2.20c). We find that $N_{\text{bins}} = 40$ is a good compromise between precision and resolution (Fig. 2.20b). It corresponds to a bin size of about 0.8 mm (approximately one grain size).

Overall, fixing the bin size of the interpolation sets the number of particle crossings we record per bins (Fig. 2.20d). The more crossings we record (typically by recording long movies), the more accurate our measurement.

To evaluate the precision of our sediment-flux measurement, we select an area of the profile in which the sediment flux is homogeneous. Then, we measure the sediment flux for several bin sizes. As the sediment flux is homogeneous in the selected area, the measurement of q_s should be equal. In practice, the flux slightly varies from one bin to another one due to experimental noise. We define the relative error as the ratio between the standard deviation of these measurements $\text{std}(q_s)$ and the mean sediment flux $\langle q_s \rangle$. As expected,

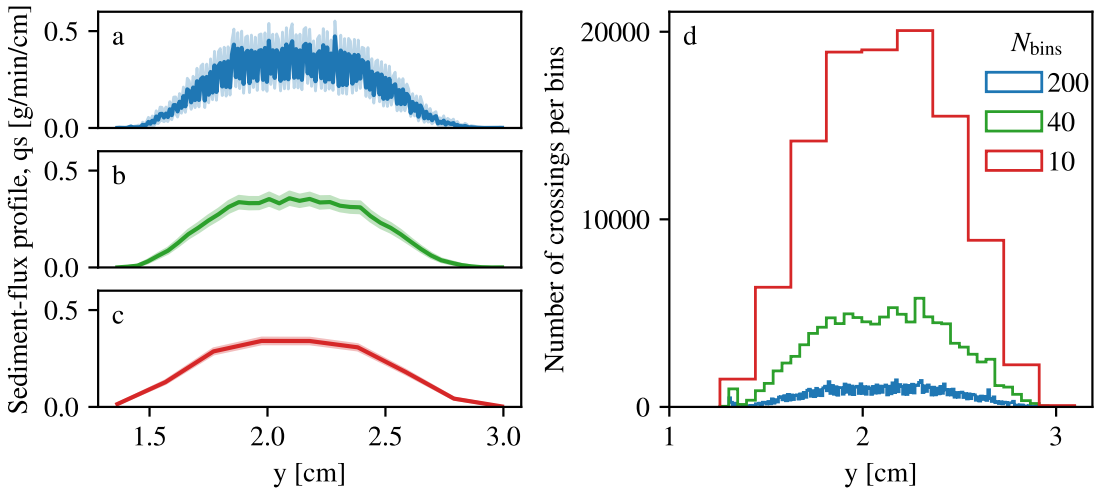

Figure 2.20 – Dependence of the sediment-flux profile on the number of bins. Left: Sediment-flux profile for different numbers of bins. Shaded areas show the measurement uncertainty. a. Number of bins N_{bins} = 200. b. N_{bins} = 40. c. N_{bins} = 10. d. Number of particle crossings per bin by varying the number of bins. N_{bins} = 10 (red), 40 (green), 200 (blue).

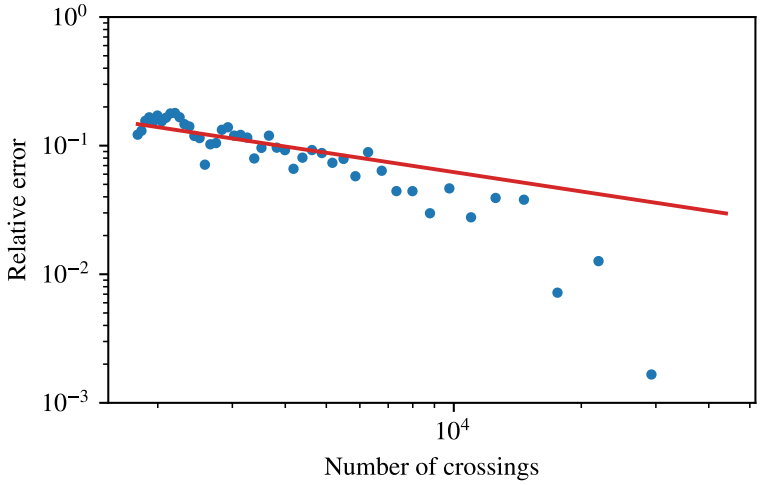

Figure 2.21 – Relative error of the sediment-flux measurement as a function of the number of particle crossings. Red line: Fit by the inverse square root of the number of particle crossings (equation (2.8)).

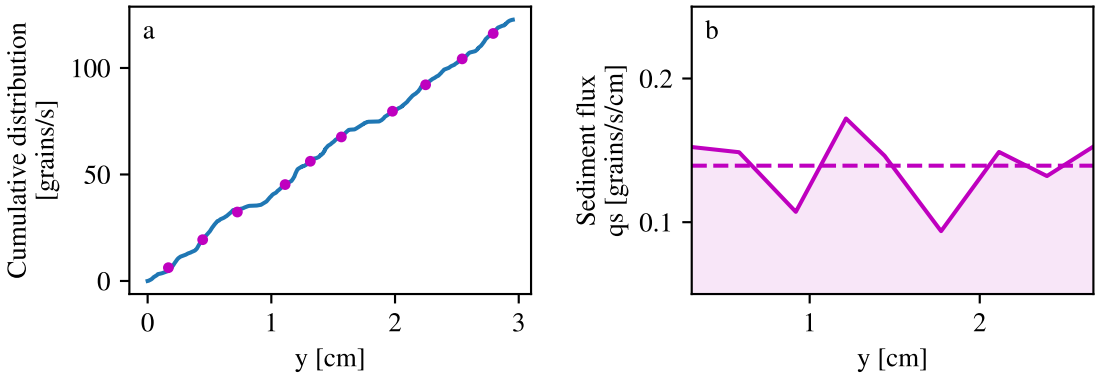

Figure 2.22 – Sediment flux of a bed translated uniformly. a. Cumulative distribution of grains crossings across the channel. The origin corresponds to the left-hand wall of the channel, and 3 cm on the right-hand wall. b. Sediment-flux profile calculated from the cumulative profile. Dashed line: mean sediment flux.

the relative error decreases with the average of the number of crossings per bin $N_{\text{crossings}}$ (Fig. 2.21). We find that the measurement is accurate within an error of 10 % if the number of crossings is higher than 3000, which is true near the center of the channel (with $N_{\text{bins}} = 40$). A fit provides:

$$\frac{\text{std}(q_s)}{\langle q_s \rangle} = \frac{6.2}{\sqrt{N_{\text{crossings}}}} . \tag{2.8}$$

In the following, we will use this formula to evaluate the error of our sediment-flux measurement, based on the number of crossings we use in each bin.

To further check if our method yields reasonable results, we measure the sediment flux on an uniformly-moving bed. To do so, we set an immobile dry sediment bed and we translate the camera at constant velocity (2 mm/s). Consequently, in the referential of the camera, all the grains move downstream uniformly. Then, we track the grains during 5 minutes. We therefore expect the sediment-flux profile to be homogeneous across the channel.

We obtain the cumulative distribution of figure 2.22a and use it to calculate the sediment-flux profile across the channel (Fig. 2.22b). As expected, the profile is approximately constant across the channel, and this ensures that there is no bias induced by the lighting conditions or the lens-induced distortions.

Figure 2.19 summarizes our combined measurements of cross section and sediment-flux profile for an experimental run. We find that the shape of the sediment bed is correlated with its sediment-flux profile. Sediment transport is more intense around the center of the channel, and virtually vanishes near the banks. Due to viscous stress on the side walls, we expect less friction on the bed near the banks. This might explain why transport is weaker there. To investigate this hypothesis, we need to calculate the shear stress exerted by the flow on the bed. We also need to characterise our grains: to measure their transport law

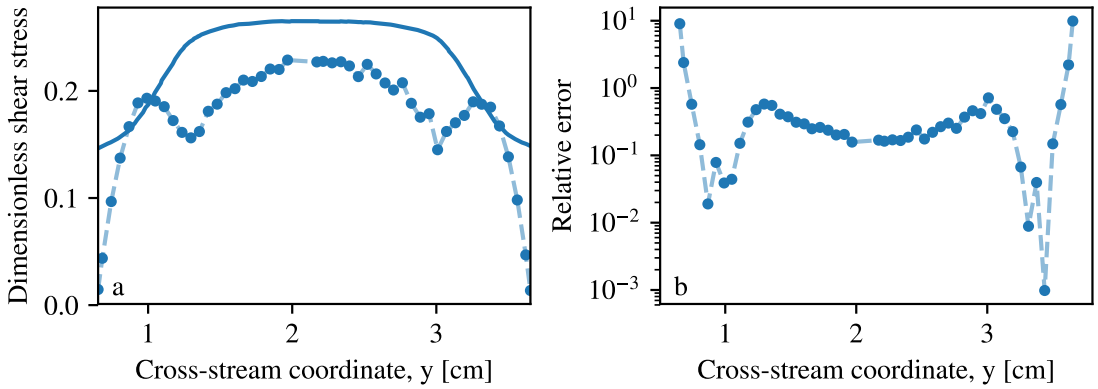

Figure 2.23 – Flow-induced shear stress. Example of run 2 (Tab. 2.1). a. Flow-induced shear stress on the bed across the channel. Points: shear stress computed with finite elements based on the experimental bed elevation. Full line: shear stress predicted by the shallow-water approximation. b. Ratio between the flow-induced shear stress computed with finite elements and the shear stress calculated with the shallow-water approximation.

and to evaluate their diffusion across the stream. We will do that in the next two sections, based on the measurements we just presented.

2.5 Transport law

In sections 2.3 and 2.4, we described our measurements of the cross section, the flow velocity and the sediment-flux profile. In this section, we infer the transport law of our grains from these measurements.

2.5.1 Flow-induced shear stress

The transport law is the relation between the density of entrained grains and the Shields parameter, which is proportional to the shear stress the flow exerts on the sediment bed (section 1.3). We have already measured the local intensity of transport with the sediment-flux profile. We now need to compute the flow-induced shear stress.

In § 2.3.3, we used finite elements to calculate the velocity field of the flow $u(y, z)$ in the channel's cross section. From this flow-velocity field, we deduce the shear stress τ exerted by the flow on the bed:

$$\tau = \eta \, \mathbf{e_n} \cdot \nabla u \,, \tag{2.9}$$

where η is the viscosity, and $\mathbf{e_n}$ is the unit vector normal to the bed surface.

Figure 2.23a presents a typical shear-stress profile. As expected, this quantity varies across the stream (Fig. 2.23a): it is higher near the center of the channel and it vanishes at its corners, because spatial derivatives of the velocity vanish at this point ($\partial_x u = \partial_y u = 0$).

In most experimental studies, the flow-induced shear stress is calculated using the

shallow-water approximation, according to which $\tau = \rho_f g D S$. To test the validity of this approximation in laboratory flumes, we compare the shear stress deduced from equation (2.9) to the prediction of the shallow-water approximation (Fig. 2.23b). In the center of the flume, the shallow-water approximation overpredicts the shear stress by about 15%. Near the side walls, this approximation further breaks down. It predicts a finite shear stress, whereas, in reality, the friction with the walls causes it to vanish.

2.5.2 Transport law

From the shear stress τ, we now calculate the Shields number by

$$\theta = \frac{\tau}{\Delta \rho g d_s^3} \,. \tag{2.10}$$

The profile of the Shields number is thus proportional to the shear-stress profile and varies across the channel. Near the banks, the Shields number is small and the sediment transport vanishes. Away from the banks, the Shields number increases, then crosses its critical value, and transport begins. Transport increases towards the center of the channel.

Therefore, a single experiment allows us to cover a wide range of Shields number θ and of sediment flux q_s. We can now plot the sediment flux as a function of the Shields number for any cross-stream coordinate y in an experimental run (Fig. 2.24).

With this single run experiment, we have a first estimation of the Shields number at the threshold: $\theta_t \approx 0.15$. Comparatively, Seizilles *et al.* (2014) found $\theta_t = 0.125$ for a particle Reynolds number of $Re_s = 25$ and Charru *et al.* (2004a) measured 0.16 for $Re_s = 0.3$.

If we plot all the runs together, we obtain the figure 2.24. All runs gather around a common transport law, indicating that this transport law is a local relationship. It depends on the grains and the viscous fluid, only.

Finally, we fit a transport law on all these runs, and we find

$$q_s = q_0 \, (\theta - \theta_t) \,, \quad \text{with } \theta_t = 0.169 \pm 0.001 \tag{2.11}$$

$$q_0 = (5.9 \pm 0.2) \cdot 10^4 \, \text{grains/m/s} \,. \tag{2.12}$$

This transport law does not account for the effect of the bed cross-stream slope on the threshold of grains entrainment. This effect is usually embedded with the force ratio μ, linked to the Shields number by (§ 1.1.4, equation (1.13)):

$$\mu = \sqrt{\left(\frac{\mu_t}{\theta_t}\theta\right)^2 + (\partial_y h)^2} \,. \tag{2.13}$$

As our sediment bed does not transport sediment over its entire width, we measure the sediment flux only in an area where the bed cross-stream slope remains smaller than 10^{-2}

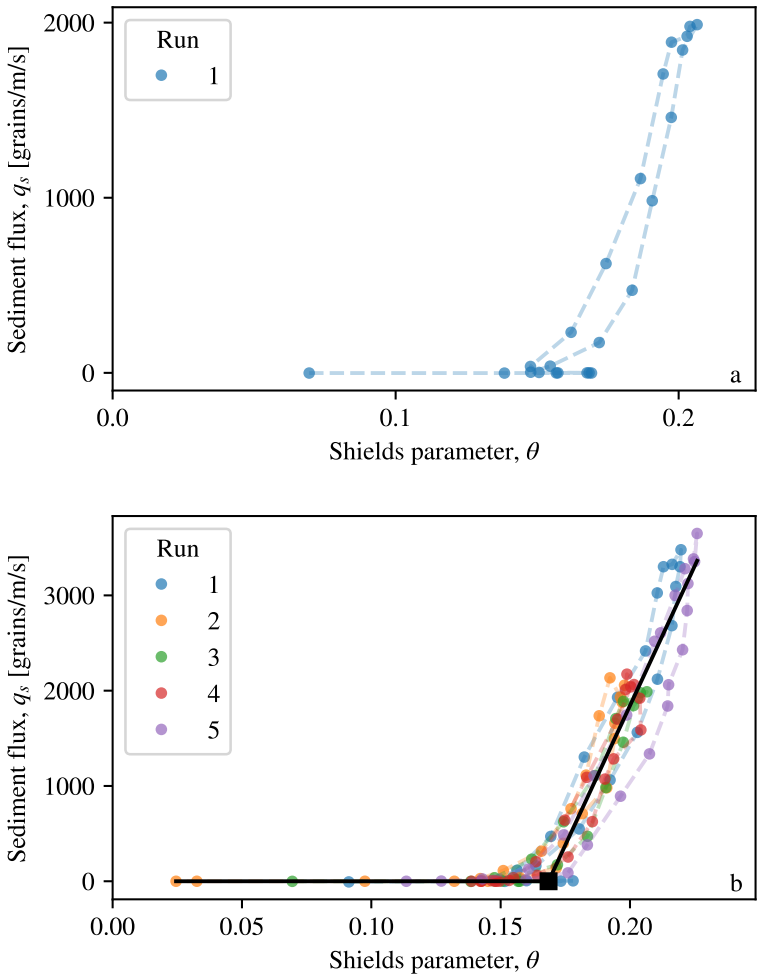

Figure 2.24 – Transport law. a. Sediment flux as a function of the Shields parameter (computed with finite elements) for run 1: $Q_w = 1.12$ L/min, $Q_s = 0.65$ g/min. This yields the transport law of grains with a single experiment. b. Sediment flux as a function of the Shields parameter for each run of table 2.1. All experiments merge on a single transport law. Black line: fit function $q_0\ (\theta - \theta_t)$. We find $q_0 = 5.9 \cdot 10^4$ grains/m/s and a critical Shields number of $\theta_t = 0.169$.

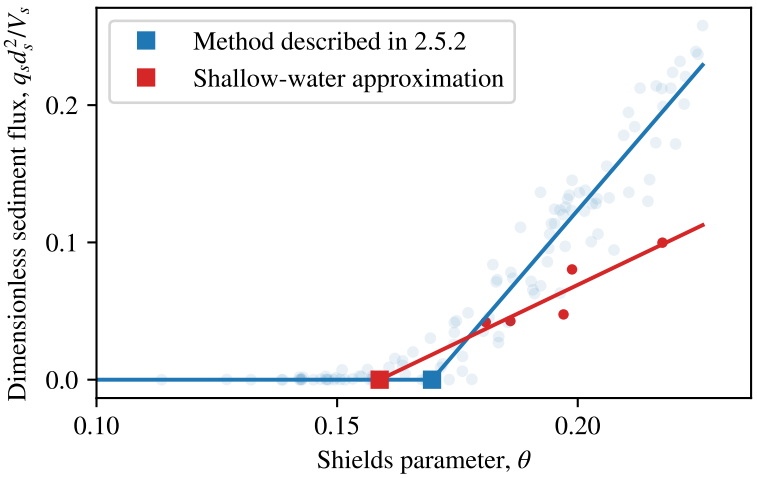

Figure 2.25 – Comparison of transport-law measurements. In blue: method described in § 2.5.2. In red: transport law calculated with the shallow-water approximation.

(Fig. 2.19). Its effect is thus negligible.

In conclusion, our experimental setup enables us to measure a transport law with a single experimental run. When the sediment input is higher, the range of sediment flux on the bed is larger and thus yields a transport law over a broader range of shear stress.

2.5.3 Comparison with the shallow-water approximation

Most experimenters measured the transport law with the shallow-water approximation. This approximation neglects cross-stream diffusion of momentum and, by definition, does not take into account the side walls. It predicts a uniform sediment flux on a flat sediment bed, sheared by a flow of depth D, and yields an expression for the local shear stress:

$$\tau = \rho_f g D S \,. \tag{2.14}$$

To compare our transport law to its shallow-water counterpart, we calculate the shear stress with equation (2.14). This expression involves the downstream slope S of the sediment bed, which we measured directly in our experiments, and the flow depth D. Assuming a one-dimensional Poiseuille flow, the flow depth depends on the fluid discharge Q_w as follows:

$$D = \left(\frac{3 Q_w \nu}{g S W}\right)^{1/3} , \tag{2.15}$$

where W denotes the width of the channel. We can thus calculate the shallow-water shear stress for each experimental run, and the corresponding Shields number.

Regarding the sediment flux q_s, it reads straightforwardly

$$q_s = \frac{Q_s}{W}\,, \tag{2.16}$$

by assuming a homogeneous sediment flux across the bed.

We report on figure 2.25 the transport law calculated with the shallow-water approximation. Each experimental run yields a data point. We fit these points by equation (2.11) and find $\theta_t = 0.15 \pm 0.01$ and $q_0 = (2.4 \pm 0.6) \cdot 10^4$ grains/m/s, or, equivalently, $q_0 d_s^2 / V_s = 1.7 \pm 0.5$. This corresponds to a relative difference for the critical Shields number of about 6% and for the coefficient q_0 of 60%. According to figure 2.23, the shallow-water approximation over-estimates the shear stress and therefore the Shields number, which explains the lower slope of the transport law.

Overall, our experiments confirm the classical assumption of bedload transport: (i) there is a local transport law (all curves are superimposed on figure 2.24), (ii) there is a well-defined threshold. Furthermore, they reveal the effect of the side walls in a confined channel, and the limits of the shallow-water approximation. However, we did not investigate the influence of the cross-stream slope of the bed, although this influence plays a role in the definition of the threshold (§ 1.1.4). In the next section, we characterize bedload diffusion of our grains.

2.6 Bedload diffusion

According to Seizilles *et al.* (2014), bedload grains collide with the bed as they travel downstream. The resulting deviations induce cross-stream diffusion. A cross-stream flux q_d appears, which is oriented towards less active areas,

$$q_d = -\ell_d \frac{\partial q_s}{\partial y}\,, \tag{2.17}$$

where ℓ_d is a diffusion length.

In our experimental flume, sediment transport is more intense in the channel center, resulting in a strong transverse gradient of concentration of bedload grains. As a result, bedload diffusion must play a role in the dynamical equilibrium of the bed.

Seizilles *et al.* (2014) measured $\ell_d = 9.5\,\mu$m for plastic grains of size $344\,\mu$m, entrained by water. In our flume, we use a more viscous fluid (mixture of water and glycerol) flowing over bigger grains ($830\,\mu$m). We now proceed to measure the diffusion length for our grains.

To do so, we use the grains' trajectories of § 2.4.2. By shifting the trajectories so they all start from the same point (Fig. 2.26a), we find that the grains disperse across the stream as they travel downstream. We measure the cross-stream variance of the particle positions σ_y^2 for different streamwise positions x (Fig. 2.26a). As expected for random walkers, this

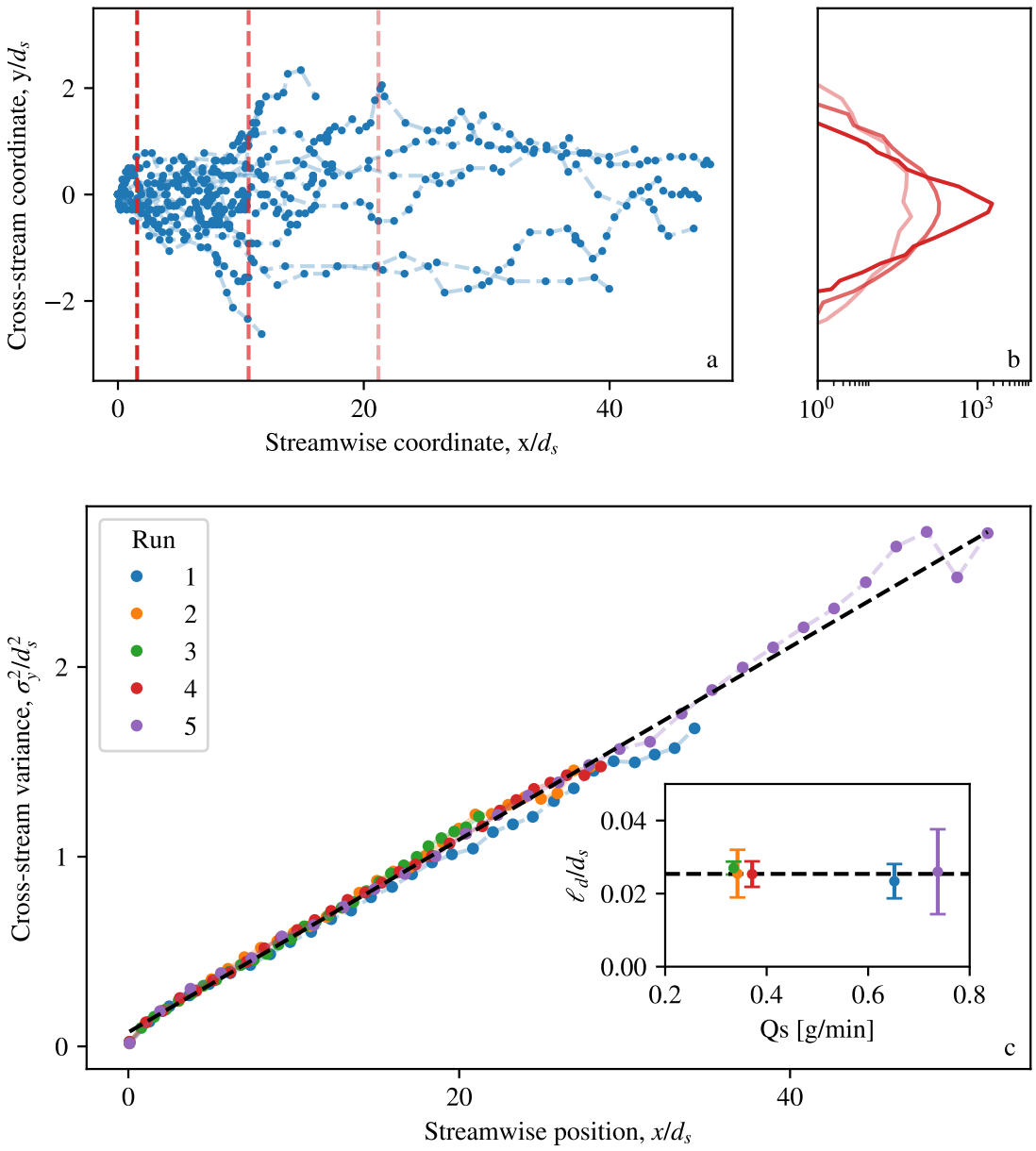

Figure 2.26 – Bedload diffusion. a. Selection of 15 grain trajectories. The trajectories are shifted so that their origin coincide. As grains travel downstream, trajectories drift away from the center. b. Distribution of grains' trajectories along the vertical dashed lines of panel a (with the same color code). c. Variance of cross-stream coordinates as a function of the streamwise position of grains. Each color corresponds to an experimental run (Tab. 2.1). Dashed black line: Linear fit of experimental data, which yields $\ell_d = (0.0254 \pm 0.0002)\, d_s$. Inset: diffusion length, fitted by independent fit for each run, as a function of the sediment discharge of the run. Dashed black line: diffusion-length value computed by the fit on multiple experiments.

variance increases linearly with the longitudinal position x (Fig. 2.26c). Following Seizilles *et al.* (2014), we then deduce the diffusion length from the slope of this relationship. We find

$$\ell_d = (0.0254 \pm 0.0002)\ d_s\,, \tag{2.18}$$

which is close to the measurements of Seizilles *et al.* (2014), where $\ell_d = (0.030 \pm 0.004)\ d_s$.

Repeating this procedure for different experimental conditions (experimental runs of table 2.1), we find that the diffusion length remains constant as the intensity of sediment transport varies (Fig. 2.26c, inset).

These results confirm the diffusive behaviour of our bedload grains and provide us with the intensity of the cross-stream flux induced by diffusion. This flux is oriented from the most active part of the channel (the center) towards the less active ones (the side walls). In the following, we investigate how this flux controls the bed's shape.

2.7 Bed equilibrium: Boltzmann distribution

As discussed in the previous section, the presence of a gradient of sediment flux in our experiments induces a diffusive flux of particles oriented from the center towards the banks. This flux carves the bed near the channel center while depositing grains near the walls. However, as the bed cross section reaches steady state, another mechanism must oppose the diffusive flux.

As first proposed by Parker (1978a), gravity likely induces such a flux, because of the cross-stream slope of the bed. We expect gravity to pull grains down the slope and bring them back to the center (Parker 1978a, Kovacs & Parker 1994, Seizilles 2013). Assuming that gravity induces a cross-stream flux in proportion to the cross-stream slope $\partial h/\partial y$ and to the local sediment flux q_s, we get:

$$q_g = -\gamma q_s \frac{\partial h}{\partial y}\,, \tag{2.19}$$

where γ is a coefficient in the range 0.1–1 (Chen *et al.* 2009). This gravity flux vanishes when the bed is horizontal, for instance at the center of the channel.

In steady state, we expect that gravity counteracts diffusion. Following this assumption, mass balance requires that the divergence of the transverse flux vanish. As the sediment bed is invariant along the flow direction (section 2.3), this translates into

$$\frac{\partial q_y}{\partial y} = 0\,, \tag{2.20}$$

where q_y is the sum of gravity and diffusion fluxes. This implies that q_y is constant across the channel.

Since the cross-stream flux vanishes at the side walls, it must therefore vanish across the entire flume. Consequently, we get

$$q_d = -q_g \,. \tag{2.21}$$

Replacing the expressions of q_d and q_g (equations (2.17) and (2.19), respectively), this condition becomes:

$$\ell_d \frac{\partial q_s}{\partial y} = -\gamma q_s \frac{\partial h}{\partial y} \,. \tag{2.22}$$

Integrating (2.22), we expect the following sediment-flux profile:

$$q_s \propto e^{-h/\lambda} \,, \tag{2.23}$$

where $\lambda = \ell_d/\gamma$. The coefficient of proportionality of this law depends on the limits of integration, which we will measure in our experiments.

If the above scenario holds, we therefore expect that sediment transport q_s and bed elevation h self-organize so that q_s decreases exponentially with h. This exponential distribution is reminiscent of the equilibrium governing the density of Brownian particles suspended in a liquid. These particles, for example colloids, are small enough to be sensitive to thermal agitation and their collisions with the molecules of the surrounding liquid make them diffuse. Eventually, they sediment and reach a steady-state distribution. The competition between gravity, pulling the particles down, and diffusion, which favors mixing, prompts them to follow a Boltzmann distribution. As a result, the density of particles decreases exponentially with the elevation. In this case, the exponential decay is the length $k_B T/mg$, where k_B is the Boltzmann's constant, T the temperature of the surrounding fluid, and m the mass particle. This length has been measured by Perrin (1913) to demonstrate the existence of atoms in fluids, as suggested by Einstein (1905). Since then, this exponential distribution has been applied to a wide range of systems in statistical physics at the equilibrium (Kramers 1940, Royall *et al.* 2005, Piazza & Parola 2008).

According to this prediction, the density of bedload particles should follow a Boltzmann distribution. In the next section, we use our measurements to test this scenario in our experiments.

2.8 Boltzmann distribution in laboratory flumes

2.8.1 Boltzmann law

Based on physical arguments, we proposed in the previous section that the shape of the sediment bed is dictated by the equilibrium between a diffusive flux, due to grains collisions with the rough bed, and a gravity flux, induced by the cross-stream slope of the bed. If

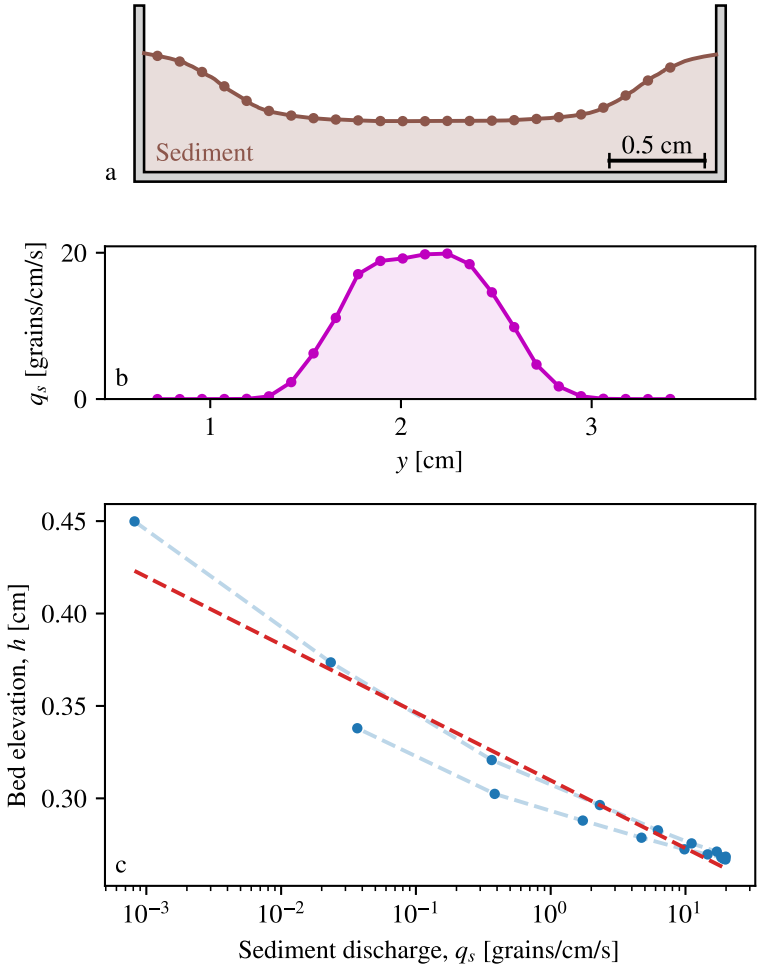

Figure 2.27 – Boltzmann distribution for a single experiment. Run 2: Q_w = 1.1 L/min, Q_s = 0.34 g/min. a. Bed elevation. Each point is interpolated onto the grid of the sediment-flux profile. b. Sediment-flux profile. c. Interpolated bed elevation as a function of the local sediment flux. Dashed red line: affine fit ($\lambda = 160 \pm 10\,\mu$m).

this scenario holds, we expect an exponential relationship between the sediment flux and the bed elevation. In our flume experiments, we measure both the bed elevation and the sediment flux at steady state (sections 2.3 and 2.4). We can use these measurements to evaluate this scenario.

We first test the Boltzmann distribution on a single experimental run. To do so, we just need to plot the logarithm of the sediment flux q_s as a function of the bed elevation h or conversely. In practice, the spatial resolution of our sediment flux measurement is lower than that of the bed elevation. To compare the two data sets, we therefore project the bed elevation onto the same grid using an interpolation (Fig. 2.27a and b). We can then plot the bed elevation h as a function of the logarithm of the sediment flux $\log(q_s)$. Figure 2.27c presents the result for the run 1 of table 2.1. In this space, the Boltzmann equilibrium predicts a straight line. We can fit these data with a linear function, and propose a first

estimate for $\lambda = 160 \pm 10$ μm.

If the theoretical scenario of section 2.7 holds, the Boltzmann length should not depend on the experimental conditions. Therefore, we now compare this distribution against all experimental runs of table 2.1.

Figure 2.28a shows the bed elevation as a function of the logarithm of the local sediment flux for all our experimental runs. Although the latter seem to have the same slope for sufficient high sediment fluxes (typically $> 10^{-1}$ grains/cm/s), each run appears to follow its own Boltzmann distribution. This is because the reference for the bed elevation is arbitrary: in our setup, it depends on the downstream slope and on the thickness of the sediment layer.

A way to set our elevation reference is to choose the lowest point of the bed $h_{\min}$ as the origin, for each run (Fig.2.28b). This has the inconvenient of basing the reference on a single measurement point. The advantage, however, is that it rids our bed elevation profiles from this arbitrary value.

The resulting curves seem to accord with equation (2.23) for sediment fluxes in the range of $[10^{-1}, 3 \cdot 10^{1}]$ grains/cm/s. However, this accordance is less obvious for lower sediment fluxes ($< 10^{-1}$ grains/cm/s). We suspect that this might be due to slow sediment motion, called "creep" (Houssais *et al.* 2015). We investigate this point in the next paragraph.

2.8.2 Creep

During our analysis, we do not discriminate mobile grains from static ones: we count all grains in our flux measurements. However, the grains caught in the static superficial layer are submitted to the collisions with moving grains (Houssais *et al.* 2015). Depending on their depth in the bed, they slowly move downstream, introducing an additional, small streamwise flux. We suggest this additional flux biases our measurements of low sediment fluxes. In this section, we try to evaluate its intensity in our experiments.

In our bedload movies, we differentiate visually the moving layer, scrolling downstream, from the static bed remaining in the background. To extract the latter automatically, we average the movies over a number of frames N_f. Then, tracking grains with the procedure described in section 2.4 enables us to get the trajectories of the background particles. From trajectories, we deduce the particles velocities.

The distribution of their downstream velocity is slightly shifted away from zero (Fig. 2.29a). Its average depends on the number of frames over which we average (Fig. 2.29b), but remains between [0.01, 0.001] d_s/s, which corresponds to

$$6 \cdot 10^{-5} < \frac{\langle v_x \rangle}{V_s} < 6 \cdot 10^{-4} \,. \tag{2.24}$$

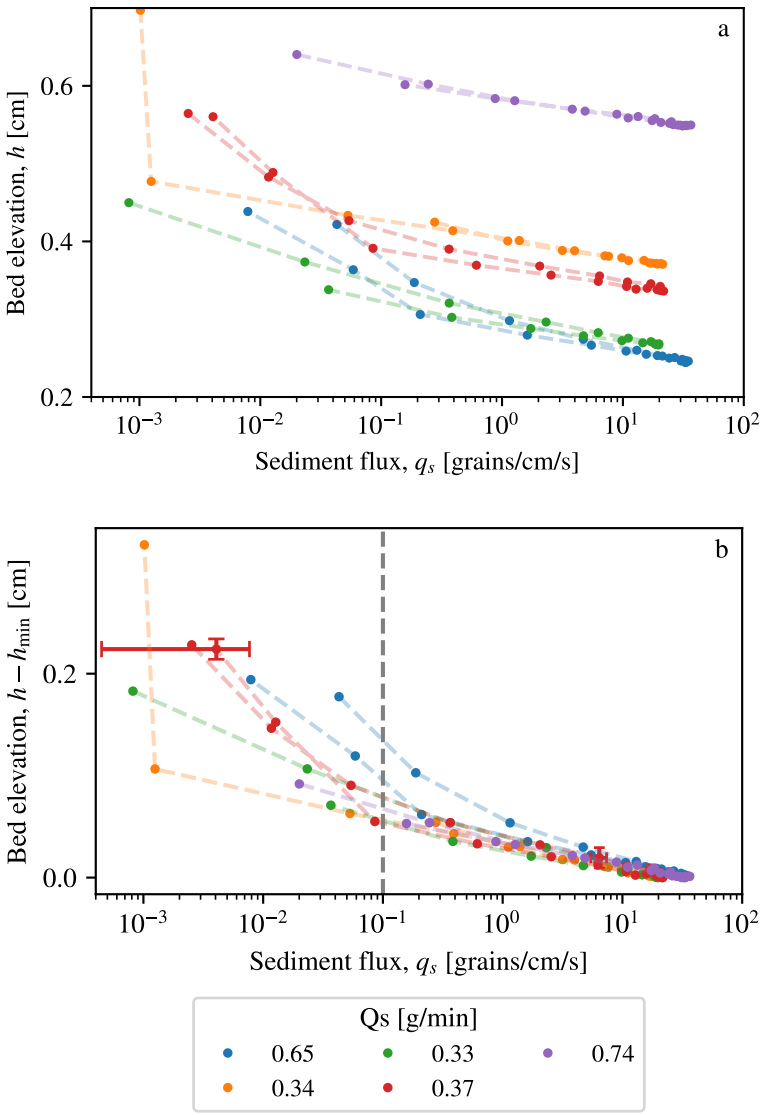

Figure 2.28 – Boltzmann distribution for multiple experiments. Each color corresponds to a run of table 2.1. a. We plot the raw data of sediment flux and bed elevation, without normalization. b. The data are translated with a reference for the bed elevation $h_{\min}$.

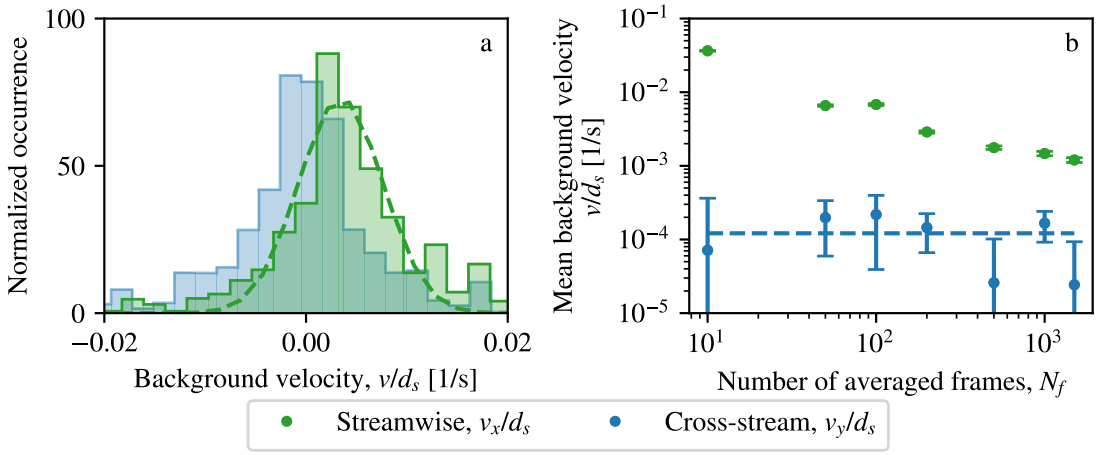

Figure 2.29 – Creep characterization. a. Distribution of streamwise velocity v_x (in green) and cross-stream velocity v_y (in blue) of particles in the background of the moving layer of grains. We average movies over $N_f = 100$ images. b. Average background velocities for run 1. Mean streamwise velocity $\langle v_x \rangle$ (in green) and mean cross-stream velocity $\langle v_y \rangle$ (in blue) as a function of the number of frames over which the movie is averaged. The dashed blue line corresponds of the mean of $\langle v_y \rangle$. Error bars correspond to the standard deviations of distribution divided by the square root of occurrences.

This range of velocities corresponds to a flux of intensity:

$$q_{s,\text{creep}} = \frac{\langle v_x \rangle}{d_s^2}\,, \tag{2.25}$$

which lies in the range [0.1, 0.01] grains/cm/s.

We now compare our estimates to the measurements of Houssais *et al.* (2015). They characterize creep in a closed, annular flume, that contains a granular bed (particle diameter $d_s = 1.5$ mm, density $\rho_s = 1190$ kg/m^3) immersed in a fluid (density $\rho_f = 1050$ kg/m^3, viscosity $\eta = 72.2$ mPa s). They find a settling velocity V_s of

$$V_s = 0.0024\,\text{m/s}\,. \tag{2.26}$$

They perform experiments with different shear stresses, above and below the threshold. In this range of shear stress, they found a creep velocity of particles on the bed between 10^{-1} and 10^{-3} d_s/s, which corresponds to

$$1.5 \cdot 10^{-6} < \frac{v_{\text{creep}}}{V_s} < 1.5 \cdot 10^{-4}\,. \tag{2.27}$$

In order of magnitude, our measurement is comparable with that of Houssais *et al.* (2015). In all our experimental runs, the creep-induced flux is more than two and a half orders of magnitude smaller than the highest bedload flux q_{max}. It may, nonetheless, explain the departure of our measurements from the Boltzmann distribution near the

flume's side walls.

To visualize the comparative order of magnitude of creep in our experiments, we materialize the limit where the sediment flux reaches the order of magnitude of the creep with a vertical dashed line on figure 2.28b. In the following, we do not consider any more our sediment-flux measurement below this limit.

Finally, we check the cross-stream motion of the background particles. We found that the distribution of their cross-stream velocity v_y, averaged over a movie, is centred around zero (Fig. 2.29a). Also, this holds regardless the number of frames over which we average (Fig. 2.29b). The fact that it is not exactly zero may be due to a small, misalignment of the camera with the flume.

2.8.3 Boltzmann length

We now take into account the creep motion of particles into our experimental verification of the Boltzmann distribution. After having translated the Boltzmann law of each experimental run by choosing a reference for the bed elevation (Fig. 2.28b), we remove the small sediment fluxes from our data (typically $< 10^{-1}$ grains/cm/s: right hand-side of the gray limit, Fig. 2.28b). The data points then gather around a straight line, as predicted by our model, over about 3 orders of magnitude for the sediment flux. The coefficient of proportionality should be the inverse of the Boltzmann characteristic length λ. We now estimate this length more precisely in our experiments.

In choosing $h_{\min}$ as the reference for the bed elevation, we set the proportionality coefficient of equation (2.23). The minimum elevation corresponds to the center of the sediment bed. At the center, the sediment flux reaches its maximum $q_{\max}$. We thus expect all the runs to follow:

$$q_s = q_{\max}\ e^{-(h-h_{\min})/\lambda}\,. \tag{2.28}$$

To check equation (2.28) against our observations, we now plot $h - h_{\min}$ as a function of the logarithm of $q_s/q_{\max}$ (Fig. 2.30). We then deduce the value of λ by fitting each data set independently (Fig. 2.30, inset). We observe that the Boltzmann length remains around the same value and we thus fit all experimental data together. A linear fit yields:

$$\lambda = 120 \pm 4\ \mu\mathrm{m}\,, \tag{2.29}$$

and thus,

$$\lambda = (0.144 \pm 0.005)\ d_s\,. \tag{2.30}$$

Equipped with this measure of λ, we can now estimate the parameter γ, which accounts for the gravity-induced flux of sediment. By definition of λ, it is the ratio between the

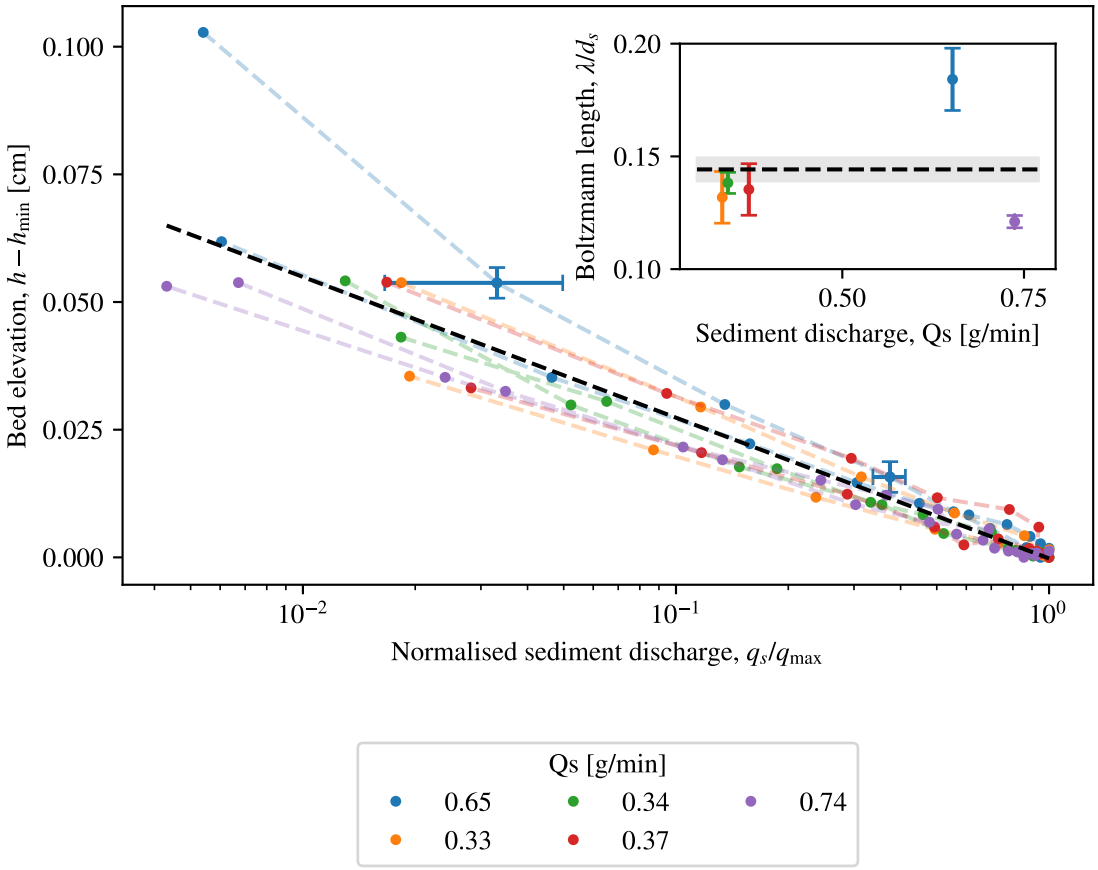

Figure 2.30 – Boltzmann distribution of sediment transport in our flume experiments. Normalized bed elevation as a function of $q_s/q_{\max}$ for each experimental run (Tab. 2.1). Two points are plotted with their error bars (estimated with equation (2.8)). Dashed black line: linear fit with $\lambda = (0.144 \pm 0.005)\ d_s$. Inset: each run is individually fitted and gives a value of λ. We plot λ/d_s as a function of the sediment discharge of the run. Black dashed line: λ computed with the fit of the multiple experiments (main panel).

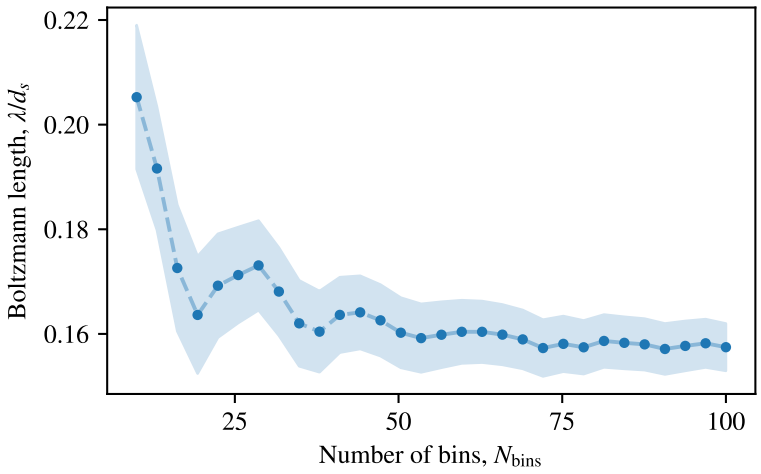

Figure 2.31 – A linear fit of the above figure give a value of λ as a function of the bin size for run 1 of table 2.1.

diffusion length and the Boltzmann length ℓ_d/λ. This yields:

$$\gamma = 0.176 \pm 0.007\,. \tag{2.31}$$

Yamasaka *et al.* (1987) measured this parameter in an inclined wind tunnel. They found a range of $0.1 - 1$ for γ, depending on the grain size, which accords with the theoretical predictions of Chen *et al.* (2009) in turbulent streams. To our knowledge, this parameter had never been measured in a laminar flow.

During all our analysis, we set the number of bins N_{bins} over which we calculate the derivative of the cumulative sediment distribution. With this procedure, we deduce the sediment-flux profile (section 2.4). We now test the sensitivity of the Boltzmann length λ to N_{bins}. We still observe the Boltzmann law for any bin size N_{bins}. However, for a very small number of bins, the data are too sparse to fit them correctly. For N_{bins} high enough, the Boltzmann length λ does not vary significantly (Fig. 2.31).

2.9 Conclusion

In this chapter, we investigated the coupling between flow and sediment transport in the simplest possible configuration: a flume with a fixed width. Even then, a sediment bed sheared by a flow is not a one-dimensional system, but rather generates a curved bed at equilibrium. Simultaneously, the coupling between flow and sediment transport adjusts the sediment-flux profile.

To characterise the bed's equilibrium, we measured its cross section and its local sediment flux. We then identified two mechanisms involved in this equilibrium. First, a diffusive flux brings grains from the center of the channel towards the side walls. Secondly,

gravity pulls grains down the slope. The balance between these two mechanisms governs the bed's equilibrium.

The signature of this gravity-diffusion equilibrium is the Boltzmann distribution, which predicts that the sediment flux decreases exponentially with the bed elevation. The bed then adjusts its shape and its slope to maintain this relation.

However, natural rivers are not confined. They have an additional degree of freedom: they adjust their own width. In the next chapter, we investigate if a sediment bed also self-organises towards a gravity-diffusion equilibrium when we remove the side walls. To do so, we build an experimental setup to reproduce laboratory rivers that transport sediment.

Chapter 3

Self organisation of sediment transport in an active laboratory river

Contents

3.1 Introduction

In the previous chapter, we investigated the coupling between flow and sediment transport in a flume. When a sediment bed is confined between two walls and sheared by a viscous flow, it adopts a curved shape. We showed that, at equilibrium, the bed elevation and the sediment transport adjust to balance cross-stream diffusion and gravity. This equilibrium translates mathematically into the exponential decay of the sediment flux with the bed elevation (Boltzmann distribution).

Could this adjustment mechanism control the cross section of an active river ? The adjustment of this confined sediment bed seems indeed analogous of that of a natural river transporting sediment. The latter differs from the flume only by its ability to adjust its own width.

To investigate the equilibrium shape of an active river, we aim at reproducing them in the laboratory. To our knowledge, only Ikeda *et al.* (1998) successfully maintained an active single channel in the laboratory, yet cut in half with a side wall to maintain it straight. Actually, maintaining an active single-thread channel in the laboratory has proven challenging. Indeed, most experimental channels turn into braids, likely due to the growth of unstable bedforms (Schumm *et al.* 1987, Paola *et al.* 2009).

Some experimenters prevent the destabilisation of their channel by adding cohesive sediment (Paola *et al.* 2009), or by growing riparian vegetation (Tal & Paola 2007). The requirement of these ingredients, however, remains a matter of debate (Métivier & Barrier 2012).

Here, we combine a viscous fluid and low-density grains to prevent the growth of bedforms. As a result, our experimental river generates a stable single-thread channel (section 3.2). With time, it reaches steady state and exhibits a well-defined cross section, while the distribution of moving grains adjusts to its elevation.

In this chapter, we propose that this equilibrium is governed by the diffusion-gravity balance introduced in chapter 2. To evaluate this hypothesis, we perform the same measurements in the laboratory rivers as in the flume: we measure the bed cross section and the sediment-flux profile (sections 3.3 and 3.4, respectively).

3.2 Laboratory rivers : experimental setup

To generate active rivers in the laboratory, we use an inclined plane ($90 \times 190\,\mathrm{cm}$), covered with a layer of sediment (Fig. 3.1). We use the same sediment than in the flume experiment (Ch. 2). Accordingly, all grains are made of the same plastic (density $\rho_s = 1520$ g/L), and have the same size ($d_s = 830 \pm 80\,\mu$m, section A.1).

At the beginning of an experiment, we flatten the dry sediment bed with a rake and carve a straight channel into it, from the inlet to the outlet. We inject at the inlet of this

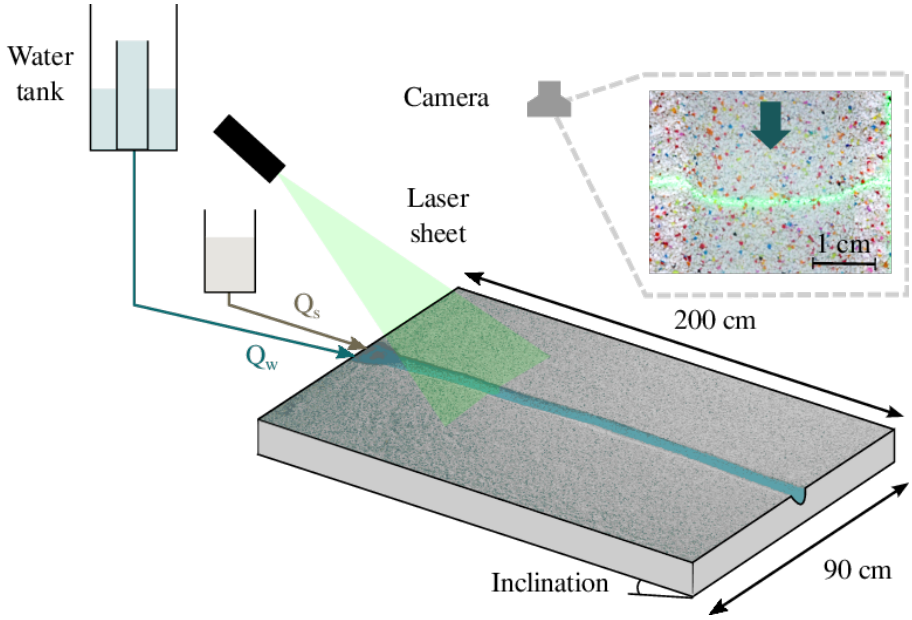

Figure 3.1 – Laboratory river: experimental setup. Q_w and Q_s are the flow and the sediment discharges, respectively. A laser sheet is projected onto the channel and is deviated by the bed topography. A camera placed above the bed displays the channel seen from the top.

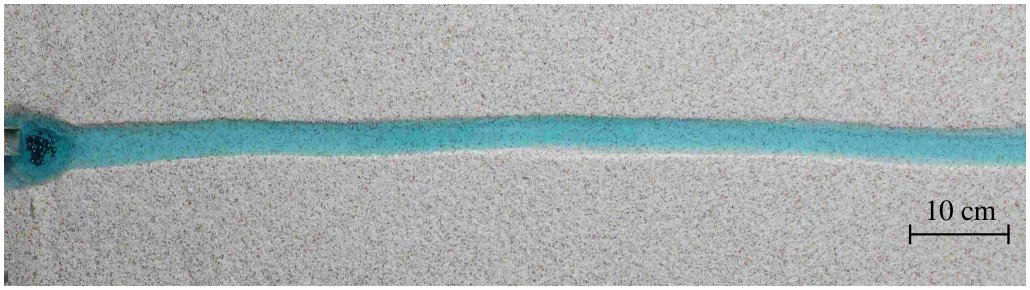

Figure 3.2 – Top view of a laboratory river. It corresponds to the experimental run 2 of table 3.1 (Q_w = 1.0 L/min and Q_s = 0.42 g/min).

channel a mixture of glycerol and water (density $\rho_f \approx 1160$ g/L, viscosity $\nu \approx 10$ cP). A tank placed above the experimental setup delivers a constant discharge Q_w (in the range [0.1,3] L/min). We measure the density of the fluid every hour, and infer its viscosity from this measurement (appendix A, Fig. A.4). During the experiment, we compensate for water evaporation by adding water to the mixture (Delorme (2017), p. 120). The Reynolds number of the river remains about 10, and we therefore expect that the flow is laminar. We can check the flow regime qualitatively, by injecting a drop of dye into the flow with a syringe: it follows a continuous path.

We also feed the channel with sediment. To do so, we use an industrial sediment feeder (Gericke), the screw of which pushes grains at the inlet of the channel. The rotation speed of the screw controls the sediment discharge (in the range [0.2,20] g/min, Fig. 3.3). Grains then fall down and concentrate near the bed. They remain near the bed as they travel

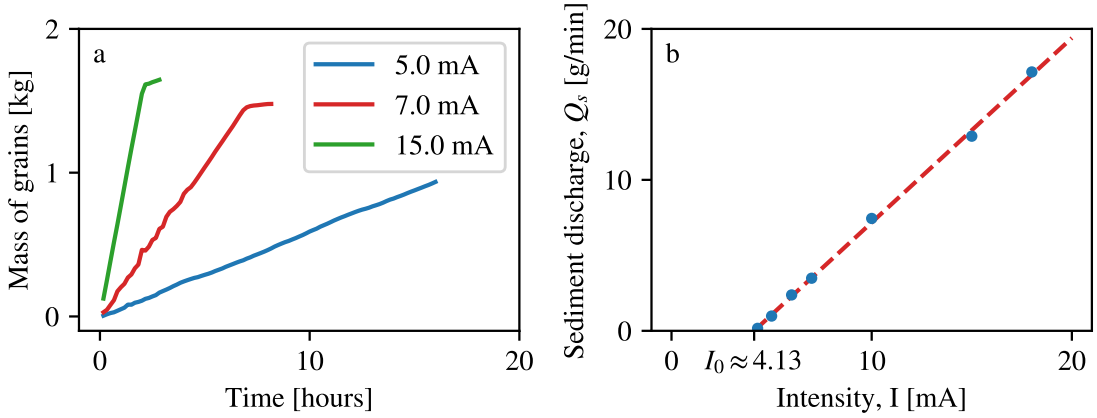

Figure 3.3 – Calibration of the sediment feeder. a. Mass of grains delivered by the worm screw per unit time, for different control intensities. The slope of each curve is the sediment discharge. b. Sediment discharge as a function of the intensity applied to the sediment feeder. Above a threshold of approximately 4.1 mA, the discharge is proportional to intensity.

downstream, entrained by the flow.

During the first hour of the experiment, the flow spreads over the entire bed and forms an almost uniform sheet of fluid. After a few hours, the flow carves a path, usually along the initial one. During this transient, the laboratory river continuously extracts more grains than it deposits, and thus erodes the bed. As a result, the sediment flux in this channel is higher than the sediment discharge we impose (Fig. 3.4). Erosion is often heterogeneous along the flow: it is usually higher downstream. Gradually, the sediment flux reaches steady state, so that it is equal to the input sediment discharge Q_s everywhere (Fig. 3.4).

At equilibrium, the flow forms a straight, single-thread channel of a few centimetres in width (Fig. 3.2). This equilibrium is dynamical: grains are constantly dislodged and deposited by the flow, but the sediment discharge is constant and the river bed does not evolve with time. The moving grains indicate that the bed is above the threshold of entrainment, unlike channels with a vanishing sediment discharge (Seizilles *et al.* 2013).

We fix the slope of the frame before an experiment, but the layer is thick enough that the laboratory river can adjust its slope according to its sediment and fluid discharges. If the frame's slope is steeper than the equilibrium slope of the river, the flow incises the bed and forms a gorge to reach equilibrium. Conversely, if the initial slope of the frame is lower than the equilibrium slope of the river, the sediment is deposited at the inlet, forming an alluvial fan. We adjust the slope of the frame as close as possible to its expected value.

Overall, the equilibrium shape of the laboratory river is mainly controlled by the input parameters: the fluid and sediment discharges. To investigate the influence of the sediment discharge on the river's shape, we perform a series of experimental runs, where we keep the fluid discharge around 1 L/min and we vary the sediment input (Table 3.1).

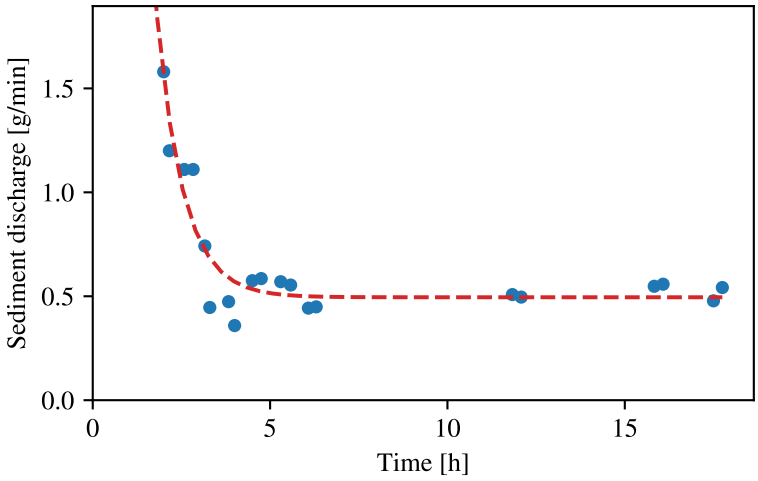

Figure 3.4 – Evolution of the sediment discharge at one half of the river's length. Blue points correspond to the sediment discharge measured with a movie sequence of 10 to 13 minutes (section 3.4). Red dashed line: decreasing exponential function fitted to the data. The decay time is about one hour.

For each run, we measure the bed's cross section and the sediment-flux profile along the cross section. We describe these measurements in the following sections.

3.3 River cross section

For a moderate sediment discharge, our rivers exhibit a well-defined cross section over a distance of approximately 1.5 meters downstream of the inlet. In this section, we describe how we measure the river's cross section. This measurement differs from that of chapter 2 (section 2.3) in that laboratory rivers are not strictly invariant in the streamwise direction. Consequently, we cannot scan the topography over more than one centimetre. Moreover, the size of the plane precludes the use of a milk bath to calibrate the bed-elevation measurement.

That being so, we still use an inclined laser placed in an area above the channel. This area is far enough from the inlet and outlet to avoid perturbations due to the entry and

Run	Q_w [L/min]	Q_s [g/min]	Tracking duration [frames]	Number of trajectories of length $> d_s$
1	1.00	0	-	-
2	0.99	0.42	218595	30747
3	1.00	0.33	437622	22501
4	0.87	0.15	530172	28890
5	0.98	0.77	324582	55741

Table 3.1 – experimental parameters for the 5 runs.

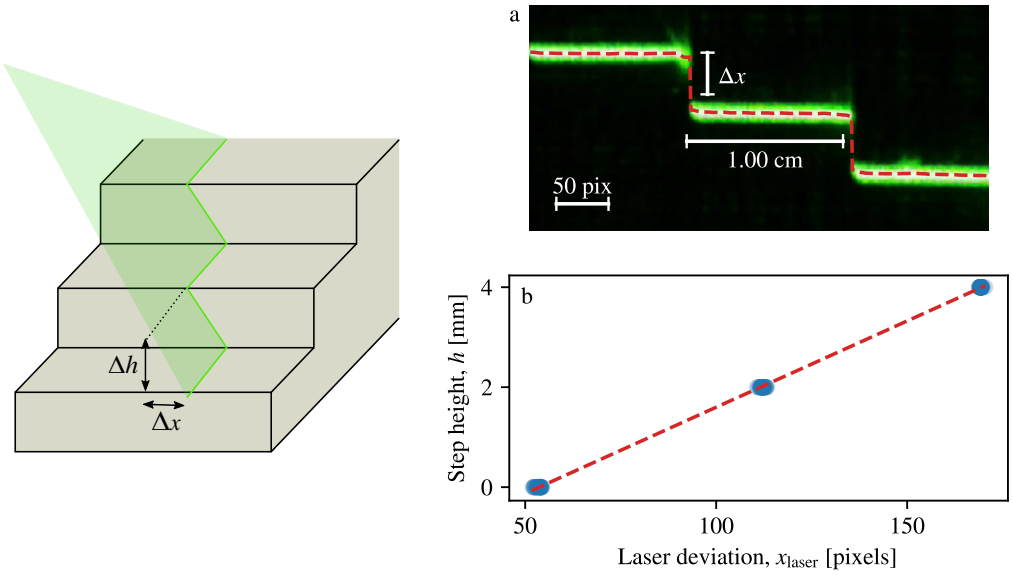

Figure 3.5 – Measure of the laser angle and calibration of bed-elevation measurement. The laser sheet is projected onto a calibration scale. Each step is 2.0 mm high and 1.0 cm wide a. Field of view of the camera, from the top. Detection of the position of the laser (red dashed line). The resolution of the image is $6.62{\cdot}10^{-6}$ m/pixels. b. Measurement of the laser angle (calibration curve). Blue points: Measurement. Red dashed line: fit by an affine function. The coefficient of proportionality is $\tan\theta_{\text{laser}}$.

exit conditions. The laser sheet is projected onto the channel in the field of view of a camera (Canon 700 D). We choose the angle θ_{laser} of the laser to focus in an area where the channel is fairly straight.

To measure the laser angle θ_{laser}, which depends on the experimental run, we place an aluminium scale in the field of view of the camera. Its shape is known accurately (machined piece): each step is 1.0 cm wide and 2.0 mm high (Fig. 3.5, left). The laser sheet crosses the stairs and is deviated further at each step. We first locate the laser deviation x_{laser} with the same method as in § 2.3.1 (Fig. 3.5a, dashed red line). This method provides us with a relation between the scale elevation h and the position of the laser line x_{laser}. For example, in the case of run 4 (Tab. 3.1, Fig. 3.5b):

$$h\ [\text{m}] = (3.451 \pm 0.002) \cdot 10^{-5}\ x\ [\text{pix}]\,. \tag{3.1}$$

The coefficient of proportionality is the tangent of the laser angle, $\tan\theta_{\text{laser}}$, which corresponds to a laser angle of $\theta_{\text{laser}} = 27.6°$.

We then remove the scale to let the laser intersect the channel's bed. As the experiment is running, the fluid still flows in the river. Therefore, the laser line is deviated by the fluid to the position x'_{laser} (Fig. 3.6). Although the laser and the camera do not move, we record a movie to average the laser position with time. We then locate x'_{laser} with the method

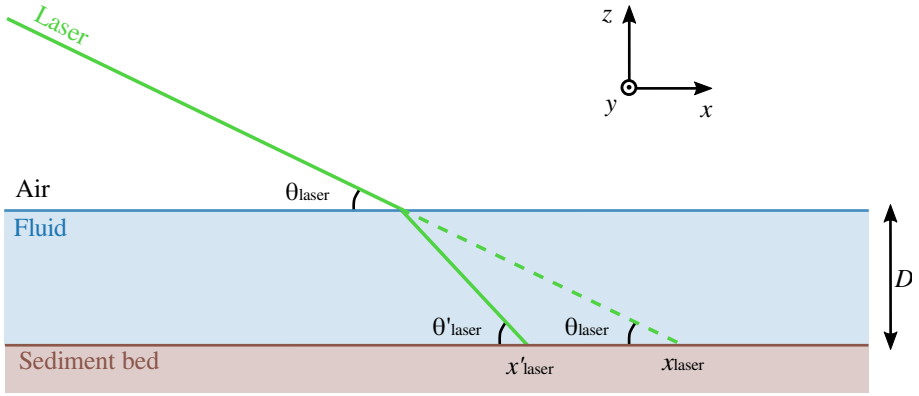

Figure 3.6 – Laser deviated by the flow x'_{laser}. Flow from right to left. When the channel is dry, the laser line is located on x_{laser}.

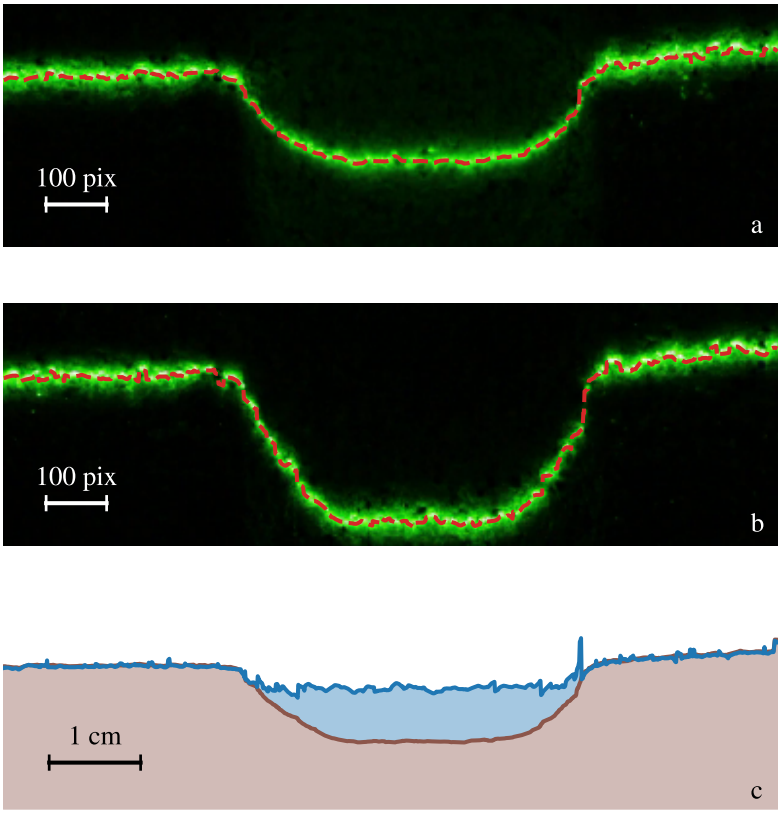

Figure 3.7 – Measurement of the bed cross section. a. Location of the laser line on a wet bed (red dashed line). b. Location of the laser line on a dry bed (red dashed line). c. Measured cross section. In brown: sediment bed. In blue: flow.

described in § 2.3.1 (Fig. 3.7a, dashed red line). The angle of refraction θ'_{laser} is related to the laser angle through the Snell-Descartes law:

$$\theta'_{\text{laser}} = \frac{\pi}{2} - \arcsin\left(\frac{1}{n}\sin\left(\frac{\pi}{2} - \theta_{\text{laser}}\right)\right), \tag{3.2}$$

where n, the refractive index of the water-glycerol mixture, is 1.41 at 20°C. This yields $\theta'_{\text{laser}} = 38.9°$.

Then, we stop the fluid and sediment inputs. As a result, bedload stops almost immediately, and water slowly drains out of the plane, leaving a dry river bed. Now, the laser line crosses the dry river bed at the coordinate x_{laser} (Fig. 3.6). Based on the laser angle θ_{laser}, we thus measure the bed elevation h with equation (3.1) calibrated on the scale. In practice, we average spatially the bed elevation by scanning the channel over about one centimetre in the streamwise direction. The channel is too sinous to average over a longer distance.

Finally, based on the wet and dry laser locations (x'_{laser} and x_{laser} respectively), we calculate the flow depth D using geometrical relations:

$$D = \frac{x_{\text{laser}} - x'_{\text{laser}}}{1/\tan\theta_{\text{laser}} - 1/\tan\theta'_{\text{laser}}} \tag{3.3}$$

with our measurements of θ_{laser} and θ'_{laser}.

We show on figure 3.7c an entire cross section for the run 4 of table 3.1. As we are not able to average the flow depth downstream, it is noisier than the bed elevation. The resulting uncertainty on the flow depth is approximately

$$\Delta D = 0.5\,\text{mm}\,. \tag{3.4}$$

Figure 3.8 shows the cross section of 3 experimental rivers produced with the same flow discharge, for different sediment discharges. In the absence of sediment input, the river resembles the cosine shape of the threshold theory (section 1.1). As we increase the sediment discharge, the river widens and flattens.

From the river cross sections, we extract the channel width W, maximum depth $D_{\max}$, and aspect ratio $W/D_{\max}$. Figure 3.9 shows the variation of these 3 quantities with the sediment discharge for a fixed fluid discharge (Tab. 3.1).

We find that the width increases of about 50% when the sediment discharge varies from 0 to 0.77 g/min. Meanwhile, the depth seems to decrease, although the variability of our measurements is comparable with the amplitude of this trend. The aspect ratio of the laboratory river increases with sediment discharge, by a factor of about 2.

These preliminary observations show that the intensity of the sediment discharge influences not only the shape of a river but also its size. To put these observations on more

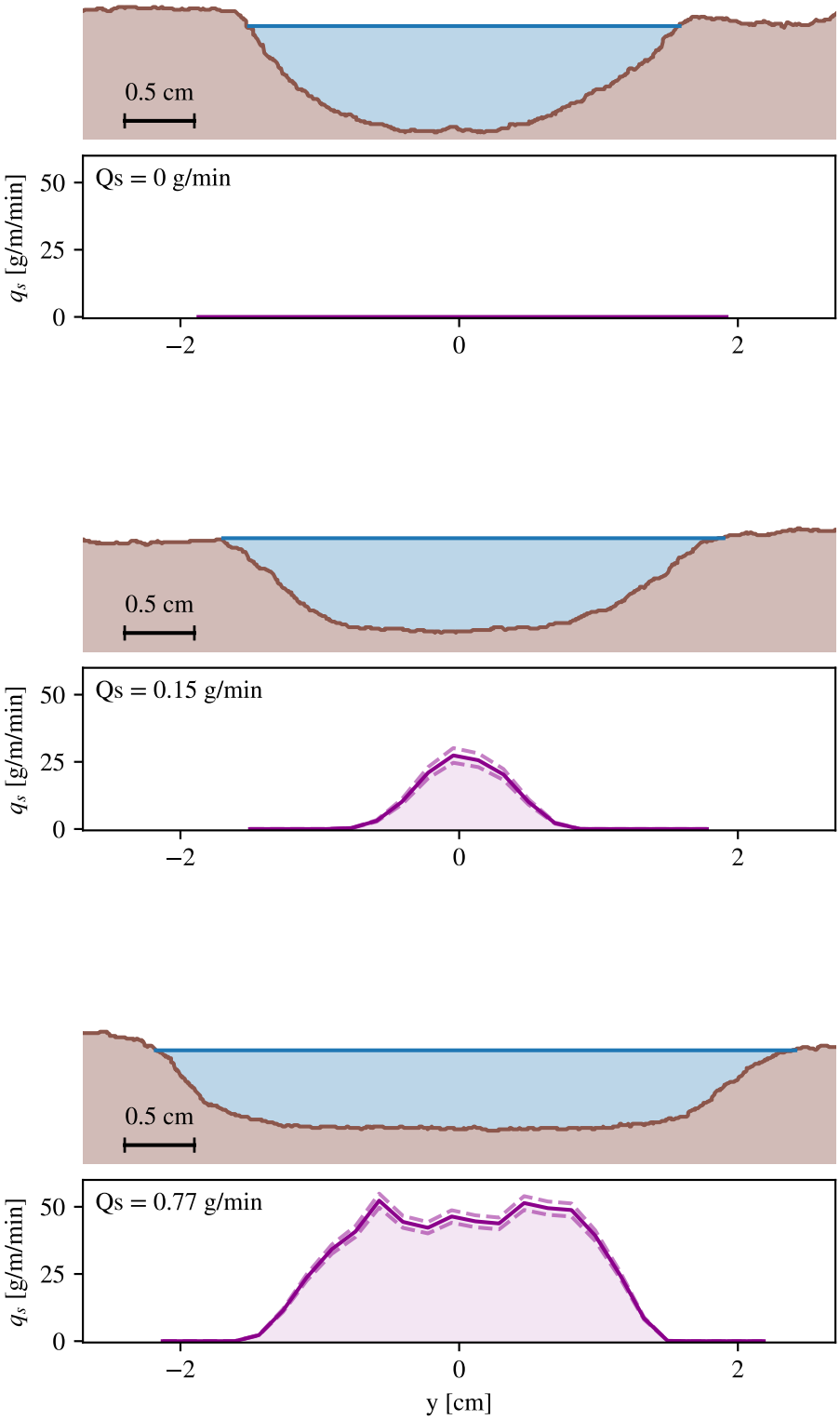

Figure 3.8 – Bed elevation and sediment-flux profile for different runs. The sediment input increases downwards (0, 0.15 and 0.77 g/min). In the same order, these profiles correspond to runs 1, 4 and 5. Dashed lines: measurement uncertainty calculated with equation (2.8).

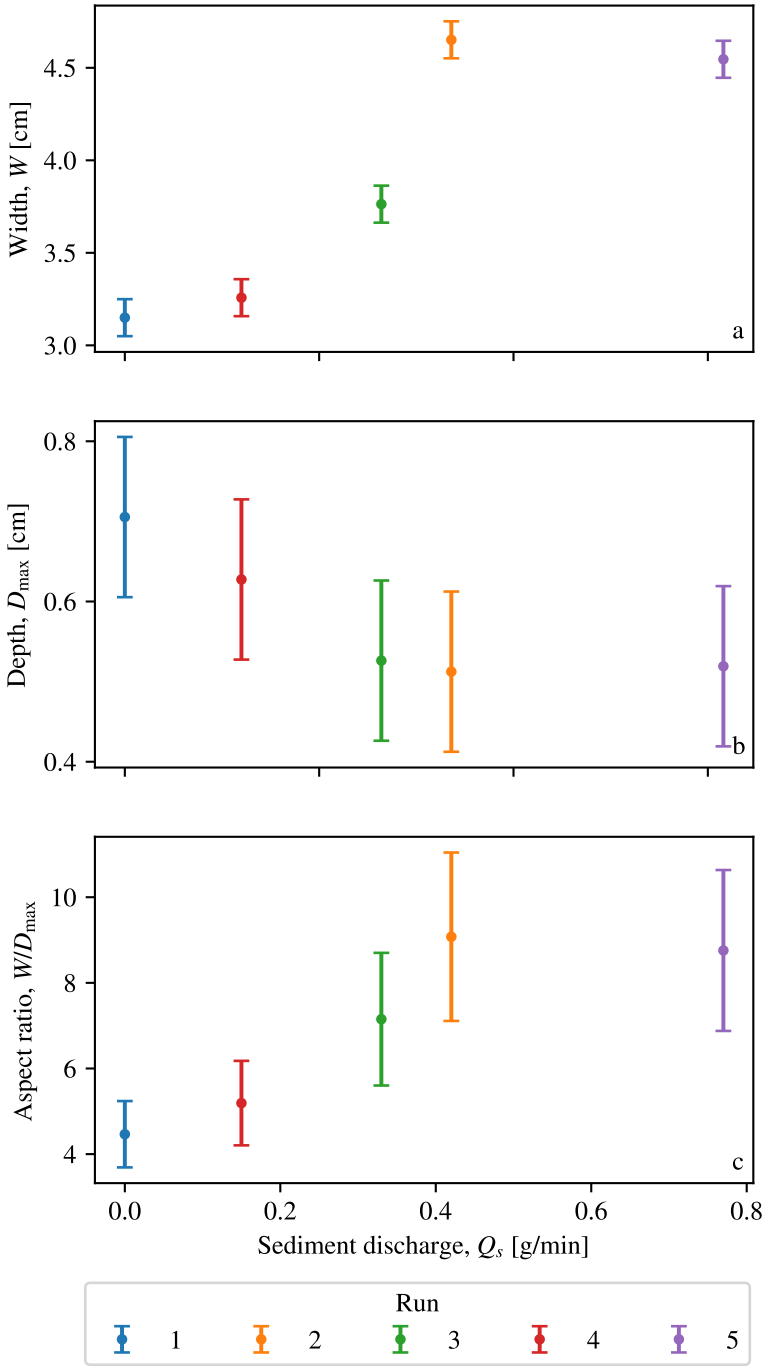

Figure 3.9 – Dependence of the morphology of laboratory rivers with respect to the sediment discharge. a. Width. b. Maximum depth. c. Aspect ratio.

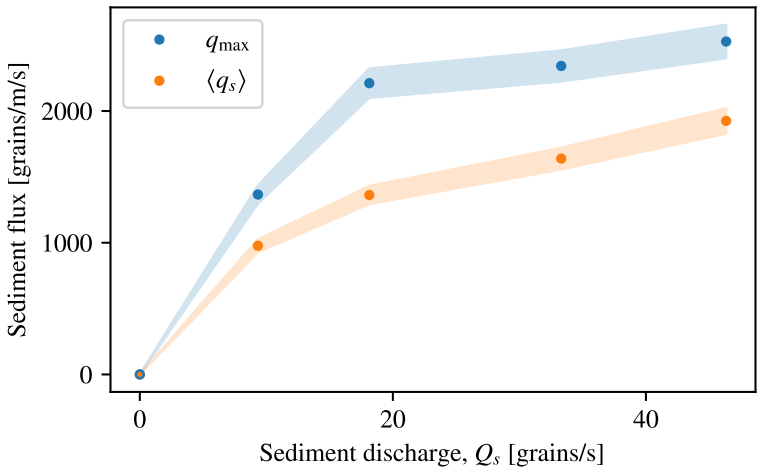

Figure 3.10 – Maximum and mean sediment flux as a function of the total sediment discharge. Each point corresponds to an experimental run (Tab. 3.1). Blue: maximum $q_{\max}$ of the sediment-flux profile. Orange: average $\langle q_s \rangle$ of the sediment-flux profile.

quantitative grounds, we now turn our attention to the transverse profile of sediment flux.

3.4 Sediment-flux profile

We track the motion of the grains entrained by the flow using the method described in section 2.4. This colorimetric method enables us to track independently blue, red and orange grains. For each run, we record one hour of bedload movie. Table 3.1 indicates the corresponding number of frames and trajectories.

From the trajectories, we deduce the cumulative sediment flux. We normalize this cumulative distribution with the input sediment discharge Q_s (Tab. 3.1, column 3). We then calculate the local sediment flux by averaging the cumulative distribution over 40 bins and deriving the resulting curve (as in § 2.4.3).

As a result, we measure both the topography and the sediment flux in our laboratory rivers, for different sediment discharge Q_s (Fig. 3.8). The area below a sediment-flux profile corresponds to the total sediment discharge, and naturally increases with it. We observe that the entire shape of the sediment-flux profile also varies with Q_s. In particular, its maximum increases, although more slowly.

On figure 3.10, we plot this maximum sediment flux $q_{\max}$ as a function of the sediment input Q_s. As one might intuitively expect, it increases with the sediment discharge. However, it seems to saturate at large sediment discharges. This suggests that the river accommodate a higher sediment discharge by widening its channel, rather than increasing the intensity of the sediment flux. We observe the same behaviour for the average of the sediment-flux profile as a function of the sediment discharge (Fig. 3.10, orange).

Overall, the cross section and the sediment-flux profile of a river appear to be correlated (Fig. 3.8). At equilibrium, the river adjusts its shape and its sediment flux to the total sediment input. Specifically, the sediment flux is more intense near the center of the river, where the latter is deeper. It virtually vanishes towards the banks, as in the flume experiment (Ch. 2, Fig. 2.19). Accordingly, we suggest that our laboratory rivers follow the same Boltzmann distribution, as in the flume experiment (section 2.8). In the next section, we test this hypothesis.

3.5 Boltzmann distribution in a laboratory river

In chapter 2, we found that a sediment bed confined between two walls and sheared by a viscous flow adopts a steady-state shape controlled by the equilibrium between diffusion and gravity (section 2.8). This equilibrium translates mathematically into an exponential relationship between the bed elevation and the local sediment flux:

$$q_s \propto e^{-h/\lambda}\,, \tag{3.5}$$

where λ is the characteristic length of the Boltzmann distribution. In this section, we test this scenario in our laboratory rivers.

3.5.1 Boltzmann distribution

We start by plotting the raw bed elevation as a function of the sediment flux for each experimental run of table 3.1 (Fig. 3.11a). The data gather around straight lines in the log-lin space, and thus each run seems to accord with equation (3.5). This suggests that a laboratory river self-organises to reach a steady state where gravity compensates cross-stream diffusion.

In this setup, the camera and the laser move independently, instead of being fixed on the same rail, like in the flume experiment. As a consequence, the reference for the bed elevation is arbitrary: it depends on the relative position between the laser line and the camera. Since the prefactor of an exponential distribution is just the reference elevation, each run appears to follow its own distribution.

We fit each distribution and measure the corresponding characteristic length λ (Fig. 3.11b). Although the latter increases slightly with the sediment discharge, it remains close to the value we measured in the flume experiment (section 2.7, $\lambda = 0.14\,d_s$). We now want to compare the Boltzmann distribution in a river to the one we measured in our flume. To do so, we need to normalise each data set.

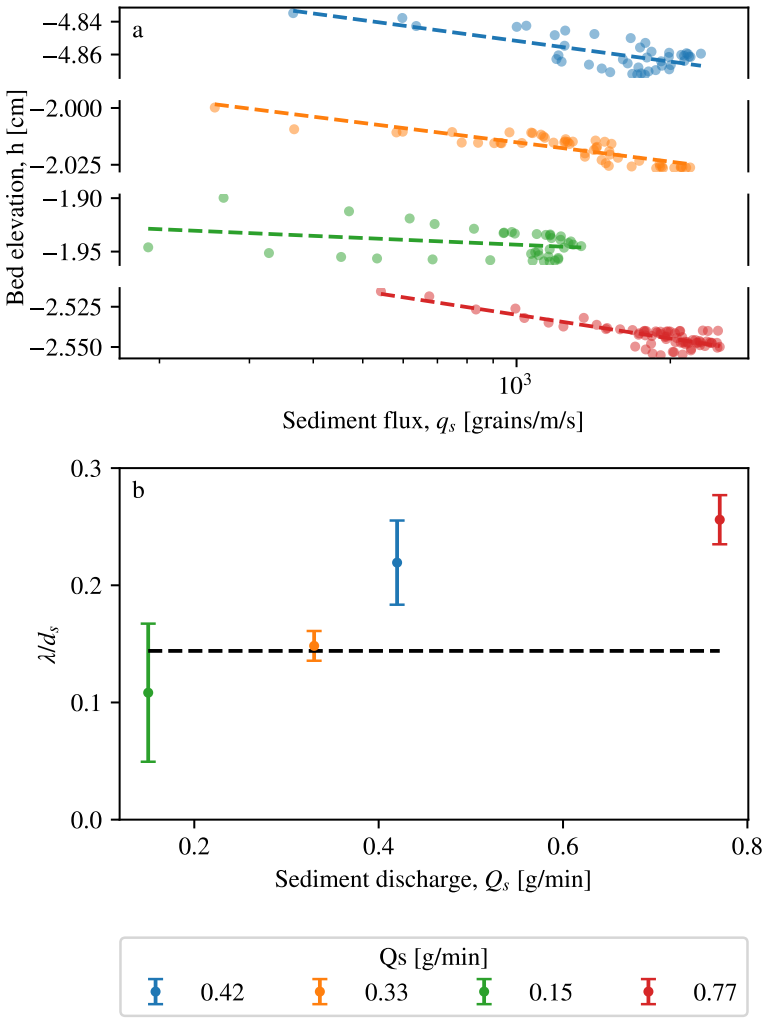

Figure 3.11 – Experimental distribution of the sediment flux in laboratory rivers. a. Bed elevation as a function of local sediment flux. Each color corresponds to a run. b. Characteristic length of the Boltzmann distribution, λ, normalized by the grain size d_s for each run. The dashed black line corresponds to the value measured in the channel experiment (section 2.7).

3.5.2 Comparison with the flume experiment

To superimpose each data set, we could use the normalisation of our measurements in the flume, by dividing the sediment flux by its maximum $q_{\max}$ and subtracting to the bed elevation its minimum $h_{\min}$ (§ 2.8.3). However, our data are noisier than those of the flume experiments. Therefore, it is not appropriate to base the data normalisation on one data point only. We choose to normalise our data by their averages: $\langle h \rangle$ and $\langle q_s \rangle$.

We thus plot $h - \langle h \rangle$ as a function of the logarithm of $q_s/\langle q_s \rangle$. We compare it with the following distribution:

$$\frac{q_s}{\langle q_s \rangle} = e^{-(h-\langle h \rangle)/\lambda}, \tag{3.6}$$

with the value of λ we measured in the flume experiment : $\lambda = 0.144\, d_s$ (§ 2.8.3).

All the data gather around this law, regardless of the sediment discharge (Fig. 3.12). The equilibrium of a river is thus governed by the same mechanisms as a confined bed: the balance between gravity and diffusion. In addition, the characteristic Boltzmann length seems to depend on the sediment grains and the viscous liquid only, as the one we measured in the flume works for the river.

Unfortunately, the cross section of a laboratory river is often not perfectly symmetric, likely due to the sinuosity of its course. This explains the dispersion of the data around this law, especially for run 4, for example (Fig. 3.12). This dispersion is independent of our measurement noise (typical error bars are plotted for two data points). This suggests that the measurement of the Boltzmann characteristic length is more accurate with a flume experiment.

More generally, we expect that these mechanisms hold regardless of the nature of the flow (laminar or turbulent). Indeed, we did not do any assumptions on the flow regime to derive the Boltzmann distribution (section 2.7). In particular, grains should also diffuse in a turbulent stream, even if the intensity of the diffusion changes (and thus the diffusion length). If confirmed, a flume experiment is then the ideal experimental setup to calibrate the Boltzmann law of natural rivers. One could use a confined bed of sampled sediment grains, sheared by water. This would enable us to measure the Boltzmann characteristic length of a natural river.

3.6 Influence of the sediment discharge on the river's width

In the previous section, we showed that, at equilibrium, a laboratory river balances cross-stream diffusion and gravity. As the river is free to adjust its width, we suggest that this mechanism also selects the river's width. We now focus on the influence of the sediment discharge on the width of a river.

We thus produce 20 laboratory rivers, but we measure only their width (which demands

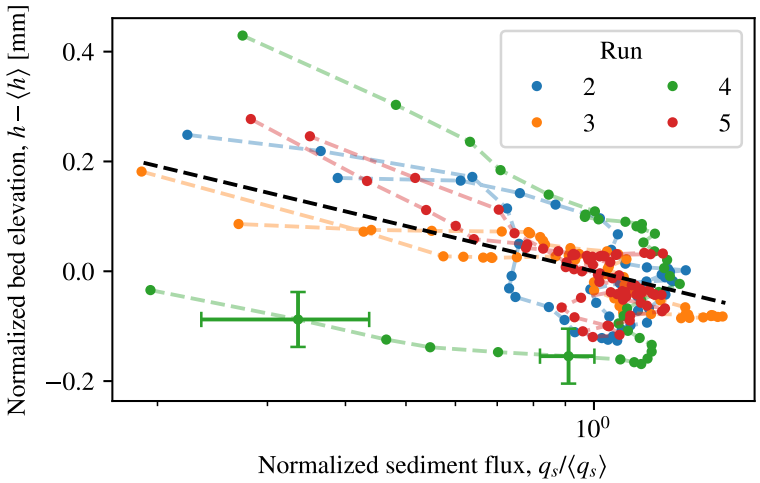

Figure 3.12 – Experimental Boltzmann distribution in laboratory rivers. Each color corresponds to an experimental run of table 3.1. The black dashed line corresponds to the law measured in the flume experiment. Two indicating error bars are plotted for run 4 (calculated with equation (2.8)).

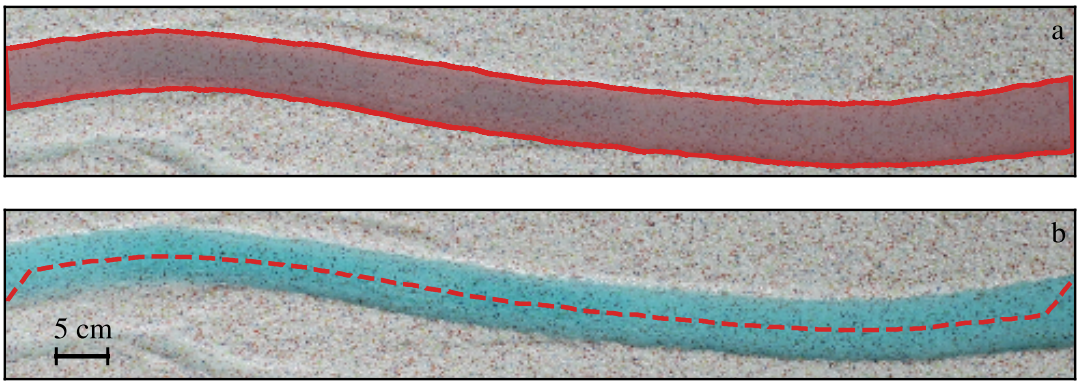

Figure 3.13 – Image analysis for the width measurement of a laboratory river (top view). We use a colorimetric detection. a. Threshold on blue and measure of the area of the channel (red). b. Detection of the curvilinear length (red dashed line) of the channel.

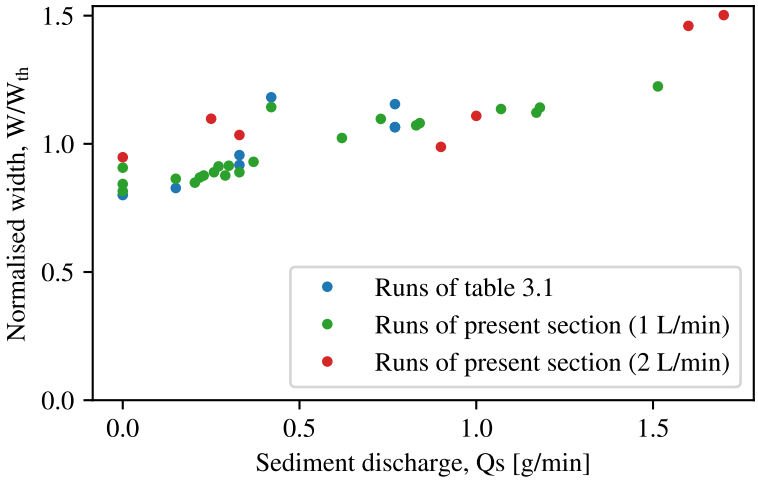

Figure 3.14 – Width of laboratory rivers as a function of the sediment discharge. The width is normalised by the threshold width W_{th} (equation (1.26)).

less time than measuring the sediment profile). We visualize their planform geometry by dying the mixture of water and glycerol. Based on a color threshold, we measure the area of the river (Fig. 3.13a). Then, we get its curvilinear length with the function `skeletonize()` in the Scikit Image Python library (Fig. 3.13b). We then define its average width as the ratio between the area and the curvilinear length.

In accordance with field observations (Ch. 1, section 1.2), the width of our laminar rivers depends on their sediment discharge: the width increases with the sediment discharge (Fig. 3.14). In chapter 4, we propose a simplified model to explain the influence of the sediment discharge on the river's shape.

3.7 Planform geometry

When we further increase the sediment input above about 1.6 g/min, the river slowly destabilizes and splits its course to form a braid, consisting of interlaced channels (Fig. 3.15). Some of them are active, other are immobile and sometimes abandoned. If we impose a sediment discharge much higher than this approximative threshold, the river destabilizes more rapidly, typically in a few tens of minutes.

This threshold above which a laboratory single-thread channel destabilizes into braids is in accordance with the existence of a critical slope (or aspect ratio) above which the river forms braids. This could also explain why single-thread channels are sparse at the laboratory: there exists only a small range of sediment discharge for which a single-thread channel is stable.

Although braided rivers move constantly, we can define a dynamical equilibrium for which the sediment output equals the input (Meunier & Metivier 2006). However, we did

not check this criterion in our experiments yet.

3.8 Conclusion

In this chapter, we successfully produced single-thread, active rivers in the laboratory by introducing a viscous fluid and sediment at the inlet of a tilted sediment layer. The flow carves its bed in the sediment and, over time, adopts a well-defined cross section.

By analogy with a confined sediment bed (Ch. 2), we measured the cross section and the sediment-flux profile of these laboratory rivers. These measurements show that the sediment flux decreases exponentially with the bed elevation, regardless of the sediment input. This relationship indicates that the equilibrium of a river is governed by the balance between cross-stream diffusion and gravity, like that of the sediment bed in a flume.

This statistical equilibrium probably controls the shape of a river's cross section, which depends on the sediment input. Specifically, a river widens and flattens with its sediment discharge. This effect qualitatively accords with field observations (section 1.2), suggesting that laboratory rivers are controlled by the same mechanism than their natural counterparts.

Our observations also support that of Stebbings (1963) about the transient of a laboratory river. In particular, he observed that a river (i) accommodates its additional bedload by widening and (ii) destabilizes into braids for larger sediment discharges. This suggests that rivers are stable for small to moderate sediment discharges, and might explain why active, single-thread channels in the laboratory are so sparse in the literature.

In the following chapters, we will further investigate the influence of the sediment discharge on the shape of a single-thread channel. We will propose a physical model, that we will test against our experiments (Ch. 4). Then, we will focus on the stability of a single-thread channel (Ch. 5).

Figure 3.15 – Planform geometry of a braided laboratory river. Input parameters: Q_w = 1.0 L/min and Q_s = 1.7 g/min.

Chapter 4

Shallow-water theory of an active laboratory river

Contents

4.1 Introduction

In chapter 3, we described how we maintain single-thread rivers which transport sediment in the laboratory. At a given fluid discharge, we observe that the shape of these laboratory rivers depends on the sediment input. When the sediment input increases, the river widens, while becoming flatter and shallower (Fig. 3.8).

To understand how a river adjusts its shape to the sediment input, we investigated its equilibrium at the grain scale by tracking bedload grains. We demonstrated that the river's equilibrium is governed by the balance between the cross-stream diffusion of grains, due to the bed roughness, and gravity, that pulls grains towards the center. The signature of this balance is the Boltzmann distribution: the sediment flux decreases exponentially with the bed elevation (section 3.5).

In this chapter, we relate this grain-scale mechanism to the river's morphological parameters, such as its width, its aspect ratio, or its slope. To do so, we need to model the flow. In particular, we must evaluate the shear stress exerted by the flow on the river's bed. However, we do not know *a priori* the river cross section, and therefore the flow boundaries. These boundaries evolve through the coupling between the flow and the bed. Therefore, the calculation of the flow inside this domain depends on the shape of the domain. In particular, we are not able to solve analytically the Stokes equation in an arbitrary domain.

We start with the simplest possible model for the flow: the shallow-water approximation. This approximation provides us with a local expression for the shear stress that depends only on the depth D of the river.

Supplemented by a model for the transport law, which relates the local sediment flux to the local shear stress, we derive a first-order differential equation for the river's depth (section 4.2). Finally, we test this model against our experimental profiles (sections 4.5 and 4.6).

4.2 Equation for the depth of an active river

In this section, we derive a differential equation for the river's depth D. To do so, we use three equations that couple the flow depth D, the local sediment flux q_s, and the flow-induced shear stress τ:

- The Boltzmann distribution relates the local sediment flux to the bed elevation, and thus the flow depth;
- The transport law relates the local sediment flux to the flow-induced shear stress;
- A flow model should link the flow-induced shear stress to the cross section of the river.

We first detail these relations, and then derive the differential equation that results from their combination.

4.2.1 Boltzmann distribution

At equilibrium, an active laboratory river self-organises to balance cross-stream diffusion and gravity (section 3.5). As a result, its local sediment flux q_s depends on its bed elevation h through,

$$q_s = q_{\max} \exp\left(\frac{h_{\min} - h}{\lambda}\right), \tag{4.1}$$

where $h_{\min}$ is the minimum elevation of the river, that we identify with its value at the center. This distribution implies that sediment transport reaches its maximum at the center ($q_s(h = h_{\min}) = q_{\max}$), and decreases exponentially with elevation, towards the banks.

This expression came up naturally with the experiments of chapters 2 and 3, as it is easier to measure the elevation h of the bed when the river is dry, than the river depth (uncertainty on the elevation of $\Delta h = 0.1\, d_s$ compared to $\Delta D \approx d_s$, section 3.3). However, noting that (Fig. 4.1)

$$h - h_{\min} = D_{\max} - D\,, \tag{4.2}$$

the Boltzmann distribution (4.1) can be rewritten in terms of the river depth, D,

$$q_s = q_{\max} \exp\left(\frac{D - D_{\max}}{\lambda}\right), \tag{4.3}$$

where we identify $D_{\max}$ with the depth of the river at the center.

Equation (4.3), provides us with a first relation between the flow depth and the local streamwise sediment flux. In turn, the sediment flux depends on the flow-induced shear stress, through a transport law. This is what we discuss in the next section.

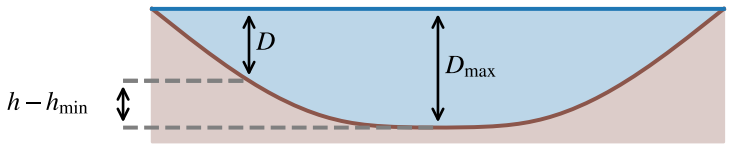

Figure 4.1 – Sketch of a river and notations. h is the bed elevation, and $h_{\min}$ its minimum. D is the depth of the river, and $D_{\max}$ its lowest elevation. Brown: sediment bed. Blue: flow.

4.2.2 Transport law

In chapter 2, section 2.5, we expressed the sediment flux as a function of the Shields parameter :

$$q_s = q_0 \left(\theta - \theta_t\right), \tag{4.4}$$

with $q_0 = 5.86 \cdot 10^4$ grains/m/s. However, this relation holds for a flat bed, whereas the cross section of a river is not flat.

In chapter 1, § 1.1.3, we introduced the force ratio μ, which takes into account the cross-stream slope on the threshold of motion. The parameter μ is the ratio of the tangential to the normal force exerted on a sediment grain,

$$\mu^2 = \frac{(\alpha\tau)^2}{(\beta\Delta\rho g d_s)^2} + \left(\frac{\partial D}{\partial y}\right)^2 = \left(\frac{\mu_t}{\theta_t}\theta\right)^2 + \left(\frac{\partial D}{\partial y}\right)^2 . \tag{4.5}$$

The second term, D'^2, takes into account the cross-stream slope in the force balance on a grain. As it provides a reasonable prediction of a river shape at the threshold of motion (§ 1.1.4), we propose to generalize the transport law (4.4) to an inclined bed by replacing the Shields parameter θ with the force ratio μ,

$$q_s = q_\mu \left(\mu - \mu_t\right), \tag{4.6}$$

with $q_\mu = q_0\,\theta_t/\mu_t$. This relation accounts for the local intensity of the flux, but does not say anything about its direction. We are not aware of any experimental observation that would support this heuristic hypothesis.

Equation (4.6) relates the shear stress to the cross-stream slope of the bed, and thus the derivative of the flow depth. Now, we need to approximate the flow-induced shear stress τ, which appears in the expression of θ, to close our system. In the following, we use the simplest possible approximation of the flow: the shallow-water approximation.

4.2.3 Flow-induced shear stress

We begin our analysis with a simple expression for the shear stress, given by the shallow-water approximation,

$$\tau = \rho_f g D S , \tag{4.7}$$

where D is the depth of the river, and S its downstream slope.

According to this approximation, we neglect the transverse gradient of the flow velocity, and thus the transverse diffusion of momentum. With this expression, the flow-induced shear stress is thus a local function of the depth. However, it remains coupled to the rest of the system, through the two quantities D and S.

4.2.4 Differential equation for the depth of a river

We now combine equations (4.3), (4.6) and (4.7) to obtain a differential equation on the depth of the river. According to the shallow-water approximation, the ratio μ reads:

$$\mu = \sqrt{\left(\frac{DS}{L}\right)^2 + \left(\frac{\partial D}{\partial y}\right)^2}, \tag{4.8}$$

where

$$L = \frac{\theta_t}{\mu_t}\frac{\Delta\rho}{\rho}\, d_s \tag{4.9}$$

is the characteristic length, defined in § 1.1.4, of the order of the grain size (equation (1.14)).

On the other hand, equations (4.6) and (4.3) combine into

$$\mu - \mu_t = \frac{q_{\max}}{q_\mu} \exp\left(\frac{D - D_{\max}}{\lambda}\right). \tag{4.10}$$

Finally, equation (4.8) and (4.10) yield a differential equation on $D(y)$, the river's depth. We introduce the dimensionless depth $\tilde{D} = DS/L$ and the dimensionless coordinate $\tilde{y} = yS/L$. These quantities depend on the downstream slope S of the river and thus, implicitly, on its sediment and fluid discharges. With these notations, we get

$$\sqrt{\tilde{D}^2 + \left(\frac{\partial \tilde{D}}{\partial \tilde{y}}\right)^2} - \mu_t = \chi \exp\left(\frac{\tilde{D} - \tilde{D}_{\max}}{\epsilon_s}\right), \tag{4.11}$$

where we define

$$\epsilon_s = \frac{\lambda S}{L}, \tag{4.12}$$

$$\chi = \frac{q_{\max}}{q_\mu} = \frac{\mu_t}{\theta_t}\frac{q_{\max}}{q_0}. \tag{4.13}$$

In the rest of the present section, we will use only dimensionless variables. To simplify the notations, we omit the symbol ˜ up to the end of section 4.4.

Equation (4.11) resembles an equation previously derived by Seizilles (2013) (p.83, equation (7.11)). In our case, however, it is a first-order, ordinary differential equation, as opposed to a second-order one. We expect it to behave similarly as it is based on the same hypotheses.

Equation (4.11) depends on 3 parameters: χ, ϵ_s, and $D_{\max}$. However, fixing a value for χ is equivalent to fixing the maximum river depth $D_{\max}$, and conversely. Indeed, $D_{\max}$ is the river's depth at the center, where D' vanishes. Equation (4.11) reads then

$$\chi = D_{\max} - \mu_t, \tag{4.14}$$

which is the dimensionless transport law in the center of the river, as χ is proportional to the maximum sediment transport $q_{\max}$. Accordingly, we rewrite equation (4.11) as:

$$(\sqrt{D^2 + D'^2} - \mu_t) \exp\left(\frac{\mu_t - D}{\epsilon_s}\right) = \chi \exp\left(\frac{-\chi}{\epsilon_s}\right). \tag{4.15}$$

Finally, equation (4.15) involves two coefficients, χ and ϵ_s, which depend implicitly on the sediment and fluid discharges of the river. In the following, we estimate their typical values in our laboratory rivers.

The slope parameter ϵ_s

We call ϵ_s the "slope parameter" as it is proportional to the downstream slope of the river, S. Unfortunately, we were not able to directly measure the slope of our laboratory rivers. As a rough estimate, we can use the slope of a threshold channel with equation (1.25) of § 1.1.5, that we rewrite here:

$$S = \mu_t \left(\frac{4g}{9\nu}\right)^{1/3} L^{4/3} Q_w^{-1/3}, \tag{4.16}$$

which gives $S = 4 \cdot 10^{-3}$, and thus,

$$\epsilon_s \approx 10^{-2}. \tag{4.17}$$

For a channel at the threshold of grains entrainment, the slope depends only on the fluid discharge Q_w (§ 1.1.5), whereas it departs from its threshold value when the channel transports sediment. Therefore, we expect that a river transporting sediment reaches a higher slope, which would increase the value of ϵ_s, while maintaining its order of magnitude. We will propose a more accurate estimate of ϵ_s in section 4.5. At this point, we will only keep in mind that ϵ_s is a small parameter.

The transport parameter χ

The parameter χ is proportional to $q_{\max}$ (equation (4.13)). For a river at the threshold, $q_{\max} = 0$ and we thus expect that $\chi = 0$. For an active laboratory river, χ depends on the sediment-flux profile. For example, in the run 3 of table 3.1 (section 3.5), $q_{\max} = 2190 \pm 100\,\text{grains/m/s}$, and thus

$$\chi = 0.18 \pm 0.03. \tag{4.18}$$

In section 3.4, we showed that the maximum sediment flux $q_{\max}$ depends on the total sediment discharge Q_s. It increases with the latter, until it seems to saturate around $q_{\max} \approx 4000\,\text{grains/m/s}$.

In the following, we investigate how equation (4.15) behaves mathematically. We will return to our experiments in section 4.5.

4.2.5 Simple solutions

Equation (4.15) is a non-linear ordinary differential equation. We are not aware of any general analytical solution. However, it presents two trivial solutions.

When χ vanishes, which means there is no sediment transport, equation (4.15) becomes

$$D^2 + D'^2 = \mu_t^2 \,, \tag{4.19}$$

which is the equation at the threshold of motion (§ 1.1.3). The solution is then the cosine profile derived by Henderson (1961) (§ 1.1.4, equation (1.15)).

On the other hand, an infinitely wide and flat river is also a solution of equation (4.15). Indeed, if we take $D'(y) = 0$ and $D''(y) = 0$ along the entire profile, we find

$$D = \mu_t + \epsilon_s \,. \tag{4.20}$$

4.3 Numerical solutions

Apart from the two simple solutions mentioned in § 4.2.5, we are not aware of any other analytical solutions of equation (4.15). As a consequence, we approach its solutions numerically. In this section, we describe our numerical method, and discuss its solutions for different values of the transport parameter χ and the slope parameter ϵ_s.

4.3.1 Numerical method

To solve numerically equation (4.15), we need the expression of D' as a function of D. The derivative of D is, after equation (4.15):

$$D' = \pm\sqrt{\left(\mu_t + \chi \exp\left(\frac{D - \mu_t - \chi}{\epsilon_s}\right)\right)^2 - D^2} \,. \tag{4.21}$$

A positive sign means that the depth increases with the cross-stream coordinate y. We expect that in a real river, the depth decreases from the center to the banks (convex bed). Therefore, we retain the negative solution only.

We supplement equation (4.21) with initial conditions at the channel center ($y = 0$). In the center, the depth is $D(y = 0) = D_{\max} = \mu_t + \chi$ and the cross-stream slope of the river vanishes ($D' = 0$).

Now, we integrate this equation with the `ode` function of the library `scipy.integrate` in Python. However, at the beginning of the integration, D' vanishes, and we cannot run the integration directly. Therefore, we need to expand equation (4.21) analytically near

the center of the channel ($y = 0$). We define δ as

$$D = D_{\max} - \delta = (\mu_t + \chi) - \delta\,, \tag{4.22}$$

$$D' = -\delta'\,, \tag{4.23}$$

with $\delta > 0$. We now assume that $\delta << D_{\max}$.

Introducing these quantities in equation (4.21), we have, at first order, a differential equation on δ,

$$\delta'^2 = 2\,(\mu_t + \chi)\left(1 - \frac{\chi}{\epsilon_s}\right)\delta = A\delta\,, \tag{4.24}$$

where we define

$$A = 2\,(\mu_t + \chi)\left(1 - \frac{\chi}{\epsilon_s}\right). \tag{4.25}$$

For $\chi < \epsilon_s$, $A > 0$ and thus δ' is negative, which corresponds to a convex bed. For $\chi > \epsilon_s$, the solution is not physically acceptable. We therefore consider the positive case only. Equation (4.24) then integrates into

$$\delta = \frac{A}{4}\,y^2\,, \tag{4.26}$$

which gives us the evolution of the depth and of the cross-stream slope near the channel's center. This provides us with two starting values of y and D for the integration, provided that $\chi < \epsilon_s$:

$$y_{\text{start}} = \sqrt{\frac{4\delta}{A}}\,, \tag{4.27}$$

$$D_{\text{start}} = \mu_t + \chi - \frac{A}{4}\,y_{\text{start}}^2\,. \tag{4.28}$$

We use these expressions as initial conditions for the numerical integration.

This method enables us to solve equation (4.15) numerically for a couple of parameters (ϵ_s, χ). In appendix B, we evaluate this method by calculating the numerical error. We find that the relative error of our numerical solutions is less than 10^{-11}. In the following paragraphs, we discuss the numerical profiles obtained with this method.

4.3.2 Profiles

Influence of the slope parameter ϵ_s

First, we set the value of χ to 0.1, and therefore the river depth to $D_{\max} = \mu_t + \chi$ (equation (4.14)). We then vary ϵ_s, keeping it larger than χ. For large values of ϵ_s, the river shape resembles a cosine (the threshold channel). When ϵ_s decreases, the river widens and a flat segment grows around its center (Fig. 4.2a).

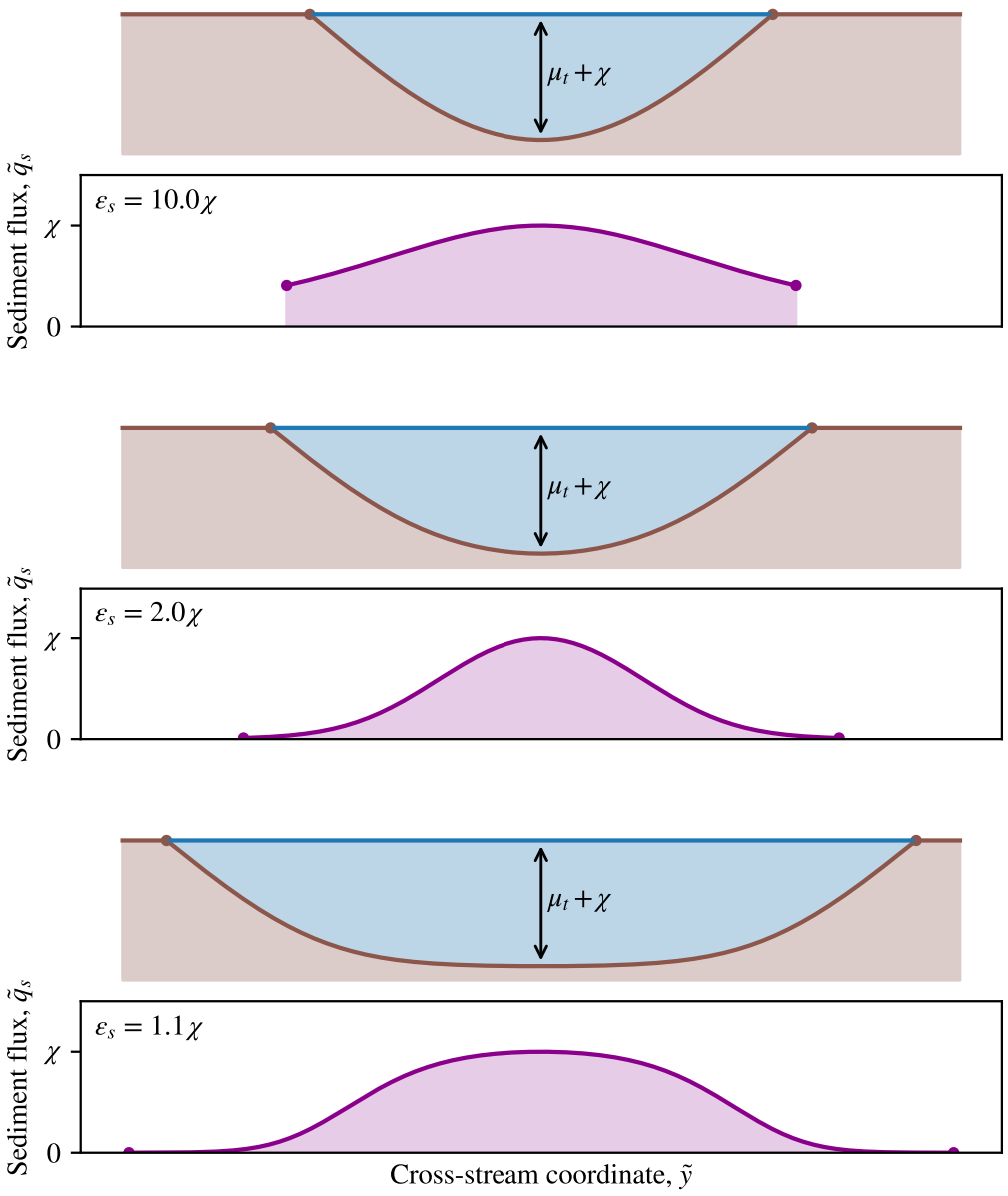

Figure 4.2 – Numerical resolution of equation (4.15). We fix $\chi = 0.1$ and vary ϵ_s. For each value of ϵ_s: Top. River cross sections. Brown: sediment. Blue: flow. Dots represent the end of each profile. Bottom: sediment-flux profiles. Dots represent the end of each profile.

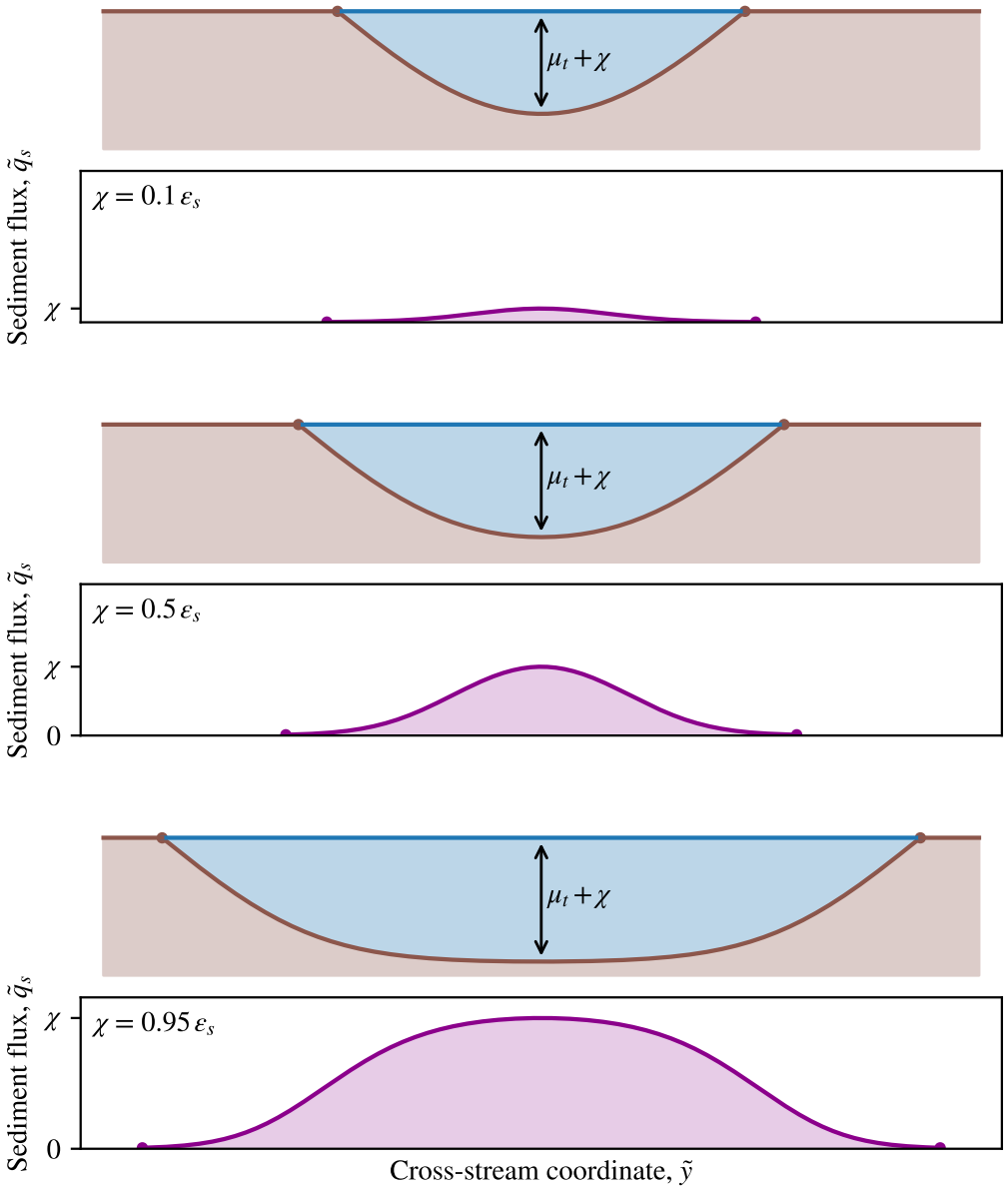

Figure 4.3 – Numerical resolution of equation (4.15). We fix $\epsilon_s = 0.1$ and vary χ. For each value of χ: Top. River cross sections. Brown: sediment. Blue: flow. Dots represent the end of each profile. Bottom: sediment-flux profiles. Dots represent the end of each profile.

As we know the maximum sediment flux ($q_{\max} = q_\mu \chi$), we can compute the sediment-flux profile of these cross sections using equation (4.3). The sediment-flux profile also varies with ϵ_s (Fig. 4.2b). Although its maximum value remains constant, its smallest value, at the banks, increases with ϵ_s. For very low values of ϵ_s, it virtually vanishes at the banks.

Influence of the transport parameter χ

Now, we fix $\epsilon_s = 0.2$, which sets the river downstream slope S. We chose this unrealistically large value for ϵ_s to separate graphically the profiles corresponding to different transport parameters. We then vary χ, which makes the river maximum depth vary. The ratio χ/ϵ_s still remains smaller than 1.

Compared to the threshold channel, where $D_{\max} = \mu_t$, our active rivers widen and grow a flat segment around their center (Fig. 4.3a). The river depth increases from μ_t to $\mu_t + \epsilon_s$ when we increase χ from 0 to ϵ_s.

The sediment-flux profile also varies with χ (Fig. 4.3b). For $\chi = 0.1$, the channel is close to the threshold, and transports virtually no sediment. When χ increases, the sediment transport increases and its profile widens. The parameter χ, which is the maximum sediment transport, varies from 0 to ϵ_s.

As expected, these results are in accordance with these of Seizilles (2013). Qualitatively, these cross sections also accord with our experiments. In particular, when a river transports more sediment, it widens by growing a flat segment near its center. However, in the laboratory, we do not fix χ and ϵ_s but rather the fluid and the sediment discharges. We thus can not compare directly these cross sections with our experiments now.

4.4 Phase portrait

In the previous section, we solved numerically equation (4.15) for given values of the parameters χ and ϵ_s. To get a broader view on the behaviour of equation (4.15), it is useful to plot its phase portrait, which is a geometrical representation of all its solutions in the phase plane (D, D'). Although the phase portrait does not provide us with analytical solutions, it provides us with qualitative insight.

On figure 4.4, we plot the contours of the following function:

$$\xi(D, D') = (\sqrt{D^2 + D'^2} - \mu_t) \exp\left(\frac{D - \mu_t}{\epsilon_s}\right), \tag{4.29}$$

which corresponds to the left-hand side of equation (4.15). To each value of ξ corresponds a river, which takes the form of a trajectory in the phase plane. The resulting figure is the phase portrait of equation (4.15). As the function ξ depends on ϵ_s only, the phase portrait is set by the value of ϵ_s. For clarity, we first chose $\epsilon_s = 1$, although it is an unrealistically

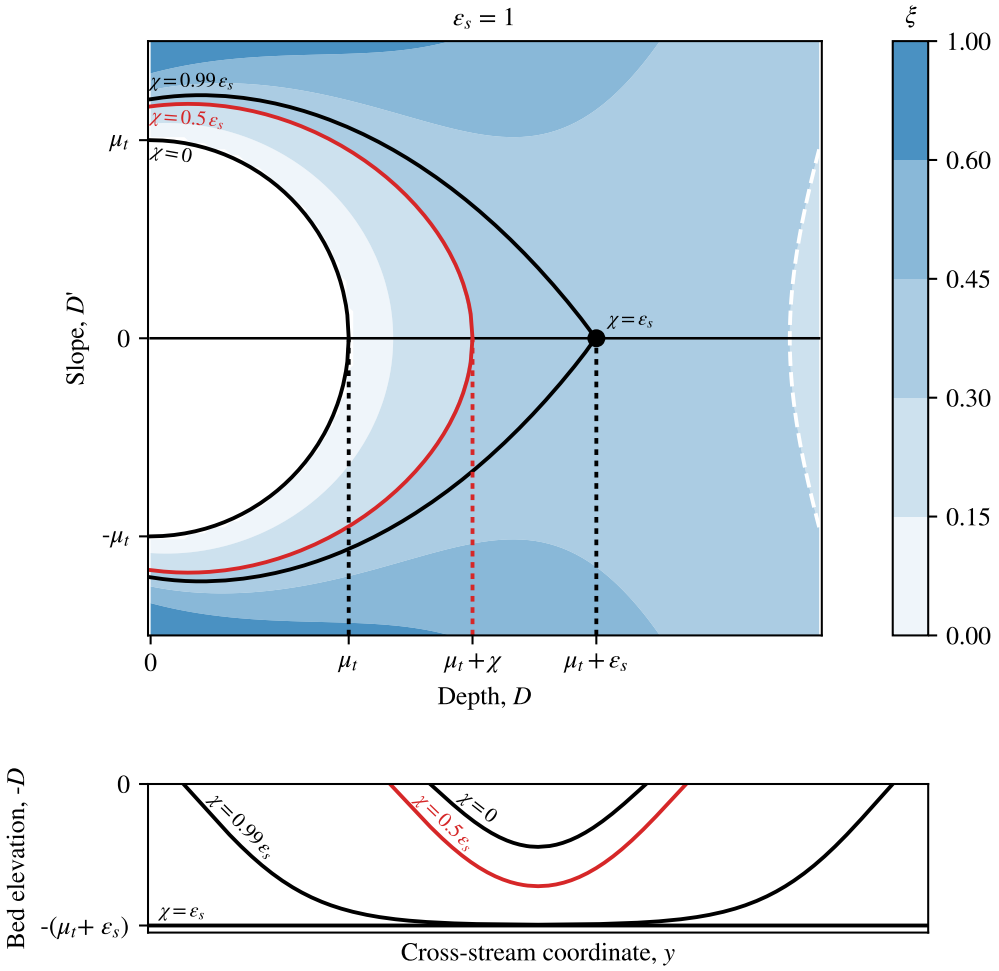

Figure 4.4 – Phase portrait of equation (4.15). The colorbar indicates the values of the parameter ξ (equation (4.29)). Each trajectory in the phase portrait corresponds to a profile plotted below in the same color. Full, black lines: river at the threshold ($\chi = 0$) and separatrix ($\chi = 0.99\,\epsilon_s$). Black point: fixed point, corresponding of an infinitely-wide, flat river ($\chi = \epsilon_s$). Red line: example of an actual river between the two boundaries. Each trajectory corresponds to a distinct value of $D_{\max}$ between μ_t and $\mu_t + \epsilon_s$. White, dashed line: trajectory corresponding to an unrealistic river. Each cross section is labelled by its value of χ.

large value.

In this phase portrait, trajectories are bounded on the left by the threshold channel which satisfies equation (1.13),

$$D^2 + D'^2 = \mu_t^2 \,, \tag{4.30}$$

and is therefore a circle of radius μ_t in the phase plane (Fig. 4.4). This trajectory corresponds to

$$\xi = 0 \,. \tag{4.31}$$

Each trajectory inside this circle corresponds to a river below the threshold and does not transport sediment. The parameter ξ is negative in this domain.

We now place a few river profiles in this phase portrait. We chose, for example, $\chi = 0.5\,\epsilon_s$, and compute numerically the river profile $D(y)$, that we plot in the $(D,\, D')$ plane. We obtain the red trajectory in the phase plane (Fig. 4.4). The left bank of the river corresponds to the point of coordinates $(D = 0,\, D' = -\mu_t - \xi\, e^{-\mu_t/\epsilon_s})$. From this left bank, the depth and the cross-stream slope simultaneously increase. In the center, D' vanishes and the trajectory thus crosses the D-axis in $D_{\max} = \mu_t + \chi$. The depth then decreases, as the cross-stream slope increases to reach the right bank of the channel (Fig. 4.4).

Figure 4.4 shows trajectories for different values of χ. When $D_{\max}$ approaches $\mu_t + \epsilon_s$, the river widens and features a flat segment, as we remarked in the previous paragraph.

When $D_{\max} = \mu_t + \epsilon_s$, the trajectory is a fixed point, meaning that D and D' are constant. Physically, this corresponds to an infinitely wide and flat river for which

$$D = \mu_t + \epsilon_s \,, \tag{4.32}$$

$$D' = 0 \,. \tag{4.33}$$

This fixed point is defined by

$$\partial_y D = 0 \,, \tag{4.34}$$

$$\partial_{yy} D = 0 \,. \tag{4.35}$$

When $D_{\max} > \mu_t + \epsilon_s$, trajectories correspond to unphysical rivers (Fig. 4.4, white dashed line), which never reach a bank. Consequently, all acceptable rivers lie between the threshold trajectory and the fixed point. A separatrix bounds this domain (black line where $\chi = 0.99\,\epsilon_s$, Fig. 4.4).

The size of this domain is set by ϵ_s, since the function $\xi(D, D')$ depends on ϵ_s only (equation (4.29)). To evaluate how this domain changes with ϵ_s, we draw the phase portrait for different values of ϵ_s (Fig. 4.5). When ϵ_s decreases, the fixed point approaches the threshold trajectory and the domain of acceptable channels narrows. In our experiments,

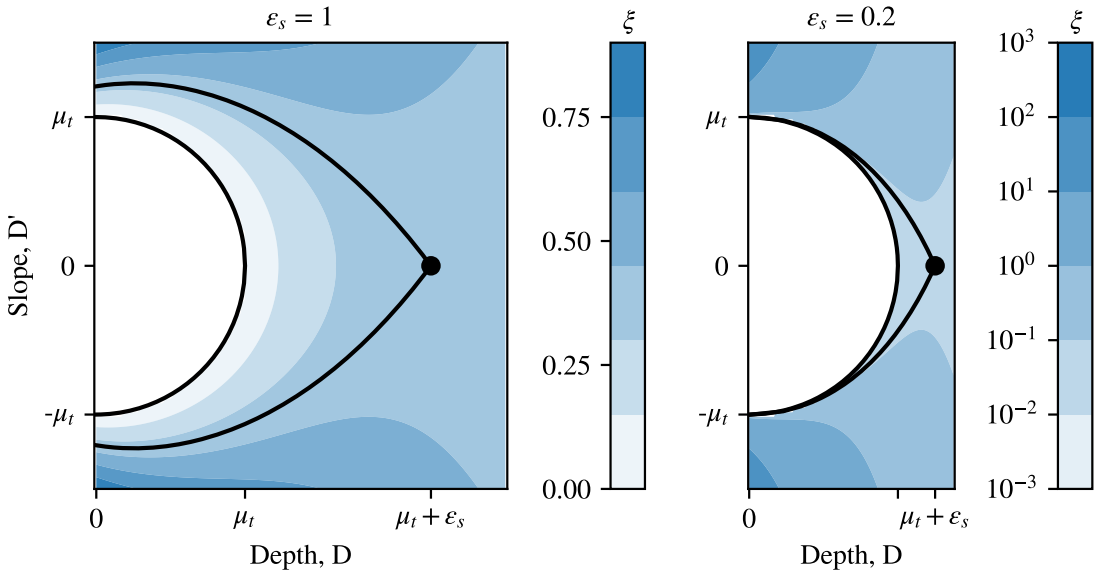

Figure 4.5 – Phase portraits of equation (4.15) with different values for ϵ_s. Colorbars indicate the values of ξ (equation (4.29)). The black, full lines bounds the region where trajectories correspond to physically acceptable rivers.

we expect ϵ_s to be about 10^{-2} (§ 4.2.4). This suggests that the domain of our laboratory rivers is very thin. The fixed point should consequently lie virtually on the threshold circle.

For any value of the slope parameter ϵ_s, however, the transport parameter χ should be less than the slope parameter,

$$\chi < \epsilon_s \,, \tag{4.36}$$

With dimensional quantities, this criterion translates into:

$$\frac{q_{\max}}{S} < \frac{\lambda q_0}{L} \frac{\theta_t}{\mu_t} \,. \tag{4.37}$$

This means that, if we fix the downstream slope S of the river, the maximum sediment flux is bounded regardless of the water discharge.

In the next section, we test these qualitative predictions against our experimental observations.

4.5 Experimental phase portrait

We now test the shallow-water model against our laboratory rivers (Ch. 3) by plotting our experimental cross sections in the phase plane. To do so, we need to plot the local cross-stream slope D' of a river cross section as a function of its dimensionless depth DS/L. However, we could not measure the downstream slopes S of our laboratory rivers.

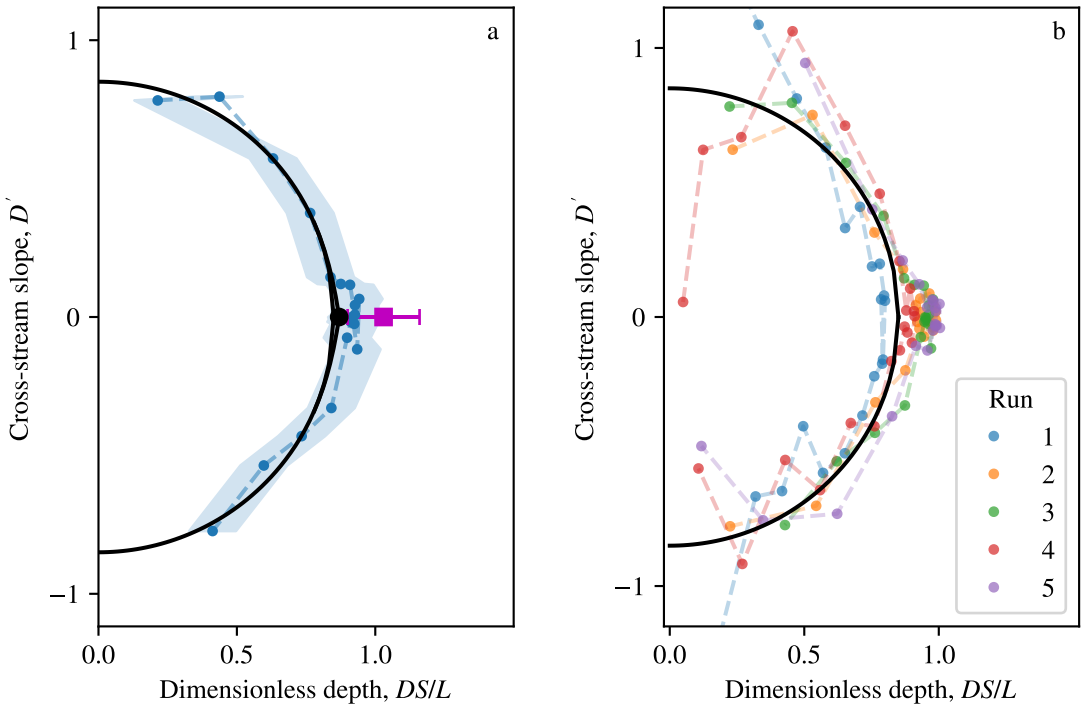

Figure 4.6 – Experimental phase portraits. a. Single experiment: run 3 of table 3.1. Black line: theoretical phase portrait for $\epsilon_s = 0.02$. The separatrix collapses onto the threshold circle, and the phase portrait is virtually reduced to the threshold circle. Blue points: experimental data. Blue area: measurement uncertainty. Magenta square: $D_{\max} = \mu_t + \chi$. b. Multiple experiments. Each color corresponds to a run in table 3.1.

Run	S	ϵ_s	χ	ξ
1	0.0047 ± 0.0008	0.011 ± 0.002	0	0
2	0.010 ± 0.002	0.026 ± 0.006	0.19 ± 0.04	$2.8{\cdot}10^{-4}$
3	0.009 ± 0.002	0.022 ± 0.005	0.18 ± 0.05	$7.8{\cdot}10^{-4}$
4	0.006 ± 0.001	0.014 ± 0.003	0.11 ± 0.03	$2.7{\cdot}10^{-4}$
5	0.008 ± 0.001	0.020 ± 0.004	0.20 ± 0.05	$6.9{\cdot}10^{-5}$

Table 4.1 – Values of the transport parameter χ, of the slope parameter ϵ_s, and of the parameter ξ for the laboratory rivers of table 3.1.

To bypass this issue, we use the transport law to estimate the slope of a river:

$$q_s = q_\mu \left(\mu - \mu_t\right). \tag{4.38}$$

In the channel center, using the shallow-water approximation, this transport law relates the sediment flux $q_{\max}$ to its depth $D_{\max}$:

$$q_{\max} = q_\mu \left(\frac{D_{\max} S}{L} - \mu_t\right). \tag{4.39}$$

We can estimate the channel downstream slope based on the above expression:

$$S = \frac{L}{D_{\max}} \left(\mu_t + \frac{q_{\max}}{q_\mu}\right), \tag{4.40}$$

We calculate the downstream slope of our experimental rivers with equation (4.40) (Tab. 4.1). We find that it remains close to the slope of the threshold channel (§ 4.2.4), and, as expected, slightly increases with sediment discharge.

Now that we have an estimate of the downstream slope of a laboratory river, we can plot its trajectory in the phase plane. Figure 4.6a shows the phase portrait of an experimental run (Run 3, Tab. 3.1). All points gather around the circle of radius μ_t, which corresponds to the threshold channel. They also accumulate near the maximum depth, where D' vanishes, which corresponds to the neighbourhood of the fixed point.

According to the shallow-water theory, these points should lie between the threshold channel and the fixed point. To locate the fixed point in this phase portrait, we need to estimate the slope parameter ϵ_s, which is proportional to the slope (section 4.4). As expected, ϵ_s is of the order of 10^{-2}, and the separatrix collapses almost perfectly with the threshold channel (Fig. 4.6a). Within the measurement uncertainty, we recover the qualitative behaviour of a river transporting sediment: it sets its bed near the threshold of motion.

An independent way to find where the trajectory crosses the D-axis is to estimate the transport parameter $\chi = q_{\max}/q_\mu$. For run 3, we have $\chi = 0.18 \pm 0.03$. We report this value on figure 4.6a and find that it lies near the fixed point, although the uncertainty on the

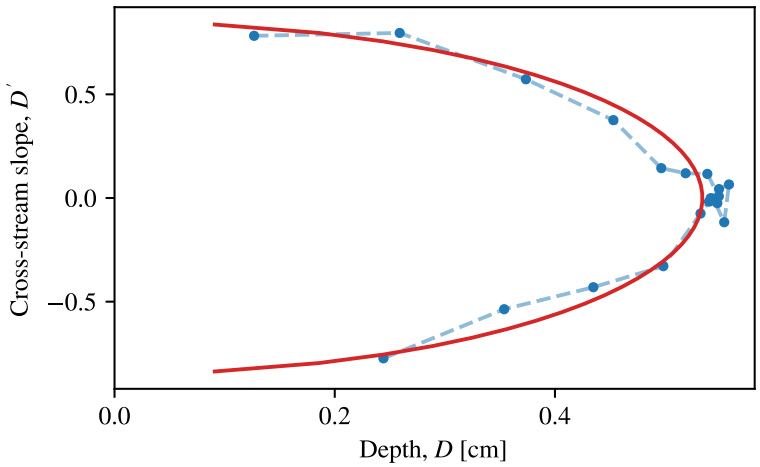

Figure 4.7 – Measure of the slope S and of the friction coefficient μ_t by fitting a river's phase portrait. Blue points: experimental data for run 3 (Tab. 3.1). Red line: fit by an ellipse.

experimental trajectory is much larger than the size of its theoretical phase portrait.

If our theoretical scenario holds, all trajectories should gather near the threshold circle. To verify that in our laboratory rivers, we now plot the phase portrait of all our experimental runs (Fig. 4.6b). Despite significant noise, all the trajectories indeed gather around this circle, showing that all rivers self-organise close to the threshold, regardless of their sediment discharge.

A remarkable consequence of this hypothesis is that the trajectory of a river in the phase plane $(DS/L,\, D')$ should be a circle. Therefore, in the absence of any sediment-flux measurement, we can plot it in the plane $(D,\, D')$ and adjust its aspect ratio to fit a circle: the fitting parameter on the D-axis should be proportional to its slope S. In principle, this method would allow us to measure the downstream slope of a river, based on its cross section only.

We test this method against our laboratory rivers. We start by plotting directly the cross-stream slope as a function of the dimensional depth D. It forms a trajectory that we fit by an ellipse (Fig. 4.7):

$$D' + \left(\frac{DS}{L}\right)^2 = \mu_t^2 \,. \tag{4.41}$$

We deduce the adjustable values of the slope S and of the friction coefficient μ_t. For example, in the case of the experimental run 3 (Tab. 3.1), we find $\mu_t = 0.9 \pm 0.2$ and $S = 0.008 \pm 0.002$.

We iterate this method for all our runs, and compare this measurement of the slope with the one measured with the sediment flux (equation (4.40)). We obtain figure 4.8. These two methods yield comparable results, with a relative error of 13% in average.

The fact that a river is close to the circle of radius μ_t in the phase plane thus provides

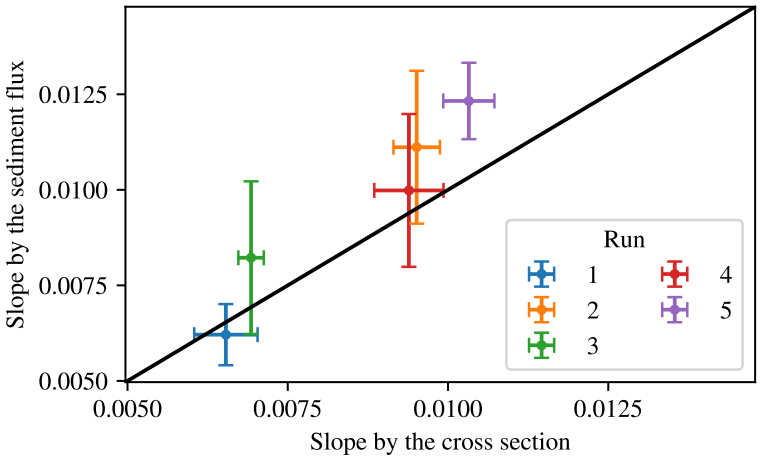

Figure 4.8 – Comparison of two methods to measure the slope of a river. y-axis: slope calculated with equation (4.40). x-axis: slope measured by the fit of a river's phase portrait.

us with a method to measure the slope of a river based on its cross section only. Moreover, it supports qualitatively the shallow-water approximation of a river. According to its phase portrait, a river self-organises close to the threshold of grain entrainment.

Moreover, we measured the slope parameter ϵ_s and the transport parameter χ of all our laboratory rivers in the present section (Tab. 4.1). These are the only two parameters that are involved in equation (4.15). In principle, provided that $\chi < \epsilon_s$, we should be able to compute numerically the shape of a river based on the experimental measurements of χ and ϵ_s.

However, we find that χ is always larger than ϵ_s in our laboratory rivers, although we are able to measure both quantities with sufficient precision (Tab. 4.1). This can be due to our assumptions on the transport law (equation (4.6)), which has never been established experimentally. Another possible failure of our theory is that the shallow-water approximation does not provide an accurate estimation of the shear stress, especially on the river's banks.

Despite this discrepancy between theory and observations, the shallow-water approximation accords qualitatively with our experiments. However, this theory is based on two quantities, χ and ϵ_s, that we can measure, but that we cannot fix in an experiment. Now, we investigate the influence of the parameters we can control directly in our experiment: the fluid and the sediment discharges, Q_w and Q_s. In the next section, we thus investigate the evolution of the river's profile as a function of the input parameters.

4.6 Regime relations

4.6.1 Numerical regime relations

In this section, we investigate the evolution of a river's profile as a function of the input parameters: the fluid and the sediment discharges (Q_w and Q_s respectively). To do so, we use numerical simulations to relate χ and ϵ_s to Q_w and Q_s.

In this aim, we generate dimensionless river profiles $\tilde{D}(\tilde{y})$ for different couples of (ϵ_s,χ), keeping $\chi < \epsilon_s$ (section 4.3 and 4.4), and using a numerical method different from the one discussed in § 4.3.1. This new method is faster and less sensitive to precision issues (Appendix B). Given a numerical river profile, we can calculate its characteristics (width, aspect ratio, fluid and sediment discharges) as follows.

For each numerical profile, we compute straightforwardly the dimensionless width and depth:

$$\tilde{W} = 2\max(\tilde{y})\,, \tag{4.42}$$

$$\tilde{D}_{\max} = \max(\tilde{D})\,. \tag{4.43}$$

The Boltzmann distribution then yields the sediment flux profile:

$$\tilde{q}_s = \frac{q_s}{q_\mu} = \chi \exp\left(\frac{D - D_{\max}}{\epsilon_s}\right). \tag{4.44}$$

from which we deduce the total sediment discharge Q_s by integrating $\tilde{q}_s$ over the river profile. In dimensional form, Q_s reads:

$$Q_s = \int q_s \,\mathrm{d}y = \frac{L}{S}\, q_\mu \int \tilde{q}_s \,\mathrm{d}\tilde{y}\,. \tag{4.45}$$

Knowing that $\epsilon_s = \lambda S/L$, the dimensionless sediment discharge $\tilde{Q}_s$ is thus:

$$\tilde{Q}_s = \frac{Q_s}{Q_s^*} = \frac{1}{\epsilon_s} \int \tilde{q}_s \,\mathrm{d}\tilde{y}\,, \tag{4.46}$$

where $Q_s^* = q_\mu \lambda$.

The fluid discharge of a given river cross section, in dimensional form, is:

$$Q_w = \int U D \,\mathrm{d}y\,, \tag{4.47}$$

where U is the vertically-averaged flow velocity. Assuming a one-dimensional Poiseuille flow profile, we get $U = gD^2S/3\nu$. In dimensionless form:

$$\tilde{Q}_w = \frac{Q_w}{Q_w^*} = \frac{1}{\epsilon_s^3} \int \tilde{D}^3 \,\mathrm{d}\tilde{y}\,, \tag{4.48}$$

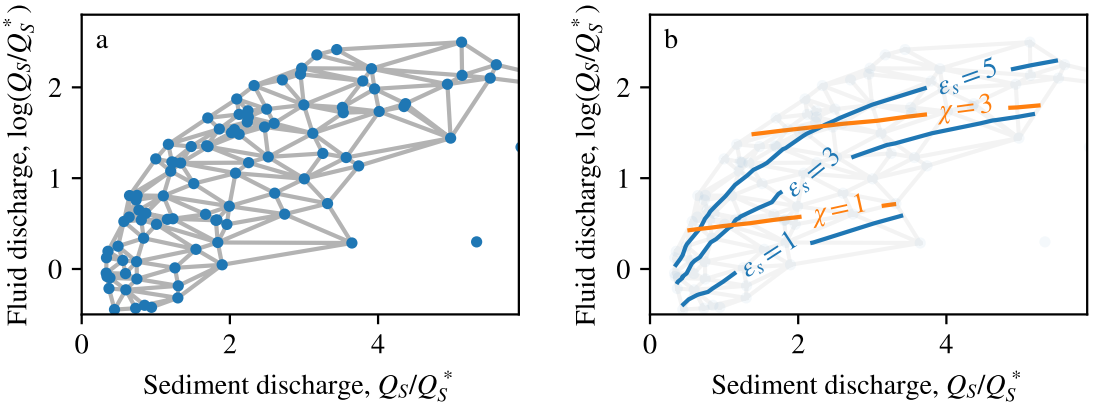

Figure 4.9 – Illustration of the method to generate an abacus. a. Blue Points: 100 numerical profiles for ϵ_s in [0.01, 10] and χ/ϵ_s in [0.5, 1]. Grey lines: Triangulation. The isolated point is due to the alha shape (α = 0.3 here). b. Contours of ϵ_s and χ according to the fluid and sediment discharges.

where we define

$$Q_w^* = \frac{gL\lambda^3}{3\nu}. \tag{4.49}$$

We thus have expressions for the width, the depth, the fluid and the sediment discharges associated to a given river profile.

We now investigate the characteristics of a large number of numerical profiles. To generate these profiles while covering a uniform range, we randomly pick values of ϵ_s and χ in given intervals (still with $\chi < \epsilon_s$). The randomness of this procedure rids us of the *a priori* definition of the number of profiles: the longer the simulations, the more data points we obtain.

We calculate the dimensionless sediment and fluid discharges of each profile with equation (4.46) and (4.48) respectively. Figure 4.9a shows the dimensionless fluid discharge Q_w/Q_w^* as a function of the dimensionless sediment discharge Q_s/Q_s^* for 100 profiles. Based on these values, we build a triangular grid (alpha-shaped Delaunay triangulation) and associate a set of parameters (ϵ_s, χ, $\tilde{W}$, $\tilde{D}$) to each node of this triangulation. Interpolating these values linearly on each triangle, we can then plot the contours of any parameter.

Specifically, figure 4.9b shows the contours of ϵ_s and χ in this space. This enables us to relate the couple of parameters (Q_w, Q_s) that we control in the laboratory to the parameters (χ, ϵ_s) that explicitly appear in equation (4.15). We find that, if we want to reach large values of the sediment and fluid discharges, we need to choose a large ϵ_s, and χ as close as possible to ϵ_s.

To explore larger ranges of ϵ_s and χ, and increase the accuracy of the interpolation, we iterate this process for a few thousands of numerical profiles. We thus obtain a wide range

of river profiles and can investigate not only the relation between (Q_w, Q_s) and (ϵ_s, χ), but also the relation between any couple of parameters. In the following, we discuss successively the evolution of the aspect ratio, the width, the slope and the maximum sediment flux of a river as a function of its sediment discharge (regime relations).

We start by investigating the evolution of the aspect ratio as a function of the sediment discharge (Fig. 4.10a). On figure 4.10a, the triangular mesh indicates the extent of the domain covered by our numerical solutions. The shape of this domain is restricted by the numerical accuracy. Indeed, large values of sediment discharge require χ to be very close to ϵ_s. For example, a sediment discharge $\tilde{Q}_s = 30$ corresponds to a value of $\chi = (1 - 10^{-15})\,\epsilon_s$, which is of the order of the numerical accuracy of a floating point number in Python. Thus, larger sediment discharges cannot be reached with our current numerical method.

Computing the contours of dimensionless fluid discharges in the $(\tilde{W}/\tilde{D},\ \tilde{Q}_s)$ plane, we obtain curves that predict the evolution of a river's aspect ratio as a function of its sediment discharge for a given fluid discharge (Fig. 4.10a).

In our laboratory experiments, we maintain the fluid discharge around 1 L/min and the characteristic fluid discharge is

$$Q_w^* = 7.9 \cdot 10^{-11}\,\mathrm{m}^3/\mathrm{s}\,. \tag{4.50}$$

As a result, the dimensionless fluid discharge is about 10^5, which corresponds to the magenta contour in figure 4.10a.

To compare this prediction to our experiments, we now place our data in this figure. In our experimental conditions, the characteristic sediment discharge is

$$Q_s^* = 1.5\ \ \mathrm{grains/s}\,, \tag{4.51}$$

or, equivalently,

$$Q_s^* = 2.6 \cdot 10^{-2}\ \ \mathrm{g/min}\,. \tag{4.52}$$

Normalizing the sediment discharge to this value, we plot the aspect ratio of our laboratory rivers as a function of the dimensionless sediment discharge (Fig. 4.10a, magenta dots). The resulting data lie significantly below the theoretical prediction, showing that the shallow-water theory overestimates the aspect ratio for a given fluid discharge by a factor of about 2.

We now investigate how the width of the river evolves as a function of the sediment discharge according to the shallow-water theory (Fig. 4.10b). Here, the width is normalized with respect to its value at the threshold W_{th} for the same fluid discharge (equation (1.26)), so that it is equal to one for a vanishing sediment discharge (Fig. 4.10b, black square). Adding our experimental data, we find again that the shallow-water model overestimates

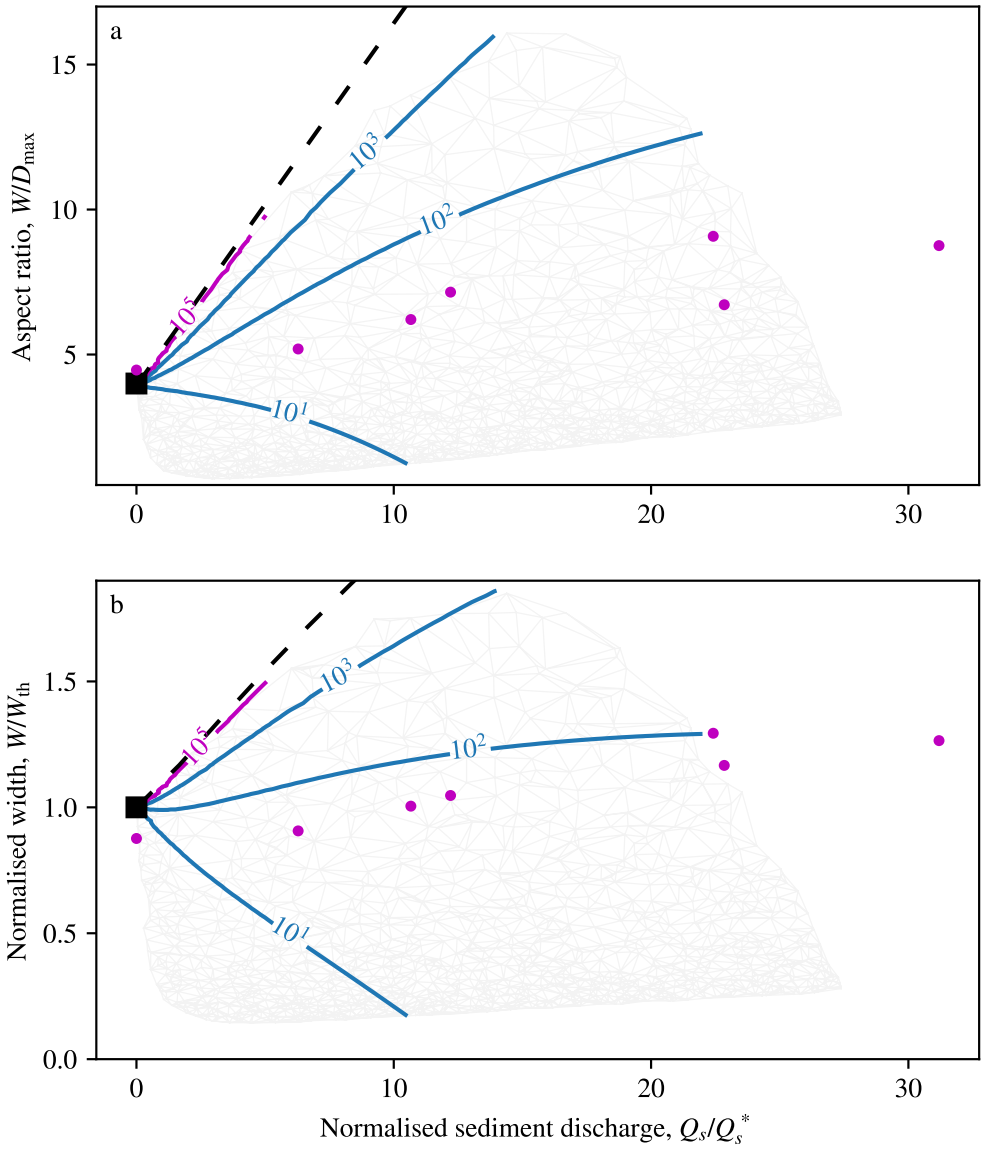

Figure 4.10 – Regime relations for the width and aspect ratio of a river. a. Aspect ratio of a river as a function of its dimensionless sediment discharge Q_s/Q_s^* at a fixed fluid discharge. Grey: triangulation. Blue lines: contours of the dimensionless fluid discharges Q_w/Q_w^*. Magenta line: contour of Q_w/Q_w^* for our experimental conditions ($Q_w = 1\,\mathrm{L/min}$). Magenta points: experimental data. Black square: Threshold theory. Black dashed line: asymptotic river described in § 4.6.2. b. Normalised width of a river as a function of its dimensionless sediment discharge Q_s/Q_s^* at a fixed fluid discharge. Grey: triangulation. Blue lines: contours of Q_w/Q_w^*. Magenta line: contour of Q_w/Q_w^*, which corresponds to our experimental conditions ($Q_w = 1\,\mathrm{L/min}$). Blue points: experiments at $Q_w = 1\,\mathrm{L/min}$. Magenta points: experimental data. Black square: Threshold theory. Black dashed line: asymptotic river described in § 4.6.2. Triangulation downsampled by a factor of ten.

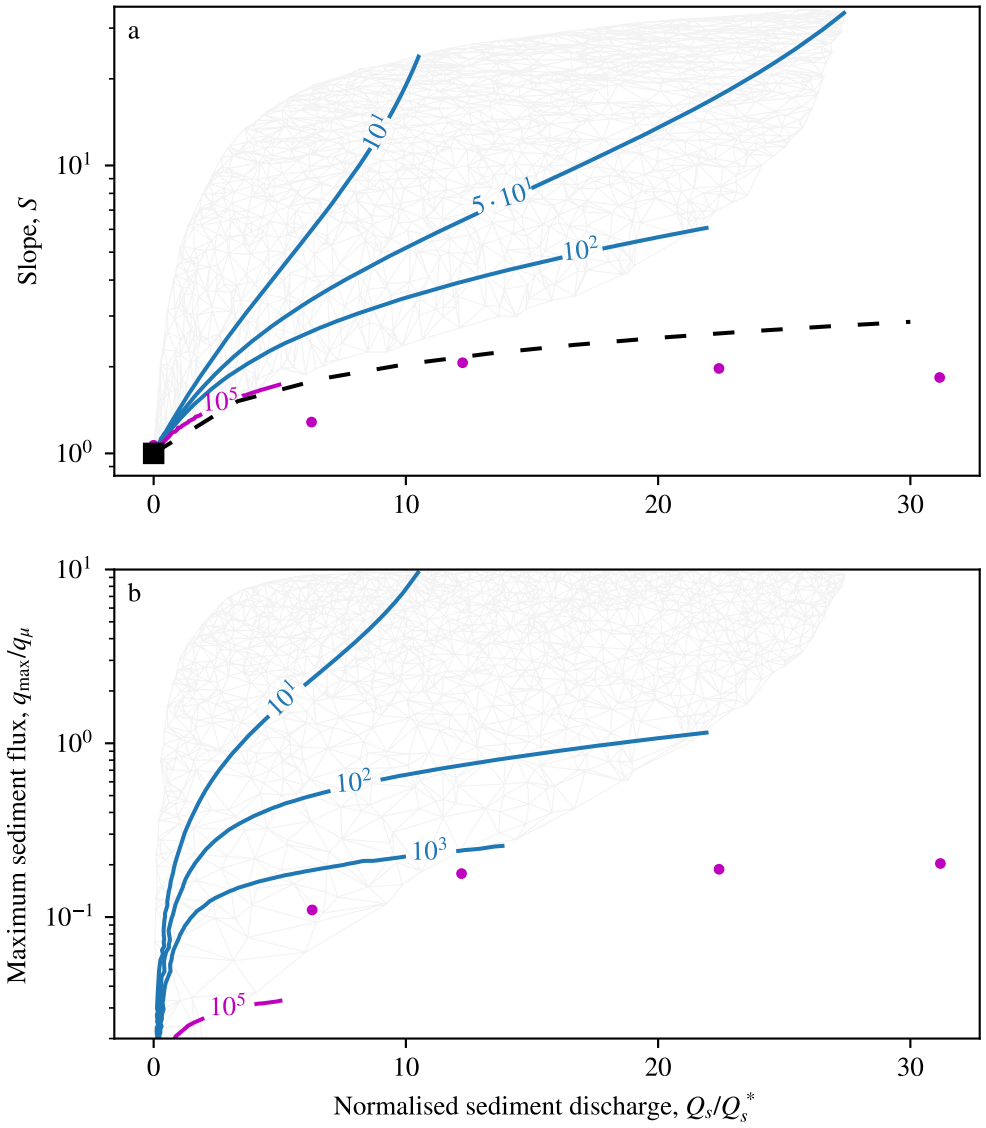

Figure 4.11 – Regime relations for the slope and the maximum sediment flux of a river. a. Downstream slope of a river S as a function of its dimensionless sediment discharge Q_s/Q_s^* at a fixed fluid discharge. Grey: triangulation. Blue lines: contours of the dimensionless fluid discharge Q_w/Q_w^*. Magenta line: contour of Q_w/Q_w^*, which corresponds to our experimental conditions ($Q_w = 1\,\mathrm{L/min}$). Magenta points: experimental data. Black square: Threshold theory. Black dashed line: asymptotic river described in § 4.6.2. b. Maximum sediment flux q_{max} of a river as a function of its dimensionless sediment discharge Q_s/Q_s^* at a fixed fluid discharge. Grey: triangulation. Blue lines: contours of the dimensionless fluid discharge Q_w/Q_w^*. Magenta line: contour of Q_w/Q_w^*, which corresponds to our experimental conditions ($Q_w = 1\,\mathrm{L/min}$). Magenta points: experimental data. Triangulation downsampled by a factor of ten.

the width of a river by a factor of 2.

Repeating the same procedure for the slope, we find that the shallow-water model yields a reasonable order of magnitude (Fig. 4.11a). However, we did not measure directly the slope of our laboratory rivers, but rather estimated it based on the maximum sediment flux, using the shallow-water approximation (section 4.5). The agreement between theory and experiments might be therefore biased.

Finally, our numerical simulations show that, according to the shallow-water theory, the maximum of the sediment-flux profile $q_{\max}$ saturates with the sediment discharge for a fluid discharge higher than Q_w^* (Fig. 4.11b). This evolution accords qualitatively with our experimental observations (section 3.4). However, once again, the theory fails to predict the experimental data quantitatively.

Overall, we have had a limited success when comparing our experiments to the model prediction. In the next paragraph, we relate our model to the analytical approximation of the shallow-water theory proposed by Seizilles (2013).

4.6.2 Asymptotic river

On figure 4.10a, we observe that the isolines of fluid discharges decreases seem to converge towards an upper limit, meaning that the shallow-water model predicts a maximum aspect ratio for a given sediment discharge.

We speculate that this limit corresponds to the separatrix we observe in the phase portrait of equation (4.15) (section 4.4). Indeed, when χ get closer to ϵ_s, its trajectory approaches asymptotically the separatrix. The resulting asymptotic river is close to the threshold at its banks, and transports sediment uniformly near its center (Fig. 4.12), as proposed previsouly by Seizilles (2013). We now compute the aspect ratio of this asymptotic river as a function of its sediment discharge.

We name W_T the width of the flat segment where the river transports sediment (Fig. 4.12). The total sediment discharge then reads

$$Q_s = q_{\max} W_T = \frac{q_0 \theta_t}{\mu_t} \epsilon_s W_T \,. \tag{4.53}$$

As $\epsilon_s = \lambda S/L$ (equation (4.12)), we get,

$$\frac{Q_s}{Q_s^*} = W_T \frac{S}{L} \,, \tag{4.54}$$

with

$$Q_s^* = q_\mu \lambda = \frac{q_0 \theta_t}{\mu_t} \lambda \,. \tag{4.55}$$

Taking into account the banks of the river, which we assume to be exactly at the

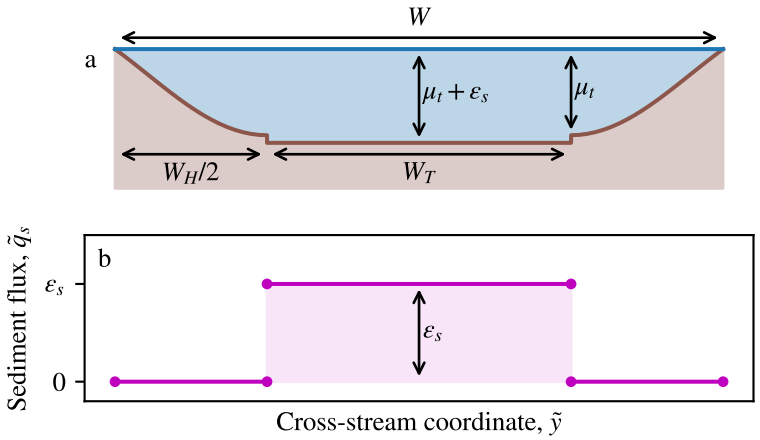

Figure 4.12 – Asymptotic river. In brown: sediment bed. In blue: flow. W_T is the width over which the river transports sediment uniformly. W_H is the width of a river at the threshold of motion. W is the total width of the river.

threshold, the total width of the river reads

$$W = \frac{L}{S}\left(\pi + \frac{Q_s}{Q_s^*}\right). \tag{4.56}$$

In addition, the dimensionless depth of this channel is equal to $\mu_t + \epsilon_s$, and thus, its depth writes

$$D_{\max} = \frac{L}{S}\mu_t + \lambda \approx \frac{L}{S}\mu_t. \tag{4.57}$$

The ratio of equation (4.57) and (4.56) then yields the aspect ratio (Seizilles 2013):

$$\frac{W}{D_{\max}} = \frac{1}{\mu_t}\left(\pi + \frac{Q_s}{Q_s^*}\right). \tag{4.58}$$

This equation is plotted on figure 4.10 (dashed black line). We observe that the trend collapses with the upper-bound limit for the aspect ratio, which confirms that the model predicts a maximum aspect ratio for a given sediment discharge.

The same reasoning can be followed for the width and the slope of the asymptotic river (dashed black lines in Fig. 4.10b and 4.11a, respectively).

4.7 Conclusion

In this chapter, we derived a differential equation for the depth of the river (equation (4.15)) assuming the simplest possible model for the flow: the shallow-water approximation. This equation involves two parameters, χ and ϵ_s, which are linked to the maximum of the sediment flux $q_{\max}$ and the downstream slope of the river S, respectively.

The differential equation (4.15) reproduces qualitatively our experimental observations

on a river cross section, provided $\chi < \epsilon_s$. In particular, as a river transports more sediment, it grows a flat, active segment near its center (Fig. 4.3).

To get an overview of the solutions to this equation, we then investigated the phase portrait of equation (4.15). We found that acceptable rivers are bounded by two limit trajectories: the threshold channel, and an infinitely flat and wide river, corresponding to the fixed point in the phase portrait. The value of ϵ_s sets the size of this physical-rivers domain. The theory also predicts that the transport parameter is bounded by the slope parameter: $\chi < \epsilon_s$.

For small values of ϵ_s, the two limits almost collapse and the phase portrait is reduced to the circle formed by the threshold channel. This is in accordance with our experimental observations: all our laboratory experiments form a circle in the phase plane (DS/L, D'), indicating that they self-organise close to the threshold of sediment transport.

However, by measuring the parameters χ and ϵ_s in our laboratory rivers, we systematically found $\chi > \epsilon_s$. We thus cannot predict the river's shape using the shallow-water theory. Despite this discrepancy, we proceeded to relate numerically ϵ_s and χ with our control parameters: the fluid and sediment discharges Q_w and Q_s, respectively. We obtained regime relations for the aspect ratio, the width, the slope and the maximum sediment flux of a river as a function of its input parameters. These regime relations accord qualitatively with our observations. Specifically, the maximum sediment flux of a river saturates, meaning that the latter accommodates a higher sediment discharge by widening its channel. Unfortunately, the numerical regime relations fail to agree quantitatively with our observations.

We suspect that this discrepancy is due mainly to the shallow-water approximation. As discussed in chapter 2, this approximation predicts the shear stress with an error of more than 15% (section 2.5). However, in the phase portrait, the river trajectories are confined in a very thin domain and therefore are very close to each other. As a consequence, any error on the flow-induced shear stress, and thus on the force ratio μ, causes a drastic change in the river's shape.

The estimation of the shear stress could be improved by taking into account two-dimensional effects in the flow. This is not an easy task, though: as we do not know the shape of the river, this would be a moving-boundary problem. If we address this problem numerically with finite elements, it would involve technical difficulties associated to the evolution of the mesh as the boundary evolves towards the stationary shape.

Overall, this model supports that a river (i) self-organises close to the threshold of motion, (ii) widens to accommodate a larger sediment discharge rather than increase the intensity of the sediment flux. When the sediment input becomes too high, we observed that a laboratory river destabilizes into braids (section 3.7). In the light of the present chapter, we suggest that it cannot accommodate its shape any more to remain close to the

threshold. This prompts us now to investigate the stability of an active river in the next chapter.

Chapter 5

Streaks induced by bedload diffusion

Contents

5.1 Avant-propos

Dans le chapitre 4, nous avons étudié l'équilibre d'une rivière. À l'aide de l'approximation d'eau peu profonde (*shallow water*), nous avons modélisé l'influence du débit de sédiments sur la section d'une rivière. Bien que notre modèle ne prédise pas correctement la forme d'équilibre d'une rivière en fonction du débit de sédiments, il permet de rendre compte, au moins qualitativement, de l'augmentation de son rapport d'aspect avec le débit de sédiments, ce que nous observons expérimentalement. Nous avons également observé qu'au-delà d'un certain rapport d'aspect, nos rivières de laboratoire se déstabilisent jusqu'à former plusieurs chenaux (section 3.7). Ce comportement nous conduit maintenant à étudier la stabilité d'une rivière.

Cependant, comme nous ne connaissons par la forme d'équilibre d'une rivière, nous ne pouvons pas l'utiliser comme état de base pour une analyse de stabilité. Nous décidons donc de nous concentrer sur la partie plate d'un profil de rivière, qui est d'autant plus grande lorsque le débit sédimentaire est grand. Dans ce chapitre, nous étudions donc la stabilité d'un lit plat de sédiments cisaillé par un fluide visqueux. Il s'agit de la retranscription d'un article soumis au *Journal of Fluid Mechanics*.

5.2 Abstract

A fluid flowing over a granular bed can move its superficial grains, and eventually deform it by erosion and deposition. This coupling generates a beautiful variety of patterns such as ripples, bars and streamwise streaks. Here, we investigate the latter, sometimes called "sand ridges" or "sand ribbons". We perturb a sediment bed with sinusoidal streaks, the crests of which are aligned with the flow. We find that, when their wavelength is much larger than the flow depth, bedload diffusion brings mobile grains from troughs, where they are more numerous, to crests. Surprisingly, gravity can only counter this destabilising mechanism when sediment transport is intense enough. Relaxing the long-wavelength approximation, we find that the cross-stream diffusion of momentum mitigates the influence of the bed perturbation on the flow, and even reverses it for short wavelengths. The diffusion of momentum thus opposes that of entrained grains to select the most unstable wavelength. This instability might turn single-thread alluvial rivers into braided channels.

5.3 Introduction

When water flows over a granular bed with enough strength, it dislodges some of the superficial grains and entrains them downstream (Shields 1936, Einstein 1937, Bagnold 1973). As long as the flow-induced force is comparable to their weight, the entrained grains remain close to the bed surface, where they travel with the flow, until they eventually settle

down. In steady state, the balance between entrainment and settling sets the number of travelling grains, which thus depends primarily on the flow-induced shear stress (Charru *et al.* 2004b, Lajeunesse *et al.* 2010). Accordingly, the sediment flux resulting from their collective motion, called bedload transport, is usually expressed as a function of shear stress (Meyer-Peter & Müller 1948).

Bedload transport is often heterogeneous—it scours away the bed somewhere, and deposits the entrained material elsewhere (Exner 1925). The flow then adjusts to the deformed bed, and alters the distribution of erosion and deposition. This fluid-structure interaction generates bedforms through various instabilities (Seminara 2010, Charru *et al.* 2013).

Current ripples are iconic underwater bedforms found in streams, on beaches and sometimes in the sedimentary record (Allen 1982, Coleman & Melville 1994). They result from the inertia of the flow, which concentrates shear stress just upstream of their crest (Kennedy 1963, Charru 2006, Charru *et al.* 2013). Nascent ripples make the most of this mechanism by orienting their crest across the flow. At least initially, they do not involve any cross-stream sediment flux. By contrast, the oblique crest of alternate bars diverts the water flow to induce the cross-stream bedload flux that makes them unstable (Parker 1976, Colombini *et al.* 1987, Devauchelle *et al.* 2010a, Andreotti *et al.* 2012).

Although less common, streamwise streaks materialise cross-stream bedload more neatly—their crest remains aligned with the stream as they grow (Karcz 1967, Colombini & Parker 1995, McLelland *et al.* 1999). To initiate a cross-stream flux of sediment, these bedforms use a subtle peculiarity of turbulence. When streamwise ridges perturb their boundary, turbulent flows generates transverse, counter-rotating vortices (Colombini 1993, Vanderwel & Ganapathisubramani 2015). Over a granular bed, these slow secondary currents transport sediment across the primary flow to accumulate it in upwelling areas, thus reinforcing the ridges that brought them about. A similar phenomenon occurs when grains of different sizes make up the bed, the heterogeneous roughness of which then plays the role of ridges (McLelland *et al.* 1999, Willingham *et al.* 2014).

In the above examples, the sediment grains travel along the force that entrains them. This is certainly true at first order, but bedload particles slide and roll over a rough bed, which makes them waver erratically around their average trajectory (Nikora *et al.* 2002, Furbish *et al.* 2012a). These fluctuations cause the grains to disperse laterally, like random walkers. Collectively, they diffuse sideways across the bedload layer, towards areas of lesser transport (Seizilles *et al.* 2014). We speculate that this Fickian diffusion could create streamwise streaks without secondary currents, provided bedload is less intense on the bedforms' crests.

To test this scenario, we investigate the stability of a flat sediment bed sheared by a laminar flow. We begin with the shallow-water approximation (section 5.4), and extend

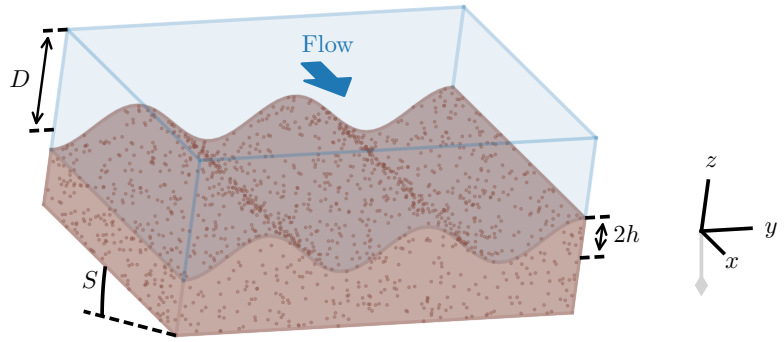

Figure 5.1 – Sediment bed perturbed by longitudinal streaks. A layer of fluid (blue) flows over a granular bed (brown). The reference frame is inclined with respect to gravity (downstream slope S). The vertical grey line with a diamond marker symbolises a plumb line.

our analysis to a full two-dimensional Stokes flow (section 5.5). We then consider a stream covered with a rigid lid, which might facilitate measurements in a laboratory experiment (section 5.6). Finally, we look for this instability in previous experiments (section 5.7).

5.4 Bedload instability

5.4.1 Base state

We consider an infinitely-wide, flat granular bed sheared by a free-surface, laminar flow (figure 5.1). A small slope S drives the fluid along x, the streamwise direction, but we will neglect its effect on the weight of a grain later on. We further assume that the size of a grain, d_s, is much smaller than the flow depth D. In steady state, the shear stress the fluid exerts on the bed, τ, is the projection of its weight on the streamwise direction:

$$\tau = \rho g D S \tag{5.1}$$

where ρ is the density of the fluid, and g the acceleration of gravity.

To entrain a grain, the fluid needs to pull it with enough strength to overcome its weight. Mathematically, this happens when the ratio of these two forces, θ, exceeds a threshold value, θ_t. Shields (1936) defined this ratio as

$$\theta = \frac{\tau}{(\rho_s - \rho) g d_s}, \tag{5.2}$$

where ρ_s is the density of a grain.

Based on laboratory observations, Charru *et al.* (2004b) suggested that the number of

grains the fluid dislodges from the bed, per unit surface and time, is proportional to the distance to threshold, $\theta - \theta_t$. The bedload layer is fed by this constant input. Conversely, it loses a fraction of its population through settling. When moving grains are too sparse to interact, the settling rate is proportional to the number of moving grains per unit area, n (Aussillous *et al.* 2016). At equilibrium, the density of moving grains thus reads

$$n = \frac{\alpha_n}{d_s^2}(\theta - \theta_t) \tag{5.3}$$

where α_n is, like θ_t, a dimensionless, empirical parameter (Lajeunesse *et al.* 2010). For illustration, $\theta_t \sim 0.1$ and $\alpha_n \sim 0.01$ are typical values for these parameters in a laminar flow (Seizilles *et al.* 2014). Equation (5.3) is valid only above threshold, that is, when $\theta \geq \theta_t$; below threshold, the bedload layer is empty ($n = 0$).

After equation (5.3), a flow near threshold can only entrain a sparse bedload layer. Then, the velocity of the travelling grains is that of the fluid near the bed, which is proportional to shear stress in a laminar flow (Seizilles *et al.* 2014). As a consequence, the average velocity in the bedload layer is proportional to Stokes' settling velocity, which reads

$$V_s = \frac{(\rho_s - \rho) g d_s^2}{18\eta} \tag{5.4}$$

where η is the viscosity of the fluid. The sediment flux, q_s, results from the collective motion of the bedload grains:

$$q_s = \alpha_v n V_s \,, \tag{5.5}$$

where α_v is a dimensionless coefficient. In a laminar flow, Seizilles *et al.* (2014) found $\alpha_v \sim 0.4$.

Most authors relate bedload directly to the Shields parameter with a sediment transport law (Meyer-Peter & Müller 1948). Combining equations (5.3) and (5.5), we find that bedload transport is proportional to the distance to threshold. The specific expression of this law, however, is still debated, and is likely to depend on the particle Reynolds number (Ouriemi *et al.* 2009). Here, we choose a simple law that compares reasonably with near-threshold, laminar experiments (Charru *et al.* 2004b, Seizilles *et al.* 2014).

Equations (5.1) to (5.5) represent a uniform base state, both in the downstream direction x and in the cross-stream direction y. In the following, we add a perturbation to it to introduce bedload diffusion.

5.4.2 Bedload diffusion

Heterogeneity drives diffusion. To introduce some of it in our system, we now carve streamwise streaks into the granular bed, in the form of a sinusoidal perturbation of amplitude h and wavelength λ (figure 5.1). The fluid flow and the sediment bed remain invariant

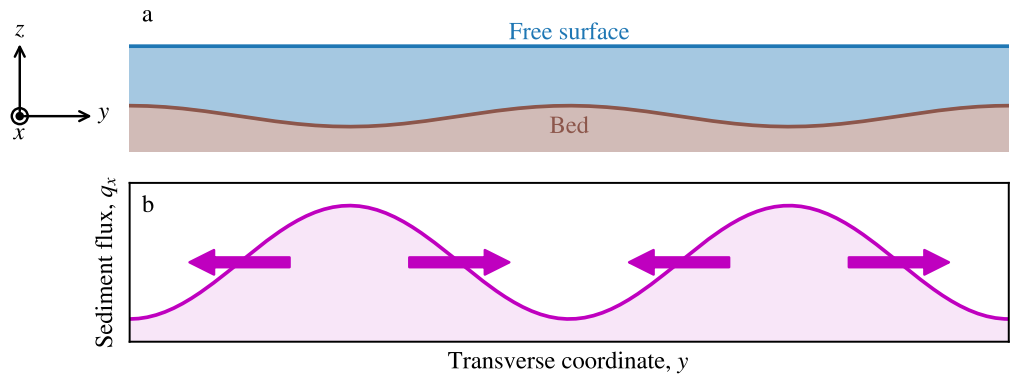

Figure 5.2 – Mechanism of the bedload instability. a: Bed elevation (brown) and free surface flow (blue). b: Distribution of the corresponding downstream sediment flux. Red arrows indicate bedload diffusion.

along x, and our system is now two-dimensional.

To illustrate the mechanism of the bedload instability, we consider, in this section, that the amplitude of the perturbation is much smaller, and its wavelength much longer, than the flow depth. With these assumptions, we expect the shallow-water approximation to yield a reasonable estimate of the shear stress τ, and therefore of the Shields parameter θ. Both are then proportional to the local flow depth, $D-h$, and therefore of lesser intensity at the crest of the perturbation. Mathematically,

$$\theta = \frac{\rho D S}{(\rho_s - \rho) d_s} \left(1 - \frac{h}{D}\right). \tag{5.6}$$

According to equation (5.3), the bedload layer is thus denser in the troughs than on the crests. Its density reads

$$n = n_0 - \frac{\alpha_n \theta_0}{d_s^2} \frac{h}{D} \tag{5.7}$$

where n_0 and θ_0 are the density of moving grains and the Shields parameter in the base state, respectively. Like equation (5.3), from which it is derived, the above equation only holds above threshold, that is, when

$$\frac{h}{D} \leq \frac{\theta_0 - \theta_t}{\theta_0}. \tag{5.8}$$

This condition sets the maximum amplitude the perturbation h can reach before the following analysis breaks down.

Following Seizilles *et al.* (2014), we now treat the bedload grains as independent random walkers. As they travel downstream at the average velocity $\alpha_v V_s$, their cross-stream velocity fluctuates around zero. We represent this process by a series of random

sideways steps, the amplitude of which is a fraction of the grain size. Statistically, the accumulation of these steps generates a diffusive flux, q_d, towards the less populated areas of the bedload layer. As long as their density remains low, the moving grains do not interact with each other, and bedload diffusion obeys Fick's law:

$$q_d = -\alpha_v \ell_d V_s \frac{\partial n}{\partial y}\,, \tag{5.9}$$

where we expect the diffusion length, ℓ_d, to be a fraction of the grain size. Seizilles *et al.* (2014) found $\ell_d \sim 0.03\ d_s$ in their laminar experiment, and we are not aware of any other measurement of this empirical parameter.

The stage is now set for the bedload instability: diffusion brings grains from the troughs, where bedload is more intense, to the less populated crests, thus furrowing further into the bed (figure 5.2). This mechanism, however, is countered by gravity, to which we now turn our attention.

5.4.3 Stability

As a grain travels over a slanting bed, gravity deflects its trajectory downwards. For an arbitrary slope, the mathematical formulation of the resulting cross-stream flux is intricate, and its experimental evaluation challenging (Kovacs & Parker 1994). Fortunately, for a linear stability analysis, we may content ourselves with a first-order formulation valid for shallow slopes, and near the threshold of motion. Accordingly, we assume that the cross-stream, slope-induced flux, q_g, is proportional to the density of moving grains, and to the cross-stream slope of the bed:

$$q_g = -\gamma \alpha_v V_s n \frac{\partial h}{\partial y}\,, \tag{5.10}$$

where γ is another empirical parameter—the last we will need. Based on the observations of Yamasaka *et al.* (1987) in a wind tunnel, Chen *et al.* (2009) proposed that γ lies in the range $0.1 - 1$. Most probably, this value depends on the Reynolds number at the grain's scale, and on the relative density of the grain. To our knowledge, it has never been measured in a laminar flow.

The gravity flux, q_g, brings bedload grains from crest to trough, and thus hinders the instability driven by the diffusion flux, q_d. Mass balance mediates this competition through the Exner equation:

$$\frac{\partial h}{\partial t} + \frac{d_s^3}{\phi} \frac{\partial}{\partial y} \left(q_d + q_g \right) = 0 \tag{5.11}$$

where ϕ and t are the packing fraction of the sediment bed and time, respectively. For randomly packed spheres, the packing fraction is about $\phi \sim 0.6$ (Bernal & Mason 1960). The bedload density equation (5.7), the cross-stream flux equations (5.9) and (5.10), and the Exner equation form a closed system, which the slope-induced flux makes non-linear.

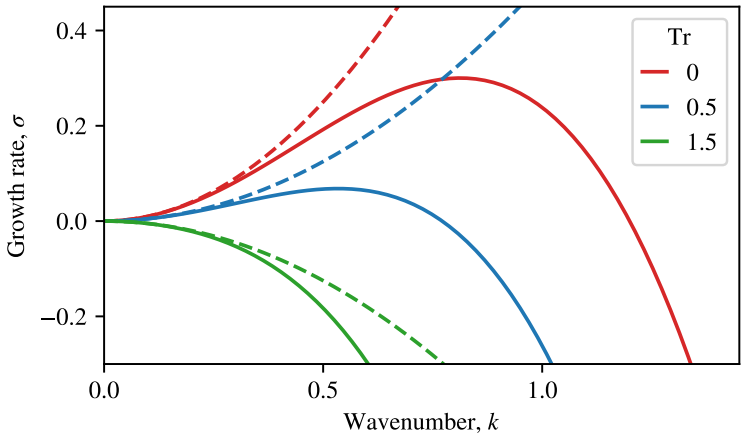

Figure 5.3 – Dispersion relation of the bedload instability, in a free-surface flow. Dashed lines: shallow-water approximation (equation (5.17)). Solid lines: two-dimensional Stokes flow (equation (5.26)).

We consider an infinitesimal perturbation of the bed, and expand our equations up to first order. When we combine its four equations, the resulting linear system takes the familiar form of the heat equation:

$$\frac{\partial h}{\partial t} - \frac{q_{s0} d_s^3}{\phi}\left(\gamma - \frac{\ell_d}{D}\frac{\theta_0}{\theta_0 - \theta_t}\right)\frac{\partial^2 h}{\partial y^2} = 0 \tag{5.12}$$

where q_{s0} is the bedload intensity of the base state. The diffusivity of this equation depends on the base state, and indeed can change sign. Its expression straightforwardly conveys the character of the two cross-stream fluxes. The slope-induced flux, represented by γ, tends to increase the diffusivity, and thus stabilises the system. Conversely, the diffusive flux, represented by ℓ_d, destabilises the bed—as anticipated, bedload diffusion drives the instability.

We now introduce the transport number, Tr, as the ratio of the two terms of the diffusivity in equation (5.12):

$$\mathrm{Tr} = \frac{\gamma D}{\ell_d}\frac{\theta_0 - \theta_t}{\theta_0}\,. \tag{5.13}$$

Combining this definition with the bedload transport law (equation (5.5)) recasts the transport number into a dimensionless sediment flux:

$$\mathrm{Tr} = \frac{\gamma D d_s^2}{\alpha_v \alpha_n \ell_d V_s}\frac{q_{s0}}{\theta_0}\,. \tag{5.14}$$

Literally, Tr depends not only on the sediment flux of the base state, but also on the Shields parameter, θ_0. Near the threshold, however, θ_t becomes a good approximation for θ_0; the transport number then bears its name rightly.

When bedload is intense in the base state, the transport number is large, and so is diffusivity in equation (5.12). Sediment transport therefore stabilises the bed. Conversely, a vanishing sediment flux brings the transport number arbitrarily close to zero. Eventually, the effective diffusivity in equation (5.12) becomes negative, and bedload diffusion destabilises the bed.

This surprising result can be understood as follows. After the shallow-water approximation, the density of moving grains is simply proportional to the local depth (equation (5.7)). As a consequence, its cross-stream gradient does not depend on the intensity of bedload in the base state. Conversely, the slope-induced flux is proportional to n_0, and therefore to the downstream sediment flux in the base state. Intense bedload thus favours the stabilising mechanism, without affecting bedload diffusion.

To formalise this discussion, we now perform the linear stability analysis of equation (5.12), an elementary undertaking that will serve as a guide for the next section. We first introduce the following characteristic time:

$$T = \frac{\phi D^3}{\theta_0 \alpha_n \alpha_v V_s \ell_d d_s} \tag{5.15}$$

which, when lengths are rescaled with D, makes equation (5.12) dimensionless. Next, we express the bed perturbation as a sinusoidal wave of dimensionless amplitude $\hat{h}$:

$$\frac{h}{D} = \mathrm{Re}\left(\hat{h} \exp\left(ik\frac{y}{D} + \sigma\frac{t}{T}\right)\right), \tag{5.16}$$

where k and σ are the dimensionless wavenumber and growth rate of the perturbation, respectively. Substituting this expression in equation (5.12) yields the dispersion relation of the instability:

$$\sigma = k^2\,(1 - \mathrm{Tr})\,. \tag{5.17}$$

When the base state transports enough sediment to bring the transport number above one, the growth rate is negative for any wavenumber, indicating that all perturbations of the bed decay (figure 5.3). This oversimplified model transitions to instability drastically: all wavelengths suddenly become unstable as the transport number is reduced below one. Short-wavelength perturbations grow infinitely fast, and equation (5.12) is then ill-posed.

In reality, of course, streamwise streaks will never grow infinitely fast. This mathematical exaggeration is only due to some rash assumption. In the next section, we attempt to fix our model by dropping the shallow-water approximation.

5.5 Regularisation by the flow

5.5.1 Stokes flow

Bedload diffusion reinforces streamwise streaks provided (i) bedload transport is weak, and (ii) the flow exerts a lower shear stress on the crests than in the troughs. When the wavelength of the perturbation is much longer than the flow depth, the shallow-water approximation ensures that the latter condition is fulfilled. Otherwise, this approximation unduly maintains the bedload instability. In this section, we replace the latter with a more accurate representation of the flow.

We still consider a streamwise-invariant, laminar flow, but its downstream velocity u is now a function of y and z (figure 5.2). This Stokes flow then obeys Poisson's equation:

$$\eta \, \nabla^2 u = -\rho g S \tag{5.18}$$

where η is the viscosity of the fluid, and the Laplacian operator ∇^2 applies to cross-stream coordinates only. We further assume that the flow does not slip along the bed surface, and that the fluid surface is free of constraint. Mathematically,

$$u = 0 \quad \text{at} \quad z = h \tag{5.19}$$

and

$$\frac{\partial u}{\partial y} = 0 \quad \text{at} \quad z = D \, . \tag{5.20}$$

Solving Poisson's equation with the above boundary conditions yields the shear stress the flow exerts on the bed surface:

$$\tau = \eta \, \mathbf{e}_n \cdot \nabla u \quad \text{at} \quad z = h \tag{5.21}$$

where $\mathbf{e}_n$ is the unit vector normal to the bed surface.

Like in section 5.4, the flow entrains superficial grains as bedload, thus altering the bed surface through erosion and deposition. Here, however, this coupling takes the form of a free-boundary problem in two dimensions, since the Exner equation transforms the domain over which Poisson's equation is to be solved. Fortunately, linearising makes its stability analytically tractable.

Let us first consider the velocity profile of the base state, u_0. Like the bed itself, it is invariant along the streamwise and cross-stream direction, and Poisson's equation reduces to the direction normal to the bed, z. Its solution is half the classical parabola of the Poiseuille flow:

$$u_0 = 9 \, \frac{\theta_0 V_s D}{d_s} \left(2 \, \frac{z}{D} - \left(\frac{z}{D} \right)^2 \right) , \tag{5.22}$$

which provides us with a velocity scale for the flow, namely $\theta_0 V_s D/d_s$.

The velocity profile of the base state equates the source term of Poisson's equation. Therefore, the velocity perturbation is a solution of Laplace's equation or, equivalently, it is the real part of some analytical function of the complex coordinate $y + iz$. This velocity profile vanishes at the surface of the bed (equation (5.19)), the elevation of which is perturbed by sinusoidal streaks (equation (5.16) at $t = 0$). In addition, its normal derivative also vanishes at the surface of the flow or, equivalently, it is symmetrical with respect to this surface (equation (5.20)). At first order, we find:

$$u = u_0 - 18\,\frac{\theta_0 V_s D}{d_s}\,\mathrm{Re}\left(\frac{\hat{h}}{\cosh(k)}\cosh\left(ik\,\frac{y+iz}{D}+k\right)\right). \tag{5.23}$$

Figure 5.4 shows the iso-velocity lines of the first-order flow, that is, the contours of the above expression. When the wavelength of the perturbation is much larger than the flow depth ($\lambda \gg D$ or, equivalently, $k \ll 1$), the Stokes flow accords qualitatively with the shallow-water approximation: its contours constrict above troughs, indicating intense shear stress on the deepest parts of the bed. This distribution of shear stress favours the instability.

The iso-velocity lines tell a different story for short wavelengths ($k \gg 1$). As the space between streaks gets narrower, the bulk of the flow cannot squeeze in between crests any more. The latter then find themselves fully exposed to the flow, from which they shelter the troughs. As a result, shear stress is more intense on the crests than in the troughs, and bedload diffusion will combine with gravity to wear the streaks down. We thus anticipate that the screening induced by the diffusion of momentum across the flow, which is the signature of Laplace's equation, will provide us with the regularisation we lacked in section 5.4.

5.5.2 Dispersion relation

To turn the above reasoning into a quantitative expression, we first need to calculate the shear stress on the sediment bed. Deriving equation (5.23) with respect to z, and evaluating the result on the bed yields the bed shear stress, and therefore the Shields parameter, at first order:

$$\theta = \theta_0\left(1 - (1 - k\tanh k)\,\mathrm{Re}\left(\hat{h}\exp\left(\frac{iky}{D}\right)\right)\right). \tag{5.24}$$

According to this expression, the perturbation of the Shields parameter is either in phase or in antiphase with the bed perturbation, depending on wavelength (figure 5.4). For long wavelengths ($k \ll 1$), the Shields parameter approaches its shallow-water expression (equation (5.6)); it then reaches its maximum above a trough, and the bed is unstable.

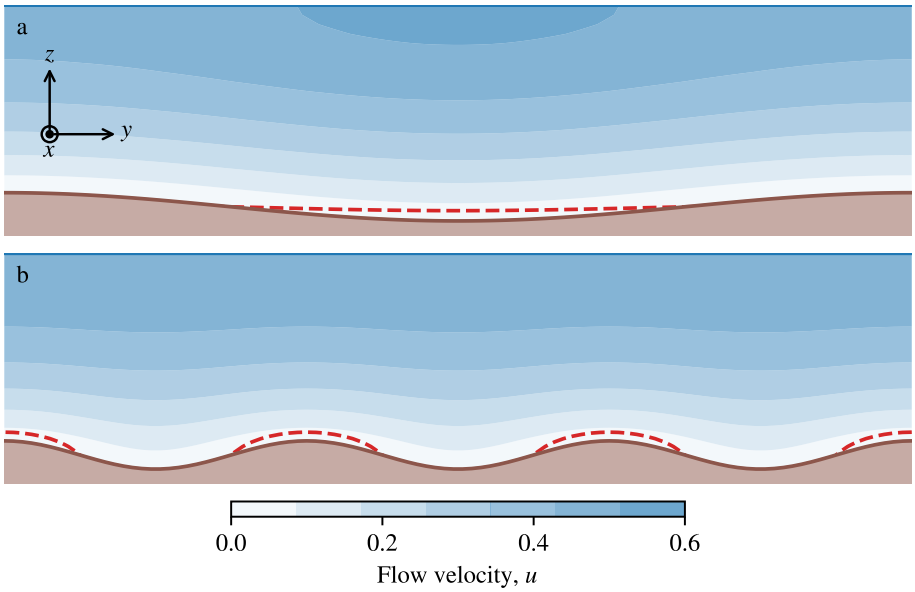

Figure 5.4 – Stokes flow above streamwise streaks. Bed elevation (brown) and iso-velocity contours (blue scale). Below the red dashed line, the shear stress is higher than in the base state. a: long wavelength ($kD = 1.4$). b: short wavelength ($kD = 4.2$).

Conversely, for short wavelengths ($k \gg 1$), equation (5.24) reduces to

$$\theta \approx \theta_0 \left(1 + k\,\mathrm{Re}\left(\hat{h}\exp\left(\frac{iky}{D}\right)\right)\right), \tag{5.25}$$

which reverses the phase of the Shields parameter with respect to the bed perturbation. The shear stress then concentrates on the crests, thus stabilising the bed.

Equipped with a new expression for the Shields parameter, we now return to the stability analysis of section 5.4. We substitute equation (5.6) for equation (5.24), and reuse the expression of the bedload fluxes, which the new flow model leaves unaffected (equations (5.3), (5.9) and (5.10)). Injecting these equations into the mass-balance equation (5.11) yields a new dispersion relation:

$$\sigma = k^2\,(1 - \mathrm{Tr}) - k^3\,\tanh k\,. \tag{5.26}$$

This expression equals its shallow-water counterpart (equation 5.17), but for an additional regularisation term. The latter, always negative, dominates the dispersion relation at short wavelength (large k). Thanks to the two-dimensional Stokes flow, equation (5.26) now behaves like a proper dispersion relation—the growth rate never diverges (figure 5.3).

The transport number still controls the global stability of the bed. Intense sediment transport ($\mathrm{Tr} > 1$) precludes the bedload instability. When the transport number becomes less than its critical value of one, however, a range of unstable wavelengths appears. Within this range, a well-defined maximum indicates the most unstable mode, which is likely to

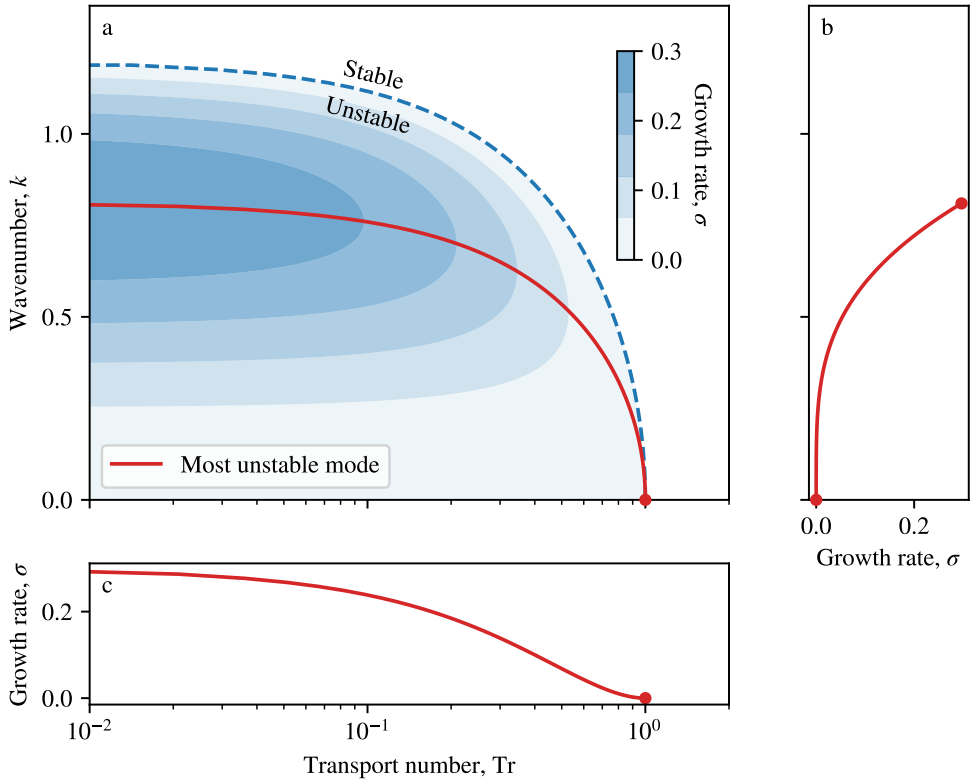

Figure 5.5 – Stability map of the bedload instability, for a free surface flow. a: Dispersion relation. Darker areas correspond to faster growth rate. Red line: most unstable wave number for a given value of the transport number. b: Growth rate of the most unstable wavenumber. c: Maximum growth rate as a function of the transport number.

emerge in experiments.

Figure 5.5a shows the trajectory of the most unstable mode on a stability map. As the transport number crosses its critical value, the bedload instability appears with a vanishing wavenumber, which quickly increases. The wavenumber of the most unstable mode then increases towards its maximum value $k_{\max}$, which it reaches when the base state transports no sediment (Tr = 0). The largest of all most unstable wavenumber, $k_{\max}$, is the positive solution of the following equation:

$$3k\,\tanh(k) + k^2\left(1 - \tanh^2 k\right) = 2\,. \tag{5.27}$$

Numerically, $k_{\max} \approx 0.813$. Returning to dimensional quantities, we find that $k_{\max}$ translates into a remarkably universal ratio. When the intensity of bedload vanishes, the most unstable wavelength, $\lambda_{\max}$, is simply proportional to the flow depth, regardless of any other

parameter:

$$\frac{\lambda_{\max}}{D} = \frac{2\pi}{k_{\max}} \approx 7.73\,. \tag{5.28}$$

This result suggests a recipe for an experiment—a hypothetical one for now. To identify the bedload instability unambiguously, one need only reduce the bedload flux until the wavelength of the instability reaches its minimum, which should be the above value. Unfortunately, laboratory experiments seldom abide by idealised theories; we will return to this question in the discussion (Section 5.7).

In addition to a wavelength, the most unstable mode also has a growth rate, $\sigma_{\max} \approx 0.300$, which we calculate by injecting $k_{\max}$ into the dispersion relation, and sending the transport number to zero. Like the wavenumber of the most unstable mode, the growth rate is at its highest when the base state transports no sediment (Tr = 0, figure 5.5c). This statement, counter-intuitive with dimensionless quantities, becomes preposterous in physical units: After equation (5.15), the dimensional growth rate also reaches its maximum when bedload transport vanishes. Since it is bedload that feeds the instability, we would expect its absence to turn off the growth of the streaks. This apparent paradox is due to the threshold of the sediment transport law (equation (5.3)), which brings the linear regime to its end.

5.5.3 End of the linear regime

As the flow-induced shear stress approaches the threshold, bedload vanishes from the base state, and so does the efficiency of the gravity-induced flux. This, however, does not affect the sensitivity of bedload, which responds as strongly as ever to any perturbation of the flow. Therefore, while the stabilising mechanism vanishes, the unstable coupling between the flow and the bed persists—the bedload instability then thrives.

Such full-blown growth, however, will quickly meet its end. The linear expansion of the transport law holds as long as the perturbed bed remains above the threshold. This gets more demanding as the base state itself approaches the threshold (figure 5.6). We define $h_{\max}$ as the amplitude of the perturbation when the Shields parameter hits the threshold. Mathematically, after equation (5.24), $h_{\max}$ reads:

$$h_{\max} = \frac{\ell_d}{\gamma} \frac{\mathrm{Tr}}{1 - k \tanh k}\,. \tag{5.29}$$

For any value of the transport number Tr, we calculate numerically the wavenumber k of the most unstable mode, and inject the result in the above expression (figure 5.6). We find that, as the intensity of bedload vanishes ($\mathrm{Tr} \to 0$), so does the maximum amplitude of the most unstable mode. Our linear stability analysis then holds for imperceptible streaks only.

Once the perturbation has outgrown $h_{\max}$, the instability enters a non-linear regime, to

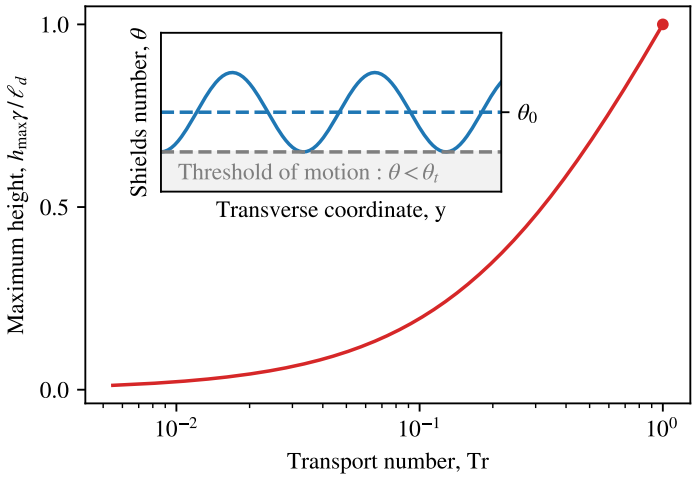

Figure 5.6 – Saturation of the bedload instability. Red line: amplitude of the bed perturbation at the transition to the non-linear regime, $h_{\max}$, as a function of the transport number. Inset: transition criterium, the amplitude of the perturbation of the Shields parameter reaches $\theta_0 - \theta_t$.

which the present analysis grants no access. We speculate, however, that the perturbation could keep growing beyond this point, since its driving mechanism—active troughs and frozen crests—should survive the end of linearity.

5.6 Rigid lid

Although most bedload experiments involve open channels, the free surface of the flow makes the tracking of sediment grains difficult. To avoid this problem, some experimenters covered the flow with a transparent lid (Charru *et al.* 2004b, Lobkovsky *et al.* 2008, Aussillous *et al.* 2016). In this section, we investigate the influence of this new boundary condition on the bedload instability.

5.6.1 Fixed lid

Like in the experiments of Lobkovsky *et al.* (2008), a fixed, flat and rigid lid now confines the fluid above the sediment bed. The flow is driven along this infinitely wide pipe either by a downstream pressure gradient or, like in the previous sections, by the tilt of the bed. Equating the pressure gradient with $\rho g S$, we may treat these configurations alike.

Following the structure of section 5.4, let us first use the shallow-water approximation, keeping its limitations in mind. Above a long-wavelength perturbation, the flow profile is essentially the Poiseuille parabola—the entire one, this time. It is symmetric with respect to the centre of the fluid gap, and therefore distributes shear stress evenly between the lid

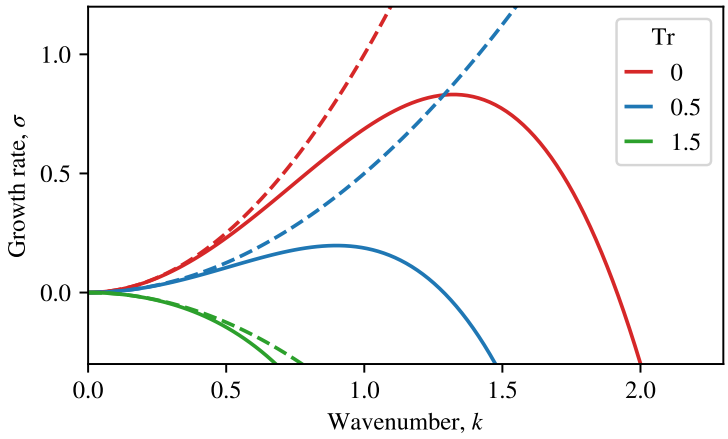

Figure 5.7 – Dispersion relation of the bedload instability, in a confined flow. Dashed lines: shallow-water approximation (equation (5.17)). Solid lines: two-dimensional Stokes flow (equation (5.32)).

and the bed. We thus replace equation (5.6) by

$$\theta = \frac{\rho D S}{2(\rho_s - \rho) d_s} \left(1 - \frac{h}{D}\right) . \tag{5.30}$$

Apart from the factor of two in the above expression, the lid does not affect our system, at least according to the shallow-water approximation. This factor of two does not even propagate beyond equation (5.3) where, by virtue of the normalisation by n_0 and θ_0, it retreats into the definition of the base state. We are thus left with equation (5.17) again, that is, the same dispersion relation as in section 5.4.

Based on the above reasoning, we expect the lid to affect the bedload instability only marginally, if at all. To check this formally, we now repeat the two-dimensional stability analysis of section 5.5, with a new boundary condition at the flow surface. Specifically, we replace the free-boundary condition with a no-slip one. At first order, we find the following velocity field:

$$u = 18 \frac{\theta_0 V_s D}{d_s} \left(\frac{z}{D} \left(1 - \frac{z}{D}\right) - \mathrm{Re}\left(\frac{\hat{h}}{\sinh k} \sinh\left(ik \frac{y + iz}{D} + k \right) \right) \right) , \tag{5.31}$$

which replaces equation (5.23). The dispersion relation associated with this expression reads

$$\sigma = k^2 (2 - \mathrm{Tr}) - \frac{k^3}{\tanh k} , \tag{5.32}$$

which, qualitatively, behaves like its open-channel counterpart, equation (5.26). Again, the bed is stable when the transport number is larger than one, and the dispersion relation shows a positive maximum otherwise. The most unstable mode grows faster as bedload

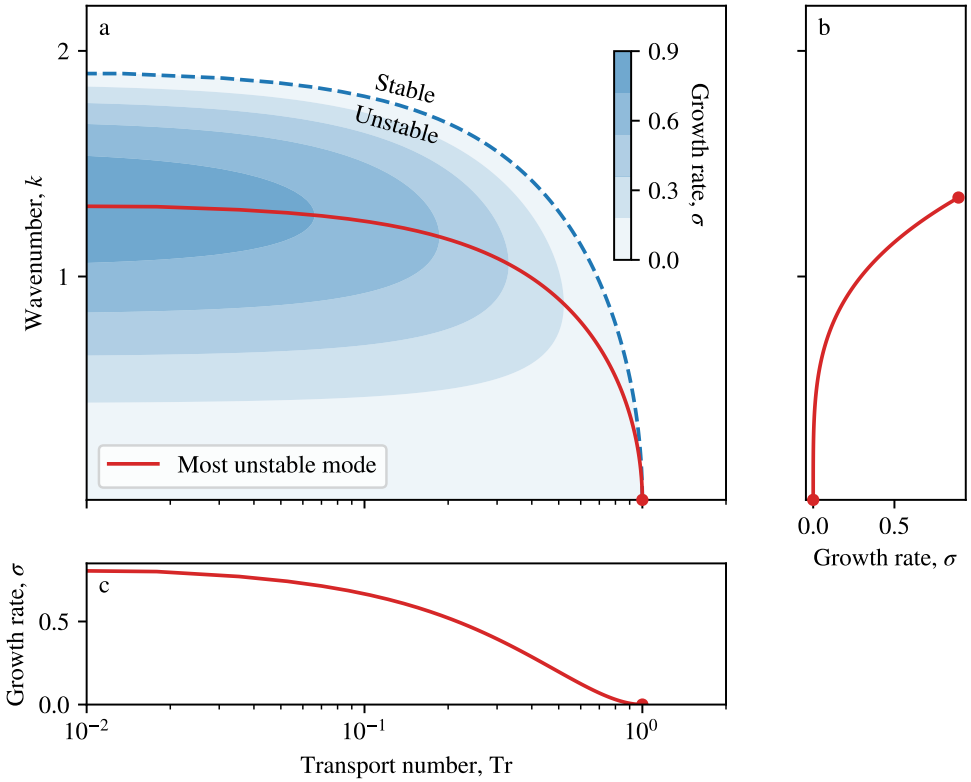

Figure 5.8 – Stability map of the bedload instability, for a confined flow. a: Dispersion relation. Darker areas correspond to faster growth rate. Red line: most unstable wave number for a given value of the transport number. b: Growth rate of the most unstable wavenumber. c: Maximum growth rate as a function of the transport number.

vanishes ($\mathrm{Tr} \to 0$), until the growth rate reaches is maximum ($\sigma_{\max} \approx 0.831$), for the mode of wavelength $\lambda_{\max}/D \approx 4.785$.

This result encourages us to look for the bedload instability in a closed channel, where their observation should be easier than in an open one—although, to our knowledge they have never been reported in any laboratory experiment.

5.6.2 Driving lid

In their experiment, Charru *et al.* (2004a) drove the flow along a circular channel with a rotating lid. The ring circumference was much larger that the channel's width; we now approximate this configuration with an infinitely long channel, covered with a rigid lid travelling downstream at velocity U. The shallow-water approximation then yields

$$\theta = \frac{\eta U}{D(\rho_s - \rho) g d_s} \left(1 + \frac{h}{D}\right) . \tag{5.33}$$

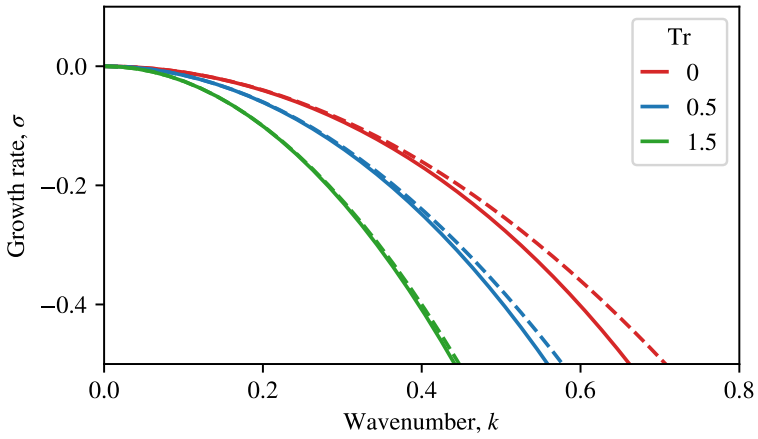

Figure 5.9 – Dispersion relation of the bedload instability, in a flow driven by a lid. Dashed lines: shallow-water approximation (equation (5.17)). Solid lines: two-dimensional Stokes flow (equation (5.32)).

Unlike equations (5.6) and (5.30), equation (5.33) indicates that the shear stress is stronger where the bed is closer to the moving lid, that is, at the crest of the perturbation. This is a dramatic change: bedload diffusion and gravity now conspire to wear away even a long-wavelength perturbation.

The two-dimensional velocity field now reads

$$u = 18\,\frac{\theta_0 V_s D}{d_s}\left(\frac{z}{D} - \mathrm{Re}\left(\frac{\hat{h}}{\sinh(k)}\sinh\left(ik\,\frac{y+iz}{D} + k\right)\right)\right), \tag{5.34}$$

and the associated Shields parameter becomes

$$\theta = \theta_0\left(1 + \left(\frac{k}{\tanh(k)}\right)\mathrm{Re}\left(\hat{h}\exp\left(\frac{iky}{D}\right)\right)\right), \tag{5.35}$$

thus confirming that, regardless of the wavenumber k, the shear stress is always stronger at the crest. As a consequence, driving the flow with a moving lid prevents the growth of the bedload instability. Experiments like that of Charru *et al.* (2004a) are therefore specially well-suited to produce wide and shallow flows with stable bedload transport.

5.7 Laboratory channels

Bedload experiments in laminar channels or pipes are not uncommon (Charru *et al.* 2004a, Ouriemi *et al.* 2007, Lobkovsky *et al.* 2008, Seizilles *et al.* 2014), and yet streamwise bed streaks were never reported in laminar flows, at least to our knowledge. We now use the linear stability analysis of the present paper to evaluate how susceptible to the instability were these experiments.

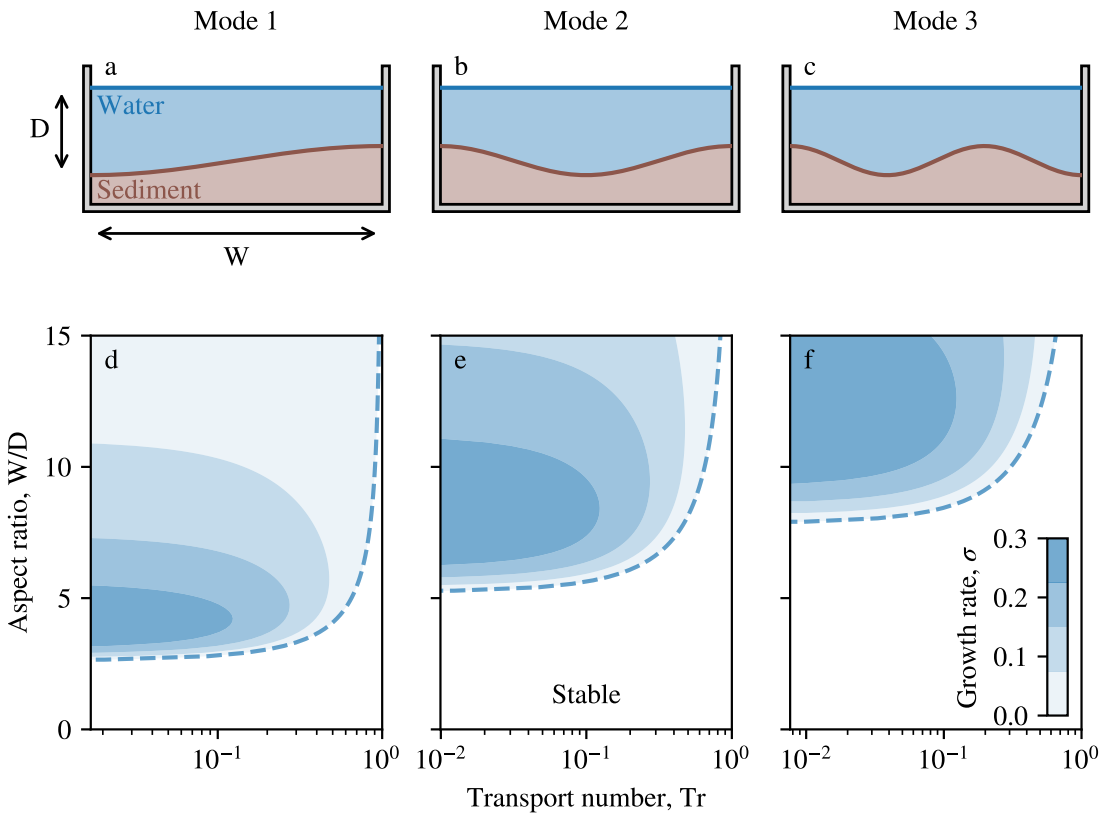

Figure 5.10 – First three modes of the bedload instability in a finite-width channel. a,b,c: Bed perturbation. d,e,f: Dispersion relation for individual modes. Blue scale indicates growth rate.

We first disqualify the experiment of Charru *et al.* (2004a), the driving lid of which precludes the instability (section 5.6.2). Next, we need to consider the side walls that confine the flow in an actual channel. In principle, we should treat them as no-slip boundaries, and account for them even in the base state. This, however, will produce a base state that varies in the cross-stream direction, thus complicating tremendously the analysis.

Instead, we will content ourselves with a less ambitious analysis which, we hope, will yield an order-of-magnitude interpretation of laboratory experiments. Accordingly, we replace the side walls with free-sleep boundaries for the fluid, and impervious boundaries for the sediment. Both conditions preserve the homogeneity of the base state, to the cost of mathematical rigour.

An expected consequence of the side walls is to select acceptable modes (figure 5.10). For the perturbation to fulfil the boundary conditions at the side walls, its wavenumber needs to belong to a discrete set of values:

$$k = n\pi \frac{D}{W} \tag{5.36}$$

where n is an integer, and W is the width of the channel. Substituting this expression into the dispersion relation for an open channel, equation (5.26), we find that no instability can grow in a too narrow channel. As the transport number vanishes, the first mode ($n = 1$) is unstable only when $W/D \gtrsim 2.26$ (figure 5.10a). The higher the mode, the wider the channel needs to be to accommodate its growth.

Considering all acceptable modes in a given experiment, we can identify the fastest growing one, and treat it as the dominant mode (figure 5.11). In the parameter space made up by the transport number and the aspect ratio, the unstable domain is tiled with individual modes. When the transport number is below one, the order of the most unstable mode increases with the aspect ratio of the channel. Overall, the unstable domain is bounded by the same curve as the first mode.

We now wish to place the laboratory experiments of Ouriemi *et al.* (2007), of Lobkovsky *et al.* (2008) and of Seizilles *et al.* (2014) on the stability diagrams of figure 5.11. Unfortunately, we can only do this approximately since, for instance, Ouriemi *et al.* (2007) used a round pipe, and let the sediment discharge decreases slowly until the bed reached the threshold for bedload transport (table 5.1). The transport number in their experiment thus ranges from zero to a finite value. Lobkovsky *et al.* (2008) also let the sediment discharge decrease, although in a rectangular, closed channel. Finally, Seizilles *et al.* (2014) used an open channel, and fed it with a constant input of sediment, thus approaching more closely the theory presented here.

Table 5.1 summarises our estimates for the parameters of these experiments—many of them are uncertain. In addition, the parameter γ, which accounts for the gravity-induced

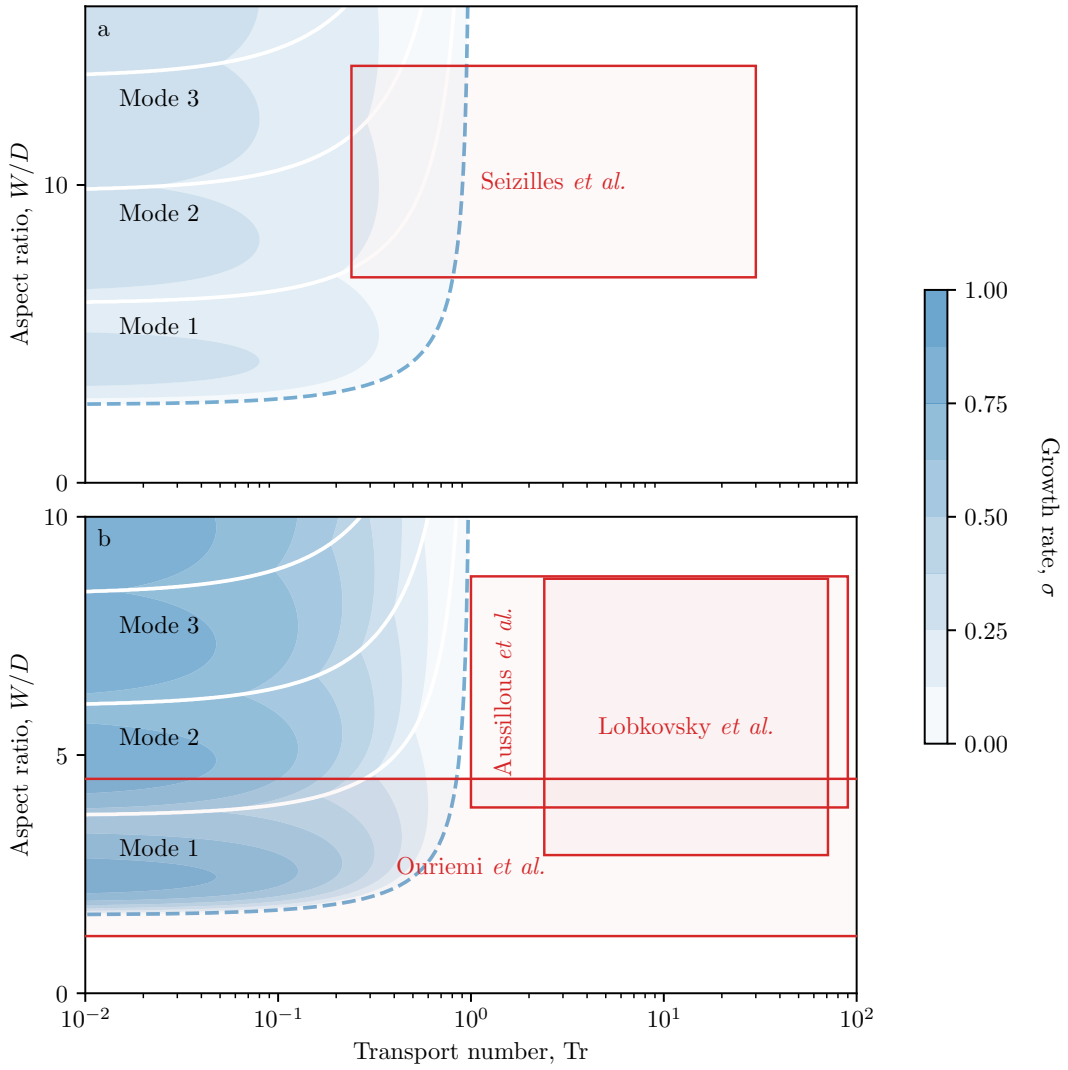

Figure 5.11 – Stability map for the bedload instability in a finite-width channel. Blue scale indicates growth rate of the fastest-growing mode. Red boxes show the range of laboratory experiments. a: open channel. b: fixed lid

	Ouriemi *et al.* (2007)	Lobkovsky *et al.* (2008)	Aussillous *et al.* (2013)	Seizilles *et al.* (2014)
Channel	Circular pipe	Rectangular channel Fixed lid	Rectangular channel Fixed lid	Rectangular channel Free surface
Steady state	No	No	No	Yes
Run duration (min)	1 – 15	10	5	60 – 120
Flow depth, D (cm)	0.5 – 2.5	0.3 – 0.9	0.4 – 0.9	0.13 – 0.31
Flow width, W (cm)	2.2 – 3	2.6	3.5	3
Reynolds number	$10^{-1} - 10^{4}$	0.3	0.2 – 1.2	500 – 1400
Grain size, d_s (μm)	130 – 540	700	1100, 2040	344
Shields number, θ	0.12 – ?	0.35 – 0.8	0.2 – 1	0.13 – 0.21
Threshold Shields, θ_t	0.12	0.3	≈ 0.18	0.12
Transport number, Tr	0 – ?	2.4 – 71	0.7 – 83	0.24 – 30

Table 5.1 – Estimated parameter values for laminar bedload-transport experiments.

flux of sediment, has never been measured in a laminar flow (section 5.4.3). For lack of a better estimate, we use the range $0.1 - 1$, based on the wind-tunnel measurements of Yamasaka *et al.* (1987). The last parameter we need is the diffusion length ℓ_d, which was measured once by Seizilles *et al.* (2014). Based on their observations, we choose $\ell_d \sim 0.03\, d_s$.

Remembering that the roughness of the above estimates matches that of our simplified boundary conditions, we may now map the explored regions of the parameter space (figure 5.11). For the most part, they lie in the stable domain, although the experiments by Ouriemi *et al.* (2007) and Seizilles *et al.* (2014) marginally overlap the stable domain on the first mode. This overlap is precarious, since we neglect the influence of side walls on a viscous flow, in a channel whose aspect ratio is less than five.

Preliminary though it may be, figure 5.11 suggests that laboratory channels are usually too narrow for the bedload instability to flourish.

5.8 Conclusion

The linear stability analysis we have presented in this paper identifies a new instability associated to bedload transport, caused by the cross-stream diffusion of the travelling grains. This instability produces bed streaks aligned with the flow, in the absence of any secondary currents. Because it can only grow near the threshold of sediment transport, the unstable perturbation quickly enters a non-linear regime which we have not investigated. The bedload instability is sensitive to boundary conditions; it persists in a rectangular pipe, but disappears when the flow is driven by a travelling lid.

Despite the simplicity of its driving mechanism, we could not find any report of this instability appearing in a laboratory experiment. This, of course, raises the question of its actual existence, but we suspect that the basic reason of its absence from the literature is that the aspect ratio of laboratory channels is usually too small to accommodate its growth. We speculate that this might not be fortuitous, as experimenters often wish the sediment bed to be invariant in the cross-stream direction.

At this point, we can only imagine an ideal setup, specially designed to observe the bedload instability. In the light of the present paper, it would involve a transparent rectangular pipe, with an aspect ratio of a few tens. The sediment and fluid discharges would be kept constant until the streaks, visualised with a laser beam, emerge. In such an experiment, the measurement of the critical transport number would yield an estimate of the parameter γ, which encapsulates the influence of gravity on cross-stream bedload transport.

Cross-stream fluxes of sediment shape the channel of alluvial rivers and, most probably, select their size (Ikeda *et al.* 1998). A reliable theory of bedload diffusion, tested against laboratory experiments, would therefore help us understand their morphology. Once such

framework is set, it will become a matter of numerical routines to explore it beyond linearity. A natural question to ask, then, will be whether the bedload instability grows as far as to split a broad channel into smaller ones, thus generating the precursor of a braided river (Stebbings 1963, Métivier *et al.* 2017).

5.9 Forme d'équilibre d'une rivière

Cette étude souligne les limites de l'approximation d'eau peu profonde (*shallow water*), qui est insuffisante pour décrire correctement l'instabilité aux courtes longueurs d'onde. De ce fait, nous pensons qu'elle est également insuffisante pour prédire la forme d'équilibre d'une rivière active, ce que nous avions déjà soupçonné dans le chapitre 4. Il faudrait donc prendre en compte la diffusion transverse de quantité de mouvement dans l'écoulement et résoudre l'équation de Stokes à deux dimensions. Cependant, ce problème est difficile, car nous ne connaissons pas a priori la forme de la rivière, et donc la limite du domaine de résolution de l'équation. Cette limite fait partie de la solution du couplage entre le lit érodable et l'écoulement. Malgré tout, nous pouvons utiliser la théorie linéarisée de l'article ci-dessus pour approcher l'écoulement de Stokes à deux dimensions.

Dans la section 5.7, nous étudions l'influence d'une largeur finie sur la sélection de longueur d'ondes des stries (Fig. 5.10). Nous mettons en évidence l'existence de modes discrets susceptibles de se développer ou non selon le rapport d'aspect du chenal, défini comme le rapport entre sa largeur et sa profondeur. En particulier, le premier mode correspond à un rapport d'aspect d'une demi longueur d'onde. Si l'on imagine que notre rivière à l'équilibre présente un profil convexe, ce mode serait le plus approprié pour la représenter (Fig. 5.12a).

Ce mode présente un domaine stable, où la moindre perturbation appliquée sur le lit décroît, et un domaine instable, pour lequel une perturbation du lit s'amplifie (Fig. 5.10). La limite entre ces deux domaines correspond à une ligne de stabilité marginale, où une perturbation ne s'amplifie ni ne diminue. Cette ligne pourrait ainsi correspondre à des formes stationnaires du lit, où le flux transverse de grains s'annule sur le profil entier ($q_y = 0$). Cette solution linéarisée est très approximative: une meilleure description devrait tenir compte des berges, où la profondeur s'annule, qui est donc inaccessible par une théorie linéarisée. Nous l'utilisons ici à titre d'illustration.

Cette limite de stabilité dépend du nombre de transport, que l'on peut relier au débit de sédiments par :

$$\mathrm{Tr} = \frac{D}{W}\frac{Q_s}{Q_s^*}\,, \tag{5.37}$$

où Q_s^* est le débit de sédiments caractéristique introduit dans la section 4.2. Nous retraçons donc la limite de stabilité de ce mode sur la figure 5.12b. Nous obtenons l'évolution du rapport d'aspect correspondant à une forme de lit stationnaire en fonction du débit de

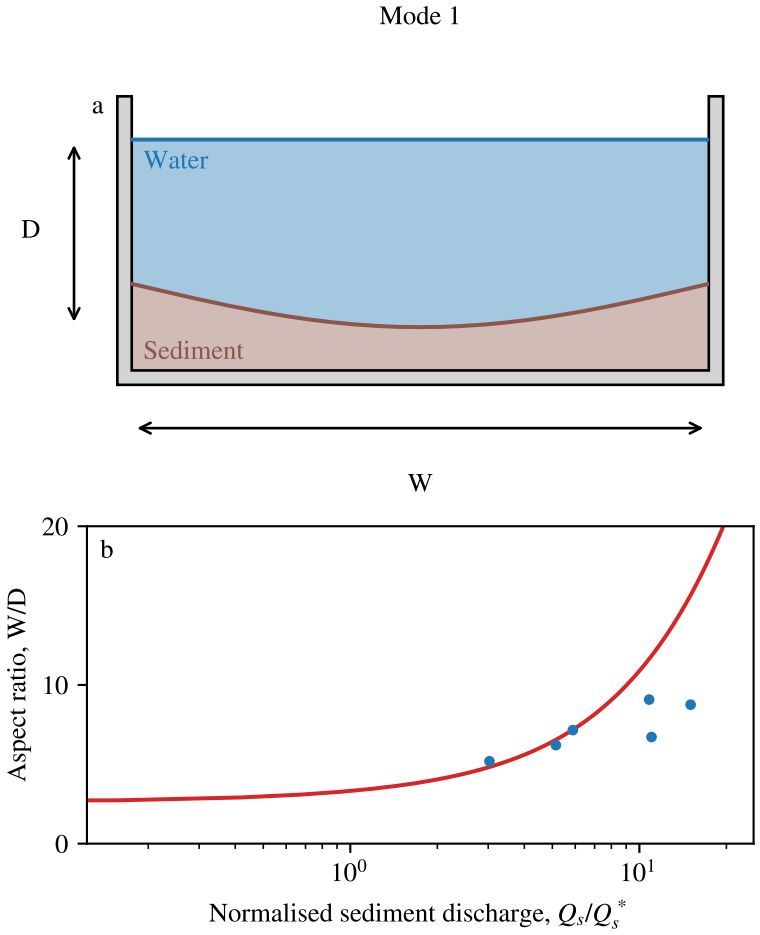

Figure 5.12 – Illustration of the equilibrium shape of a river with a two-dimensional flow. a. Mode 1 of the instability (shifted). b. Aspect ratio of laboratory rivers as a function of dimensionless sediment discharge. Blue points: laboratory rivers (Tab. 3.1). The red line corresponds to the stability domain limit for the first mode.

sédiments. Lorsque le débit de sédiments augmente, la largeur autorisant une perturbation neutre augmente. Elle croît ensuite de manière significative pour des valeurs de Q_s égales à une dizaine de fois Q_s^*.

Nous plaçons maintenant les rapports d'aspect des rivières de laboratoire obtenues chapitre 3 (Fig. 5.12): l'ordre de grandeur est bien comparable. Bien sûr, ces résultats restent préliminaires car l'équation de Stokes a été ici linéarisée.

Malgré tout, cela indique qu'en remplaçant l'approximation d'eau peu profonde par l'équation de Stokes dans la théorie du chapitre 4, nous pourrions constituer une théorie plus réaliste de l'équilibre d'une rivière alluviale. Une telle théorie réunirait les deux mécanismes diffusifs initialement proposés par Parker (section 1.2): la diffusion des sédiments, et la diffusion de la quantité de mouvement.

Conclusion

An alluvial river selects its own shape through the coupling between flow and sediment transport. Accordingly, it adjusts its width and slope to its water and sediment discharges. In this manuscript, we used simplified experiments to investigate this coupling in the laboratory.

We first investigated this coupling in an idealised geometry: that of a sediment bed confined in a laboratory flume and sheared by a viscous flow. We found that the sediment bed selects its shape and its sediment-flux profile to reach equilibrium. By tracking travelling grains on the bed, we identified two mechanisms involved in this equilibrium. First, grains are pulled towards the center by gravity. Second, they collide with the rough bed and thus behave as random walkers. As they are more numerous in the channel center, they diffuse towards the banks, which are the less populated areas. The balance between these two fluxes governs the bed's equilibrium. The signature of this equilibrium is the exponential decay of the sediment flux with the bed elevation. This relation is analogous to the Boltzmann distribution that governs the density of Brownian particles suspended in a liquid. Although this statistical equilibrium applies to a wide range of systems, it had never been observed in the context of sediment transport.

We then produced laboratory rivers which transport sediment. For a moderate sediment input, they form a single-thread channel at equilibrium. We showed that these channels adjust their cross section and their downstream slope to satisfy the Boltzmann distribution, like in the confining flume. Their shape depends on their fluid and sediment discharges. Specifically, at a fixed fluid discharge, they widen and flatten with the sediment discharge. The Boltzmann distribution alone, however, does not predict the equilibrium shape of these rivers.

To understand how a river adjusts its shape to the sediment discharge, we modelled the flow with the shallow-water approximation. This simple model predicts that rivers remain slightly above the threshold of grains entrainment. We checked this prediction in our laboratory rivers by plotting their trajectories in the phase plane. We found that, regardless of their sediment discharge, they all gather around the circle that corresponds to the threshold channel. Phillips & Jerolmack (2016) showed that the flow-induced shear stress on the bed of a natural river is seldom more than 10% above the critical value,

suggesting that natural rivers also self-organise to maintain their bed near the threshold.

However, two rivers may exert a comparable shear stress on their bed, while adopting significantly distinct cross sections. Indeed, according to our shallow-water model, all trajectories lie in a narrow domain of the phase plane, such that they are very close to each other. Inside this domain, however, a river's profile varies from the cosine shape to an infinitely-wide, flat river. It means that the river's shape is extremely sensitive to shear stress variations. In the range of sediment discharges we explored, the aspect ratio of our laboratory rivers doubles, while the shear stress varies by less than 20%.

When the aspect ratio of our laboratory rivers reaches about ten, the channel destabilizes into a braid. This observation prompted us to investigate theoretically the stability of a sediment bed sheared by a viscous flow. In doing so, we identified a new instability, caused by bedload diffusion. This instability generates streamwise streaks, provided sediment transport is weak enough. If the streaks grow enough to reach the flow surface, this instability would split a wide channel into smaller ones. We suggest that it is a similar instability that turns our single-thread rivers into braids. This instability, however, has not been observed in the laboratory yet.

Perspectives

Bedload instability in the laboratory

The bedload instability presented in chapter 5 suggests that a flat sediment bed sheared by a viscous flow is unstable, provided the sediment flux is weak. This instability should produce streaks aligned with the flow, but this pattern has never been observed in the laboratory (section 5.7). Here, we briefly expose how a laboratory setup could produce these streaks.

The ideal setup would consist of a transparent rectangular pipe, with an aspect ratio of a few tens, half filled with sediment grains. Using a pipe, rather than a an open channel, rids us of other bedforms, such as chevrons or bars, and should boost the growth of the streaks (Fig. 5.11b). At the inlet, we would inject a viscous fluid, such as a mixture of glycerol and water, at a constant discharge. Meanwhile, we would inject sediment at a constant discharge using the sediment feeder of our flume experiment (section 2.2). The difficulty, however, would be to produce an homogeneous base state.

To do so, we would initially impose a high sediment discharge, to bring the transport number above one. According to our theory, the bed should then be stable. Over time, this procedure should produce an homogeneous base state. We would then decrease suddenly the fluid discharge, which would lessen the sediment flux almost immediately. This process would bring the transport number below one, so that the system should cross the instability threshold. Hopefully, streaks should then appear, at the wavelength predicted by the theory (Fig. 5.11b).

Apart from supporting our theory -or proving it wrong-, observing these streaks could also provides us with an independent measurement of the Boltzmann length we have introduced in this manuscript, λ. Indeed, the threshold of the instability is set by the transport number, which is inversely proportional to λ. In addition, it would inform us about the non-linear evolution of these instability, and thus about the ability of the streaks to reach the flow surface, and to produce a braid.

Beyond the shallow-water approximation

The bedload instability underlines the limitations of the shallow-water approximation (Ch. 5). These limitations are probably responsible for the failure of our shallow-water theory to predict the equilibrium shape of a river (Ch. 4). To improve this theory, we are now convinced that we need to account for the diffusion of momentum across the stream. We should then replace the shallow-water approximation with the Stokes equation in two dimensions. Here, we explain how we would address this problem numerically.

We would first define an initial cross section, to which we assign a fixed slope. With finite elements, we would then solve the Stokes equation in this domain (for instance, using FreeFem). As this is not an equilibrium shape yet, the cross-stream flux of sediment should be finite. We would then evolve the bed based on the sediment mass balance. Considering that the river is invariant in the streamwise direction, the mass balance keeps the cross section area constant. Re-meshing this new cross section would enable us to compute the new flow, and to repeat the same procedure. After a few iterations, the river should converge to its equilibrium profile.

As a first attempt, we would run this numerical simulation for a flume, where our measurements are more accurate than in our laboratory rivers. We suspect, however, that the re-meshing procedure might generate instabilities. In addition, the convergence of this numerical scheme is still uncertain.

Natural rivers

The results of this manuscript are based on laboratory experiments where the flow is laminar. Natural rivers, however, are turbulent. Still, we expect that bedload grains collide with the rough bed and diffuse across the flow in turbulent flows as well. Turbulence could affect the intensity of this diffusion, and thus the diffusion length, but the basic mechanism should hold. Therefore, we expect that the equilibrium between gravity and diffusion, and thus the Boltzmann distribution, should hold in natural rivers.

To test this scenario against field data, we need both the sediment flux and the bed elevation across a river. In most cases, however, only the total sediment discharge is measured in the field. To our knowledge, only Liu *et al.* (2008) measured both the cross section and the sediment-flux profile in a natural river: the Urumqi river, China (Fig. 5.13). Liu *et al.* (2008) measured the intensity of bedload 8 km downstream of the source, at an elevation of 3300 m, where gravels make up most of the stream's bed (the median grain size is d_{50} = 21.5 mm). They surveyed the river every day during two flow seasons (approximately 3 months) from June to August (2005 and 2006). To measure the bedload, they used a Helley Smith sampler of inlet 30×15 cm (Helley & Smith 1971).

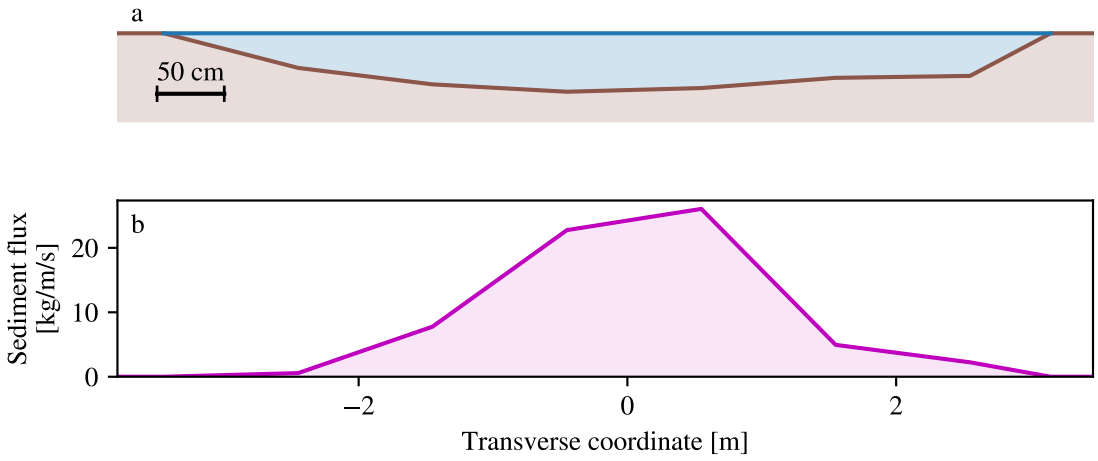

Figure 5.13 – Bed cross section and sediment flux of the Urumqi river (China). a. River cross section. Brown: sediment bed. Blue: water. b. Sediment-flux profile across the channel.

Using these data, we now test the Boltzmann distribution,

$$q_s = q_{\max}\, e^{-h/\lambda}\,, \tag{5.38}$$

by plotting the bed elevation h as a function of the sediment flux (Fig. 5.14). In the semi-log space, the data gather around the straight line of slope $1/\lambda$, where $\lambda = 0.046\,\mathrm{m}$. If we compare this value to the median grain size, we find:

$$\lambda = 2.1\; d_{50}\,. \tag{5.39}$$

This preliminary example suggests that bedload diffusion not only occurs in natural rivers, but also controls their shape. If it is so, this mechanism would also select the slope of a river. In turn, this slope controls the morphology of sedimentary structures, such as alluvial fans, that rivers sometimes build by depositing sediment at the outlet of mountain ranges. During their formation, these fans gradually accumulate the sediment deposition in stratigraphic layers, recording the history of climate changes. By measuring the slopes of the layers that make up the fan, we could in principle estimate the paleo-fluxes of water and sediment (Delorme *et al.* 2018). With our shallow-water model, we had a limited success to predict this relation. An improved theory, however, would allow us to establish a physically-based relation between the slope of an alluvial fan, and the discharges of the river that built it.

Finally, the measurements of Liu *et al.* (2008) should encourage us to collect sediment-flux profiles across alluvial rivers, instead of the total sediment discharge. We could then evaluate how the Boltzmann length varies with the grain size and how a broad distribution

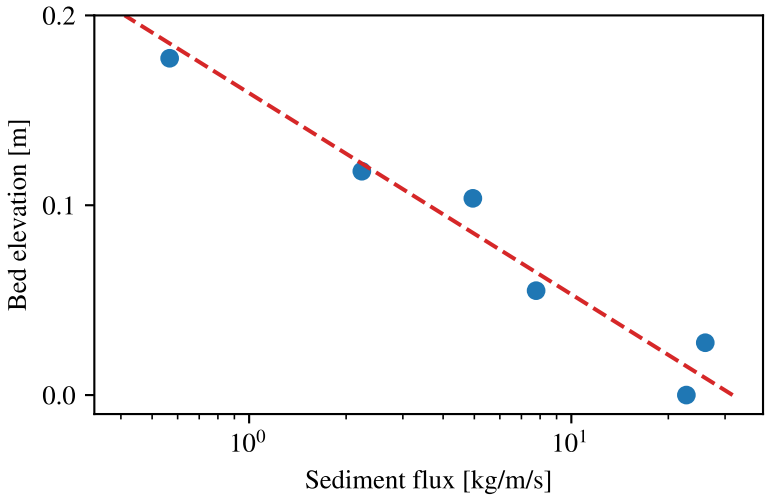

Figure 5.14 – Boltzmann distribution in the Urumqi river. Bed elevation as a function of the logarithm of the sediment flux. Red dashed line: linear fit.

of grain sizes affects it.

Appendices

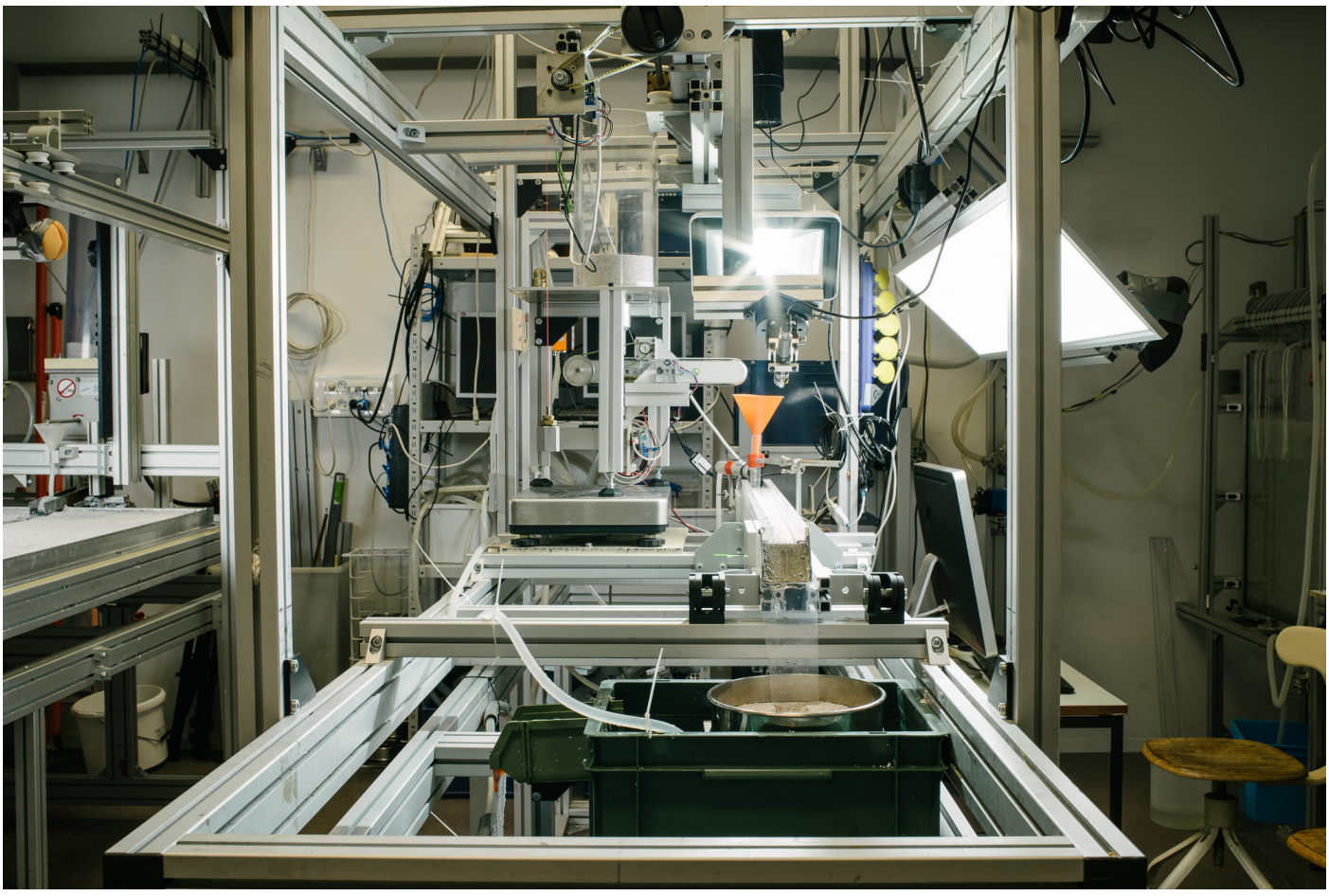

Appendix A

Experimental methods

A.1 Grain size

In the experiments of sections 2.2 and 3.2, we use the same plastic grains. They are sold by the company Guyson and made of a urea-based thermoset resin. According to the manufacturer, their density is 1520 kg/m^3. Using a pycnometer, we found $\rho_s = 1488\,\mathrm{kg/m^3}$.

To produce these grains, the manufacturer crushes the initial material. This process yields angular, irregular grains, which are then sieved. The manufacture provides an approximate granulometry (mean diameter in [650, 800] μm). To measure the gain size accurately, we take a top-view picture of grains spread over a black surface. Using a threshold on the image intensity, we measure their areas (Fig. A.1a). Then, we divide the square root of this area by $\pi/4$, which provides us with an estimation of the grain diameters. We obtain the cumulative distribution of grain diameters of figure (A.1b) and then the distribution of grain diameter by deriving the latter. We define the grain diameter d_s as the mean diameter and therefore

$$d_s = 827 \pm 86\,\mu\mathrm{m}\,. \tag{A.1}$$

We can also deduce the median diameter d_{50} and the diameter d_{90}, for which 90% of the sample has a smaller size: $d_{50} = 0.8\,\mathrm{mm}$, $d_{90} = 1\,\mathrm{mm}$.

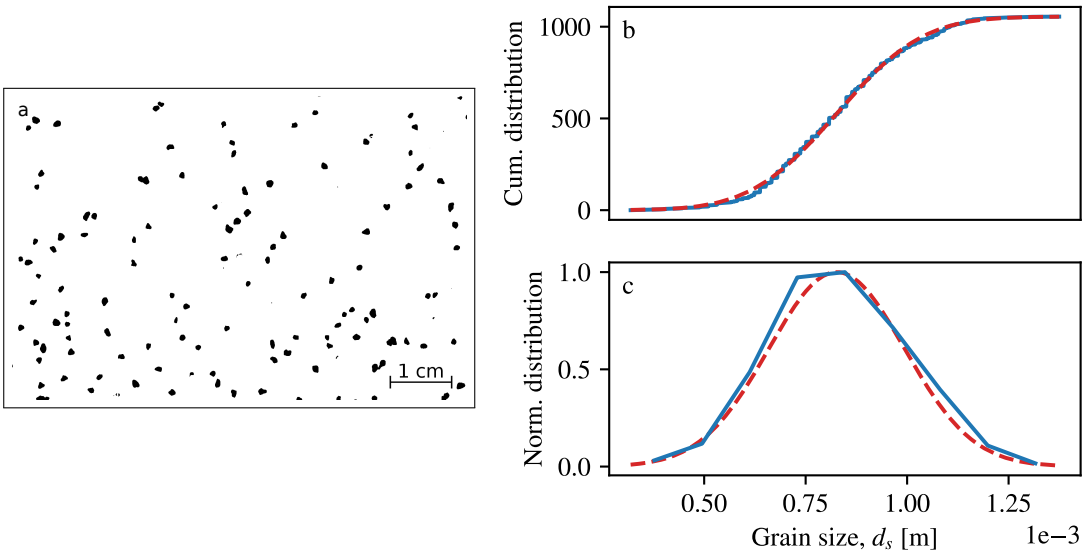

Figure A.1 – Grain size measurement. a. Top view picture of grains. We enhance the contrast, apply a threshold on the image intensity and then measure the area of each grain by computing the number of pixels of each cluster. b. Cumulative grain size distribution. c. Grain size distribution.

A.2 Friction coefficient

The static friction coefficient μ_t of a granular material is usually measured from the angle of repose of a conical heap (Jaeger & Nagel 1992). However, in our case, the interstitial fluid may influence the packing stability of the heap. Therefore, we measure the angle of repose of an immersed heap.

To do so, we use an independent experimental setup, consisting in a tank filled with a mixture of water and glycerol (Fig. A.2). We slowly pour grains into the tank, using the sediment feeder described in section 2.2. It delivers 1 g/min at a constant rate (motor delay = 100). As grains accumulate onto the bottom of the tank, they gradually form a conical heap, which is entirely immersed. This pile grows with time (Fig. A.2). We take pictures of the heap at regular time intervals (30 seconds) and we detect the heap's edges using image analysis. Fitting the latter by two straight lines, we deduce the slope of the heap as a function of time (Fig. A.3). This slope evolves through a succession of avalanches. Courrech Du Pont *et al.* (2003) described exhaustively this phenomenon, in a rotating drum filled with grains immersed in a fluid.

Here, we content ourself with the mean value of the heap's slope, which provides us with a friction coefficient of

$$\mu_t = 0.8 \pm 0.1\,. \tag{A.2}$$

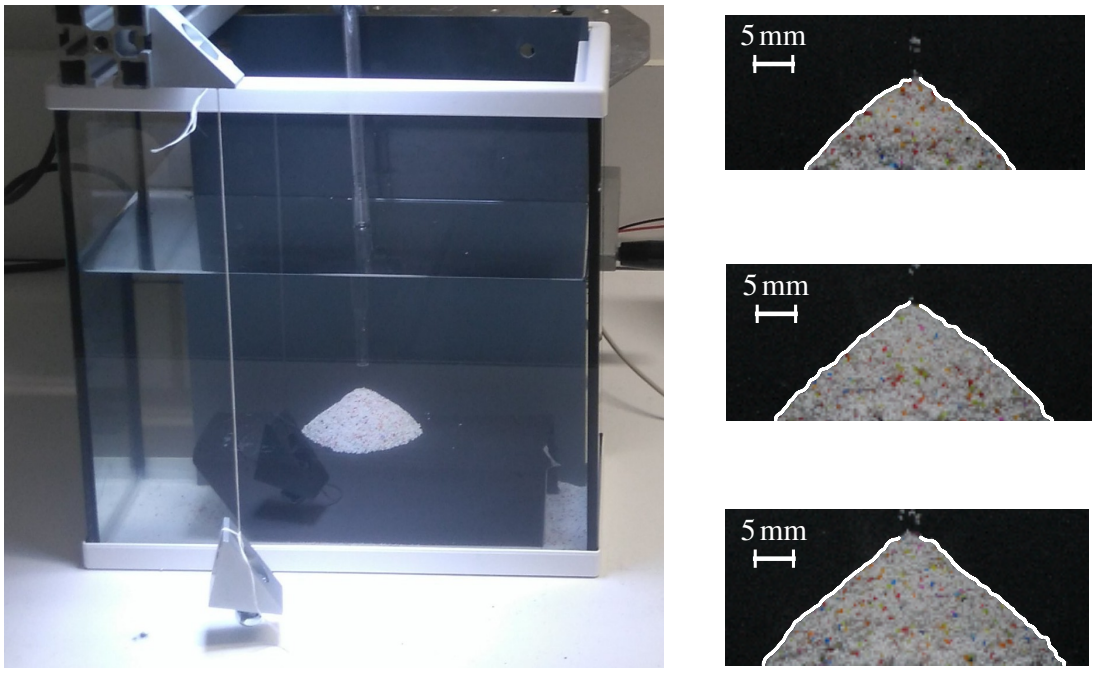

Figure A.2 – Experimental setup. Evolution of the pile of grains immersed in the mixture of water and glycerol. Top to bottom : time = 25 min, 50 min, 1 h 15 min. The edge, detected using image analysis, is plotted in white.

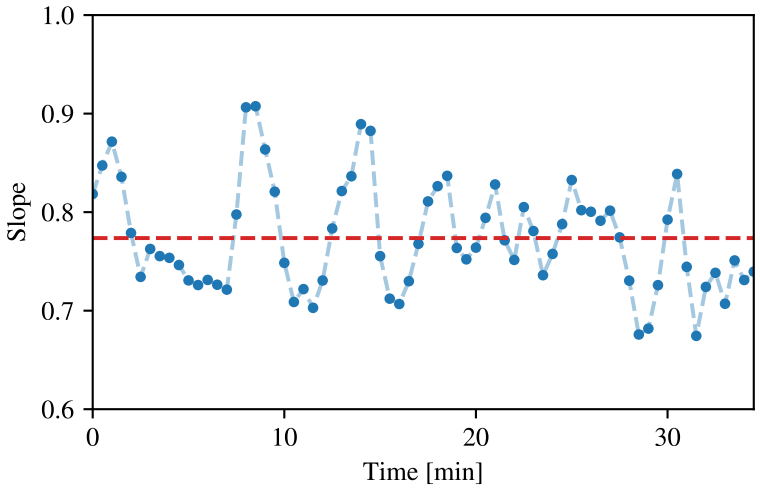

Figure A.3 – Angle of repose of an immersed pile of grains with time. Red dashed line: slope average.

This method yields an estimate of the friction coefficient. It does not take into account the packing rearrangement of the heap over long times. Our laboratory rivers, however, flow during tens of hours, and their bed has time to rearrange. We expect then a larger angle of repose when the packing is denser, although we were not able to check it.

In section 4.5, we suggested another method to evaluate the friction coefficient of our immersed grains, based on the cross section of a laboratory river. For run 3 (Tab. 3.1), we found $\mu_t = 0.85 \pm 0.05$. This value is compatible with the heap method.

A.3 Mixture of glycerol and water

The viscous fluid used in our experiments (sections 2.2 and 3.2) is a mixture of water and glycerol, the density and the viscosity of which increase with the proportion of glycerol (Fig. A.4a). Working with the same fluid, Delorme (2017) observed variations of the density over time, due to the evaporation of water (Fig., p. 120). As explained in section 2.2, we regularly measured the density of the fluid during an experimental run, and compensated for evaporation by adding water to the mixture.

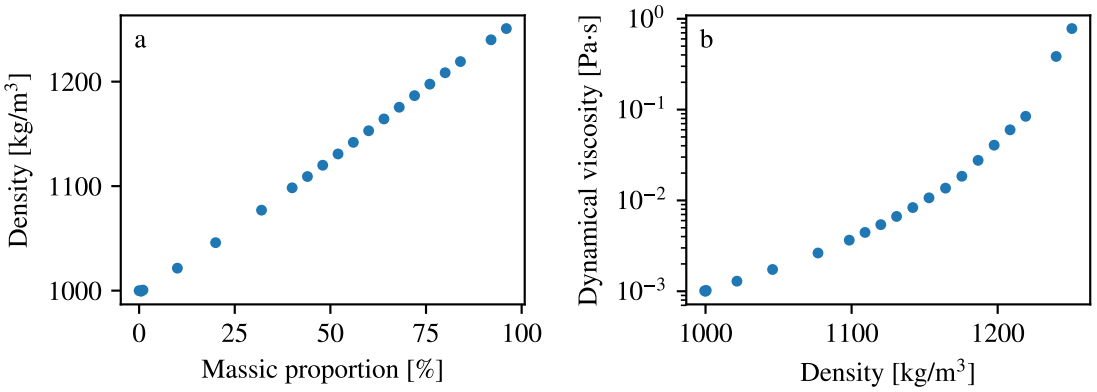

Figure A.4 – Characteristics of the mixture of glycerol and water a. Density of the mixture as a function of the glycerol proportion. b. Viscosity of the mixture as a function of its density. From Shankar & Kumar (1994).

A.4 Tracking of particles

We provide here the library we used to track our colored grains in sections 2.2 and 3.2.

```
from pylab import *
from munkres import Munkres, print_matrix
from numpy.random import rand
from scipy.cluster.vq import kmeans,vq
from scipy import ndimage
from skimage.feature import peak_local_max
import cv2
import json
import matplotlib.colors as colors

#################### PARTICLES DETECTION ###################

'''
RGB return the hue of an RGB image
'''
def RGB_2_HSV( frame, color_angle ):
    hsv_image = colors.rgb_to_hsv( frame )
    hue, sat, value = map( transpose, tuple( hsv_image.T ) )
    hue = angle( exp( 1j*( 2*pi*hue + color_angle*pi/180. ) ) )*180./pi
    return hue, sat, value

'''
Compute the coordinates of the particles detected on a RGB image.
'''
def particles_coordinates( frame, parameters ) :

    hue_range = parameters[ "detected hue range"]
    sat_min = parameters[ "minimum saturation"]
    filter_size = parameters["filter size (p)"]
    min_distance = parameters["minimum distance (p)"]
    threshold_abs = parameters["absolute threshold"]
    color_angle = parameters["color angle (deg.)"]

    hue, sat, value = RGB_2_HSV( frame, color_angle )

    detection = ( hue > hue_range[0] )*( hue < hue_range[1] )*( sat > sat_min )
    *1.
    detection = ndimage.gaussian_filter( detection, filter_size )
    detection = detection/detection.mean()
    coordinates =  fliplr( peak_local_max( detection, min_distance = min_distance
    , threshold_abs =  threshold_abs ) )

    return coordinates


################### TRAJECTORIES ###################
```

```
46 class Trajectory :
       '''2D trajectory, with a starting time.'''

       def __init__( self, birth_time = None, X = None, mummy = None ) :

51         try :
               self.birth_time = birth_time
               self.x = [ X[0] ]
               self.y = [ X[1] ]
               self.end_time = birth_time + len(self.x)
56
           except :
               self.birth_time = mummy[0]
               self.x = mummy[1]
               self.y = mummy[2]
61
       def addPoint( self, X ) :
           self.x += [ X[0] ]
           self.y += [ X[1] ]
           self.end_time += 1
66
       def getEnd( self ) :
           return [ self.x[-1], self.y[-1] ]

       def mummify( self ):
71
           ''' Converts to Python dictionnary '''

           return [
               self.birth_time,
76             self.x,
               self.y
               ]

   def load_trajectories( traj_file, max_number_of_trajectories = inf, theta = None
       ) :
81
       trajectories = []

       for line in traj_file :

86         if len( trajectories ) >= max_number_of_trajectories :
               break

           try :

91             trajectory = Trajectory( mummy = json.loads( line ) )

               if theta != None : # redressement
                   y = array(trajectory.y); x = array(trajectory.x)
                   trajectory.x = list( cos(theta)*x + sin(theta)*y )
96                 trajectory.y = list( sin(theta)*x - cos(theta)*y )
```

```
                trajectories += [ trajectory ]

            except :
                pass

        return trajectories


def load_trajectories_metadata( traj_file, metadata_line = 1 ):

        return json.loads( traj_file.readlines()[ metadata_line ] )

#################### BUNCH (i.e. bunch of trajectories) ###################

class Bunch :
    '''Collection of 2D trajectories, from class Trajectory.'''

    def __init__( self, live_trajectories, dead_trajectories ) :
        self.live_trajectories = live_trajectories
        self.dead_trajectories = dead_trajectories

    def getAllTrajectories( self ) :
        return self.live_trajectories + self.dead_trajectories

    def addTrajectory( self, trajectories ) :

        if type(trajectories) == list :
            self.live_trajectories += trajectories

        elif isinstance(trajectories, Trajectory) :
            self.live_trajectories += [ trajectories ]

        else :
            print 'This is not a trajectory or a list of trajectories.'

    def getEnds( self ) :

        end_points = []

        for trajectory in self.live_trajectories :
            end_points += [ [ trajectory.x[-1], trajectory.y[-1] ] ]

        return end_points

    def kill( self, kill_list ) :

        killed_trajectories = []
        surviving_trajectories = []

        for n in range( len(self.live_trajectories) ) :
            if n in kill_list :
```

```
                killed_trajectories += [self.live_trajectories[n]]
            else :
                surviving_trajectories += [self.live_trajectories[n]]

        self.live_trajectories = surviving_trajectories
        self.dead_trajectories += killed_trajectories

    def undertake( self ) :
        self.dead_trajectories = []

    '''save trajectories in a text file
       a user defined filetr traj_filter may be used to filter trajectories
       before saving them.
    '''
    def bury( self, traj_file, traj_filter = lambda trajectory: True ) :

        for traj in self.dead_trajectories :

            if traj_filter( traj ):
                json.dump( traj.mummify(), traj_file, separators = ( ',', ':' ) )
                traj_file.write('\n')

    def killAllTrajectories( self ) :
        self.dead_trajectories += self.live_trajectories
        self.live_trajectories = []

    def grow( self, tracks, new_points ) :

        for track in tracks :
            self.live_trajectories[ track[0] ].addPoint( new_points[ track[1] ] )

    def getTrajectoriesTime( self, t ) :

        x = []
        y = []

        for trajectory in self.getAllTrajectories() :
            if trajectory.birth_time < t < trajectory.end_time :
                x += [ nan ] + trajectory.x[:(t-trajectory.birth_time)]
                y += [ nan ] + trajectory.y[:(t-trajectory.birth_time)]

        return x,y
```

Appendix B

Numerical approximation of the shallow-water river

Dans la section 4.2, nous étudions une équation différentielle du premier ordre qui régit la profondeur de la section d'une rivière. Cette équation est non linéaire, et nous ne connaissons pas de solution analytique générale. Nous procédons donc à une résolution numérique que nous détaillons dans la section 4.3. Dans cette annexe, nous calculons l'erreur numérique de la méthode expliquée dans paragraphe 4.3.1. Ensuite, nous développons une seconde méthode numérique, plus précise, pour générer les abaques du paragraphe 4.6.1.

B.1 Numerical error

According to section 4.4, the parameter ξ, defined as,

$$\xi = \chi \; e^{-\chi/\epsilon_s} \,, \tag{B.1}$$

should be constant along the profile of a river (right-hand side of equation (4.15)). In this section, we check how accurately our numerical method fulfils this evolution.

To do so, we compute a river cross section for $(\epsilon_s, \chi) = (0.5, 0.25)$, which corresponds to $\xi = 0.1516$ (equation (B.1)). We obtain both the depth of the river D and its cross-stream slope D'. Then, we calculate the value of ξ_{num} with (left-hand side of equation (4.15)):

$$\xi_{\text{num}}(y) = (\sqrt{D^2(y) + D'^2(y)} - \mu_t) \; e^{-D(y)/\epsilon_s} \tag{B.2}$$

for the whole profile. Accordingly, we define the relative numerical error as,

$$\text{err}(y) = \frac{|\xi_{\text{num}}(y) - \xi|}{\xi} \tag{B.3}$$

Figure B.1a shows its value along a river profile. The error is slightly higher on the banks, and its mean value is $3.4 \cdot 10^{-16}$, which corresponds to the floating point precision in Python.

Now, we evaluate the integral of this error along the profile as a function of the ratio χ/ϵ_s, which varies between 0 and 1. First, we fix $\chi = 0.1$ (which is equivalent to fixing a maximum river depth), and we calculate all the cross sections for χ/ϵ_s from 0 to 1 (Fig. B.1b). Then, we fix $\epsilon_s = 0.01$ (which is equivalent to fix a phase portrait), and we vary χ/ϵ_s from 0 to 1 (Fig. B.1c). In all cases, we find an error smaller than 10^{-11}, which supports the use of this numerical method to compute river profiles.

B.2 Another numerical method to solve equation (4.15)

Although the numerical method used in section 4.3 is accurate, it is slow and sensitive to low values of ϵ_s (typically < 0.01). This method is based on the integration of an ordinary differential equation on D with the solver `ode` in Python, that we can not parametrize.

Thus, to accelerate the computation of a profile, we developed another numerical method, which is also less sensitive to the precision issues. This enabled us to calculate thousands of profiles in a few seconds and for broader ranges of the parameters χ and ϵ_s. We used it to generate the abacuses (section 4.6).

To do so, we introduce new notations, based on the phase portrait (section 4.4). Specif-

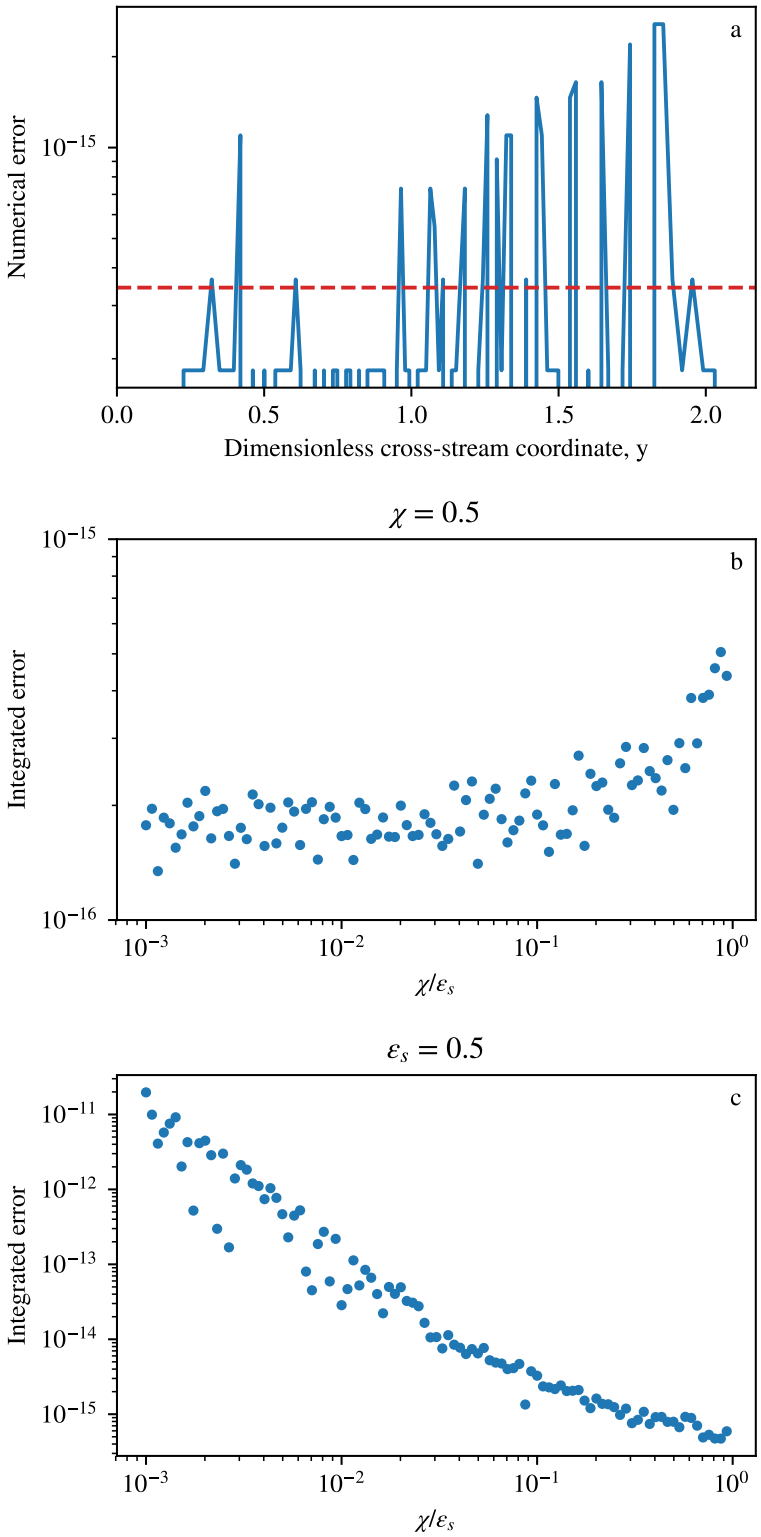

Figure B.1 – Estimate of the relative numerical error. a. Error along a cross section profile for $\epsilon_s = 0.5$ and $\chi = 0.25$. In blue: relative numerical error. Red, dashed line: mean of the relative numerical error. b. Relative numerical error as a function of χ/ϵ_s for $\chi = 0.5$. c. Relative numerical error as a function of χ/ϵ_s for $\epsilon_s = 0.5$.

ically, it is natural to define ϕ, by analogy with polar coordinates, as:

$$D = \mu \cos\phi\,, \tag{B.4}$$

$$D' = \mu \sin\phi\,. \tag{B.5}$$

ϕ vanishes where $(D, D') = (D_{\max}, 0)$, that is the center of the river. It is $\pm\pi/2$ on the banks, where $(D', D) = (0, D'_{\max})$. When $\mu = \mu_t$, D and D' forms a circle in the phase space: it corresponds to the threshold channel.

With these notations, equation (4.15) reads

$$(\mu - \mu_t) \exp\left(\frac{\mu_t - \mu\cos\phi}{\epsilon_s}\right) = \chi\, e^{-\chi/\epsilon_s}\,. \tag{B.6}$$

The ratio μ varies from its value at the banks, μ_{banks}, where it is the smallest (closest to the threshold), to its value at the center of the river's channel, μ_{center}, where it reaches a maximum (where transport is the most intense), with

$$\mu_{\text{center}} = \mu_t + \chi\,, \tag{B.7}$$

$$\mu_{\text{banks}} = \mu_t + \chi\; e^{-(\mu_t+\chi)/\epsilon_s}\,. \tag{B.8}$$

The angle ϕ is linked with μ through equation (B.6):

$$\phi = \arccos\left(\frac{\mu_t + \chi}{\mu} + \frac{\epsilon_s}{\mu}\log\left(\frac{\mu - \mu_t}{\chi}\right)\right). \tag{B.9}$$

Once we have μ and ϕ, we deduce the depth and the cross-stream slope with equation (B.5). To get the river cross section, we need the cross-stream coordinates y which correspond to the depths. We use:

$$\frac{dy}{d\phi} = \frac{1}{\dfrac{\mu - \mu_t}{\epsilon_s}\cos\phi - 1} \tag{B.10}$$

By integrating equation (B.10), we deduce the cross-stream coordinates y, and then the whole profile of a river, for given values of (ϵ_s, χ).

Overall, this numerical method does not require any solver as `ode`, but only an integration with a basic function `trapz` in Python.

B.3 Numerical codes

B.3.1 Method with `ode`

We provide here the code corresponding to the method described in section 4.3.1. This method is based on an implicit method to solve the differential equation (4.15).

```
from pylab import *
from scipy.integrate import ode

def river_profile( epsilon, chi, mu_t, dy = 1e-3, delta = 1.e-5) :

    '''
    Numerical river profile with ode
    '''

    D_max = mu_t + chi

    # comportement asymptotique en y=0

    A = - 2 * D_max * ( chi/epsilon - 1.)

    y_start = dy * sqrt( 4. * delta/A )
    D_start = D_max - A*( y_start/2. )**2.

    def F( y, D ):
        dD_dy = -sqrt( ( chi*exp(-chi/epsilon)*exp((D-mu_t)/epsilon) + mu_t )**2.
     - D**2. )
        return dD_dy

    integrator = ode(F)
    integrator.set_initial_value( [D_start] , y_start )

    print 'starting value y,D:', y_start, D_start

    y_num = [0]
    D = [mu_t + chi]
    i = 0
    while integrator.y[0] > 0: #and abs( integrator.y[0] ) < 1.e+5 :
        print i
        y_num += [ integrator.t ]
        D += [ integrator.y[0] ]
        integrator.integrate( integrator.t + dy )
        i +=1

    y_num = array(y_num)                              # adim by L/S
    D = array(D)                                      # adim by L/S
    qs = chi*exp( (D - D_max) /epsilon )              # adim by q_mu


    y_num = hstack( [ -y_num[::-1], y_num ] )  # half profile -> full profile
    D = hstack( [ D[::-1], D ] )
    qs = hstack( [ qs[::-1], qs ] )

    return y_num, D, qs
```

B.3.2 Method used for the regime relations

We provide here the code corresponding to the method described in section B.2, and which we used in section 4.6 to generate abacuses.

We first define an array of μ which is between μ_{bank} and μ_{center} (equation (B.8)). We then calculate the corresponding array of ϕ with equation (B.9), and deduce the depth with equation (B.5). Finally, we have the derivative of y, that we integrate with `trapz` (equation (B.10)). We then have the dimensionless profile $D(y)$.

```
from pylab import *
from scipy.integrate import cumtrapz

############################################################"

def river_profile( epsilon, delta_c, mu_t, Npts = 100, spit_phi = False ) :

    '''
    Numerical river profile.
    '''

    epsilon_log_delta_c = epsilon*log(delta_c)
    epsilon_log_delta_b = epsilon_log_delta_c - ( mu_t + epsilon*delta_c )

    epsilon_log_delta = epsilon_log_delta_b + ( epsilon_log_delta_c -
    epsilon_log_delta_b )*( 1. - array( [0.] + list( logspace( log10( 1. -
    delta_c ) - 3., 0, Npts) ) )[::-1] )
    delta = exp( epsilon_log_delta/epsilon )

    cos_phi = ( epsilon_log_delta - epsilon_log_delta_b)/( mu_t + epsilon*delta )


    ###################################

    D = ( mu_t + delta*epsilon )*cos_phi
    dy_dphi = 1./( delta*cos_phi - 1. )
    phi = array( list( arccos( cos_phi[:-1] ) ) + [0.] ) # just because arccos is
     ambiguous

    y = array( [ 0. ] + list( cumtrapz( dy_dphi, phi ) ) )


    ###################################

    y = y - max(y)  # center profile on 0

    y = hstack( [ y, -y[::-1] ] )  # half profile -> full profile
    D = hstack( [ D, D[::-1] ] )
    delta = hstack( [ delta, delta[::-1] ] )

    if spit_phi :
```

```
        phi = hstack( [ phi, -phi[::-1] ] )
        return y, D, delta, phi

42  else :
        return y, D, delta
```

Appendix C

Buckling of an elastic shell

Avant propos

Durant ma thèse, j'ai effectué un séjour de recherche à l'étranger grâce à l'aide financière de l'école doctorale STEP'UP. J'ai étudié le flambage de coques cylindrinques, un problème qui m'a ouverte aux instabilités mécaniques. J'ai effectué cette étude dans le laboratoire de Shmuel Rubinstein (Harvard University, Cambridge, USA) pendant 3 mois, où j'ai travaillé conjointement avec Emmanuel Virot, chercheur postdoctorant. Je fais ici un court rapport de ce travail.

C.1 Introduction

When we compress a cylindrical shell from its top, it remains stable over a considerable load range until it finally collapses at the critical buckling load. The shell then deforms, displays plasticity and sometimes exhibits well-defined diamond shapes as on figure C.1a (Miura 1969).

Seide *et al.* (1960) performed a series of experimental measurements of the critical buckling load for cylindrical shells of different radii R and thickness t (Fig. C.1b). They showed that this load drastically varies from on cylinder to another and that the linear stability analysis systematically overestimates it (Wierzbicki 2017). The ratio between the lowest-experimental and theoretical loads is known as the "knock-down" factor. The industry uses this empirical curve to estimate the strength of thin-walled cylinders, such as the shell of space rockets.

Since then, it has been established that the primary cause for this knock-down factor is the extreme sensitivity of shell structures to imperfections (Babcock 1983, Calladine 1995).

Recently, a new theoretical framework suggested to investigate the buckling of shells by probing them. Following this framework, Virot *et al.* (2017) built an experimental set-up to do so. During my stay, I used this set-up to characterize the effect of a defect on the buckling load of a can.

C.2 Stability landscape

Poking a material is a natural way to test its mechanical properties: with our finger, we estimate the stiffness of objects in every-day life, and deduce for example if a bicycle

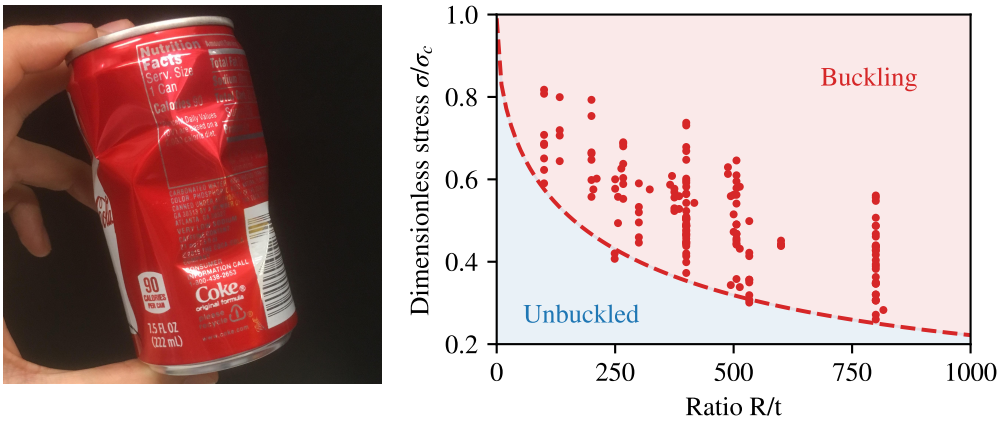

Figure C.1 – Buckling of a cylindrical shell. Left: post-buckling Miura (or Yoshimura) patterns. Credits: Emmanuel Virot. Right: critical buckling load, normalised by its linear-stability prediction, for different shell geometries, of radius R and thickness t. From Seide *et al.* (1960).

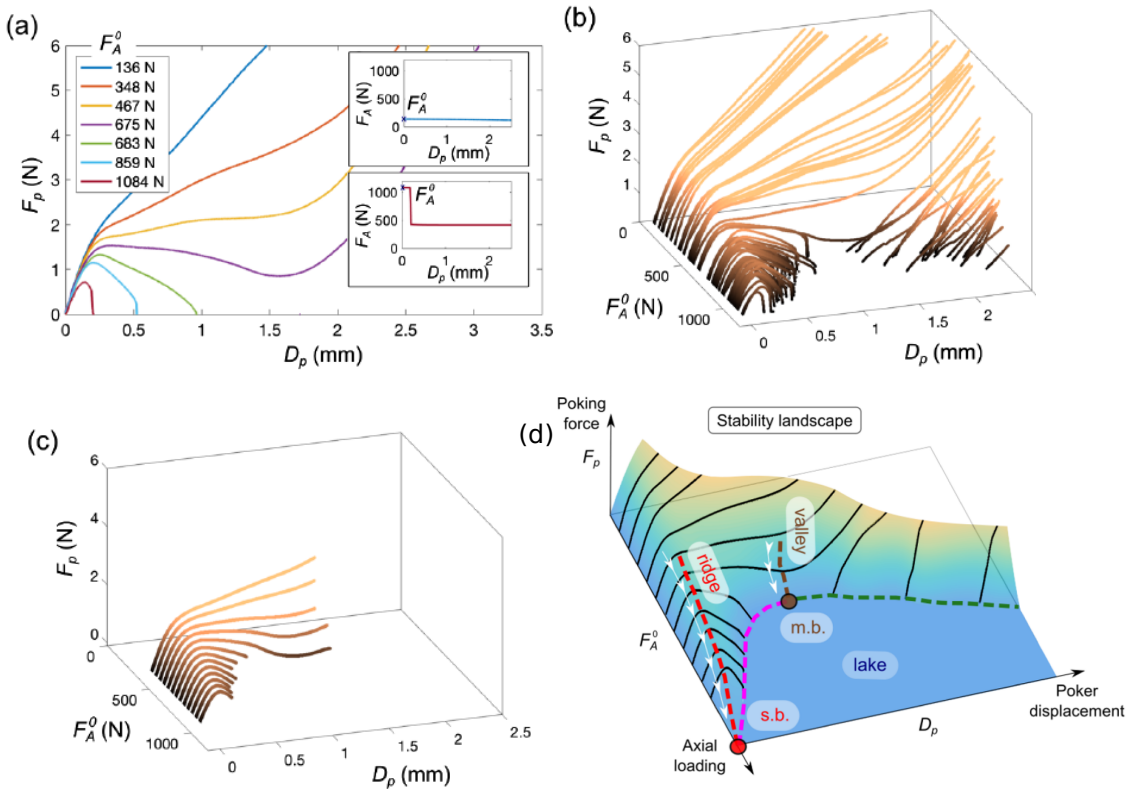

Figure C.2 – Investigation of a can stability by probing its side with a poker. Experiments of Virot *et al.* (2017). a. Force-displacement curve for seven cans: poker force F_P as a function of the poker displacement D_P for different axial loads F_A. Inset: axial load measurement. b. Three-dimensional representation of these independent curves for 89 cans in the space (F_A, F_P, D_P). c. Three-dimensional representation of these curves probed on the same can without make it buckle. d. Stability landscape of shell buckling. The red point (s. b.) corresponds to the spontaneous buckling, and the brown point (m. b.) to the minimum buckling.

tyre needs to be inflated.

Similarly, many experimenters use indentation to measure the elastic modulus of graphene (López-Polín *et al.* 2015) and of biological tissues (Sen *et al.* 2005) with an atomic force microscope (AFM). To test the resistance of a thin shell to buckling, Thompson & T. (2015) suggested to also probe it with a controlled lateral displacement.

Following this suggestion, Virot *et al.* (2017) investigated experimentally the stability of a thin cylindrical can by poking its side, while it is clamped vertically by an axial load. To do so, Virot *et al.* (2017) used a custom-made bi-axial machine (Fig. C.3, without hole). They initially compress the can axially by moving the upper plate at a constant velocity. When the axial load reaches a preset load F_A, smaller than the critical buckling load, the upper plate stops, while the displacement and the force are recorded. Then, a poker slowly advances towards the can. When it reaches the can's side, it slightly deflects its shell. Both the probing force and the poker displacement are registered simultaneously.

The response of the can depends on the axial load. Figure C.2a shows the evolution of the poker force F_P as a function of its displacement D_P. For a weak axial force (typically smaller than 400 N), the poker force increases with its displacement, as it enters into the can. For intermediate axial forces (between 400 and 700 N), it decreases and then increases again. In these two regimes, the poker can enter deeply into the can without triggering the buckling.

If we now clamp the can with an axial load higher than approximately 700 N, its response to poking changes drastically and the curve $F_p(D_P)$ is surprising. As the poker enters into the can, the force it applies on it increases, decreases, and then vanishes. At this point, we hear a snap and the can buckles, showing a simple dimple. The moment when the poker force vanishes means that it does not touch the can any more. The shell then accelerates toward the center of the cylinder, away from the poker.

Making the can buckle with the poker on the side is equivalent to triggering the instability with a finite-amplitude perturbation. This suggests that this instability is intrinsically non-linear, and may explain why the linear stability analysis of the can fails to predict the buckling events. This bifurcation is reminiscent of the transition towards turbulence in a pipe flow (Darbyshire & Mullin 1995, Peixinho & Mullin 2007).

Virot *et al.* (2017) performed a series of poking experiments on 89 different Coke cans. They measured the evolution of the poker force as a function of its displacement for any axial forces. Then, they combined these curves in a three-dimensional phase space (F_A, F_P, D_P) (Fig. C.2b). They reveal a stability landscape which tells whether the can is buckled for any values of the axial load, of the poker force and of the poker's displacement.

This landscape presents a "ridge" of stability, which corresponds to an energy barrier the poker needs to cross to make the can buckle (Fig. C.2d). If the can goes over this ridge to reach the "lake", it buckles. The ridge gets narrower when the axial compressing

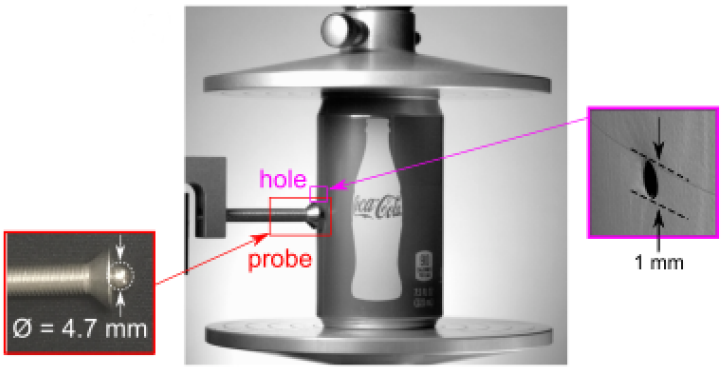

Figure C.3 – Experimental setup. We apply an axial load F_A on the can by lowering the upper plate. The poker is a marble place on a rod that can advances towards the shell surface, just below a drilled hole of 1 mm of diameter.

force increases. Although the end of this ridge seems to tend towards a buckling force, it is experimentally difficult to probe it, as the can buckles before.

If the poker stops before the lake, the can does not buckle while we probe it. In this case, the ridge is reversible, and leaves no plasticity in the can. Consequently, we can compute the whole stability landscape of a can just in probing it, by stopping the poker just after it reaches its maximum force. When the poker is back to its origin, Virot *et al.* (2017) sequentially increased the can compression (Fig. C.2c).

Virot *et al.* (2017) showed that all cans have the same general landscape. However, they speculated that the part of the landscape close to the critical axial load should depend on the can, and on its defects. It should be smoothly distorted there.

To test this scenario, we now introduce intentionally a defect in the can and investigate how it alters the stability landscape in the next section.

C.3 Stability landscape of a defected can

We start by drilling a hole of diameter 1 mm in the can's shell, at mid-height. Then, we use the same custom-made bi-axial machine to probe a commercial Coke can (7.5 fl.oz.). We initially compress the can by lowering the upper plate of the machine, while recording continuously the axial force and displacement of this plate (Fig. C.3).

While the can is clamped by the axial plates, the poker advances slowly towards it (typically 2 mm/s). The can is placed such that the poker reaches the surface 5 mm below the hole (Fig. C.3). The poker force increases with its displacement, reaches a maximum and then decreases, as it was the case in the experiments of Virot *et al.* (2017). We manually stop the poker just after its maximum, and return it to the origin. This does not damage the can. We obtain one curve of the landscape stability (Fig. C.4, in blue). We then increment the axial load and probe it again until the maximum corresponds to very

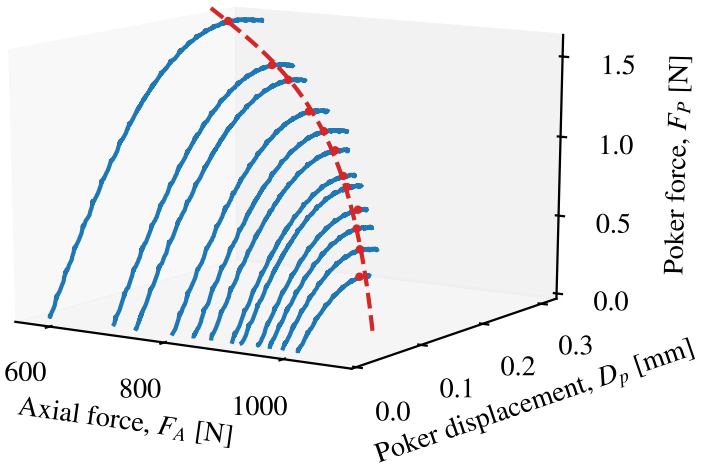

Figure C.4 – Stability landscape of a defected can probed close to the hole. Blue: each curve is measured with a back and forth of the poker. Red points: maxima of each curves. Red dashed line: second-polynomial fit.

low displacements of the poker (typically 50 μm), because the perturbation needed for the can to buckle becomes too small.

This time, the stability landscape seems to converge towards a critical axial force more drastically than a can without hole. Is this converging load related to the buckling load of the can ? We investigate this question in the next section.

C.4 Buckling load prediction

In section C.3, we measured the stability landscape of a can with a hole. We showed that the ridge of the stability landscape is much sharper and converges towards an axial load which is of the order of can's buckling loads. This procedure is reversible, and we did not damage the can. Therefore, we can now measure the buckling load of the shell.

To do so, we keep the poker away from the can and we compress axially the can by lowering the upper plate of the machine at a constant velocity (5 mm/min). The axial load increases until it reaches the can's buckling load. Simultaneously, a dimple appears in the neighbourhood of the hole and we hear a snap sound. The can is now irreversibly damaged.

We now compare the buckling load that we measured to the convergence of the stability landscape. On figure C.5, we plot in blue the projection of the can's ridge in the plan (F_A, F_P). We also place on the F_A-axis its buckling load (blue star). The ridge seems to converge towards the buckling load. We then fit the ridge with a second-order polynomial

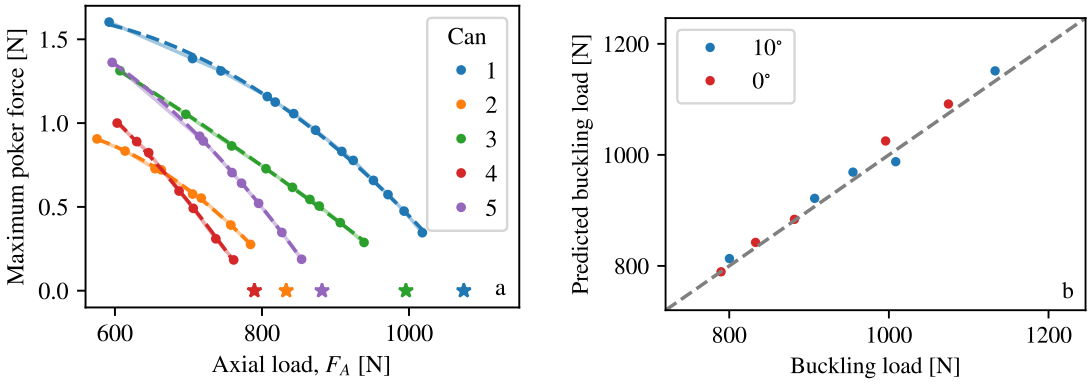

Figure C.5 – Buckling load prediction. a. Convergence of the ridge by probing a can just above the hole. Each color corresponds to a different can, in which we introduced the same hole (1 mm of diameter). Points: maxima of the landscape's ridge measured by the procedure described in section C.3. Dashed line: second-dimensional polynomial fit. Stars: buckling load measured by the procedure described in section C.4. b. Comparison of the buckling load prediction with the measured one.

and define the predicted buckling load as the crossing of this polynomial with the F_A-axis.

We repeat this procedure with 10 cans. Each time, we can predict the buckling load with an accuracy of 5% (Fig. C.5b).

C.5 Spatial influence of the hole

We now turn the can to probe it slightly away from the hole with the procedure of section C.4. For example, if the poker reaches the can's surface also below the hole, but 5 mm on its side, the landscape ridge still converges towards the buckling load of the can (Fig. C.6). As a result, we predict the can buckling load with an accuracy of 5 % (Fig. C.5b). At which distance from the hole can we still predict the buckling load of a can, based on the convergence of its ridge ?

To answer this question, we probed the can sequentially around the hole (from -50 mm to 50 mm around). We track the amplitude of the ridge for different axial loads, without damaging the can. We then normalise it by its value at an axial force of $F_A = 600$ N (Fig. C.7a). We find that the ridge quickly decreases and converges when we probe it just below the hole, as expected (vanishing distance to the hole, Fig. C.7a). At 5 mm away from the hole, we still observe that the ridge decreases significantly with the axial load. The convergence is slightly smoother but is enough to predict accurately the buckling load (Fig. C.6). Further 10 mm, however, the ridge does not converge and our procedure to predict the buckling load does not work any more. This seems that a can acquires a peculiar stability landscape for each point of its shell.

To estimate how this landscape is distorted by the hole, we probed a can before and after

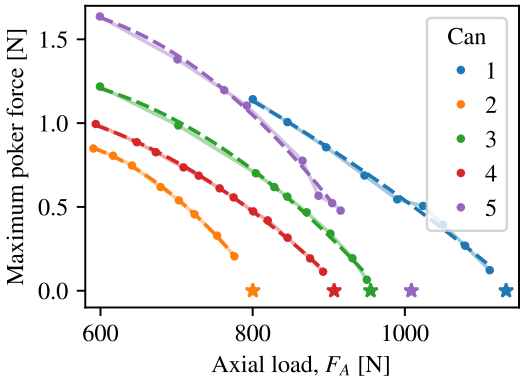

Figure C.6 – Buckling prediction by probing a can above the hole, but 5 mm on its left. Each color corresponds to a different can, in which we introduced a hole. Points: maxima of the landscape's ridge measured by the procedure described in section C.3. Dashed line: 2-dimensional polynomial fit. Stars: spontaneous buckling load measured by the procedure described in section C.4.

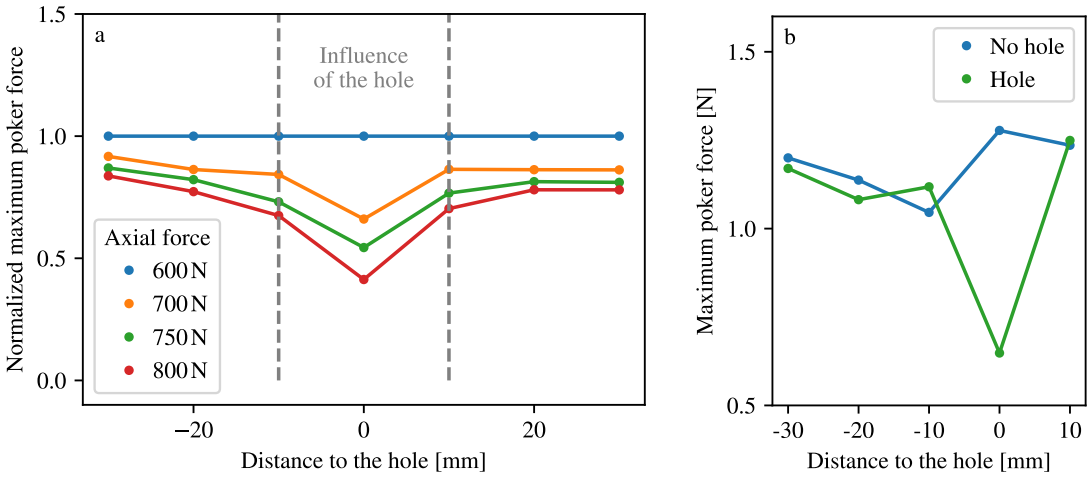

Figure C.7 – Local influence of the hole. a. Amplitude of the ridge around the hole drilled in the can. Maximum poker force for different axial loads, normalized by its value for $F_A = 600$ N. b. Probing of the can before and after drilling the hole in its shell.

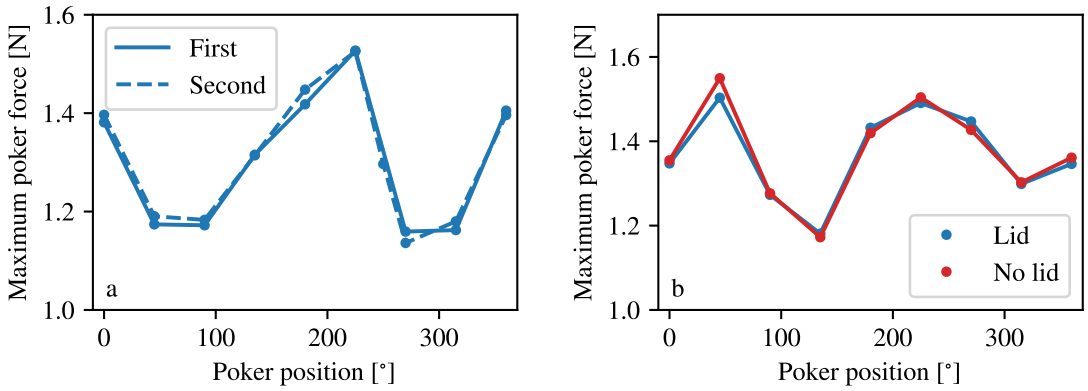

Figure C.8 – Probing of a non-drilled can around its mid plane. a. Probing of a can from 0 to 360°(twice) Filled line: first sequence of probes around the can. Dashed line: second sequence of probes around the can. b. Probing of a can without hole around its mid plane, before and after removing the lid.

drilling it. We observe that the presence of the hole decreases significantly the amplitude of the ridge (Fig. C.7b). However, it seems to impact only its neighbourhood, in a range of ±10 mm, as suggested by our previous measurements. The hole then only locally distort the ridge of the stability landscape.

We now investigate how the stability landscape changes on a same can, without manufactured hole. We use a commercial can and expect it to have defects due to the fabrication process or the transportation. We turn it sequentially to probe the amplitude of the ridge for 10 different positions in its mid plane (around 360°). We observe that the amplitude of the ridge for a given axial load varies of about 20% with the poker position (Fig. C.8a). If we perform the same measurements twice, we observe that these variations are remarkably reproducible (Fig. C.8a). These measurements suggest a local correlation between the defect of a can and the amplitude of the stability-landscape ridge.

So far, to ensure that this discrepancy is not due to the asymmetry of a Coke can lid, we probed the can in its mid plane with and without its lid (Fig. C.8b). We did not observe any difference, suggesting that a defect on the top of the can does not influence the stability landscape at all.

C.6 Conclusion

During this project, we investigated the effect of a defect on the stability of Coke cans. We developed a non-destructive procedure to measure accurately the buckling load of a can in which we drilled a hole. By probing the can close to this hole, we measure the decrease of the ridge in its stability landscape without damaging it. The amplitude of this ridge converges towards the buckling load of the can, that we independently measure by

compressing the can axially.

The influence of the hole, however, is only local. We thus have to probe near the main defect of the shell, which is possible only because we introduced it intentionally.

Though, in the light of our analysis, we suggest the following procedure if we do not know where the main defect of the can is. We fix the axial compression load, and we probe the can on the whole surface, with a resolution of 10 mm×10 mm. We speculate, that, for a sufficient high compression, the lowest value of the maximum poker force corresponds to the main defect's neighbourhood. We could then predict the buckling load of the can by tracking the convergence of the ridge at this point.

List of Notations

List of Figures

List of Tables

Bibliography

Agudo, JR, & Wierschem, A. 2012. Incipient motion of a single particle on regular substrates in laminar shear flow. *Physics of Fluids*, **24**, 093302. 20

Allen, J.R.L. 1982. *Sedimentary structures, their character and physical basis.* Vol. 1. Elsevier. 137

Allen, J.R.L. 1985. *Principles of Physical Sedimentology.* The Blackburn Press. 16

Allen, P.A. 1997. *Earth Surface Processes.* Blackwell Science. 10

Ancey, C., & Heyman, J. 2014. A microstructural approach to bedload transport: mean behavior and fluctuations of particles transport rates. *J. Fluid Mech.*, **744**, 129–168. 20

Anderson, R. S., & Anderson, S. P. 2010. *Geomorphology Geomorphology, the Mechanics and Chemistry of Landscapes.* Cambridge University Press. 10

Andreotti, B., Forterre, Y., & Pouliquen, O. 2011. *Les milieux granulaires: entre fluide et solide.* EDP Sciences. 24

Andreotti, B., Claudin, P., Devauchelle, O., Durán, O., & Fourrière, A. 2012. Bedforms in a turbulent stream: ripples, chevrons and antidunes. *Journal of Fluid Mechanics*, **690**, 94–128. 31, 137

Aussillous, P., Chauchat, J., Pailha, M., Médale, M., & Guazzelli, E. 2013. Investigation of the mobile granular layer in bedload transport by laminar shearing flows. *Journal of Fluid Mechanics*, **736**, 594–615. 156

Aussillous, P., Zou, Z., Guazzelli, E., Yan, L., & Wyart, M. 2016. Scale-free channeling patterns near the onset of erosion of sheared granular beds. *Proceedings of the National Academy of Sciences*, 201609023. 37, 139, 149

Babcock, C.D. 1983. Shell stability. *Journal of applied mechanics*, **50**(4b), 935–940. 188

Bagnold, R. 1973. The nature of saltation and of Bedload transport in water. *Proc. R. Soc. Lond.*, **A 332**, 473–504. 136

Berger, C., McArdell, B.W., & Schlunegger, F. 2011. Sediment transfer patterns at the Illgraben catchment, Switzerland: Implications for the time scales of debris flow activities. *Geomorphology*, **125**(3), 421–432. 29

Bernal, JD, & Mason, J_. 1960. Packing of spheres: co-ordination of randomly packed spheres. *Nature*, **188**(4754), 910. 141

Buffington, J.M. 1999. The legend of AF Shields. *Journal of Hydraulic Engineering*, **125**(4), 376–387. 19, 20

Buffington, J.M., & Montgomery, D.R. 1997. A systematic analysis of eight decades of incipient motion studies, with special reference to gravel-bedded rivers. *Water Resour. Res.*, **33**(8), 1993–2029. 20

Calladine, C.R. 1995. Understanding imperfection-sensitivity in the buckling of thin-walled shells. *Thin-Walled Structures*, **23**(1-4), 215–235. 188

Carson, M.A. 1984. The meandering-braided river threshold: a reappraisal. *Journal of Hydrology*, **73**(3-4), 315–334. 29, 31

Charru, F. 2006. Selection of the ripple length on a granular bed sheared by a liquid flow. *Physics of fluids*, **18**(12), 121508. 137

Charru, F., Mouilleron, H., & Eiff, O. 2004a. Erosion and deposition of particles on a bed sheared by a viscous flow. *Journal of Fluid Mechanics*, **519**, 55–80. 33, 35, 36, 57, 68, 151, 152, 154

Charru, F., Mouilleron, H., & Eiff, O. 2004b. Erosion and deposition of particles on a bed sheared by a viscous flow. *Journal of Fluid Mech.*, **519**(Nov), 55–80. 36, 137, 138, 139, 149

Charru, F., Andreotti, B., & Claudin, P. 2013. Sand ripples and dunes. *Annual Review of Fluid Mechanics*, **45**, 469–493. 31, 137

Chen, X., Ma, J., & Dey, S. 2009. Sediment transport on arbitrary slopes: Simplified model. *Journal of Hydraulic Engineering*, **136**(5), 311–317. 73, 81, 141

Church, M. 1992. Channel morphology and typology. *The river handbook*, **1**, 126–143. 31

Church, M. 2006. Bed material transport and the morphology of alluvial river channels. *Annu. Rev. Earth Planet. Sci.*, **34**, 325–354. 31

Coleman, S.E., & Melville, B.W. 1994. Bed-form development. *Journal of hydraulic engineering*, **120**(5), 544–560. 137

Colombini, M. 1993. Turbulence-driven secondary flows and formation of sand ridges. *Journal of Fluid Mechanics*, **254**, 701–719. 137

Colombini, M., & Parker, G. 1995. Longitudinal streaks. *Journal of Fluid Mechanics*, **304**, 161–183. 137

Colombini, M., Seminara, G., & Tubino, M. 1987. Finite-amplitude alternate bars. *Journal of Fluid Mechanics*, **181**, 213–232. 31, 137

Courrech Du Pont, S., Gondret, P., Perrin, B., & Rabaud, M. 2003. Granular avalanches in fluids. *Physical review letters*, **90**(4), 044301. 171

Dancey, C.L., Diplas, P., Papanicolaou, A., & Bala, M. 2002. Probability of individual grain movement and threshold condition. *Journal of Hydraulic Engineering*, **128**(12), 1069–1075. 20

Darbyshire, A.G., & Mullin, T. 1995. Transition to turbulence in constant-mass-flux pipe flow. *Journal of Fluid Mechanics*, **289**, 83–114. 190

Delorme, P. 2017. *Morphologie des cônes alluviaux*. Ph.D. thesis, Université Paris-Diderot-Paris VII. 40, 47, 87, 172

Delorme, P., Devauchelle, O., Barrier, L., & Métivier, F. 2018. Growth and shape of a laboratory alluvial fan. *Physical Review E*, **98**(1), 012907. 165

Devauchelle, O., Malverti, L., Lajeunesse, E., Josserand, C., Lagrée, PY, & Métivier, F. 2010a. Rhomboid beach pattern: A laboratory investigation. *J. Geophys. Res*, **115**, F02017. 137

Devauchelle, O., Malverti, L., Lajeunesse, E., Lagrée, PY, Josserand, C., & Thu-Lam, K.D.N. 2010b. Stability of bedforms in laminar flows with free surface: from bars to ripples. *Journal of Fluid Mechanics*, **642**, 329–348. 31

Einstein, A. 1905. On the motion of small particles suspended in liquids at rest required by the molecular-kinetic theory of heat. *Annalen der physik*, **17**, 549–560. 74

Einstein, H. A. 1937. Bed load transport as a probability problem. *Pages C1 – C105 of: Sedimentation: 746 Symposium to Honor Professor H.A. Einstein, 1972. translation from 747 German of H.A. Einstein doctoral thesis. Originally presented to Federal Institute of Technology, Zurich, Switzerland, 1937.* 136

Exner, F.M. 1925. Uber die wechselwirkung zwischen wasser und geschiebe in flussen. *Akad. der Wiss in Wien, Math-Naturwissenschafliche Klasse, Sitzungsberichte, Abt IIa*, **134**, 165–203. 137

Furbish, D.J., Haff, P.K., Roseberry, J.C., & Schmeeckle, M.W. 2012a. A probabilistic description of the bed load sediment flux: 1. Theory. *Journal of Geophysical Research*, **117**(F3), F03031. 137

Furbish, D.J., Roseberry, J.C., & Schmeeckle, M.W. 2012b. A probabilistic description of the bed load sediment flux: 3. The particle velocity distribution and the diffusive flux. *Journal of Geophysical Research*, **117**(F3), F03033. 37

Furbish, D.J., Ball, A.E., & Schmeeckle, M.W. 2012c. A probabilistic description of the bed load sediment flux: 4. Fickian diffusion at low transport rates. *Journal of Geophysical Research*, **117**(F3), F03034. 37

Glover, R. E., & Florey, Q. L. 1951. Stable channel profiles. *U. S. Bur. Reclamation, Hydr. 325.* 17, 20, 21

Gole, C.V., & Chitale, S.V. 1966. Inland delta building activity of Kosi river. *Journal of the Hydraulics Division*, **92**(2), 111–126. 9, 11

Hecht, F. 2012. New development in FreeFem++. *Journal of numerical mathematics*, **20**(3-4), 251–266. 56

Helley, E.J., & Smith, W. 1971. *Development and calibration of a pressure-difference bedload sampler.* Tech. rept. 164

Henderson, F. M. 1961. Stability of alluvial channels. *J. Hydraul. Div. ASCE*, **87**, 109–138. 21, 46, 111

Heyman, J., & Ancey, C. 2014. Tracking bed load particles in a steep flume: Methods and results. *In: Proceedings of River Flow 2014, Seventh International Conference on Fluvial Hydraulics.* 57, 60

Houssais, M., Ortiz, C.P., Durian, D.J., & Jerolmack, D.J. 2015. Onset of sediment transport is a continuous transition driven by fluid shear and granular creep. *Nature communications*, **6**, 6527. 20, 76, 78

Ikeda, S., Parker, G., & Kimura, Y. 1998. Stable width and depth of straight gravel rivers with heterogeneous bed materials. *Water Resour. Res.*, **24**, 713–722. 86, 157

Jaeger, H.M., & Nagel, S.R. 1992. Physics of the granular state. *Science*, **255**(5051), 1523–1531. 171

Jaumann, R., Brown, R.H., Stephan, K., Barnes, J.W., Soderblom, L.A., Sotin, C., Le Mouélic, S., Clark, R.N., Soderblom, J., Buratti, B.J., *et al.* . 2008. Fluvial erosion and post-erosional processes on Titan. *Icarus*, **197**(2), 526–538. 40

Julien, P. 1995. *Erosion and sedimentation.* Cambridge university press. 19, 20

Karcz, I. 1967. Harrow marks, current-aligned sedimentary structures. *The Journal of Geology*, **75**(1), 113–121. 137

Kennedy, J.F. 1963. The mechanics of dunes and antidunes in erodible-bed channels. *Journal of Fluid mechanics*, **16**(4), 521–544. 137

King, J.G., Emmett, W.W., Whiting, P.J., Kenworthy, R.P., & Barry, J.J. 2004. Sediment transport data and related information for selected coarse-bed streams and rivers in Idaho. *Gen. Tech. Rep. RMRS-GTR-131. Fort Collins, CO: US Department of Agriculture, Forest Service, Rocky Mountain Research Station. 26 p.*, **131**. 29

Kovacs, A., & Parker, G. 1994. A new vectorial bedload formulation and its application to the time evolution of straight river channels. *Journal of fluid Mechanics*, **267**, 153–183. 73, 141

Kramers, H.A. 1940. Brownian motion in a field of force and the diffusion model of chemical reactions. *Physica*, **7**(4), 284–304. 74

Lacey, G. 1930. Stable channels in alluvium. *Pages 259–292 of: Minutes of the Proceedings*, vol. 229. Thomas Telford. 17, 46

Lajeunesse, E., Malverti, L., & Charru, F. 2010. Bedload transport in turbulent flow at the grain scale: experiments and modeling. *J. Geophys. Res. Earth Surface*, **115**, F04001, doi:10.1029/2009JF001628. 36, 37, 137, 139

Lajeunesse, E., Devauchelle, O., & James, F. 2017. Advection and dispersion of bed load tracers. *Earth Surface Dynamics*, **6**(2), 389–399. 34

Leopold, L.B., & Maddock, T. 1953. *The hydraulic geometry of stream channels and some physiographic implications.* Vol. 252. US Government Printing Office. 17

Leopold, L.B., & Wolman, M.G. 1957. *River channel patterns: braided, meandering, and straight.* US Govt. Print. Off. 9, 29, 31

Li, C., Czapiga, M.J., Eke, E.C., Viparelli, E., & Parker, G. 2015. Variable Shields number model for river bankfull geometry: bankfull shear velocity is viscosity-dependent but grain size-independent. *Journal of Hydraulic Research*, **53**(1), 36–48. 18, 25

Liu, Y., Metivier, F., Lajeunesse, E., Lancien, P., Narteau, C., & Meunier, P. 2008. Measuring bed load in gravel bed mountain rivers : averaging methods and sampling strategies. *Geodynamica Acta*, **21**, 81–92, doi:10.3166/ga.21.81–92. 164, 165

Lobkovsky, A.E., Orpe, A.V., Molloy, R., Kudrolli, A., & Rothman, D.H. 2008. Erosion of a granular bed driven by laminar fluid flow. *Journal of Fluid Mechanics*, **605**(1), 47–58. 20, 149, 152, 154, 156

Loiseleux, T., Gondret, P., Rabaud, M., & Doppler, D. 2005. Onset of erosion and avalanche for an inclined granular bed sheared by a continuous laminar flow. *Physics of Fluids*, **17**, 103304. 20

López-Polín, G., Gómez-Navarro, C., Parente, V., Guinea, F., Katsnelson, M.I., Perez-Murano, F., & Gómez-Herrero, J. 2015. Increasing the elastic modulus of graphene by controlled defect creation. *Nature Physics*, **11**(1), 26. 190

McLelland, S.J., Ashworth, P.J., Best, J.L., & Livesey, J.R. 1999. Turbulence and secondary flow over sediment stripes in weakly bimodal bed material. *Journal of hydraulic engineering*, **125**(5), 463–473. 137

Métivier, F., & Barrier, L. 2012. Alluvial Landscape Evolution: What Do We Know About Metamorphosis of Gravel-Bed Meandering and Braided Streams? *Gravel-Bed Rivers: Processes, Tools, Environments*, 474–501. 10, 28, 29, 86

Métivier, F., Lajeunesse, E., & Devauchelle, O. 2017. Laboratory rivers: Lacey's law, threshold theory, and channel stability. *Earth Surface Dynamics*, **5**(1), 187. 18, 24, 32, 33, 46, 158

Meunier, P., & Metivier, F. 2006. Sediment transport in a microscale braided stream: From grain size to reach size. *Pages 212–226 of:* Sambrook-Smith, G.H., Best, J.L., Bristow, C.S., & Petts, G.E. (eds), *Braided River, Process, Deposits, Ecology and Management*. Blackwell, Malden, Massachussetts. 100

Meyer-Peter, E., & Müller, R. 1948. Formulas for Bed-Load Transport. *Pages 39–64 of:* Stockholm, Sweden (ed), *Proceedings, 2nd Congress, International Association of Hydraulic Research*. 137, 139

Milliman, J.D., & Meade, R.H. 1983. World-wide delivery of river sediment to the oceans. *The Journal of Geology*, **91**(1), 1–21. 26

Mishra, D.K., People's Science Institute (Dehra Dun, India), on Dams Rivers, South Asia Network, & People. 2008. *Trapped! Between the Devil and Deep Waters*. Peoples' Science Institute. 9

Miura, K. 1969. *Proposition of pseudo-cylindrical concave polyhedral shells*. Institute of Space and Aeronautical Science, University of Tokyo. 188

Mouyen, M., Longuevergne, L., Steer, P., Crave, A., Lemoine, J.-M., Save, H., & Robin, C. 2018. Assessing modern river sediment discharge to the ocean using satellite gravimetry. *Nature communications*, **9**(1), 3384. 40

Mueller, E.R., & Pitlick, J. 2013. Sediment supply and channel morphology in mountain river systems: 1. Relative importance of lithology, topography, and climate. *Journal of Geophysical Research: Earth Surface*, **118**(4), 2325–2342. 26

Mueller, E.R., & Pitlick, J. 2014. Sediment supply and channel morphology in mountain river systems: 2. Single thread to braided transitions. *Journal of Geophysical Research: Earth Surface*, **119**(7), 1516–1541. 31

Munkres, J. 1957. Algorithms for the assignment and transportation problems. *Journal of the society for industrial and applied mathematics*, **5**(1), 32–38. 60

Nikora, V., Habersack, H., Huber, T., & McEwan, I. 2002. On bed particle diffusion in gravel bed flows under weak bed load transport. *Water Resources Research*, **38**(6), 17–1. 37, 137

Ouriemi, M., Aussillous, P., Medale, M., Peysson, Y., & Guazzelli, E. 2007. Determination of the critical Shields number for particle erosion in laminar flow. *Physics of Fluids*, **19**(6), 061706. 20, 152, 154, 156, 157

Ouriemi, M., Aussillous, P., & Guazzelli, E. 2009. Sediment dynamics. Part 1. Bed-load transport by laminar shearing flows. *Journal of Fluid Mechanics*, **636**, 295–319. 139

Paola, C. 2001. Modelling stream braiding over a range of scales. *Retrieved from the University of Minnesota Digital Conservancy*. 29

Paola, C., & Leeder, M. 2011. Environmental dynamics: Simplicity versus complexity. *Nature*, **469**(7328), 38. 11

Paola, C., Straub, K., Mohrig, D., & Reinhardt, L. 2009. The "unreasonable effectiveness" of stratigraphic and geomorphic experiments. *Earth-Science Reviews*, **97**(1), 1–43. 11, 86

Papanicolaou, AN, Diplas, P, Evaggelopoulos, N, & Fotopoulos, S. 2002. Stochastic incipient motion criterion for spheres under various bed packing conditions. *Journal of Hydraulic Engineering*, **128**(4), 369–380. 20

Paphitis, D. 2001. Sediment movement under unidirectional flows: an assessment of empirical threshold curves. *Coastal Engineering*, **43**(3-4), 227–245. 19

Parker, G. 1976. On the cause and characteristic scales of meandering and braiding in rivers. *Journal of fluid mechanics*, **76**(3), 457–480. 31, 137

Parker, G. 1978a. Self-formed straight rivers with equilibrium banks and mobile bed. Part 1. The sand-silt river. *J. Fluid Mech.*, **89**, 109–125. 28, 73

Parker, G. 1978b. Self-formed straight rivers with equilibrium banks and mobile bed. Part 2. The gravel river. *J. Fluid Mech.*, **89**, 127–146. 28

Parker, G., Wilcock, P.R., Paola, C., Dietrich, W.E., & Pitlick, J. 2007. Physical basis for quasi-universal relations describing bankfull hydraulic geometry of single-thread gravel bed rivers. *Journal of Geophysical Research: Earth Surface*, **112**(F4). 17

Peixinho, J., & Mullin, T. 2007. Finite-amplitude thresholds for transition in pipe flow. *Journal of Fluid Mechanics*, **582**, 169–178. 190

Perrin, J. 1913. *Les atomes.* CNRS. 74

Phillips, C.B., & Jerolmack, D.J. 2016. Self-organization of river channels as a critical filter on climate signals. *Science*, **352**(6286), 694–697. 161

Piazza, R., & Parola, A. 2008. Thermophoresis in colloidal suspensions. *Journal of Physics: Condensed Matter*, **20**(15), 153102. 74

Romans, B.W., Castelltort, S., Covault, J.A., Fildani, A., & Walsh, J.P. 2016. Environmental signal propagation in sedimentary systems across timescales. *Earth-Science Reviews*, **153**, 7–29. 11

Royall, C.P., van Roij, RHHG, & van Blaaderen, A. 2005. Extended sedimentation profiles in charged colloids: the gravitational length, entropy, and electrostatics. *Journal of Physics: Condensed Matter*, **17**(15), 2315. 74

Schumm, S.A., Mosley, M.P., & Weaver, W.E. 1987. *Experimental fluvial geomorphology.* Wiley: New York. 86

Seide, P, Weingarten, VI, & Morgan, EJ. 1960. *The development of design criteria for elastic stability of thin shell structures.* Tech. rept. TRW Space Technology Labs Los Angeles CA. 188

Seizilles, G. 2013. *Forme d'équilibre d'une rivière.* Ph.D. thesis, Université Paris-Diderot-Paris VII. 19, 28, 41, 73, 109, 115, 128, 129

Seizilles, G., Devauchelle, O, Lajeunesse, E., & Métivier, F. 2013. Width of laminar laboratory rivers. *Phys. Rev. E.*, **87**, 052204. 21, 22, 23, 24, 25, 37, 88

Seizilles, G., Lajeunesse, E., Devauchelle, O., & Bak, M. 2014. Cross-stream diffusion in bedload transport. *Phys. of Fluids*, **26**(1), 013302. 20, 35, 37, 38, 39, 57, 68, 71, 73, 137, 139, 140, 141, 152, 154, 156, 157

Seminara, G. 2010. Fluvial sedimentary patterns. *Annual Review of Fluid Mechanics*, **42**, 43–66. 31, 137

Sen, S., Subramanian, S., & Discher, D.E. 2005. Indentation and adhesive probing of a cell membrane with AFM: theoretical model and experiments. *Biophysical journal*, **89**(5), 3203–3213. 190

Shankar, P.N., & Kumar, M. 1994. Experimental determination of the kinematic viscosity of glycerol-water mixtures. *Proc. R. Soc. Lond. A*, **444**(1922), 573–581. 173

Shields, A. S. 1936. Anwendung der Aehnlichkeitsmechanik und der Turbulenzforschung auf die Geschiebebewegung. *Mitteilung der Preussischen Versuchsanstalt fur Wasserbau und Schiffbau*, **26**. 19, 136, 138

Shvidchenko, A.B., Pender, G., & Hoey, T.B. 2001. Critical shear stress for incipient motion of sand/gravel streambeds. *Water Resources Research*, **37**(8), 2273–2283. 20

Sinha, R. 2008. Kosi: Rising waters, dynamic channels and human disasters. *Economic and Political Weekly*, 42–46. 9

Sinha, R. 2009. The great avulsion of Kosi on 18 August 2008. *Current Science*, **97**(3), 429–433. 9, 26

Smith, L.C., Isacks, B.L., Bloom, A.L., & Murray, A.B. 1996. Estimation of discharge from three braided rivers using synthetic aperture radar satellite imagery: Potential application to ungaged basins. *Water Resources Research*, **32**(7), 2021–2034. 40

Smith, Norman D, & Smith, Derald G. 1984. William River: An outstanding example of channel widening and braiding caused by bed-load addition. *Geology*, **12**(2), 78–82. 27, 28, 29

Stebbings, J. 1963. The shapes of self-formed model alluvial channels. *Proceedings of the Institution of Civil Engineers*, **25**(4), 485–510. 32, 33, 101, 158

Tal, M., & Paola, C. 2007. Dynamic single-thread channels maintained by the interaction of flow and vegetation. *Geology*, **35**(4), 347. 86

Thompson, J., & T., Michael. 2015. Advances in shell buckling: theory and experiments. *International Journal of Bifurcation and Chaos*, **25**(01), 1530001. 190

Vanderwel, C., & Ganapathisubramani, B. 2015. Effects of spanwise spacing on large-scale secondary flows in rough-wall turbulent boundary layers. *Journal of Fluid Mechanics*, **774**. 137

Virot, E., Kreilos, T., Schneider, T.M., & Rubinstein, S.M. 2017. Stability landscape of shell buckling. *Physical review letters*, **119**(22), 224101. 188, 189, 190, 191

Wierzbicki, T. 2017. *Structural Mechanics: Course notes.* None. 188

Willingham, D., Anderson, W., Christensen, K.T., & Barros, J.M. 2014. Turbulent boundary layer flow over transverse aerodynamic roughness transitions: induced mixing and flow characterization. *Physics of Fluids*, **26**(2), 025111. 137

Yalin, M.S. 1977. *Mechanics of sediment transport.* New York, U.S.A.: Pergamon Press Inc. 20

Yamasaka, M., Ikeda, S., & Kizaki, S. 1987. Lateral sediment transport of heterogeneous bed materials. *Doboku Gakkai Ronbunshu*, **1987**(387), 105–114. 81, 141, 157

Yan, L., Barizien, A., & Wyart, M. 2016. Model for the erosion onset of a granular bed sheared by a viscous fluid. *Physical Review E*, **93**(1), 012903. 37

Auto-organisation du transport de sédiments dans les rivières alluviales

par

Anaïs Abramian

Résumé

Les rivières alluviales construisent leur propre lit avec les sédiments qu'elles transportent. En effet, l'écoulement qui les parcourt entraîne, transporte et dépose des sédiments, déformant ainsi le lit qui le conduit. Ce couplage sélectionne la forme d'équilibre d'une rivière.

Dans cette thèse, nous étudions l'influence du transport sédimentaire sur la forme et la stabilité d'une rivière alluviale. Pour ce faire, nous reproduisons des rivières en laboratoire en laissant s'écouler un liquide visqueux sur un lit granulaire. L'aspect du chenal ainsi formé dépend des débits de liquide et de sédiment injectés en entrée.

A l'aide de ces expériences, nous mettons en évidence les deux mécanismes qui contrôlent l'équilibre d'une rivière. D'abord, la gravité entraîne les grains vers le centre du chenal. Ce mécanisme érode continuellement les berges de la rivière, et tend donc à l'élargir. Cependant, les collisions d'un grain avec le lit dévient sa trajectoire dans la direction transverse à l'écoulement. Les grains se comportent ainsi comme des marcheurs aléatoires, qui, collectivement, diffusent vers les berges de la rivière. A l'équilibre, cette diffusion compense la gravité, et fixe ainsi la forme de la rivière.

Lorsque la diffusion prend le dessus sur la gravité, elle peut induire une instabilité. En effet, si on perturbe un lit sédimentaire avec des stries longitudinales, le cisaillement fluide est plus faible là où l'écoulement est moins profond. Par conséquent, les grains diffusent depuis les creux de la perturbation vers ses crêtes. Cette rétroaction déstabilisante pourrait générer de nouveaux chenaux, et expliquer la formation des rivières en tresses.

Mots clés : géomorphologie fluviale, diffusion, instabilités.

Self organisation of sediment transport in alluvial rivers

by

Anaïs Abramian

Abstract

An alluvial river builds its own bed with the sediment it transports. The channel bounds the flow, which in turns deforms the channel through erosion and deposition. This coupling between flow and sediment transport selects the shape and the size of the river. In this manuscript, we investigate it using laboratory experiments.

The first ingredient of this coupling is gravity, which pulls the moving grains towards the center of the channel, thus continually eroding the banks. However, due to the roughness of the bed, the trajectory of a moving grain fluctuates across the stream. The bedload layer is therefore a collection of random walkers which diffuse towards the less active areas of the bed. In a river at equilibrium, this diffusion counteracts gravity to maintain the banks.

When gravity and diffusion are out of balance, their interaction causes an instability. Indeed, if an initially flat bed of sediment is perturbed with longitudinal streaks, the flow-induced shear stress is weaker where the flow is shallower. Therefore, bedload diffusion induces a sediment flux towards the crests of the perturbation. This positive feedback induces an instability which can generate new channels. We suggest that this mechanism could initiate the braiding of alluvial rivers.

Keywords : Geomorphology, sediment transport.

Photo courtesy

- Ch. 1 : Bertrand Stofleth "La rhodanie"
- Ch. 2 : Bertrand Stofleth "La rhodanie"
- Ch. 3 : Vasantha Yogananthan, "The Crossing" (Madhubani, Bihar, Inde, 2014)
- Ch. 4 : Bertrand Stofleth "La rhodanie"
- Ch. 5 : Vasantha Yogananthan, "Ramayana Schooltrip" (Valmiki Nagar, Bihar, Inde, 2014)